PAUL SCHERRER INSTITUT

PSI

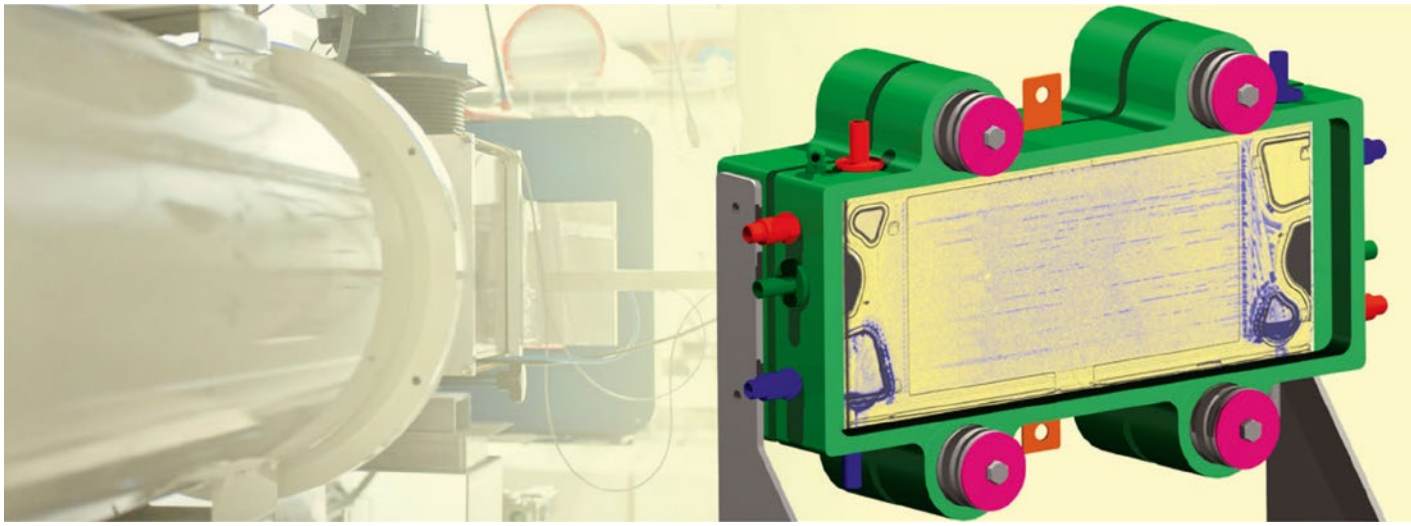

Annual Report 2017

Electrochemistry Laboratory

Cover
Neutron imaging at the NEUTRA beamline of the water distribution in a commercial-size fuel cell for the AutoStack CORE project (http://autostack.zsw-bw.de).

PAUL SCHERRER INSTITUT

PSI

Annual Report 2017

Electrochemistry Laboratory

Paul Scherrer Institut
Electrochemistry Laboratory
5232 Villigen PSI
Switzerland

Secretary
Phone +41 56 310 29 19
Fax +41 56 310 44 15

Hardcopies of this report are available from

Cordelia Gloor
cordelia.gloor@psi.ch
Paul Scherrer Institut
5232 Villigen PSI
Switzerland

A full version of this report is also available on the web
http://www.psi.ch/lec

Publisher
Electrochemistry Laboratory
Paul Scherrer Institut
5232 Villigen PSI
Switzerland

Editorial Team
Cordelia Gloor / Peter Lutz
Felix N. Büchi
Lorenz Gubler
Thomas J. Schmidt
Claire Villevieille

Printing
Paul Scherrer Institut

ISSN 1661-5379
DOI: 10.3929/ethz-a-007047464
PSI Electrochemistry Laboratory : : Annual Report 2017

CONTENTS

3 **Editorial**

4 **The Electrochemistry Laboratory at a Glance**

6 **Energy Storage Research in Switzerland**

9 Scientific Achievements 2017

Batteries – Materials & Diagnostics

10 **Structural investigation of $Li(Ni,Co,Mn)O_2$ cathode material using *operando* neutron powder diffraction**

12 **Towards high-performance Li-rich cathode batteries: A facile surface modification of composite electrodes using functional polyacrylate coatings**

13 **Structural characterization of layered $Li_xNi_{0.80}Co_{0.15}Al_{0.05}O_2$ ($0 < x \leq 2$) oxide electrode for Li-ion cells**

14 **Investigation of the promising P2-$Na_{0.67}Mn_{0.6}Fe_{0.25}Al_{0.15}O_2$ cathode material**

16 **The surface evolution of aged NCA particles monitored by XPEEM during the early stages of cycling**

17 **The controversial surface reactivity of $Li_4Ti_5O_{12}$ in the aprotic electrolyte disclosed with XPEEM**

18 **Improved electrochemical performance of Mn_XO_Y as an anode for Li-ion batteries**

20 **GITT analysis of silicon-graphite electrodes**

21 **Binder evaluation for Si-graphite electrodes**

22 **All-solid-state Li-ion batteries based on garnet solid electrolyte using high-energy alloy anode materials**

24 **Impact of the electrode engineering on the electrochemical performance of $LiCoO_2$ as cathode material in Li_3PS_4 based all-solid-state lithium-ion batteries**

26 **Bio-waste lignin-based as carbonaceous materials for Na-ion batteries**

28 **Modelling the performance of alkali-ion batteries**

29 **Voltaic losses of vanadium flow batteries at different states of charge**

31 **Chemical reactivity of tristrimethylsilylphosphate (TMSPa) towards fluorides in Li-ion battery electrolytes**

32 **Diffusion of solid reaction products during SEI formation in Li-ion batteries**

33 **Development of a Raman spectro-electrochemical cell**

34 **Injection cell setup for online electrochemical mass spectrometry (OEMS)**

35 **Real-time observation of the interfacial reactions in all-solid-state Li-ion battery using *operando* XPS**

Fuel Cells & Electrolysis – Materials & Diagnostics

38 **Experimental study of the water management in the Autostack-Core Evo2 fuel cell with neutron radiography**

40 **Selective visualisation of water in gas diffusion layers with neutron dark field imaging**

42 **High resolution visualization of GDL coating with combined X-ray and neutron tomography**

44 **Convection driven droplet detatchment from gas diffusion layers**

46 **The impact of phosphoric acid migration on the performance of HT-PEFCs**

48 **Providing secondary control with PEM electrolyzer technology**

49 **Correlation between the morphology of the porous transport layers and the performance characteristics of a polymer electrolyte water electrolysis cell**

51 **Surface characterization of porous transport layer**

52 ***In-operando* neutron imaging of PEWE cation mitigation**

Electrocatalysis & Interfaces

56 **Co-electrolysis cells for efficient reduction of carbon dioxide from gas phase at low temperature using bipolar like membrane**

58 **CO_2 reduction to valuable products: a Differential Electrochemical Mass Spectrometry (DEMS) study**

60 **Sputter deposited Cu and CuO_x thin films for electroreduction of CO_2**

62 **Versatile calibration method for mass spectrometry of interfering gases such as mixtures of CO, N_2, and CO_2**

64 **Highly active nano-perovskite catalysts for oxygen evolution reaction: Insights into activity and stability in alkaline and quasi-neutral pH electrolytes**

66 **Correlating the local structure and electronic properties of nanoparticulate $Ni_xFe_{1-x}O$ with the oxygen evolution activity and stability via *operando* XAS**

68 **Investigating PEFC anode durability under fuel starvation conditions**

70 **Boosting Pt oxygen reduction reaction activity by tuning the oxide support**

71 **Quantifying Pt-nanoparticle detachment and growth under PEFC-relevant potential cycling conditions through combined XAS and SAXS**

72 **Impact of the pyrolysis temperature on the performance of Fe-based oxygen reduction catalyst for polymer electrolyte fuel cell cathodes**

74 **A combined XAS and SAXS setup for the *operando* study of carbon supported Pt nanoparticle catalysts**

77 The Electrochemistry Laboratory

Facts & Figures

78 **Structure 2017**

79 **Personnel 2017**

82 **Dissertations 2017**

84 **Exchange Students, Diploma Theses, Summer Students, Guest Scientists**

86 **Seminar, Invited Speakers**

87 **Awards**

88 **Conferences – Symposia**

91 **Review Activities of the Laboratory**

93 **Industrial Partners**

94 **Documentation**

EDITORIAL

PSI's Electrochemistry Laboratory is the leading center for electrochemical research in Switzerland, carrying out a great variety of projects in the electrochemical energy storage and conversion areas. The Lab bridges fundamental electrochemical science with applied electrochemical engineering, which is unique even on international standards and allows us to keep a systemic view even when addressing basic scientific questions.

Significant parts of our groups are partners within the Swiss Competence Centers for Energy Research (SCCERs) *Mobility* and *Heat & Electricity Storage,* respectively. These Centers, inaugurated in 2014, are multi-year programs addressing the challenges of the Swiss Energy Strategy 2050. The work in these centres is transitioning research from basic research to more applied development of new technologies and is increasing the technological readiness levels.

In this Annual Report 2017, you will not only find details on PSI's Electrochemistry Laboratory and the SCCER *Heat and Electricity Storage,* but also short insights into the ongoing projects and activities, summarized in 39 short reports authored by our researchers demonstrating some of our contributions to the grand challenge of electrochemical energy storage and conversion. Further the Laboratory's key facts and figures for 2017 are given, including a full list of our 65 publications and numerous talks demonstrating the leading role of PSI's Electrochemistry Laboratory at the national and international level.

In April 2017, the Lab held the 33rd annual Electrochemistry Symposium *From the Lab to the Market* with world-class scientists as speakers attracting an audience of more than 120 participants. Details of this event you will find also in this annual report on page 89.

2017 was also a successful year for five of our PhD students who successfully defended their theses. All of the new PhDs were able to directly continue their careers either in an academic or industrial environment.

At this point, it needs to be mentioned that all our projects and results could not have been achieved without the funding we received over the years from industrial partners and the different funding agencies in Switzerland and abroad. Therefore, we would like to take this opportunity to thank all our funding sources hoping to continue our successful collaborations in the years to come.

With the year 2017 ending, however, also important changes took place. Thomas J. Schmidt resigned his duty as the Laboratory head, taking over new responsibilities with leading the Energy and Environment Division of PSI. Felix N. Büchi will take over the lead of the Laboratory as of 2018 as acting head. The change secures a smooth transition into a successful future for the Lab.

Thomas J. Schmidt & Felix N. Büchi

THE ELECTROCHEMISTRY LABORATORY AT A GLANCE

Our Mission

Advancement of electrochemical energy storage and conversion by

- **developing novel electrochemical materials, cells and devices;**
- **providing insights into electrochemical materials, cells and device properties.**

PSI's Electrochemistry Laboratory is Switzerland's largest Center for Electrochemical Research with about 70 employees. Our mission is to advance the scientific and technological understanding of electrochemical energy storage and conversion specifically in the context of a sustainable energy system, where renewable energy is required to be stored in secondary batteries or chemicals such as hydrogen and (re-)converted into electricity. The Laboratory's R&D, is hence focused on secondary batteries – specifically Li- and Na-based systems –, polymer electrolyte fuel cells and electrolyzers, as well as redox flow cells.

As a research institute's laboratory we are bridging the gap between fundamental science and applied engineering by combining both academically and industrially relevant questions. For all outlined devices we not only develop fundamental understanding of materials on atomic and molecular level (electrochemical materials sciences and electrocatalysis), but also in the applied development of technical cells and devices, e.g., fuel cell systems.

On all technical complexity levels, we are developing and utilizing advanced *in situ* and *operando* diagnostic tools to gain insights in properties and processes from the nanometer to the centimeter scale, respectively, often making use of PSI's unique large scale facilities such as the Swiss Light Source (SLS) and the Swiss Neutron Spallation Source (SINQ).

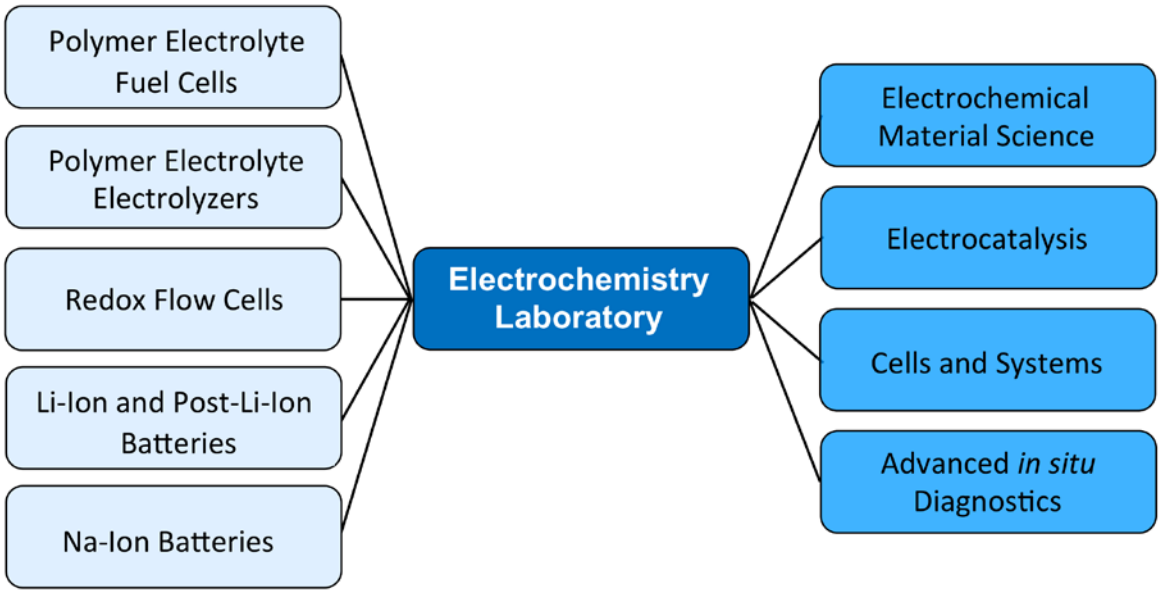

Electrochemical energy storage

The vision of the Electrochemical Energy Storage Section is the development of the best energy storage system.

We work on rechargeable batteries which are mainly lithium and sodium based. The scientific goal is a profound understanding of electrochemical processes in complex non-aqueous systems. In particular, of utmost scientific interest are the numerous interactions of all components of electrochemical energy storage systems (batteries, supercapacitors, and hybrids) determining the safety and life time of such systems.

Rechargeable battery assembly in an Argon glove box.

The work equally considers the synthesis of novel materials for electrochemical energy storage, the modification of known materials (e.g., carbon) and material characterization, keeping in mind the entire span from basic science to industrial applications.

To answer the scientific questions, we develop various sophisticated *in situ* and *operando* methods for use in the field of non-aqueous solid-state electrochemistry and investigate the physical and electrochemical properties of insertion materials and electrochemical interfaces *in situ*.

Also, we do electrochemical engineering work on three-dimensional electrodes and characterize industrial batteries.

Electrochemical energy conversion

The Electrochemical Energy Conversion Section is focused on the development and in-depth understanding of materials, processes and devices for the conversion of renewable power to hydrogen (or syngas) and back to power. Especially in the context of a sustainable energy system utilizing hydrogen as an energy carrier, these electrochemical energy conversion steps are of particular importance.

In this topical context the work is focused on Polymer Electrolyte Fuel Cells (PEFC), Polymer Electrolyte Water Electrolyzers (PEWE) for water electrolysis and the co-electrolysis of CO_2 and water, respectively. In addition, work is devoted on the materials development for Redox Flow Cell systems.

The R&D strategy involves activities on four pathways:

- system, stack and cell engineering;
- development of new ion conducting membranes with tuned properties for fuel cells, water electrolyzers, and redox flow batteries;
- research in electrocatalysis and the reaction kinetics of the relevant reactions (e.g., the oxygen electrode reactions) for improved understanding of intrinsically limiting factors; and
- the development and application of advanced *in situ* and *operando* diagnostic imaging tools on stack, cell and component levels (X-rays and neutrons).

Device level characterization of an all-vanadium redox flow cell with a membrane developed in-house.

ENERGY STORAGE RESEARCH IN SWITZERLAND

The SCCER «Heat and Electricity Storage» highlights of Phase II

Thomas J. Schmidt, Jörg Roth, Petr Novák, Claire Villevieille

The SCCER «Heat and Electricity Storage» (HaE) has the overarching goal to provide the capacity in terms of competencies as well as technologies to help making the energy strategy 2050 successful. Since the boundary conditions that the Swiss society will have to cope with in terms of resources, energy supply, distribution and demand are hard to predict 30 years in advance, respectively, the portfolio of technical solutions and competencies within energy storage has to cover a wide range.

This comprises short term and long term heat and electricity storage but also power-to-hydrogen and hydrocarbon, making not only the energy supply, but also the supply of hydrocarbons renewable.

During phase I the cornerstone was set by exploring and proving the principles of storage concepts for short term high temperature heat and seasonal low temperature heat storage, nano-structured battery materials, hydrogen production based on non-precious metal catalysis and advanced storage concepts. The first steps towards electro-catalytic and catalytic CO_2 reduction under near ambient conditions was taken. The tools and methods for technology evaluation were developed and applied. A system study on power-to-gas demonstration plants was carried out. In addition, an important part of phase I was the investigation of the flexible generation and storage of power and heat, as well as the manufacturing and durability aspects of batteries.

The SCCER «Heat and Electricity Storage» started successful into its second phase in 2017. In comparison to the first phase where the research topics were broader, in phase II the research focuses in on the most promising topics for implementation:

- ***Approaches like power-to-heat-to-power were dropped mainly for economic reasons, while taking seasonal heat storage into the focus. The battery material development now focuses on the advancement of two selected prospective battery systems, the high-end lithium-ion battery and the potentially cost-effective sodium-ion battery.***
- ***The co-electrolysis explores mainly formation of methanol and hydrocarbons, rather than methane, also for economic reasons.***
- ***The system assessment activities of phase I had the model development in focus, while in phase II the application of the models is the main activity.***

Besides the established eight SCCERs of phase I, in phase II additional networking structures between the SCCERs were supported by Innosuisse (formerly CTI). Four smaller joint activities between CREST and SOE, CREST and Mobility, CREST and FURIES and one to produce a whitepaper on power to product were established, as well as two bigger activities on scenario and modeling and one to harmonize all the technology demonstrators, installed by the SCCERs in phase I.

Phase II has successfully started and made good progress in 2017. Focusing the research topics and partly restructuring of the SCCER work packages improved the cooperation and collaboration on one hand. On the other hand the resources given to the Competence Center either by the funding agency Innosuisse, SFOE, SNF and others, the partner's home institutions, and the numerous industrial partners (which are kindly acknowledged) promotes the most promising technologies to the next level towards the implementation readiness.

The roadmap for phase II and main results of 2017, where groups from ECL are involved, are described in more detail in the next section. A complete picture of the SCCER HaE results in 2017 can be obtained from the SCCER HaE Annual Report 2017 (www.sccer-hae.ch)

Battery

While in phase I the focus was set on the chemistry of the anode side, now the chemistry of the cathode will be adapted and both scaled-up for the nano Li- and the Na-type systems, respectively. In parallel the prototype manufacturing line for battery cells will be developed.

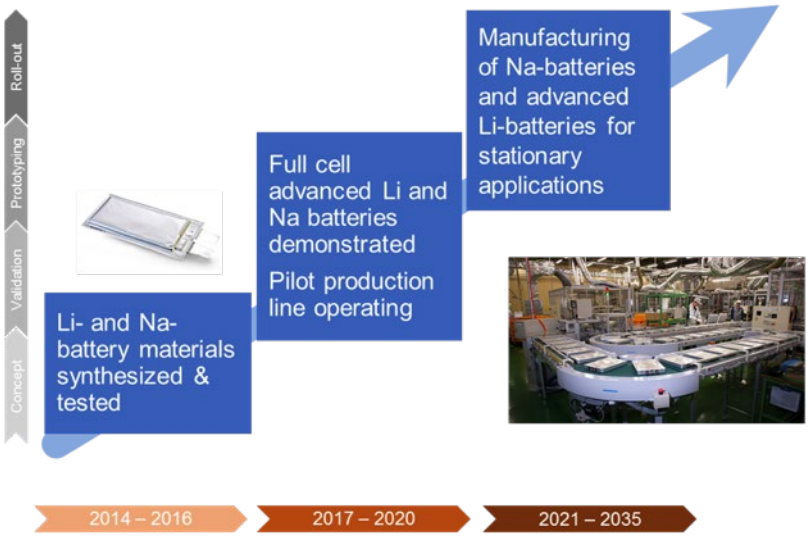

Figure 1. *The roadmap for the battery materials and manufacturing activity.*

At the end of phase II, the new chemistry will be proven in full cells, while a pilot manufacturing line will not only be ready to produce the new cells in small series for pre-production evaluation, but also will be a stepping stone to a fully automated manufacturing line (Figure 1). The knowhow to design this manufacturing line helps the Swiss industry to export the technology and may also offer the chance to profitably produce battery cells in Europe.

The SCCER research activities focusing on Na-ion batteries targeted grid storage applications, with the goal to lower current cost by ca. 20%.

In commercial full cells where both anode and cathode are based on Na host materials, the energy density gap between Na and Li systems is considerably reduced to only 30 % instead of a factor of 3 (if judged on metal mass). Additionally, Na is one of the most abundant and cheap elements on earth and Al, which does not alloy with Na, can be used as a cheap current collector in Na systems, leading to cost and mass reductions for the entire battery [ref: SCCER HaE *Annual Activity Report 2016*, p. 24–26].

Research in the SCCER HaE demonstrated that it is possible to develop low cost carbonaceous, biowaste based anode materials with reversible specific charge > 270 mAh/g.

On the cathode side, also cheaper elements are targeted to ensure that the Na-ion batteries are developed at lower costs than the Li-ion counterpart. A new Co-free cathode P2 $Na_{0.67}Mn_{0.6}Fe_{0.25}Al_{0.15}O_2$ was successfully synthesized and characterized. The rate capability tests showed higher specific charge and a better cycling stability than the analogous P2 $Na_{0.67}Mn_{0.6}Fe_{0.25}Co_{0.15}O_2$ cathode demonstrating that tuning the cathode chemistry is important not only to improve the electrochemical performance but also the cost. [ref: SCCER HaE *Annual Activity Report 2017*].

Catalytic CO_2 reduction

The focus of catalytic CO_2 reduction in phase I was set on methane generation, but for economic reasons methanol and ethene was identified to be more favorable. Phase II, hence, will focus on production of these molecules.

While the proof of principle was given that electrochemical CO_2 reduction works on the cell level at technical conditions, the next step is to develop durable, selective and efficient catalysts and implement them into reactor systems for the CO_2 reduction on both, the electrochemical and chemical pathway. A successful development will result in demonstration units ready to be taken by implementation partners.

The next steps for the direct and indirect conversion of CO_2 to methanol will target the improvement of the selectivity in CO_2 conversion and benchmarking processes by comparison to industrial catalysts.

The direct hydrogenation of CO_2 to methanol is investigated by ETHZ, where supported Cu catalysts (heterogeneous) are being developed. Following the discovery that interfacial sites in Cu/ZrO_2 are essential for the increase activity and high methanol selectivity in 2016, scalable catalysts using flame spray pyrolysis have been developed; they show higher catalytic performances (activity and selectivity) than commercial catalysts. In addition, an alternative approach, which is currently being patented, has been developed that consists of tailoring the interface of Cu nanoparticles supported on high surface area oxides through selective doping. This approach allows an increase of activity and methanol selectivity of the Cu-catalysts (Figure 2). Discussion with industrial partners on the development of more efficient industrial catalysts based on this approach is currently ongoing.

With homogeneous catalysts, indirect conversion of CO_2 to methanol and hydrocarbons are being pursued by EPFL. Through the development of efficient trapping of CO_2 using ionic liquids, the concentrated CO_2 can be converted first to cyclic carbonate and then to methane, using a complementary Ru-based heterogeneous hydrogenolysis catalyst. CO_2 can also be converted to methanol using N-formylation of amines as a key step followed by hydrogenation. Discovered with homogeneous catalysts, this process is currently being investigated using heterogeneous catalysts based on both precious metal and earth abundant metals. [Ref: SCCER HaE *Annual Activity Report 2017*]

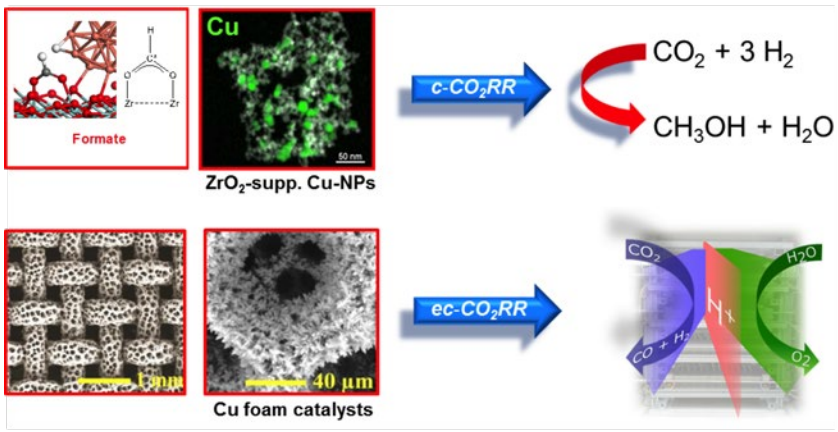

Figure 2. *Approaches towards commercially viable CO_2 reduction.*

SCIENTIFIC ACHIEVEMENTS 2017

Batteries –

Materials & Diagnostics

Structural investigation of $Li(Ni,Co,Mn)O_2$ cathode material using *operando* neutron powder diffraction

L. Vitoux, D. Sheptyakov, C. Villevieille
phone: +41 56 310 5655, e-mail: laura.vitoux@psi.ch

Lithium layered oxides $LiNi_xMn_yCo_2O_2$ (Li-NMC) are considered as one of the most promising cathode materials for high-energy lithium-ion batteries. They have a α-$NaFeO_2$-type layered structure (space group R-3m) [1] illustrated in Figure 1. With oxygen transition metals TM (TM = Ni, Mn, Co) form slabs of edge-sharing octahedra. Lithium ions intercalate in octahedral interstitial sites between these TM slabs. Because of similar ionic radii, Li^+ and Ni^{2+} ions can exchange crystallographic sites. It results that less lithium ions can be (de)intercalated, leading to loss in specific charge.

This Li/Ni exchange, also called cation mixing, is reported as a main cause for electrochemical performance fading [2]. Understanding the reaction mechanism of the different NMC family members during battery operation is essential to improve the battery performance. To this end, neutron powder diffraction is a technique of choice, as it is sensitive to light elements, such as oxygen and lithium, and thus can be effectively used to enable to localize and quantify lithium ions in the structure. Moreover, the difference in coherent scattering lengths of lithium and nickel would enable to evidence the possible Li/Ni exchange.

A cylindrical cell was designed at PSI to perform *operando* neutron diffraction experiments (Figure 2) and the structural evolution during delithiation of $LiNi_{1/3}Mn_{1/3}Co_{1/3}O_2$ was investigated.

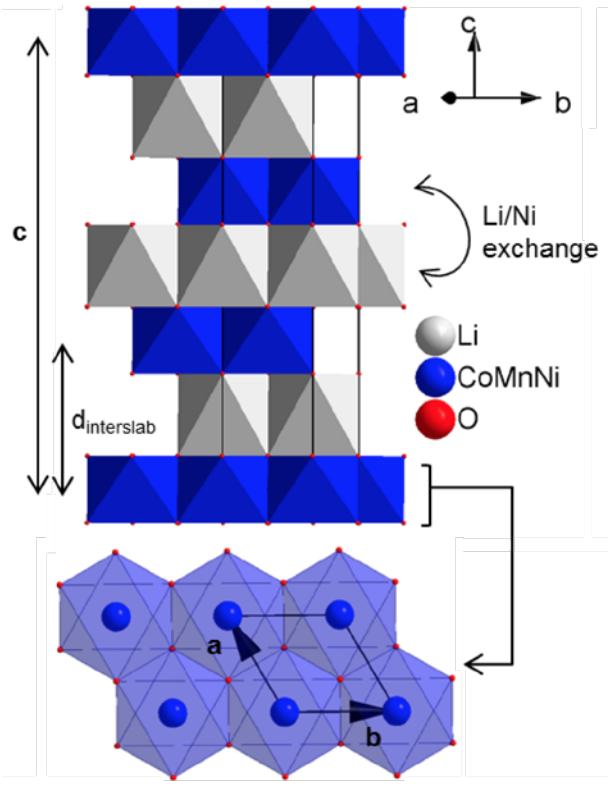

Figure 1. *α-$NaFeO_2$-type layered structure of $Li(Ni,Mn,Co)O_2$ described in an hexagonal lattice.*

Experimental

Self-standing films were prepared by dissolving 20 %wt of PVDF binder (Kynar Flex 2801, Arkema, France) in acetone and few drops of ethanol. 70 %wt $LiNi_{1/3}Mn_{1/3}Co_{1/3}O_2$ (hereafter referred to as NMC111, Imerys, Switzerland) and 10 %wt conductive carbon (Super P, Imerys, Switzerland) were then mixed with the binder using a mechanical turbo stirrer.

The slurry was immediately cast with a 300 µm wet thickness using a doctor blade technique on a glass plate. The film detaches itself after drying under ambient condition.

Two layers of self-standing films were coated on both sides of an aluminium mesh using a calendering machine at 80 °C and 5 bars. The positive electrode is resized at the correct dimensions (2.8 x 12 cm) with a thickness of 120 µm achieved after calendering, and contains about 700 mg of active material.

Lithium metal, with a calendered thickness of 170 µm, was used as counter-electrode.

Positive and negative electrodes, separated by Celgard 2500 foils were rolled together around the mandrel and inserted inside the cylindrical cell (Figure 2). Finally, 0.8 mL of deuterated electrolyte (1 M $LiPF_6$ in d-EC : d-DMC (30 : 70)) were added on the top of the rolled layers.

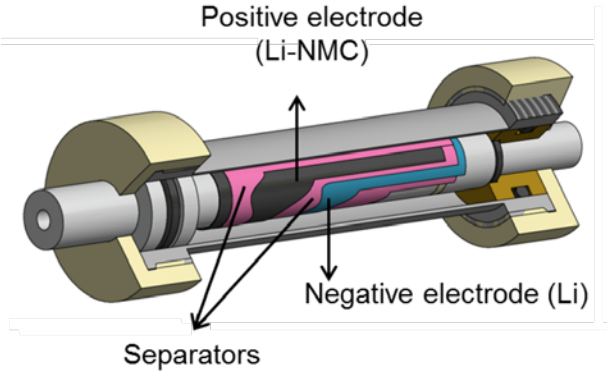

Figure 2. *Home-made cylindrical cell developed at PSI for operando neutron powder diffraction experiment.*

Each component put inside the cylindrical cell is carefully chosen to optimize the signal on the neutron powder diffraction pattern. To reduce the content of hydrogen, which generates a high background on the neutron diffraction pattern, the use of deuterated electrolyte is essential. Similarly Celgard 2500 was selected as separator because of its lower background contribution. Aluminium mesh instead of aluminium foil as current collector for the positive electrode is also expected to reduce the signal of aluminium on the diffraction pattern.

All neutron diffraction experiments were performed on the HRPT diffractometer at SINQ spallation source (PSI).

Results

The structure of the pristine material was assessed by neutron powder diffraction. Rietveld refinements of the structural parameters highlighted 2.8 % of lithium ions are exchanged with nickel ions in NMC111 (Table 1 and Figure 3). This validates the choice of neutron powder diffraction to follow the evolution of cation mixing upon lithium (de)lithiation.

Space group *R* -3 *m* (# 166), Z=3 a_{hex} = 2.85894(3) Å, c_{hex} = 14.2280(1) Å					
Atom	x	y	z	Biso	occ.
Li	0	0	1/2	0.43 (4)	0.971(1)
Li (in Ni site)	0	0	0	0.11 (2)	0.028(1)
Ni	0	0	0	0.11 (2)	0.306(1)
Ni (in Li site)	0	0	1/2	0.43 (4)	0.028(1)
Co	0	0	0	0.11 (2)	1/3
Mn	0	0	0	0.11 (2)	1/3
O	0	0	0.25898 (4)	0.668 (9)	1

Table 1. *Refined crystal structure parameters of the* $(Li_{1-x}Ni_x)[(Ni_{1/3-x}Li_x)Co_{1/3}Mn_{1/3}]O_2$ *pristine compound.*

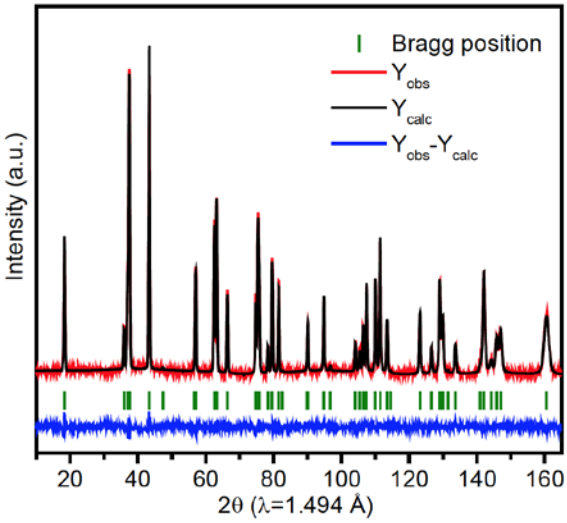

Figure 3. *Rietveld refinement of the neutron powder diffraction pattern of* $LiNi_{1/3}Mn_{1/3}Co_{1/3}O_2$.

A cylindrical half-cell containing NMC111 as positive electrode was cycled from 3.4 V (OCP) to 4.3 V vs. Li^+/Li at C/20 rate (C/n means 1 Li reaction in *n* hours). Neutron diffraction data were acquired in *operando* mode, meaning while the battery cycles without any relaxation/pause period. One scan is collected during 4 minutes. To improve the statistics, we merged sixteen scans into one pattern (~1 h). Contour plot representation of the *operando* neutron diffraction experiment is presented in Figure 4. Enlargement of specific 2θ ranges are shown alongside the electrochemical curve to follow the structural evolution during cycling.

Delithiation occurs along a solid solution process, as indicated by the slight and continuous shifting of the diffraction peaks. As NMC111 material crystallizes in a hexagonal lattice, the position of the (00*l*) lines is directly correlated to the value of the c-parameters, i.e. the distance between the TM slabs, called interslab distance ($d_{interslab} = c_{hex}/3$) (Figure 1). Because the (003) diffraction lines appear in the 2θ-range where a significant background is generated from the electrolyte, the color scale was adapted to help the understanding. Therefore the intensity of the diffraction lines in both enlargements cannot be compared. The (003) line shifts towards lower 2θ, i.e. higher d-spacings, which indicates that the c-parameter is increasing when lithium content decreases. This higher interslab distance results from higher electrostatic repulsions forces between the oxygenated layers due to the fewer amount of lithium ions in the interslab.

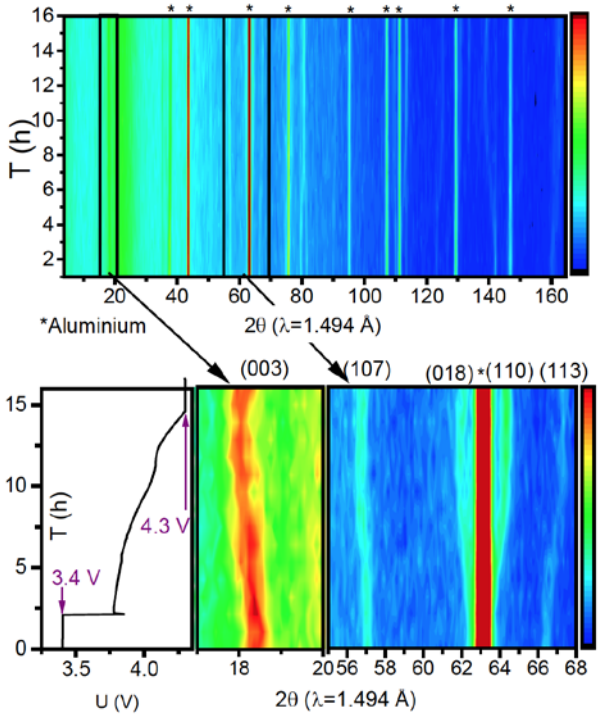

Figure 4. *Contour plot representation of the operando neutron powder diffraction measurement during the delithiation of* $LiNi_{1/3}Mn_{1/3}Co_{1/3}O_2$.

Moreover the shifting of the (110) line towards higher 2θ, i.e, lower d-spacings, illustrates the shrinking of the a_{hex} axis (and b_{hex} axis since $a_{hex} = b_{hex}$), which is directly correlated to the in plane TM-TM distance (TM = Ni, Mn or Co) in the hexagonal lattice (see Figure 1). This can be explained by the higher oxidation state of the nickel ions, which then have a smaller ionic radius.

The refinement of the atomic parameters by the Rietveld method would give us more insight on the structural changes occurring during the cycling. However it requires further data treatments to improve the signal to noise ratio achieved in this experiment.

References

[1] N. Yabuuchi, T. Ohzuku, *J. Power Sources* **119–121**, 171–174 (2003).
[2] E. Zhao, L. Fang, M. Chen, D. Chen, Q. Huang, Z. Hu, Q. Yan, M. Wu, X. Xiao, *J. Mater. Chem. A* **5**, 1679–1686 (2017).

Towards high-performance Li-rich cathode batteries: A facile surface modification of composite electrodes using functional polyacrylate coatings

B. Sun, M. El Kazzi, E. Müller, E.J. Berg
phone: +41 56 310 3968, e-mail: bing.sun@psi.ch

Surface modification of battery electrode materials provides cost-effective solutions to promote electrode surface stability and overall cell performance. By pre-forming thin coatings of ceramics or polymers, some existing problems (e.g., voltage fade and structural transformation) of high-voltage cathode materials, exemplified by Li-rich NCM [1], could be mitigated.

This work demonstrates the integration of polyacrylate (PAA) – a category of polyelectrolyte materials which are featuring superior adhesion capability [2, 3] – as surface coatings for the cathode composite electrodes. The operation mechanism of these coatings is also investigated in-depth using complementary techniques.

Experimental

Li-rich NCM active materials with PVdF binder and carbon additives were processed into composite electrode sheets. The LiPAA solutions at varied mass percentages (e.g., 0.1 %, 0.5 % and 5 %) were prepared and subsequentially blade-coated to produce coatings onto the composite electrodes. XPS and TEM, respectively, were applied to evaluate surface coating distribution through the composite electrodes and estimate the coating thickness. Galvanostatic cycling and *operando* gas analysis by online electrochemical mass spectrometry (OEMS) in half-cell configuration were used to assess the electrochemical impact post modification. LP47 (1 M $LiPF_6$ in EC : DEC = 3 : 7) was used in the experiments.

Results

The cycling performance of the pristine and modified electrodes is compared in Figure 1. Electrodes with LiPAA coatings demonstrated enhanced specific charge from initial cycles, following by noticeable improvements during long-term cycling – up to 50 mAh g^{-1} at the 100th cycle – as well as superior capacity retention.

Surface analysis using XPS demonstrated the presence of LiPAA coatings on the composite electrode surfaces, also detected in the bulk electrode at the regions approaching to the current collector. TEM further confirmed the thickness of these coatings is less than 5 nm. OEMS study on both the composite electrodes and the glassy carbon-based model electrodes was performed. Figure 2 demonstrated that *post modification* there is an overall reduction in gas evolutions. Much suppressed CO_2 evolution was seen from modified composite electrodes as well. This all indicates the effectiveness of LiPAA coatings to suppress interfacial decomposition (e.g., electrolyte side-reactions) under high anodic potentials.

Conclusions

A simple yet effective approach was developed using functional polymers as surface coating materials to stabilize Li-rich NCM cathode interphase. Improved specific charge and cycling stability were achieved *post modification*. Identifying the key properties controlling interfacial reactions would be instructive for the further manipulation of cathode interphase layers towards high energy and durable Li-ion batteries.

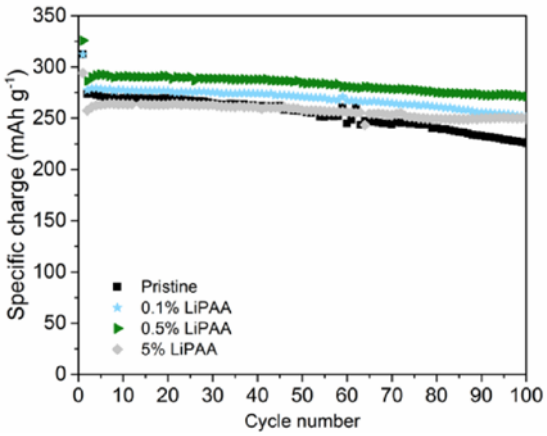

Figure 1. *Galvanostatic cycling performance of Li-rich NCM half cells using the pristine electrode and with varied coating loadings of LiPAA: 0.1 %, 0.5 % and 5 %. Voltage window 2.0–4.7 V at a cycling rate of 0.1 C under 25 ± 1 °C.*

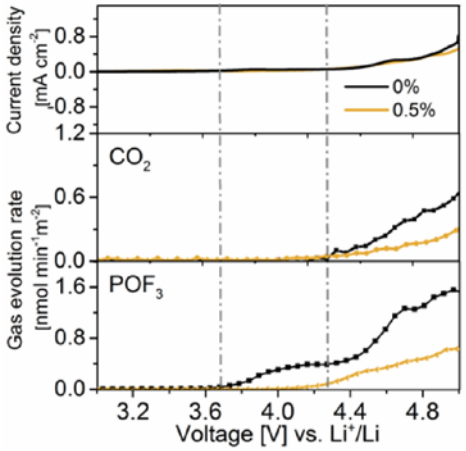

Figure 2. *OEMS results from the electrochemical stability measurement of the LiPAA-coated and the pristine glassy carbon electrodes between 3.0–5.0 V at 0.05 mV/s scan rate. The approximate quantities of CO_2 and POF_3 gases were normalized with respect to the electrochemical surface arear of the electrode.*

Acknowledgement

BASF SE is acknowledged for the financial support.

References

[1] P. Rozier, J.M. Tarascon, *J. Electrochem. Soc.* **162**, A2490 (2015).
[2] N.P.W. Pieczonka, V. Borgel, B. Ziv, et al., *Adv. Energy Mater.* **5**, 1501008 (2015).
[3] S. Komaba, K. Okushi, T. Ozeki, et al., *Electrochem. Solid-State Lett.* **12**, A107–A110 (2009).

Structural characterization of layered $Li_xNi_{0.80}Co_{0.15}Al_{0.05}O_2$ ($0 < x \leq 2$) oxide electrode for Li-ion cells

R. Robert, P. Novák

phone: +41 56 310 5426, e-mail: rosa.robert@psi.ch

High specific energy values for lithium-ions cells are achieved when cathodes operate at high potentials vs. Li^+/Li. Therefore, layered $LiTMO_2$ (TM = transition metal) cathodes that can operate at potentials above 4.3 V vs. Li metal are intensively investigated. One of the main drawbacks of these types of materials is their characteristic irreversible specific charge «loss» after the first cycle. Here we report on a careful investigation of reversible and irreversible specific charge «losses» of the layered $LiNi_{0.8}Co_{0.15}Al_{0.05}O_2$ (NCA) in the 1st cycle within the operating potential window of 4.3 V and 1.2 V vs. Li^+/Li. The associated structural reorganizations are thoroughly examined using *operando* X-ray powder diffraction. In this study, we particularly focus on the effect that deep discharge has on the structural stability of the NCA. Furthermore, we evaluate the degree of reversibility of the different processes involved during electrochemical cycling.

Experimental

The positive electrode and coin-type cells were prepared as in [1]. *Operando* XRD measurements were carried with an in-house constructed cell in reflection geometry, cycled galvanostatically between 4.3 V and 1.2 V at a rate of 10 mA/g. The diffraction patterns were recorded continuously by step scanning (with a step size of 0.017 °) over the 2Θ range of 16 ° ≤ 2Θ ≤ 23 ° and 34 ° ≤ 2Θ ≤ 47 °. X-ray powder data was treated using the FullProf suite [2] software.

Results

Figure 1 displays the electrochemical cycling of an NCA electrode within 4.3 and 1.2 V vs. Li metal. The discharge curve down to 3.0 V represents the well-known lithiation processes that occur within the NCA lattice [1]. On further discharge, bellow 3.0 V vs. Li^+/Li, the galvanostatic profile is divided in two stages. During stage I, down to 2.14 V, NCA's specific charge «loss» of the first cycle is partially recovered via solid solution mechanism. Bellow 2.14 V and throughout the plateau, the two-phase reaction mechanism takes place which involves the R-3m to P-3m_1 phase transition responsible for further lithium storage in this system.

Figure 2 displays two selected 2Θ regions of the *in situ* X-ray patterns taken during cell operation. Evidence of the stages named solid solution and two-phase reaction are seen by the observation of the following facts: 1) until a potential of 2.14 V is reached, the (101) line shifts to lower angles, 2) from this potential down to 1.2 V no clear shift towards lower 2-Theta angles is observed and the (101) reflection suffers a severe intensity reduction, together with 3) the visualization of a new Bragg reflection appearing at about 17.7 ° 2Theta, assigned to the (001) reflection of the P-3m_1 space group for $Li_{1+x}Ni_{0.80}Co_{0.15}Al_{0.05}O_2$ phase. All these facts state that relithiation of the NCA lattice occurs up to 2.14 V, beyond that a phase transformation occurs to allow additional lithium to incorporate into the NCA framework. At such low potentials it is usual to observe a displacement reaction where the transition metal is reduced to its elemental form. However, during this study no evidence of metallic cobalt or nickel was found.

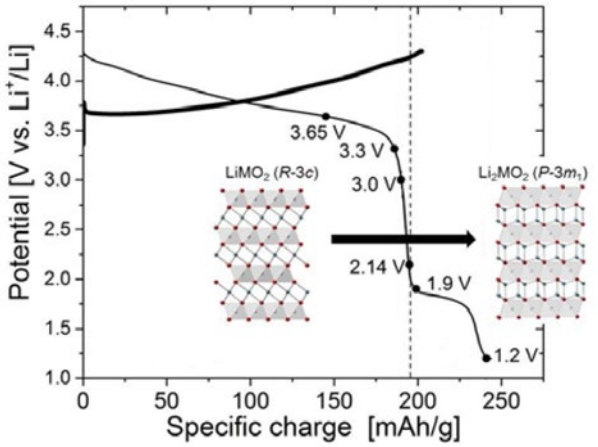

Figure 1. *Galvanostatic curves for the first cycle of an NCA electrode cycled vs. Li at 10 mA/g at room temperature – the dots displaying specific potentials on the galvanostatic profile corresponding to the X-ray diffractograms that are shown in Figure 2.*

Operando X-ray powder diffraction provides conclusive evidence that only c.a. 5 mAh/g of the specific charge «loss» can be regained via solid solution and that deep discharge alters irreversibly the NCA structure. The additional 5–6 mAh/g of specific charge «loss» on the first cycle is due to irreversible phase changes, and presumably also particle disconnection that leads to sluggish reactions within the electrode.

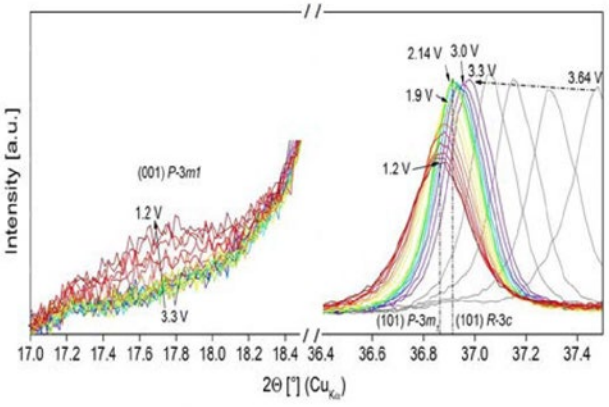

Figure 2. *In situ X-ray diffraction patterns at selected 2Θ regions for NCA with Bragg peaks according to space group R-3m and P-3m_1.*

References

[1] R. Robert, C. Bünzli, E.J. Berg, P. Novák, *Chem. Mater.* **27**, 526-536 (2015).

[2] J. Rodríguez-Carvajal, FullProf computer program 1998, ftp://charybde.saclay.cea.fr/pub/divers/fullprof.98/windows/winfp98.zip.

Investigation of the promising P2-$Na_{0.67}Mn_{0.6}Fe_{0.25}Al_{0.15}O_2$ cathode material

E. Marelli, C. Marino, C. Villevieille
phone: +41 56 310 5737, e-mail: elena.marelli@psi.ch

Na-ion batteries (SiBs) are considered the most promising complementary storage system due to their low-cost compared to Li-ion batteries. The electrochemical performance of the first prototype illustrates a good example of the ability of SiBs [1].

Among the possible cathode materials, layered oxides proved to deliver large specific charges [2]. P2-phases in particular, present higher voltage stability and better Na diffusion than the O3 equivalent phases. Cobalt is often used to stabilise layered structures upon cycling [3], despite being expensive and toxic. Recently we investigated $Na_{0.67}Mn_{0.5}Fe_{0.25}Co_{0.25}O_2$ and demonstrated that we can lower the Co content (P2-$Na_{0.67}Mn_{0.6}Fe_{0.25}Co_{0.15}O_2$ (NaMFC) [4]) and keep remarkable electrochemical performance. Based on this approach, we developed and studied the less expensive and toxic Co-free analogous $Na_{0.67}Mn_{0.6}Fe_{0.25}Al_{0.15}O_2$ (NaMFA).

Experimental

NaMFA was prepared through solid state synthesis from stoichiometric quantities of aluminium and manganese acetate, iron acetylacetonate and an excess of sodium acetate dissolved in EtOH / H_2O (1 : 3). The mixture was then calcined at 400 °C for 3 h and annealed at 900 °C for 12 h. The obtained powder was stored in an Ar filled glovebox.

The electrodes were prepared by casting a mixture of 80 / 10 / 10 (NaMFA / Carbon black / polyvinylidene fluoride (PVDF)) dispersed in N-methyl-2-pyrrolidone (NMP), onto an aluminium foil. Electrodes were dried, calendared, punched and further dried at 120 °C. Electrochemical tests were performed in half-cell configuration using Na as counter electrode, glass fibre as separator and 1 M $NaPF_6$ in ethylene carbonate (EC):diethyl carbonate (DEC) mixture as electrolyte. The cells were cycled galvanostatically at 25 °C between 2.1 V and 4.5 V (versus Na^+/Na) with rate capability measurements consisting of series of three cycles at C/10, C/5, C/2.5, C/1.25 and C/0.625, followed by a constant C/5 rate.

Operando XRD patterns were collected on a PANalytical Empyrean diffractometer using Cu Kα radiation and an *operando* XRD cell. Synchrotron data were acquired at the MS-X04SA beamline at the SLS using a 0.563315 Å wavelength.

XAS measurements were performed at the SuperXAS beamline at the SLS using the quick EXAFS monochromator on *ex situ* samples. [5]

Results

The XRD refinement of the pristine NaMFA confirms the formation of the desired P2-phase ($P6_3/mmc$ space group with a = 2.89366(4) Å and c = 11.1781(3) Å) with minor impurities identified as O_3-NaMFA and $NaFe_{0.25}Al_{0.75}O_2$ (Figure 1). The SEM image shows micron sized hexagonal-platelet particles, ascribed to the P2-phase, and smaller spherical particles due to the impurities.

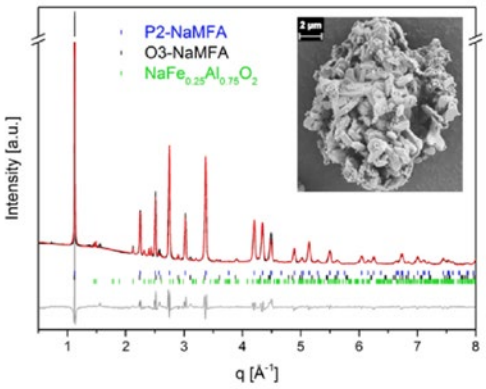

Figure 1. *Synchrotron XRD Rietveld refinement and SEM image (inset) of NaMFA.*

In Figure 2, the XRD patterns of the carbonized samples reveal characteristic broad peaks at 2θ values ca. 22° and 44° corresponding to the (002) and (100) peaks, respectively. A minor impurity (CaS) was detected at 32° and 45° in the patterns of the carbonaceous materials and originated most probably from the calcination of $CaSO_4$ present in the almond shell.

The electrochemical performance of P2-NaMFA is compared with that of the parent NaMFC in Figure 2. At the end of the 1st cycle, the specific charge of NaMFA is higher than that of NaMFC, with 163 and 141 mAh·g^{-1} respectively. Despite the absence of Co, a similar trend is observed at C/0.625 with values higher than 130 mAh·g^{-1} for NaMFA and only 110 mAh·g^{-1} for NaMFC. Once the current is back to C/5 rate, the Coulombic efficiency for NaMFA is restored and a value close to 100 % is obtained 10 cycles later. In comparison, the Coulombic efficiency for NaMFC does not exceed 95 %. After 80 cycles, the specific charge of NaMFA is 91 % of the capacity obtained with the current restored at C/5 rate (22nd cycle), while only 72 % of the specific charge is maintained for NaMFC.

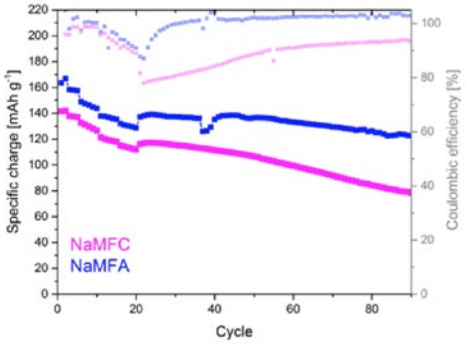

Figure 2. *Electrochemical performance of NaMFA and NaMFC in the rate capability test.*

The galvanostatic curves obtained upon first cycle present three different features, labelled on Figure 3 as i, ii and iii. The initial plateau from 2.75 V to 3.0 V counting for ca. 10 % of the total specific charge is followed by ascending curves till

ca. 4.15 V ascribed to a solid-solution mechanism. Between 4.15 and 4.5 V the coincident voltage profiles of NaMFA and NaMFC flatten indicating the Fe(III)/Fe(IV) oxidation. [6] On discharge both galvanostatic curves present a potential plateau centred at 3.65 V for NaMFA and 3.8 V for NaMFC, the difference probably due to the presence of the electrochemical activity of Co in the material. Both curves then slope down to reach 2.1 V, contributing for 60 % and 45 % of the specific charge for NaMFA and NaMFC respectively.

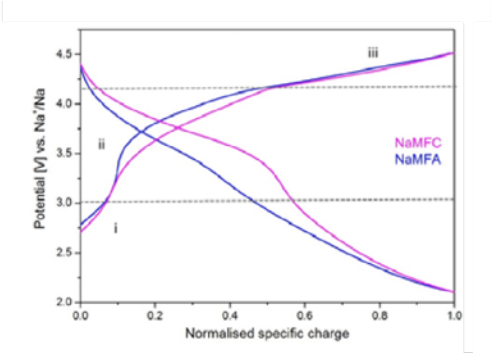

Figure 3. *Comparison of the 1st cycle galvanostatic curves for NaMFA and NaMFC.*

Figure 4 shows the Mn K-edge of pristine, charged and discharged samples. Due to presence of Al instead of Co, the charges are compensated by a higher average oxidation state of Mn in the pristine NaMFA. The half-height of the Mn K-edge moves to higher energies as the desodiation proceeds and the oxidation state of the Mn in the two samples increases, respectively. On sodiation, the Mn K-edge moves to lower energies than in the pristine samples, indicating a lower Mn oxidation state. The discrepancy between the two samples spectra, however, is reduced, which could indicate a higher amount of sodium being involved in NaMFA and thus could explain the better electrochemical performance shown in Figure 2.

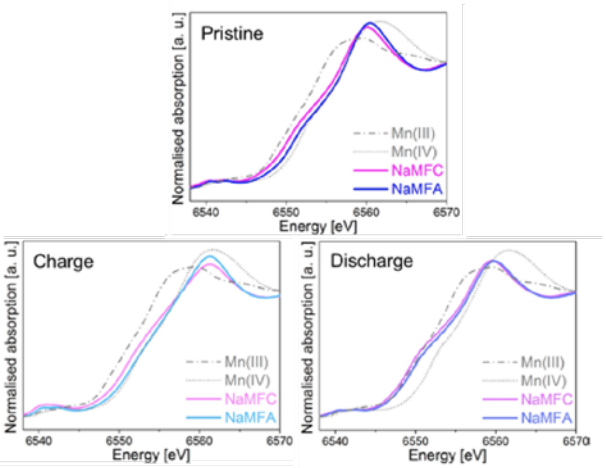

Figure 4. *XANES Mn K-edge spectra of NaMFA (blue) and NaMFC (magenta). Reference Mn(III) and Mn(IV) spectra are shown for comparison.*

In Figure 5, the reaction mechanism is also investigated by means of *operando* XRD. On charge, the *a* lattice parameter shrinks (e.g. (100) reflection in Figure 5) as a consequence of the reduced metals-metals distances. The interlayer distance instead barely moves on charge (e.g. (002) reflection) but a clear decrease of the intensity is observed at the end of charge coupled to the formation of new peaks (e.g. at ~17 °). This high-potential phase possibly corresponds to the O2-phase [7] in which the metals slabs glide to a more stable octahedral geometry around the Na atoms. The P2-phase is restored on discharge with, however, an orthorhombic distortion (P'2-phase [8, 9]) at the end of discharge caused by a Jahn-Teller distortion.

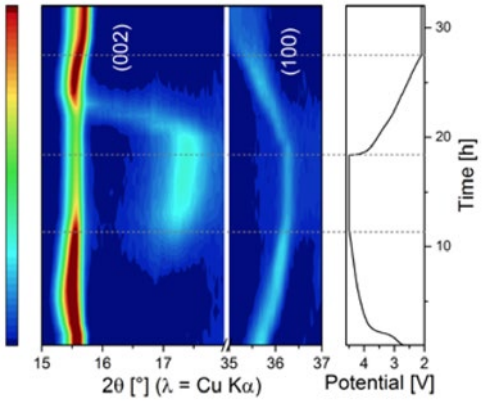

Figure 5. *Operando XRD patterns of NaMFA vs. Na and the corresponding first cycle galvanostatic plot.*

Conclusion

The Co-free P2-$Na_{0.67}Mn_{0.6}Fe_{0.25}Al_{0.15}O_2$ was successfully synthesised and characterised. The rate capability test showed higher specific charge and a better cycling stability than the analogous P2-$Na_{0.67}Mn_{0.6}Fe_{0.25}Co_{0.15}O_2$ cathode. The better electrochemical performance of NaMFA could be associated with the deeper Mn reduction on discharge and thus the higher number of Na re-intercalated. The reduced phase transition on charge (P2 – O2), instead, insures a better structural stability upon cycling.

Acknowledgement

the Swiss Competence Center for Energy Research *Heat and Electricity Storage* (SCCER HaE) and the PSI Career Return Program are kindly acknowledged for the financial support. The authors are thankful to Dr O. Safonova and Dr. M. Nachtegaal (SuperXAS beamline, SLS, PSI, proposal number 20161347) and, Dr N. Casati (MS beamline, SLS, PSI, Mesquick proposal number 20170006).

References

[1] L. Cailloce (quoting J.-M. Tarascon), «A battery revolution in motion», *CNRS news* (2015) – On-line available https://news.cnrs.fr/articles/a-battery-revolution-in-motion.
[2] Y. Liu, X. Liu, T. Wang, L-Z. Fan, L. Jiao, *Sustainable Energy Fuel* **1**, 986–1006 (2017).
[3] L. Liu, X. Li, S-H. Bo, Y. Wang, H, Chen, N., Twu, D. Wu, G. Ceder, *Adv. Energy Mat.* **5** (22), 1500944 (2015).
[4] C. Marino, E. Marelli, C. Villevieille, *RSC Adv.* **7** (23), 13851–13857 (2017).
[5] O. Muller, M. Nachtegaal, J. Just, D. Lutzenkirchen-Hecht, R. Frahm, *J. Synchrotron Radiat.* **23** (1), 260–266 (2016).
[6] N. Yabuuchi, M. Kajiyama, J. Iwatate, H. Nishikama, S. Hitoi, R. Okuyama, R. Usui, Y. Yamada, S. Komaba, *Nat. Mater.* **11** (6), 512–517 (2012).
[7] C. Delmas, J.-J. Braconnier, P. Hagenmuller, *Mater. Res. Bull.* **17** (1), 117–123 (1982).
[8] E. Talaie, V. Duffort, H. Smith, B. Fultz, L. Nazar, *Energy Environ. Sci.* **8** (8), 2512–2523 (2015).
[9] B. Mortemard de Boisse, D. Carlier, M. Guignard, L. Bourgeois, C. Delmals, *Inorg. Chem.* **53** (20), 11197–11205 (2014).

The surface evolution of aged NCA particles monitored by XPEEM during the early stages of cycling

M. Mirolo, C.A.F. Vaz, P. Novák, M. El Kazzi
phone: +41 56 310 2694, e-mail: marta.mirolo@psi.ch

Understanding the electrolyte / electrode interaction for 5 V cathode materials is crucial for the further development of the next generation of high energy density Li-ion batteries. Despite their enhanced specific charge, such cathodes suffer from strong fading during cycling, arising mainly from detrimental structural and surface changes, especially at potentials above 4.5 V vs. Li^+/Li. A first undesired modification occurs with contact to air. As described in Reference [1], the Li present in the near-surface region reacts with atmospheric CO_2 to form Li_2CO_3. As a consequence, a surface structural reorganisation can occur that leads to a different structure with respect to the bulk. The evolution of the cathode surface continues upon cycling and further reactions are triggered as a function of the applied potential, including decomposition of Li_2CO_3, electrolyte oxidation, changes in oxygen content at the cathode surface, and dissolution of transition metals in the electrolyte, which affect both the structure and the properties of the high-voltage-cathode surface. Despite all the significant efforts carried out to elucidate the nature and origin of the surface reactivity of the electrodes, a basic knowledge of the various reaction mechanisms occurring at the surface is still lacking. The scatter in the reported findings is caused mainly by the surface complexity of the commercial electrodes (multiple particles, high roughness and porosity) and by the intrinsic limitations of the commonly used surface characterization techniques [2, 3], especially the poor lateral resolution. For this reason, we make use of the synchrotron X-ray photoelectron emission microscopy (XPEEM) to gain localized information on single particles of $LiNi_{0.80}Co_{0.15}Al_{0.05}O_2$ (referred to as NCA), while keeping the complex formulation of Li-ion battery electrodes (i.e. mixture of active material, carbon, and binder). In such way, we are able to explain the surface evolution of aged NCA particles during the first delithiation process (Figure 1 b) in its working environment in commercial-like electrodes. Specifically, we can track the formation and dissolution of organic/inorganic species (e.g. carbonates) by following the C K-edge spectral features, along with the electronic changes of the active material at the Ni L-edge and relate them to the electrochemical behavior. For the latter, we clarify the origin of the overpotential «bump» at 3.8 V vs. Li^+/Li in the galvanostatic curve shown in Figure 1 b.

Results

Local X-ray absorption spectroscopy (XAS) is performed on the NCA particle only (refer to the XPEEM contrast image on Figure 1 a) and compared between pristine and cycled electrodes. The C K-edge spectra acquired on the pristine electrode confirm the coverage of NCA particles with carbonated species, whereas the Ni L-edge spectra show the characteristic features associated to an oxidation state of +2, lower than the expected +3 state in the bulk (Figure 2, sample I). However, already at ~3.8 V vs. Li^+/Li (Figure 1, sample II) we find that all the surface species are decomposed, explaining the unexpected overpotential course observed in the galvanostatic curve (Figure 1 b). Additionally, we demonstrate that Ni is oxidized to +4 at the end of the 1st delithiation at 4.3 V vs. Li^+/Li. Similarly, we confirm the absence of any electrolyte oxidation byproducts on the cathode surface, since no evolution is observed in the C K-edge acquired on the cycled NCA particles (Figure 2 b, sample II and III).

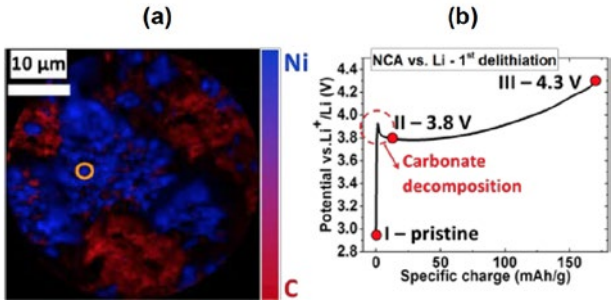

Figure 1. *(a) Elemental contrast image performed on pristine NCA electrode at Ni L-edge (blue, NCA particles) and C K-edge (red, conductive carbon). The yellow spot marks out the single NCA particle on which the XAS spectra are acquired.*
(b) Galvanostatic curve of the 1st delithiation of NCA cycled vs. Li^+/Li up to 4.3 V in LP30 electrolyte (1 M $LiPF_6$ dissolved in dimethyl and ethylene carbonates (DMC : EC, 1 : 1)) at C/5 rate.

In summary, our results show the decomposition of the carbonate species at the surface of the NCA particles, which are not reforming along the 1st delithiation process and explain the anomalous overpotential «bump» at 3.8 V vs. Li^+/Li. We demonstrate as well that XPEEM provides an innovative solution to investigating the complex surface of commercial-like Li^+ batteries, thanks to its capability to probe single particles, which is determinant for obtaining a better insight into the mechanisms governing the electrolyte–electrode interface reactivity.

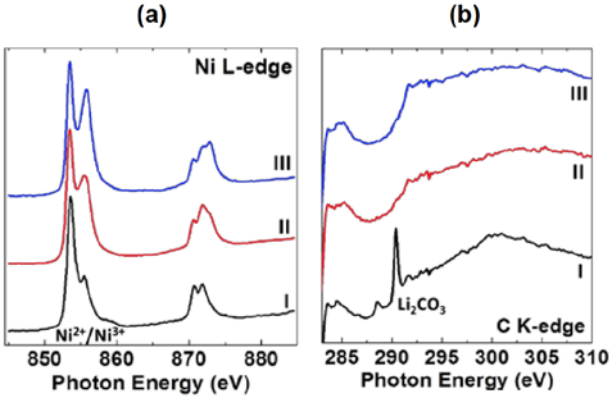

Figure 2. *Local XAS measurement performed on NCA particles (I) pristine, (II) after the potential «bump» at 3.8 V vs. Li^+/Li and (III) at 4.3 V vs. Li^+/Li; for the absorption photon energies of (a) Ni L-edge and (b) C K-edge.*

References

[1] D. Aurbach, *J. Power Sources* **89**, 89 (2000).
[2] R. Robert, C. Bünzli, E.J. Berg, P. Novák, *Chem. Mater.* **27**, 526 (2015).
[3] S. Hwang, W. Chang, S.M. Kim, D. Su, D.H. Kim, J.Y. Lee, K.Y. Chung, E.A. Stach, *Chem. Mater.* **26**, 1084 (2014).

The controversial surface reactivity of $Li_4Ti_5O_{12}$ in the aprotic electrolyte disclosed with XPEEM

D. Leanza, C.A.F. Vaz, I. Czekaj, P. Novák, M. El Kazzi
phone: +41 56 310 2797, e-mail: daniela.leanza@psi.ch

Whether $Li_4Ti_5O_{12}$ (LTO) electrodes can induce reduction of the liquid carbonate electrolytes, commonly used in Li-ion batteries, and develop a stable surface layer at 1.55 V vs. Li^+/Li remains a subject of controversy [1, 2]. Understanding the reactivity of both electrode and electrolyte is considered to be a key step to ensuring a stable electrolyte / electrode interface and thus a long-life span of Li-ion batteries.

Here, we make use of X-ray photoemission electron microscopy (XPEEM) to gain information on individual particles of a composite commercial-like LTO electrode to determine the nature and origin of the LTO surface instability. In XPEEM, the X-ray absorption spectra (XAS) are acquired with nanometer spatial resolution to yield surface-sensitive local electronic and chemical characteristics.

The local XAS spectra acquired at the C K-edge on carbon (Figure 1 a) and LTO particles (Figure 1 b) show that reduction of the electrolyte occurs only on the latter particles and exclusively during lithiation. Simultaneously, we detect a second reaction at the same potential, leading to a partial dissolution of the organic / inorganic species covering the LTO particles, as confirmed via the C K-edge after the 1st delithiation. This behavior correlates strongly with the Li^+ insertion / de-insertion and the thermodynamic stability of the electrolyte.

With the support of DFT calculations (Figure 2) we conclude therefore that the origin and the mechanism of the electrolyte reduction is related to the adsorbed solvents on the LTO outer plane, driven by their co-insertion with solvated Li-ions. The adsorption of solvents leads to a shift of their LUMO to energies below the Fermi Level of the lithiated LTO thus favoring a reductive electron transfer process.

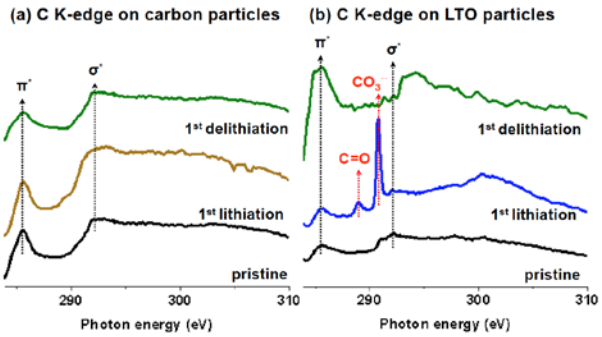

Figure 1. *Local X-ray absorption spectra (XAS) at the C K-edge carried out on pristine and after the 1st lithiation and 1st delithiation of LTO electrodes, acquired separately on (a) carbon and (b) LTO particles. Only the latter shows the characteristic components of EC / DMC decomposition at the end of the 1st lithiation.*

Conclusions

This study highlights the potential of XPEEM to investigate the complex electrode / electrolyte interface reactions for improving our understanding and the development of solutions to engineer the surface of Li-ion battery electrodes.

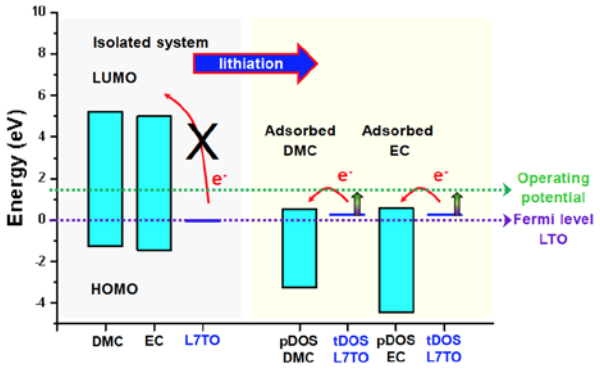

Figure 2. *HOMO/LUMO levels of DMC, EC and Fermi level position of L7TO (lithiated LTO) calculated on isolated systems and on adsorbed DMC and EC on L7TO surface. To simplify our model, we estimated the Fermi level (FL) at the same position of the VB. The FL is set to 0 eV and all the other levels shifted accordingly.*

Thanks to the nanoscale XPEEM spectroscopy, we demonstrate the preferential formation of electrolyte reduction only on lithiated LTO particles, whereas the conductive carbon remains free of any organic / inorganic species at the same operating potential. However, the weak chemical bonding of the surface by-products layer to the outer plane of the LTO particles let us witness a competitive reaction that takes place at same potential (1.55 V vs. Li^+/Li). This reaction is correlated to the observed dissolution of the EC/DMC by-products, which is the dominant process when Li^+ ions are de-inserted from the LTO structure (1st delithiation).

At room temperature and during the early stage of cycling a stable passivating layer on LTO is not formed and the reduction/dissolution mechanism is then responsible for the continuous electrolyte consumption, thus to the potential gas release, which is detrimental for the battery lifetime and safety.

Tracking such complex reactions at the interface electrolyte–electrode is feasible now, thanks to the XPEEM and enables a complete description of the battery degradation mechanism.

References

[1] M.-S. Song, R.-H. Kim, S.-W. Baek, K.-S. Lee, K. Park, A. Benayad, *J. Mat. Chem. A* **2**, 631–636 (2014).
[2] T. Nordh, R. Younesi, D. Brandell, K. Edström, *J. Power Sources* **294**, 173–179 (2015).
[3] D. Leanza, C.A.F. Vaz, I. Czekaj, P. Novák, M. El Kazzi, *J. Mater. Chem. A* **6**, *3534-3542 (2018).*

Improved electrochemical performance of Mn_XO_Y as an anode for Li-ion batteries

J. Billaud, V. Oliveros Colon, M. Fievez, C. Villevieille
phone: +41 56 310 5303 e-mail: juliette.billaud@psi.ch

Lithium-ion batteries represent the most advanced technology for portable energy storage thus far. Current negative electrodes, such as graphite or $Li_4Ti_5O_{12}$ with respective specific charges of 370 mAh/g and 175 mAh/g, react through an insertion reaction mechanism [1]. However, the need for higher energy density devices is pushing the research towards alternative materials, especially alloy/conversion-based materials. They exhibit much higher specific energy compared to insertion materials but suffer from large volume changes, up to 300 %, upon lithiation/delithiation. This leads to the pulverisation of the electrodes and subsequent loss of electrical contact between the particles.

Among conversion compounds, manganese oxides are particularly interesting due to their natural abundance, thus relatively low cost, and high theoretical specific charge above 1000 mAh/g [2].

In this work, we propose to:
1) study the electrochemical performance of various manganese oxides and
2) propose a method to improve their electrochemical performance by the 3D nano-architecturation of the Cu current collector.

Experimental

MnO, Mn_3O_4 and Mn_2O_3 (Sigma-Aldrich) active materials were tested in Li-ion batteries. Electrodes were prepared by casting a slurry based on 60 %wt active material, 20 %wt Super C65 carbon black and 20 %wt PVdF binder on Cu foil, unless stated otherwise. Compared to insertion materials, a larger amount of binder and conductive carbon is necessary to buffer the volume expansion and the resulting poor electrode stability and electronic conductivity.

Electrochemical tests were performed in half-cells using Li metal as a counter electrode and 1 M $LiPF_6$ in ethylene carbonate / dimethylcarbonate (1 : 1 weight ratio) as electrolyte. A rate of C/10 on lithiation was chosen and the cells were cycled between 10 mV and 3 V vs. Li^+/Li. Along this report all the potentials will be given using Li^+/Li as a reference.

Scanning electron microscopy (SEM) was performed on a Zeiss Ultra55 SmartSEM electron microscope.

The 3D nano-architectured current collectors were prepared by electrodeposition, using $Cu(SO_4)$, $(NH_4)_2(SO_4)$ and diethylenetriamine as electrolyte solution. The pulsed current applied consisted of two steps: -3 mA/cm^2 for 50 ms followed by -2 mA/cm^2 for 250 ms. A porous anodised aluminium oxide membrane with 10^{10} cm^{-2} pore density (Whatman) was used as a template for the Cu electrodeposition.

Results

Electrochemical performance of Mn_XO_Y compounds

Figure 1 shows that the Mn_2O_3 oxide outperforms MnO and Mn_3O_4 by presenting a remarkable cycling stability with almost no fading of the specific charge along 50 cycles.

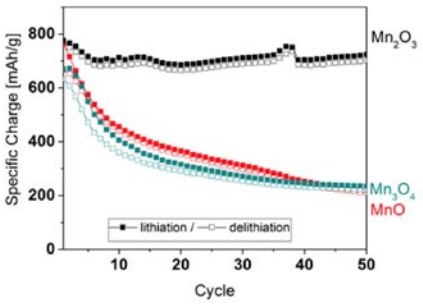

Figure 1. *Evolution of the specific charge as a function of cycles for various manganese oxides.*

Mn_2O_3 delivers a specific charge of ca. 800 mAh/g during the first cycle with 93 % capacity retention after 50 cycles compared to ca. 30 % capacity retention for MnO and Mn_3O_4.

Evolution of the potential as a function of the normalised specific charge for Mn_3O_4 and Mn_2O_3 is shown in Figure 2.

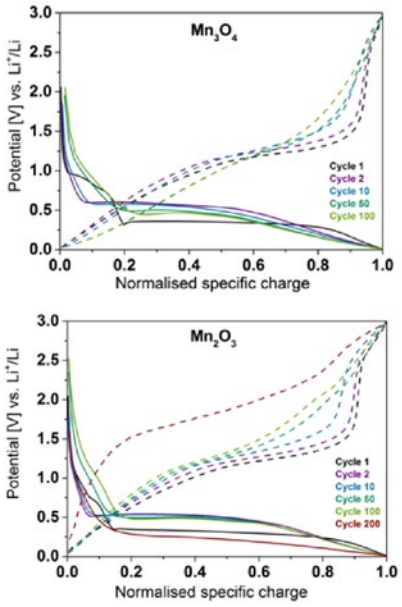

Figure 2. *Evolution of the potential as a function of the normalised specific charge for Mn_3O_4 and Mn_2O_3 between the 1st, 2nd, 10th, 50th, 100th and 200th cycles.*

For both Mn_3O_4 and Mn_2O_3, the first cycle (black line) differs from the following ones, due to the conversion-based reaction so called also formation cycle.

Mn_3O_4 is reacting along the first cycle through three potential plateaus: one around 1 V, one around 0.8 V, counting each for 10 % of the specific charge and the third one located around 0.35 V counting for roughly 70–75 % of the total specific charge. Mn_2O_3 reacts through a similar process with a very short slopping potential plateau at ca. 0.8 V with almost no specific charge (less than 10 % of the specific charge) and a very long potential plateau at ca. 0.3 V. On delithiation, the processes are similar with a long slopping potential plateau and a very large polarisation.

On extended cycling, Mn_3O_4 exhibits fluctuations of the potential plateau and the quasi-disappearance of the upper potential plateaus to the benefit of a sloppy process, which indicates a non-reproducible reaction pathway. On delithiation we observe the same with changes occurring in the reaction pathway. Mn_2O_3 presents an overlap of the galvanostatic curves along each cycling, indicating a similar reaction pathway, even if the small sloppy plateau is gaining importance after each cycle. On delithiation, the polarisation is increasing along cycling and the curves become smoother, likely due to the volume change occurring along cycling. Additionally, a potential plateau at 2.5 V is observed for Mn_2O_3 in delithiation after multiple cycles. When the cut-off potential was set below 2.5 V, the specific charge collapsed rapidly, suggesting that this electrochemical feature is in part responsible for the good stability observed. The origin of this process is currently under investigation.

Long term cycling of Mn_2O_3

Extended cycling has been performed on the Mn_2O_3 compound (Figure 3). For this test, the optimal slurry composition was 50 %wt active material, 25 %wt Super C65 carbon black and 25 %wt PVdF binder.

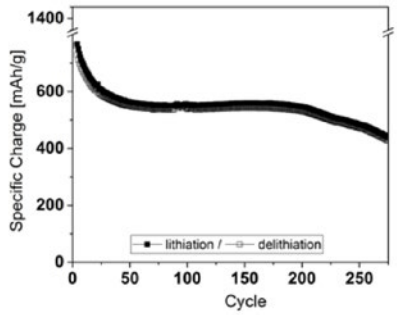

Figure 3. *Evolution of the specific charge as a function of cycles for Mn_2O_3.*

The specific charge decreases until the 25th cycle, from ca. 1300 mAh/g to 550 mAh/g, and this is associated with a higher polarisation seen in Figure 2. Between the 25th and the 200th cycle, the specific charge is stable, in correlation with a stable potential profile in Figure 2. After the 200th cycle, the specific charge drops and this phenomenon is associated with a larger polarisation. An explanation for this behaviour, common to conversion-based materials, is the unstability of the solid electrolyte interphase (SEI) that is then reformed at each cycle, consuming charge and damaging the electrode.

Elaboration of 3D Cu current collectors and deposition of Mn_XO_Y

In order to buffer the volume changes observed upon lithiation / delithiation of Mn_XO_Y compounds, 3D nano-architectured Cu current collectors were prepared, following a protocol previously established [3].

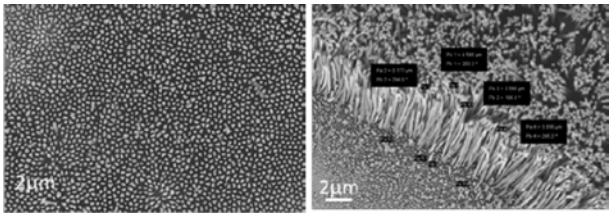

Figure 4. *SEM micrographs of the nanostructured Cu nanopillars obtained by electrodeposition.*

The nanopillars have a diameter of ca. 200 nm and a length of ca. 5 µm. They are homogeneously distributed on the current collector. Synthesis and deposition of Mn_XO_Y nanoparticles on the nanostructured Cu current collector was performed following the synthesis conditions detailed in [4, 5]. This would provide an enhanced electron transfer at the current collector – active material interface and offer more space for the volume expansion [3, 6].

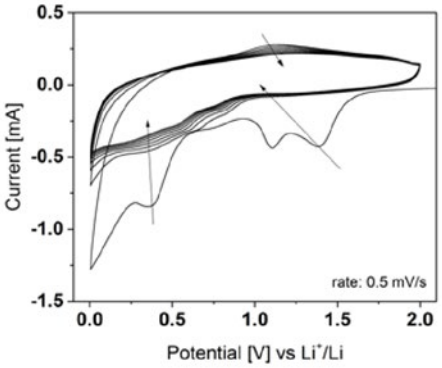

Figure 5. *Cyclic voltammogram of nanoparticles of Mn_XO_Y deposited on 3D Cu-nanopillars at a rate of 0.5 mV/s, between 5 mV and 2 V.*

Preliminary cyclic voltammetry results are shown in Figure 5, indicating that the deposition of Mn_XO_Y was successful. The peaks related to the electrochemical reactions are observed at a potential matching the one of Mn_XO_Y compounds.

Conclusions

Various manganese oxides have been tested as anode materials for lithium-ion batteries. Mn_2O_3 exhibited the higher specific charge and the most stable behaviour upon cycling. The cycling performance however rapidly collapsed, due to surface reactions. A 3D nano-architecturation of the Cu current collector and subsequent deposition of Mn_XO_Y on the surface would enhance the electron transfer and buffer the volume changes thus preventing the pulverisation of the particles.

References

[1] M.S. Whittingham, *Chem. Rev.* **104**, 4271 (2004).
[2] J. Cabana, L. Monconduit, D. Larcher, M.R. Palacín, *Adv. Mater.* **22**, E170 (2010).
[3] P.L. Taberna, S. Mitra, P. Poizot, P. Simon, J.-M. Tarascon, *Nat. Mater.* **5**, 567 (2006).
[4] T.P. Niebel, F.J. Heiligtag, J. Kind, M. Zanini, A. Lauria, M. Niederberger, A.R. Studart, *RSC Adv.* **4**, 62483 (2014).
[5] N. Kränzlin, M. Niederberger, *Adv. Mater.* **25**, 5599 (2013).
[6] C. Villevieille, F. Robert, P.L. Taberna, L. Bazin, P. Simon, L. Monconduit, *J. Mater. Chem.* **18**, 5956 (2008).

GITT analysis of silicon-graphite electrodes

F. Jeschull, S. Trabesinger
phone: +41 56 310 3792, e-mail: fabian.jeschull@psi.ch

The Galvanostatic Intermittent Titration Technique (GITT) is an electroanalytical tool to gain insights into internal resistances, solid state diffusion and overpotentials in an electrochemical cell [1]. For the measurement the current is interrupted in regular intervals and the potential is allowed to relax. Initially, the IR drop will lead to a rapid potential change, whereas the establishment of an equilibrium potential occurs over a significantly longer time scale – of up to several hours. The difference between the open-circuit potential (OCV) and the electrochemical potential further allows to conlude about the kinetics of the reaction. The advantage over other techniques is that all this information can be acquired collectively in a single experiment. The processing of the thus obtained data for each pair of current and relaxation sequences requires custom data treatment in order to compute the desired parameters straightforwardly. In this study, rapid data analysis was achieved using the programming language «R». The analysis was carried out in a lithium-ion half-cell setup, employing a silicon-graphite working electrode, containing 5 or 10 %wt Si as well as 90 or 85 %wt graphite, respectively. GITT measurements were performed at different charge/discharge rates, in order to understand the effect of the silicon content on the electrode resistance and the overpotential as a function of the state-of-charge (SoC).

Results

In Figure 1 & 2 the potential is plotted versus state-of-charge for the two silicon-graphite electrode formulations. The cycling rate in this case was C/10 (1 C = 540 mAh g^{-1} (5 %wt Si) / 710 mAh g^{-1} (10 %wt)). The red dots mark the OCV potential after 30 min of relaxation and the blue dots indicate the potential during a constant current sequence just before the current was switched off. The lower panel shows the potential difference between these two points in each sequence.
The electrode containing 5 %wt Si shows a higher potential difference (dE) over the first 20 % of the lithiation (> 200 mV vs. Li^+/Li). As the potential drops below 200 mV, a notable decrease of dE from 50 mV to about 25 mV is observed that coincides with the first voltage plateau of graphite. Conversely, during delithiation dE increases back to 50 mV from 60 % SOC onwards. The electrode comprising 10 %wt Si shows the same features but the drop of dE occurs later upon lithiation and starts earlier upon delithiation.
Generally, the increase of dE is observed in regions that are outside of the (de)intercalation potentials of graphite, which suggest that the (de)alloying potential of Si is the dominating reaction and cause of the increased overpotentials.

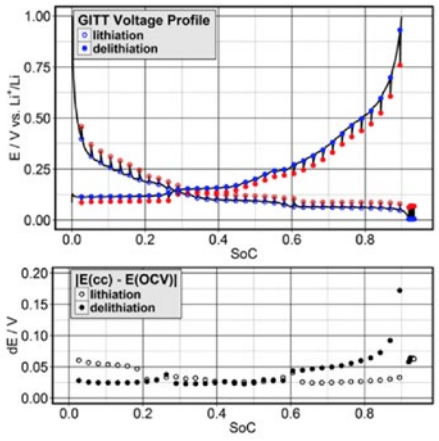

Figure 1. *GITT measurement of a graphite electrode with 5 %wt of Si (cycling rate: C/10). The lower panel is the corresponding potential difference between the end of a current step and the end of the relaxation step.*
Open circles: lithiation process; solid circles: delithiation.

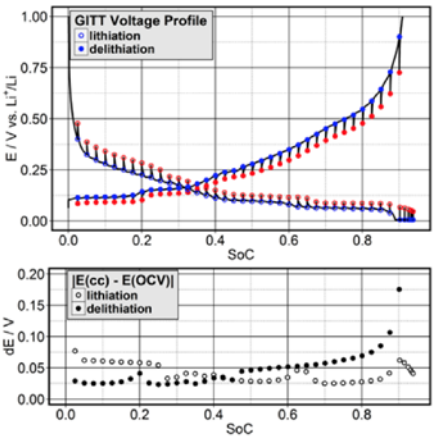

Figure 2. *GITT measurement of a graphite electrode with 10 %wt of Si (cycling rate: C/10). The lower panel is the corresponding potential difference between the end of a current step and the end of the relaxation step.*
Opel circles: lithiation process; solid circles: delithiation.

Conclusions

The example above shows that it is possible to discriminate active electrode component contribution to voltage profiles in a multi-component battery anode, if their electrochemical window is not fully overlapping. Here, the electrochemical window for the (de)alloying of Si is wider than for the (de)intercalation reaction of graphite. In regions where only silicon is active, the overpotential is twice as large as compared to «shared» potential regions.
The analysis provides useful information on the limiting of the charge/discharge processes that has been a bottle-neck for fast charging batteries.

Acknowledgement

Kindly acknowledged is financial support from the Commission for Technology and Innovation (CTI) and Imerys Graphite & Carbon for providing the electrode materials used in this study.

References

[1] W. Weppner, R.A. Huggins, *J. Electrochem. Soc.* **19**, 1569–1578 (1977).

Binder evaluation for Si-graphite electrodes

Y. Surace, S. Trabesinger
phone: +41 56 310 4396, e-mail: yuri.surace@psi.ch

Silicon has been investigated in the last years as one of the most promising anode materials for Li-ion batteries due to its low potential vs. Li^+/Li and its high theoretical specific charge (3579 mAh/g). However, silicon-based electrodes suffer from strong performance fading upon cycling due to significant volume changes of silicon during lithiation and delithiation. One way to cope with the Si volume changes and aiming to increase the cycling stability is to minimize the volume expansion at the electrode level. This can be achieved by using Si nanoparticles smaller than 50 nm and by decreasing the amount of Si in the electrode to 5–10 %wt. Furthermore, by adding this amount of Si to a graphite electrode the specific charge of the anode can be increased up to 700 mAh/g. The electrochemical performances of Si electrodes are also strongly dependent on the electrode composition [1], in particular, the binder plays a prominent role alleviating volume expansion and helping to obtain cycling stability [2].
In our work, Si-graphite electrodes have been prepared with five different commercially available binders. The aim was to find the binder which would allow obtaining the highest specific charge retention.

Experimental

The electrodes were made with the following composition: 90 %wt graphite KS6L, 5 %wt Si, 1 %wt Super C45 carbon additive and 4 %wt binder. The binders tested were: 1) A mixture of polyacrylic acid (PAA, 25 %wt sol. in H_2O, average M.W. 240,000, Alfa Aesar) and carboxymethyl cellulose (CMC, Alfa Aesar) 1 : 1. 2) A mixture of CMC and styrene butadiene rubber (SBR, MTI corporation) 1 : 1. 3) Guar Gum (GG, Sigma-Aldrich). 4) Na-Alginate (Sigma-Aldrich). 5) PVDF (Arkema).
In a standard preparation the binder was initially dissolved in the solvent (a mixture of water : ethanol 70 : 30 %wt in case of PAA : CMC, CMC : SBR and Na-Alginate, water in case of GG, and NMP in case of PVDF) then SC45 additive (C-NERGY, Imerys Graphite and Carbon) and Si (Nanostructured and Amorphous Materials 30–50 nm) were stirred into the binder solution. Successively, KS6L graphite (C-NERGY, Imerys Graphite and Carbon) were added to the mixture and the slurry was stirred until a honeylike texture was obtained. The slurries were cast onto copper foil and heat treated (at 150 °C for 2 h then 80 °C overnight for PAA : CMC, at 80 °C overnight for the other binders) under vacuum.
Electrochemical testing was performed in half-cell configuration with metallic Li as counter electrode, LP30 with 2 %wt FEC as electrolyte, and glass fiber separators. The cells were cycled using a CCCV cycling protocol as reported elsewhere [3]. The specific charge is presented per mass of electroactive material, i.e graphite and Si. The specific charge retention was calculated considering the 2nd and the 50th cycle.

Results

In Figure 1 the electrochemical performance of the Sigraphite electrodes is shown. The theoretical specific charge for these electrodes, containing 5 %wt Si is 541 mAh/g (per mass of EAM). Electrodes with PVDF binder showed the lowest both specific charge (around 450 mAh/g) and columbic efficiency (around 70 %) in the 1st cycle confirming that the standard PVDF binder is not suitable for electrodes undergoing large volume expansion. However, electrodes with water-based binders were able to provide in the initial cycles a specific charge very close to the theoretical one, ranging from 510 mAh/g for Na-Alginate to 535 mAh/g for PAA : CMC. By using this type of binders an improvement in 1st columbic efficiency of 10–12 % was obtained in comparison with PVDF. Furthermore, the cycling stability was also improved as shown in Table 1. Among them, PAA : CMC proved to be the best binder allowing to reach a specific charge retention of 93.4 % and a specific charge of 502 mAh/g after 50 cycles.

Binder	Columbic efficiency 1st cycle, %	Specific charge retention after 50 cycles, %
PAA:CMC 1:1	82.6	93.4
CMC:SBR 1:1	79.8	89.3
Guar Gum	79.6	88.2
Na-Alginate	80.0	92.7
PVDF	70.7	83.3

Table 1. *Electrochemical retention related data for Si-graphite electrodes with various binders.*

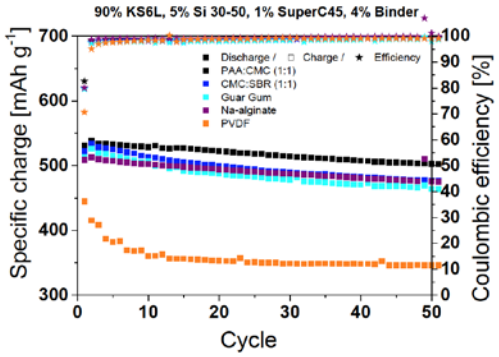

Figure 1. *Specific charge vs. cycle of Si-graphite electrodes with different binders.*

Conclusions

Five commercial binders have been tested for Si-graphite electrodes. The highest specific charge retention was obtained for electrodes with PAA : CMC and Na-alginate binders.

Acknowledgement

Kindly acknowledged is financial support from the Commission for Technology and Innovation (CTI) and Imerys Graphite & Carbon for providing the electrode materials used in this study.

References

[1] J.S. Bridel, et al., *Chem. Mater.* **22** (3), 1229–1241, (2010).
[2] N.S. Hochgatterer, et al., *Electrochem. Solid-State Lett.* **11** (5), A76–A80, (2008).
[3] PSI Electrochemistry Laboratory, *Annual Report 2016*, 57 (2016).

All-solid-state Li-ion batteries based on garnet solid electrolyte using high-energy alloy anode materials

G. Ferraresi, M. El Kazzi, L. Czornomaz, C.L.Tsai, S. Uhlenbruck, C. Villevieille
phone: +41 56 310 4542, e-mail: giulio.ferraresi @psi.ch

All-solid-state Li-ion batteries based on garnet Ta-$Li_7La_3Zr_2O_{12}$ (LLZTa) solid electrolyte are a promising alternative to conventional Li-ion batteries thanks to their improved electrolyte safety [1]. However, to date, their viability is still questioned owing to the constraints of electrode–electrolyte interface that limits their electrochemical performance. Such interface is the limiting factor owing to the presence of surface species such as LiOH and Li_2CO_3 (formed upon exposure of the solid electrolyte to air/moisture) which provides high barrier to Li ion conduction [2]. Thus, the electrode–electrolyte interface needs to be enhanced according to the following requirements:

- buffering the impact of surface species on top of LLZTa;
- ensuring proper electrode adhesion at the electrode–electrolyte interface.

For the former, the surface species could be removed thermally or mechanically, but these approaches should ensure the total absence of air/moisture exposure of the solid electrolyte to prevent further surface degradation. The latter could be tackled by co-sintering of the two materials, but this approach has to be conducted at high temperature resulting in possible chemical reactivity. [3]

Here, we show a proof of concept to tackle the two precited issues and provide good electrochemical performance by using a model system based on thin film electrodes (Si or Sn) and bulk LLZTa solid electrolyte. The interface is improved by reducing interfacial species by *in situ* Argon plasma etching prior to electrode film deposition in the sputtering chamber.

Experimental

LLZTa pellets were synthesized by solid-state reaction and sintered at 1175 °C for 5 h in air. Both surfaces of the LLZTa pellets were manually polished with silicon carbide grinding papers to obtain a mirror-like surface. The LLZTa samples were inserted in a sputtering deposition chamber for the deposition of the 50 nm Si or 50 nm Sn film. Beforehand, a plasma Ar^+ etching treatment of 30 sec was conducted in the sputtering chamber to obtain a «clean» surface (removal of surface species) without breaking vacuum. Ion-milling cross-section coupled to scanning electron microscopy (SEM) helped to monitor the effective sample preparation and film deposition. The electrochemical tests were conducted with a VMP-300 Bio-Logic potentiostat in a controlled temperature chamber at 80 °C. Swagelok-type cells were assembled in half-cell configuration. Galvanostatic cycle measurements were carried out by building half-cell vs. Li metal (along this report all the potential will be given using Li^+/Li as a reference). Specifically for the Sn thin film, a pre-lithiation step was conducted by contacting the Sn film with Li metal at 200 °C for 15 min in Ar atmosphere.

Results

The LLZTa solid electrolyte pellets were prepared with a relative density of 93 % measured by geometrical parameters. The samples were manually polished to reach a mirror-like surface by removing surface inhomogeneity, as shown in Figure 1a. The polishing step reduced the final pellet thickness to ca. 500 µm and achieved a flat surface, crucial for the electrode film deposition.

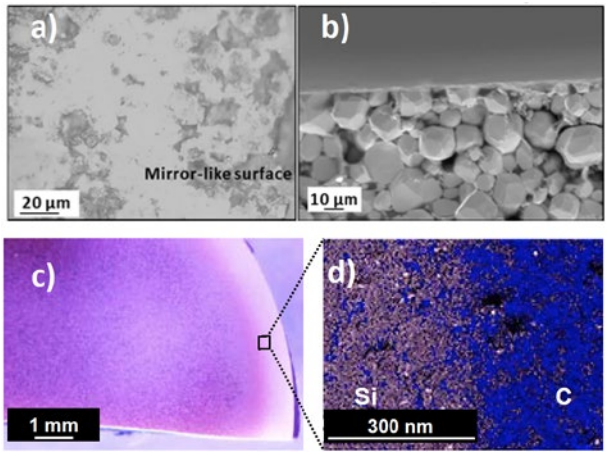

Figure 1. *a, b) LLZTa pellet after sintering and polishing; c, d) Image and EDX analysis after in situ Argon plasma etching and Si deposition.*

Subsequently, LLZTa pellets were transferred in a sputtering deposition chamber where the Argon plasma etching followed by the film deposition was conducted.
Figure 1c and 1d show the Si film deposited on one surface of the LLZTa pellet. Figure 1c shows the difference of color between the Si-coated area (pink) and the uncoated LLZTa pellet (pale yellow). Figure 1d shows the EDX analysis at interface of the coated/uncoated pellet. As can be seen, there is a net presence of carbon species on the uncoated area whereas almost nothing is detected on Si-coated area. These results show the successful *in situ* treatment with initial removal of carbon-rich surface species and direct deposition of Si film on the «clean» surface.

The Si/LLZTa stack was then investigated electrochemically in half-cell vs. Li metal. The cell was maintained at 80 °C in a T-controlled chamber to limit the resistivity of the bulk LLZTa electrolyte.
Figure 2a shows the potential profile for the 1st, 2nd, 3rd, 5th, 10th and 20th cycles at C/18 rate. During the first cycle an initial irreversible activity at ~0.4 V is detected. The first delithiation results in sloping potential plateau evolving smoothly from 0.2 V to 0.5 V. From the 2nd to the 20th galvanostatic cycle, there are no relevant changes except the disappearance of the initial irreversible activity at 0.4 V during discharge. Figure 2b shows the cycling performance able to provide an initial delithiation capacity of 2885 mAh/g with an increase after few cycles up to 3023 mAh/g. High delithiation capacity above 3000 mAh/g was retained for at least twelve cycles before starting to fade down to 2174 mAh/g after 45 cycles. The overlapping of the potential profiles from 2nd to 20th cycle suggests that the capacity fades due to film «loss» rather than irreversible reactivity.

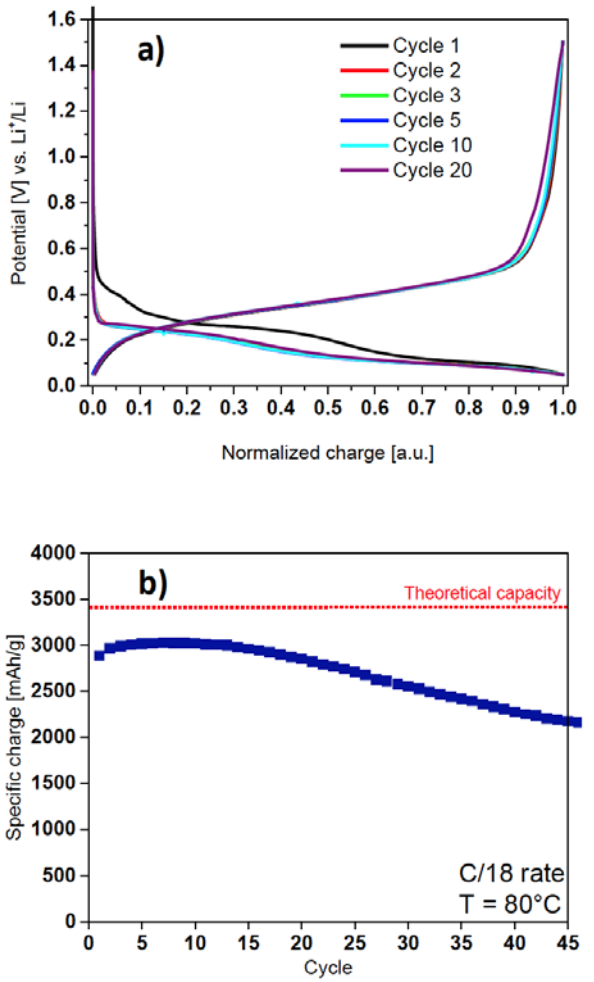

Figure 2. *a) Normalized galvanostatic cycling of 50 nm Si film at C/18 rate (T = 80 °C); b) Delithiation performance at C/18 rate.*

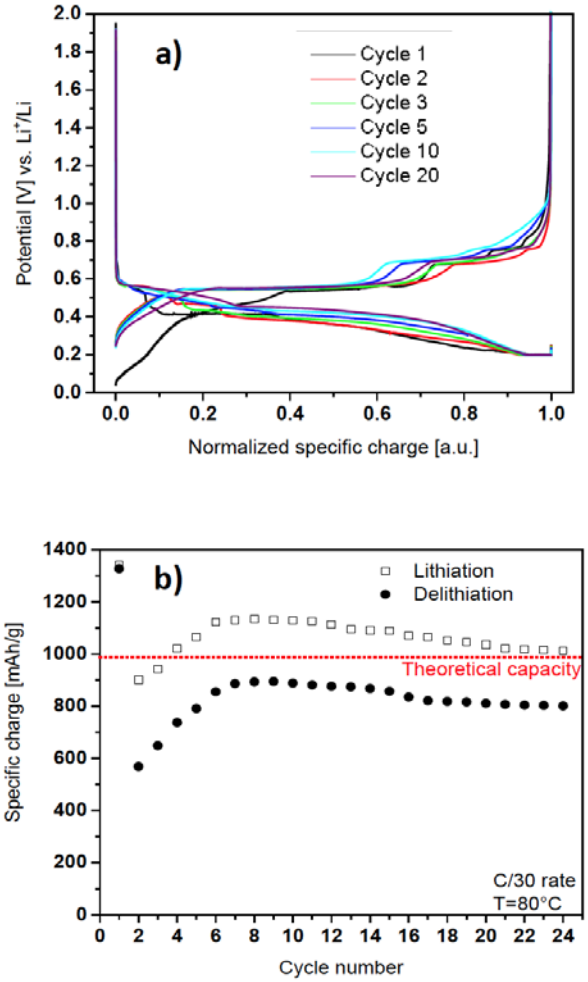

Figure 3. *a) Galvanostatic cycling of 50 nm pre-lithiated Sn film at C/45 rate (T = 80 °C); b) Lithiation/delithiation performance at C/45 rate.*

Similar investigation was also conducted by depositing 50 nm Sn thin film on LLZTa pellet. In this case, an initial chemical lithiation step to form LixSn was necessary to ensure proper cycling.

Figure 3a shows the normalized potential profile for selected cycles. The first cycle shows the initial delithiation to Sn^0 through multiple potential plateaus related to the different Li-Sn dealloying steps. Figure 3b shows that the first cycle was able to deliver up to ~1350 mAh/g, higher than the theoretical capacity of Sn (995 mAh/g). This high value can be attributed to the enhanced oxidation at this temperature of the film to SnO_x, as the oxide component can deliver up to 1500 mAh/g capacity, also an error on the thin film mass cannot be excluded. The second lithiation step shows a decrease to ~900 mAh/g while the delithiation shows a drop in the capacity to one third of the initial (~570 mAh/g). From the 3rd cycle the specific capacity increases reaching its maximum at the 10th cycle where a lithiation of 1110 mAh/g and a delithiation of 900 mAh/g is obtained. After more than 20 cycles, the delithiation capacity retained was more than 800 mAh/g. Along these cycles, slight changes can be found in the potential range 0.4–0.6 V during both lithiation and delithiation and are not related to overpotential.

Conclusion

We proposed here a proof of concept enabling the cycling of solid state batteries using garnet LLZTa electrolyte. We have demonstrated that intimate contact at the interface between the electrode and the solid electrolyte can be obtained by a proper surface etching under vacuum. Based on this approach, we successfully deposited and cycled reversibly two different model systems (Si, Sn) and high specific charge could be obtained for multiple cycles. Further investigation will be conducted to characterize by *ex situ* and *in situ* techniques the possible inter-diffusion / reactivity at such interfaces.

Acknowledgement

Competence Center Energy and Mobility (CCEM) and the Swiss Electric Research (SER) are acknowledged for financial support.

References

[1] R. Murugan, V. Thangadurai, W. Weppner, *Angew. Chem. Int. Ed.* **46**, 7778–7781 (2007).

[2] A. Sharafi, J. Sakamoto, et al., *J. Mater. Chem. A* **5**, 13475–13487 (2017).

[3] K. Park, J.B. Goodenough, et al., *Chem. Mater.* **28** (21), 8051–8059 (2016).

Impact of the electrode engineering on the electrochemical performance of $LiCoO_2$ as cathode material in Li_3PS_4 based all-solid-state lithium-ion batteries

L. Höltschi, C. Jordy, C. Villevieille
phone: +41 56 310 2115, e-mail: laura.hoeltschi@psi.ch

Safety (no thermal runaway or leakage) could be guaranteed with the so-called solid state batteries made of solid electrodes and electrolytes [1]. So far, sulfide-based solid electrolytes offer the most promising ionic conductivity at room temperature and allow relative ease of fabrication [2]. However, they suffer from a small electrochemical stability window [3].

To improve the electrochemical performance of all-solid-state battery, one has to find an optimal intimate contact between the active material and the solid electrolyte. The ionic conduction pathway should be maximized while simultaneously, good electronic percolation has to be established in the electrode. We study here the impact of the ratio between $LiCoO_2$ (semiconductor) and the solid electrolyte in composite electrodes on the electrochemical performance of all-solid-state batteries.

Experimental

Li_3PS_4 (LPS) has been successfully synthesized from two commercially available precursors Li_2S and P_2S_5 (with a molar ratio 75:25) via mechano-synthesis (ball milling with 5 mm dia. ZrO_2 in 45 ml ZrO_2 jar). The active milling time was 10 min with intervals of 5 min during 180 cycles at 510 rpm [4].

The surface of the $LiCoO_2$ (LCO) particles was coated with $LiNbO_3$ via a sol-gel technique to enlarge the electrochemical stability window of the solid electrolyte [5].

Four different composites electrodes have been prepared by hand-mixing three different coated LCO:LPS ratios (50:50, 60:40, 70:30 in %wt) and one uncoated LCO:LPS (50:50 in %wt) ratio.

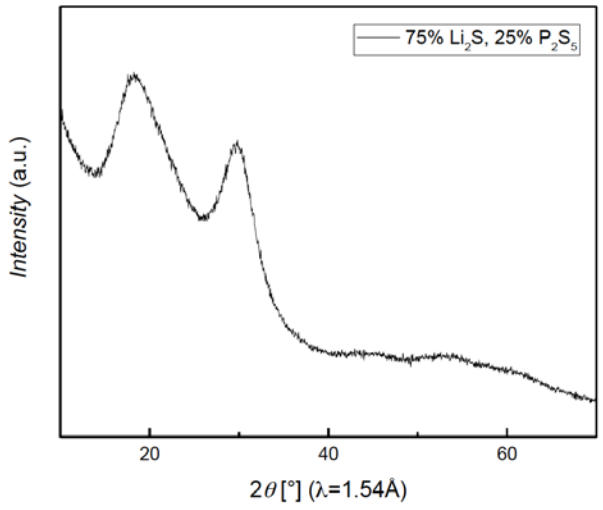

Figure 1. *X-ray pattern of LPS solid electrolyte obtained via mechano-synthesis.*

Results

As the XRD data in Figure 1 show a glassy solid electrolyte with very broad peaks, it is assumed that the synthesis has reached completion. The ionic conductivity, measured via Electrochemical Impedance Spectroscopy (EIS) at room temperature (25 °C), is around 0.4 mS/cm.

Scanning electron microscopy (SEM) images have been taken on a composite pellet made of LCO:LPS (50:50 in %wt) (Figure 2). The pellet is not 100 % dense as significant pores are visible between the micro-sized particles. Optimisation could be achieved by hot pressing.

In Figure 3 a coated LCO particle of about 12 µm is depicted. A coating of a few nm is present as the morphology of the bare LCO looks differently (SEM image not shown).

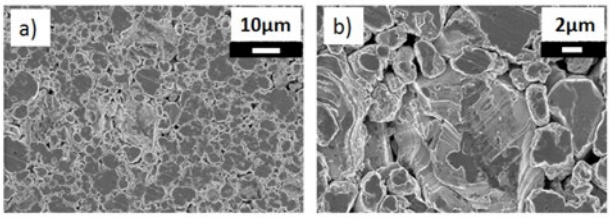

Figure 2. *SEM images of an LCO:LPS (50:50 in %wt) electrode. a) Lower magnification. b) Higher magnification.*

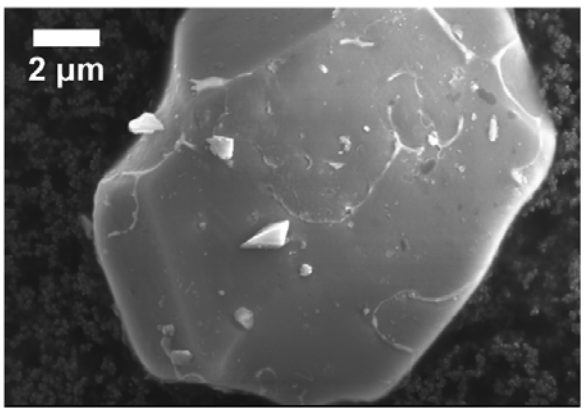

Figure 3. *SEM image of a coated LCO particle.*

Regarding the electrochemical performance obtained, we would like to highlight the importance of coating the active material LCO in order to deliver higher specific charges. When the electrodes containing both 50:50 (in %wt) LCO:LPS with and without coating and cycled at C/10 are compared (Figure 4 and 5), the initial specific charge is around 105 mAh/g and 91 mAh/g, respectively. These values are much lower than the specific charge of 140 mAh/g reached in conventional Li-ion cells. Besides, the loss of capacity during the first discharge is smaller for the coated electrode as they reached 91 mAh/g and 74 mAh/g, respectively, representing a loss of 15 % and

19 %. The possible reason for the observed difference might come from the important electrolyte decomposition at the interface of the uncoated oxide electrode/electrolyte. During the first cycle (Figure 4), a significant overpotential is noted for the uncoated sample which highlights the importance of a coating layer to limit the electrolyte decomposition when reaching high potentials.

Additionally, in order to deliver higher specific charges over many cycles, the optimal electrode composition (optimized ratio between LCO and LPS) needs to be found. As LCO is a semiconductor, a higher ratio will improve the electronic pathway over the electrode leading to higher specific charge. The sample containing the highest amount of active material delivered an initial capacity of 144 mAh/g which is 20 % higher than the 60 : 40 mixture and 30 % more than the 50 : 50 coated composite electrode. A similar trend can be observed for the discharge during the first cycle.

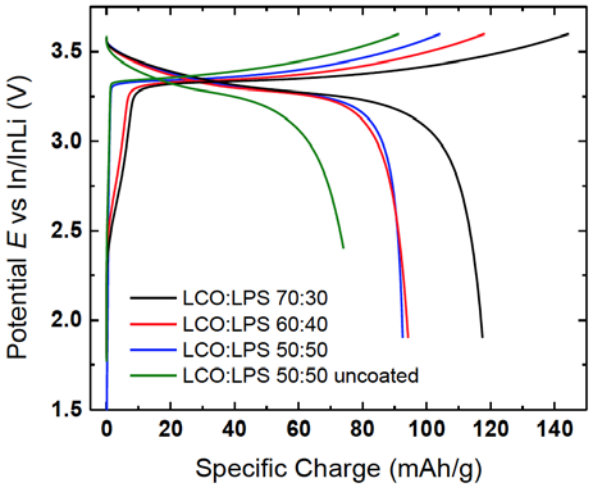

Figure 4. *Discharge/charge voltage profiles of coated LCO : LPS (50 : 50; 60 : 40; 70 : 30) and uncoated LCO : LPS (50 : 50) tested in half-cell configuration versus In-Li at a rate C/10 with CC protocol at room temperature. The cycles were measured between 1.9 and 3.6 V vs. In/InLi.*

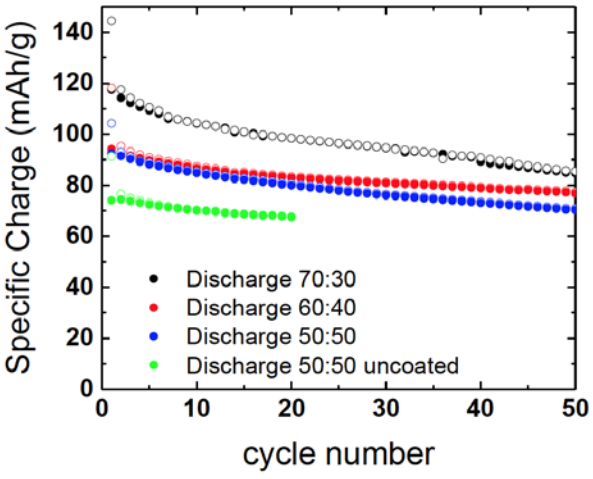

Figure 5. *Cycling stability of LCO : LPS (50 : 50; 60 : 40; 70 : 30) and uncoated LCO : LPS (50 : 50) tested in half-cell configuration versus In-Li at a rate C/10 with CC protocol at room temperature. The cycles were measured between 1.9 and 3.6 V vs. In/InLi. The open circles represent the charge capacities whereas the closed circles represent the discharge capacities.*

Moreover, on the long term cycling (Figure 5), the improved electronic pathway from the coated 60 : 40 is more favorable than the coated 50 : 50 composite electrode.

Conclusion

We demonstrated the importance of coatings and appropriate electrode composition (amount of active material and electrolyte) for improved long-term cycling performance of LCO as cathode material for all-solid-state batteries.

Finally, the interface issues in all-solid-state batteries seem at least as complex as in conventional liquid batteries and highlight the importance of interface engineering to achieve high performance.

Acknowledgement

SAFT, SE in Bordeaux (France) is gratefully acknowledged for financial support.

References

[1] Y. Kato, S. Hori, T. Saito, K. Suzuki, M. Hirayama, A. Mitsui, M. Yanemura, H. Iba, R. Kanno, *Nature* **1**, 1–7 (2007).
[2] A. Hayashi, A. Sakuda, M. Tatsumisago, *Front. Energy Res.* **4**, 1–13 (2016).
[3] Y. Zhu, X. He, Y. Mo, *ACS Appl. Mater. Interfaces* **7**, 23685–23693 (2015).
[4] X. Wu, M. El Kazzi, C. Villevieille, *J. Electroceram.* **38**, 1-8 (2017).
[5] W. Zhang, D.A. Weber, H. Weigand, T. Arlt, I. Manke, D. Schröder, R. Koerver, T. Leichtweiss, P. Hartmann, W.G. Zeier, J. Janek, *ACS Appl. Mater. Interfaces* **9**, 17835–17845 (2017).

Bio-waste lignin-based as carbonaceous materials for Na-ion batteries

C. Marino, C. Villevieille
phone: +41 56 310 5304, e-mail: cyril.marino@psi.ch

Na-ion batteries are currently investigated as a complementary system to Li-ion batteries and already demonstrated promising results [1]. Unfortunately, lower energy density is expected due to the size of the Na, thus the viability depends on the achieved energy density and the production cost [2]. The use of alternative cheap precursors like bio-waste material to develop electrodes would contribute to the reduction of the cost of the battery.

In the literature, several bio-waste materials such as banana peels [3], rice straw [4], apples [5] and argan shells [6] were pyrolised under various conditions and the resulting carbonaceous materials were tested as negative electrode for Na-ion batteries. Lignin-based polymer could provide a non-graphitized carbon suitable for Na-ion battery. Dou *et al.* [7] investigated the impact of biopolymers precursors annealed at 1100 °C under Ar for 1 h in Na-ion batteries. Calcined peanut shells (lignin-based) demonstrated a specific charge of 285 mAh g^{-1} for 300 cycles at 0.1 C (electrode loading 1.5 mg cm^{-2}). In comparison apple waste (pectin-based) and corncob (hemicellulose-based) reached only 210 mAh g^{-1} and 250 mAh g^{-1}, respectively.

In this work, we investigate the impact of the lignin-based materials such as almond shells (ALM), walnut shells (WN) and scrap wood (FIR) on the electrochemical performance of Na-ion batteries. The physical and morphological properties of the synthesized carbonaceous materials were assessed by means of scanning electron microscopy (SEM), X-ray diffraction (XRD), Raman spectroscopy and Brunnauer Emmett Teller specific surface area measurements (BET).

Experimental

Shells of almonds and walnuts as well as scrap wood (Obize SA) were grinded by ball milling for 45 min at 300 rpm in stainless steel vessels with 3 balls of 15 mm diameter. The obtained powder was sieved taking only particles below 125 µm. The powder was washed with a solution of 1 M H_2SO_4 to remove pesticides [6] and rinsed until reaching a neutral pH. The resulting powder was then placed in a tubular oven under Ar at 1000 °C for 6 h and then cooled down to room temperature in 10 h.

Electrodes were prepared by casting a mixture of 90 %wt carbonaceous material and 10 %wt of carboxymetyl cellulose (Na-CMC) dissolved in a water / ethanol solution (3 : 1). After drying at 80 °C under vacuum, 13 mm electrodes with a loading of ca. 5 mg cm^{-2} were punched.

Batteries were assembled in an Ar-filled glove box using a Na metal disk as counter electrode and a glass fibre separator. Electrolyte consisted of a mixture of 1 M $NaPF_6$ salt dissolved in a mixture of ethylene carbonate and diethyl carbonate (1 : 1) used as solvents. Cells were cycled in galvanostatic mode at 25 °C at C/10 rate (300 mAh g^{-1} as theoretical specific charge) with a potentiostatic step of 1 h at 5 mV and 30 min at 1.1 V.

Results

The SEM pictures of the carbonaceous materials reveal primary particles ranging from 4 to 10 µm with agglomerates reaching 50 µm for ALM and WN samples. At higher magnification, small spheres (< 1 µm) are detected on the surface of the ALM sample whereas, in the case of the WN sample, they are replaced by open pores with similar size (< 1 µm). As expected from the morphology of wood, a fibre-like morphology is seen for the FIR sample.

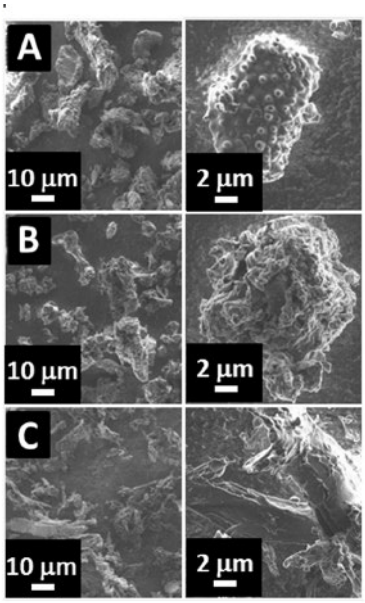

Figure 1. *SEM pictures of the carbonaceous materials.*

Figure 2a displays the XRD patterns of the carbonaceous materials. Each pattern is characterized by two broad Bragg peaks at 22.0 ° and 43.7 °, typically related to graphitic domains (sp2 domains). Two additional Bragg reflections at 27.8 ° and 46.1 ° (marked with * in Figure 2a) are detected in the WN sample, meaning that the washing procedure removed only partially the pesticides. The Raman spectra of the carbonaceous materials (Figure 2b) are identical and independent from the used precursors. It is described with a narrow G band and a broad intense D band, confirming the amorphous property of the synthesized carbons.

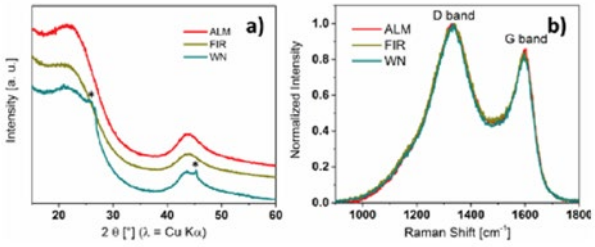

Figure 2. *a) XRD patterns and b) Raman spectra of the carbonaceous materials.*

The N_2 absorption/desorption isotherms of the samples (Figure 3) are described with a type IV isotherm and a type H4 hysteresis, characteristic for micro-mesoporous materials. Moreover, the increase of volume at very low pressure in the case of the WN sample might reveal the presence of micropores. The BET specific surface area values are 21 $m^2 g^{-1}$, 30 $m^2 g^{-1}$ and 88 $m^2 g^{-1}$ respectively for ALM, FIR and WN samples. The open pores seen in the SEM picture of the WN sample could explain the slight difference observed in the BET data.

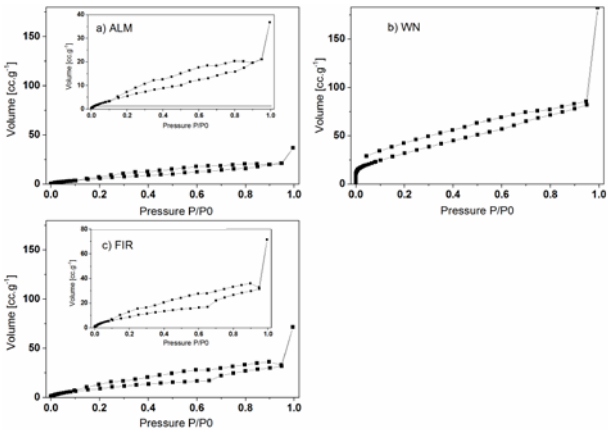

Figure 3. *N_2 absorption/desorption isotherms of the materials.*

The electrochemical performance of the carbonaceous materials are presented in Figure 4. Despite similar specific charge between 320 and 308 mAh g^{-1} reached for the 1st cycle, a drop in the specific charge occurs on the 2nd cycle due to the electrolyte decomposition. For the ALM and WN samples, a specific charge of 250 mAh g^{-1} is sustained during 60 cycles whereas 270 mAh g^{-1} are obtained after 80 cycles for the FIR sample with a Coulombic efficiency maintained higher than 99.5 %. The fibrous aspect of the FIR sample is probably beneficial for a direct access to the graphene sheet.

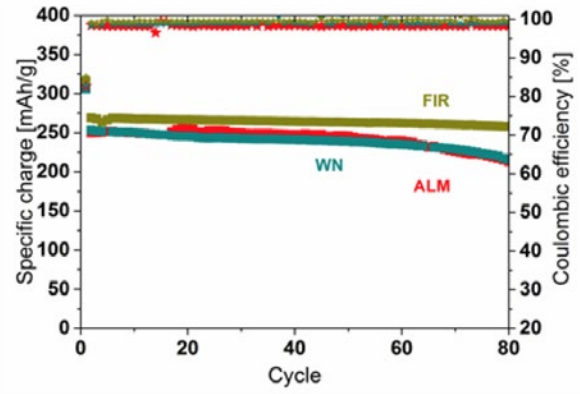

Figure 4. *Electrochemical performance of the materials at C/10 rate.*

The galvanostatic curves of the carbonaceous materials for the 2nd cycle are displayed in Figure 5. Similar profiles are seen independently from the precursor used for the synthesis. The sodiation starts by a slopping curve until 80 mV which was assigned to the insertion of Na into the disordered graphene layers [8]. Then, it is followed by a potential plateau accounting for 50 % of the specific charge and corresponding to the absorption of Na into the mesopores [8]. On desodiation, the electrochemical curve is characterized by a potential plateau from 5 mV to 100 mV followed by a slopping profile until 1.1 V.

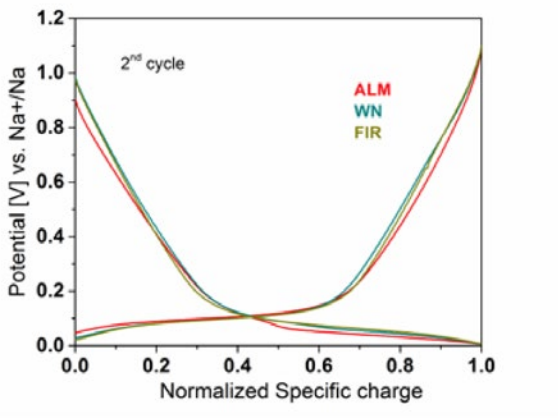

Figure 5. *Electrochemical performance of carbonaceous materials at C/10 rate.*

Conclusion

Three bio-waste lignin-based compounds were used as precursors for synthesising carbonaceous materials. Despite similar physical properties of these, the material derived from scrap wood showed an unique fibre-like morphology. This difference was translated in the electrochemical performance by a reversible specific charge of 270 mAh g^{-1} sustained for 80 cycles whereas only 250 mAh g^{-1} were reached for ALM and WN samples.

Acknowledgement

This work was performed within the Network of the Swiss Competence Center for Energy Research *Heat and Electricity Storage* (SCCER HaE). The authors thank Mr Eibar Flores for the help with the Raman measurements, Dr Sigita Trabesinger and Dr Joanna Conder for the helpful discussion about BET measurements.

References

[1] H. Li, L. Peng, Y. Zhu, D. Chen, X. Zhang, G. Yu, *Energy Environ. Sci.* **9**, 3399–3405 (2016).
[2] E.J. Berg, C. Villevieille, D. Streich, S. Trabesinger, P. Novák, *J. Electrochem. Soc.* **162**, A2468–A2475 (2015).
[3] E.M. Lotfabad, J. Ding, K. Cui, A. Kohandehghan, W.P. Kalisvaart, M. Hazelton, D. Mitlin, *ACS Nano* **8**, 7115–7129 (2014).
[4] E. Schröder, K. Thomauske, B. Oechsler, S. Herberger, in *Progress in Biomass and Bioenergy Production*, ed. D.S. Shaukat, 333–356 (2011).
[5] L. Wu, D. Buchholz, C. Vaalma, G.A. Giffin, S. Passerini, *ChemElectroChem* **3**, 292–298 (2016).
[6] M. Dahbi, M. Kiso, K. Kubota, T. Horiba, T. Chafik, K. Hida, T. Matsuyama, S. Komaba, *J. Mater. Chem. A* **5**, 9917–9928 (2017).
[7] X. Dou, I. Hasa, M. Hekmatfar, T. Diemant, R. Jürgen Behm, D. Buchholz, S. Passerini, *ChemSusChem* **10**, 2668–2676 (2017).
[8] D.A. Stevens, J.R. Dahn, *J. Electrochem. Soc.* **148**, A803 (2001).

Modelling the performance of alkali-ion batteries

S.F. Schneider, P. Novák, E. Jämstorp Berg
phone: +41 56 310 2161, e-mail: simon.schneider@psi.ch

Rechargeable Li-ion batteries (LIBs) today are considered the state-of-the-art technology for a wide range of energy storage applications due to their unmatched energy density. However, due to concerns regarding the future price and availability of lithium, increased efforts have been devoted to developing alternative chemistries. Na-ion (NIBs) and K-ion batteries (KIBs) are particularly interesting candidates to eventually complement the LIB technology. Whereas it is commonly expected that NIBs and KIBs cannot compete with LIBs in terms of energy density, it is often speculated that they might be more suitable for high-power applications. Na^+ and K^+ have larger ionic radii than Li^+ and could therefore enable faster diffusion in the electrolyte and faster charge transfer at the electrode–electrolyte interface. [1–2] The aim of the report is to compare the expected performance of future alkali ion batteries at varying discharge rates by modelling Ragone plots for LIBs, NIBs, and KIBs.

Modelling

An electrochemical battery model consisting of a set of coupled partial differential equations (PDEs) was employed. [3] The PDEs describe ionic and electronic diffusion in the porous anode and cathode, ionic diffusion in the electrolyte, and charge transfer kinetics at the electrode–electrolyte interface. A detailed model description is provided in [3]. We used this model framework to simulate potential–time discharge curves for varying current densities.

For the LIB, we selected graphite as anode active material and $LiNi_{1/3}Mn_{1/3}Co_{1/3}O_2$ (NMC) for the cathode. The default values specified in [3] were assumed for the battery cell design parameters, i.e. electrode thickness and porosity. A NIB and KIB were modelled by adapting the following parameters:

- specific charge and operating potential of active materials,
- electrolyte diffusion coefficient of Na^+ and K^+,
- transference number of Na^+ and K^+,
- rate constant for charge transfer at electrode–electrolyte interface.

In the case of the NIB and KIB, the literature provides only rough estimates for the input parameters and the model output is thus subject to uncertainties. We therefore performed a Monte Carlo simulation to model discharge profiles of the NIB and KIB.

For the Ragone plots, energy densities (Ed) and average power densities (Pd) were calculated from the discharge profiles using the below relationships.

$$E_d = \frac{J}{v}\int_{t=0}^{t_{cutoff}} V(t)dt \qquad (1)$$

$$P_d = \frac{J}{v t_{cutoff}}\int_{t=0}^{t_{cutoff}} V(t)dt \qquad (2)$$

J, v, and *V(t)* denote the current density, the battery cell volume, and the discharge potential, respectively.

Results

Figure 1 shows that the LIB displays superior energy density at low power density, i.e. at low discharge rate. At increased discharge rate, the energy density of both the NIB and KIB approach the one of the LIB and at power-to-energy ratios (P/E) of ca. 20, all three chemistries offer roughly the same energy density.

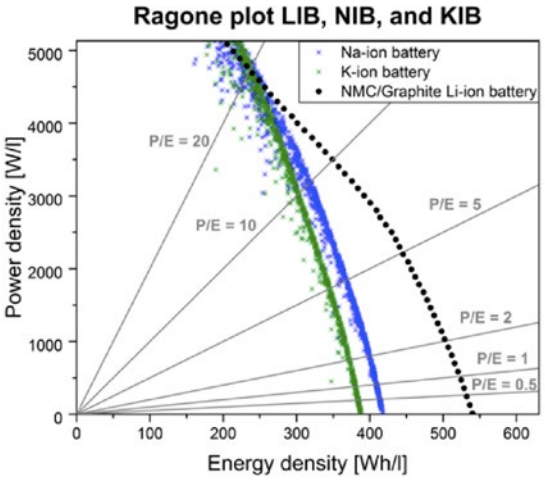

Figure 1. *Ragone plot for LIB, NIB, and KIB as computed with the electrochemical battery model.*

Our preliminary results support the suggestion that NIBs and KIBs could compete with the currently more advanced LIB technology in high-power energy storage applications, such as ultrashort-term uninterrupted power supply. NIBs and KIBs are thus promising technologies not only due to eventual cost advantages but also because of their compelling predicted high-power performance.

Whereas the presented analysis was restricted to one set of battery cell design parameters (the same electrode thickness and porosity was assumed for all three battery chemistries), we plan to systematically optimize electrode thickness and porosity for varying power requirements. This will shed more light on the importance of battery cell engineering.

Acknowledgement

We are grateful to Christian Bauer and Tom Kober from the Laboratory for Energy Systems Analysis at PSI for their support.

References

[1] A. Ponrouch, D. Monti, A. Boschin, B. Steen, P. Johansson, M.R. Palacín, *J. Mater. Chem. A* **3**, 22 (2015).
[2] V.A. Nikitina, S.S. Fedotov, S.Y. Vassiliev, A.Sh. Samarin, N.R. Khasanova, E.V. Antipov, *J. Electrochem. Soc.* **164**, A6373–A6380 (2017).
[3] M. Torchio, L. Magni, R.B. Gopaluni, R.D. Braatz, D.M. Raimondo, *J. Electrochem. Soc.* **163**, A1192–A1205 (2016).

Voltaic losses of vanadium flow batteries at different states of charge

F.J. Oldenburg, T.J. Schmidt, L. Gubler
phone: +41 56 310 2920, e-mail: fabio.oldenburg@psi.ch

Within the current energy transition scenario, 160 GW net capacity for renewable power generation is expected to be added worldwide annually until 2040 [1]. Of this more than 77 % is accounted for by solar and wind power, which are both intermittent, non-dispatchable and difficult to predict. The key to match demand and supply of electricity are energy storage solutions.

The vanadium flow battery (VFB) is a modular large-scale stationary storage technology in which energy and power can be scaled independently. Compared to competing technologies (e.g. Li-ion batteries) they can have life-times of several decades with no significant performance loss due to the ability of recycling all components separately. Within the discharge process the electrolytes undergo the following half-cell reactions:

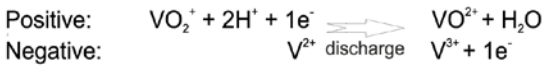

A decreasing proton concentration limits the conductivity, whereas changing oxidation states could affect charge-transfer overpotentials, both contributing to voltaic losses of the cell. In order to optimize the operation conditions of the VFB, the cell performance was evaluated depending on the state of charge (SOC) of the battery.

Experimental

For all experiments, the RFB test system Model 857 from Scribner was used. A single cell with 25 cm^2 active area was assembled with SGL Sigracell® GFD4.6EA carbon felt electrodes on each half-cell, compressed to 35 % and heat-treated at 400 °C for 30 h. A preswollen Nafion® N117 membrane and 200 mL of Oxkem electrolyte with a concentration of 1 M vanadium in 2.1 M H_2SO_4 was used (with 40 mL min^{-1} flowrate). To set a defined state of charge, the cell was charged at constant current (40 mA cm^{-2}). The open circuit voltage was measured to monitor the charging process (Figure 1). At each SOC, the specific area resistance was determined by high frequency impedance experiments at the open circuit potential from 100 k–0.1 Hz. A $Hg/HgSO_4$ reference electrode was used in an edge-type configuration as described by Taylor *et al.* to distinguish between polarization of the positive and negative electrode [3].

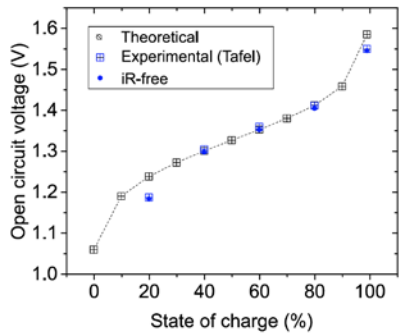

Figure 1. *Open circuit voltage of the cell compared to the theoretical value calculated according to [2].*

Results and discussion

The cell performance is influenced by three major electrolyte characteristics, which change with the state of charge: the oxidation state of the vanadium ions, the concentration of protons and the electrolyte viscosity. The latter has been evaluated by Xu *et al.* and will only be briefly discussed within the scope of this work [5]. To evaluate the performance at different SOCs, polarization and impedance measurements were performed. Therefore, the VFB was charged to a defined SOC and polarized at constant charge and discharge currents. Close to 0 % and 100 % high overpotentials result from limiting substrate concentrations during discharge and charge, respectively (Figure 2).

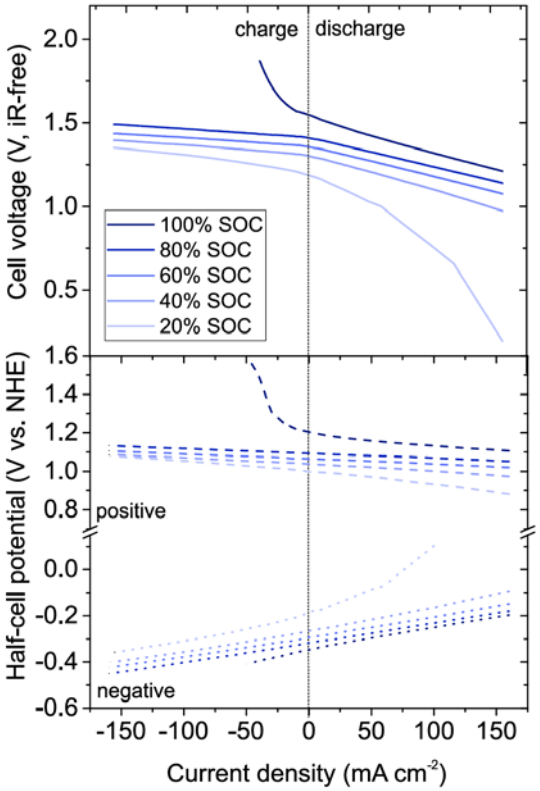

Figure 2. *Polarization curves of a VFB at different SOC for the full-cell (top) and each half-cell (bottom).*

Figure 3 depicts Tafel plots for all polarization curves. They are shifted according to the open circuit voltage, which was used to determine the exchange current density by linear fitting of the Tafel region. The exchange current densities of the two half-cells are very similar and both have their maximum at around 60 % SOC corresponding to similar symmetry coefficients. The data was fitted according to

$$j_0 = k_0' \cdot SOC^{1-b} \cdot (1 - SOC)^b$$

with k_0' representing a fitting constant and b the symmetry coefficient with a value of 0.4.

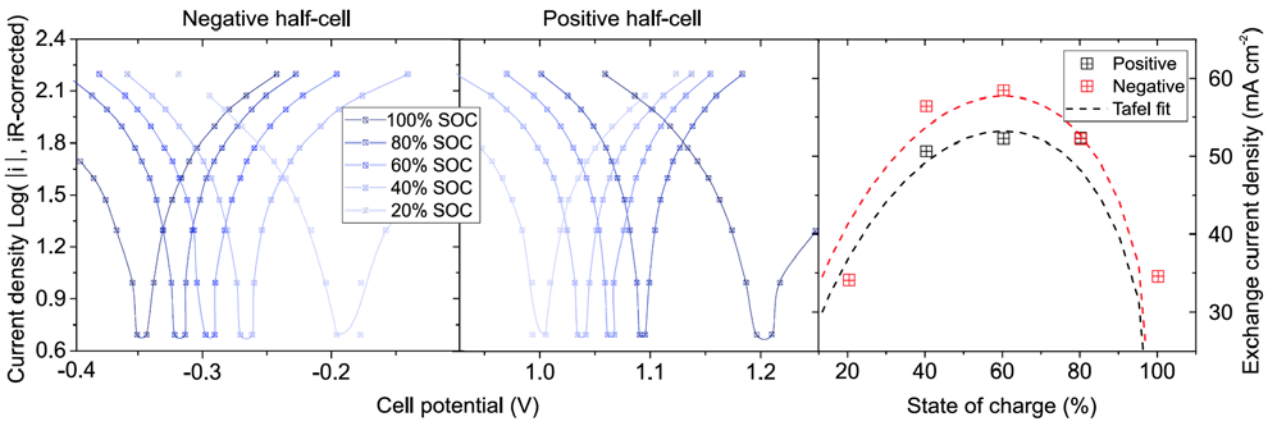

Figure 3. *Tafel plots of the negative and positive half-cell and the respective exchange current densities at each SOC.*

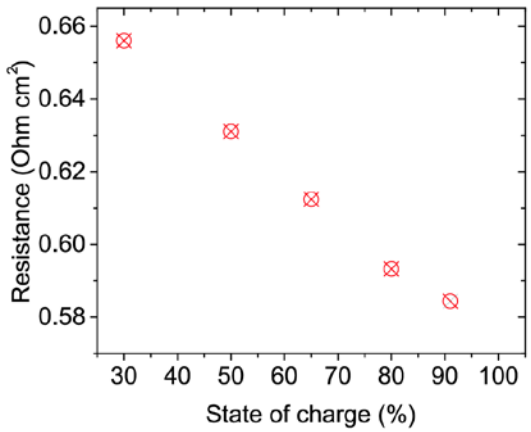

Figure 4. *High frequency area resistance at different SOC.*

Figure 4 presents the ohmic area resistance for different states of charge. The electrolyte resistance mostly depends on the free proton concentration and decreases with the proton producing charge reaction. This can affect the voltaic performance in two ways: a lower electrolyte conductivity increases ohmic losses as well as concentration overpotentials since two protons are needed per transfer of one electron during the discharge reaction. The latter effect however is negligible in view of the excess of protons and their high mobility.

The exchange current density is a measure of the redox kinetics. Its value depends, according to the Butler-Volmer equation, on the concentration of all ions participating in the redox-reaction and on the electrode surface area. It reaches a maximum if the concentration ratio equals the transfer coefficient. However, an influence of the decreasing proton concentration on the exchange current density of the positive half-cell is not observed.

Another limitation of the redox kinetics at low states of charge was reported by Derr *et al.* Here, the charge-transfer resistance obtained from electrochemical impedance spectroscopy increased significantly with decreasing SOC and was 5 times higher at 0 % compared to 100 % SOC [4]. The reduction of V(III) was observed to be the slowest of all four reactions taking place in the VFB.

The concentration of each vanadium ion additionally influences the viscosity of the electrolyte solution and has thereby another effect on the cell performance [5]. With an increasing electrolyte viscosity, the ion mobility is decreased resulting in higher concentration overpotentials during the charge and discharge process. Xu *et al.* calculated the SOC-dependent viscosity according to Eyring's absolute rate theory and predicted a higher viscosity at low SOC, mostly resulting from the high viscosity of the dissolved VO^{2+}. When accounting for the varying viscosity, the theoretical round-trip efficiency was 1 % lower than with a constant viscosity. A further loss of 3 % system efficiency was predicted, resulting from a higher pressure drop and related pumping power losses.

Conclusion

Generally it is favourable to operate the battery at moderate-high states of charge due to less pronounced voltaic losses. High electrolyte resistance, a low exchange current density and high solution viscosities were identified as limiting factors at a low SOC.

For optimizing the electrolyte composition further limiting effects must be considered, such as the vanadium solubility and the temperature window of stability. Higher sulfuric acid concentrations would decrease the voltaic losses; however, the vanadium solubility and the lower operation temperature limit decrease simultaneously. Another important factor is the corrosiveness of the electrolyte, which is significantly higher at high SOC. Hence storing the electrolytes might be preferable in the fully discharged state.

Acknowledgement

The authors kindly acknowledge the Swiss Federal Office of Energy (SFOE) for their financial support within the RFBmem project (Grant No. SI/501421-01).

References

[1] International Energy Agency, *World Energy Outlook 2017*, https://www.iea.org/weo2017/ (28.11.2017).
[2] K.W. Knehr, E.C. Kumbur, *Electrochem. Commun.* **13**, 342–345 (2011).
[3] O. Nibel, S.M. Taylor, A. Pătru, E. Fabbri, L. Gubler, T.J. Schmidt, *J. Electrochem. Soc.* **164**, A1608–A1615 (2017).
[4] I. Derr, M. Bruns, J. Langner, A. Fetyan, J. Melke, C. Roth, *J. Power Sources* **325**, 351–359 (2016).
[5] Q. Xu, T. Zhao, C. Zhang, *Appl. Energy* **130**, 139–147 (2014).

Chemical reactivity of tristrimethylsilylphosphate (TMSPasdf) towards fluorides in Li-ion battery electrolytes

A. Guéguen, C. Bolli, E.J. Berg
phone: +41 56 310 2176, e-mail: aurelie.gueguen@psi.ch

Our previous studies based on Online Electrochemical Mass Spectrometry (OEMS) confirmed the autocatalytic decomposition loop of $LiPF_6$ salt used in carbonate-based electrolytes present in commercial Li-ion batteries [1, 2]. Some of these reactions produce HF, whose presence favours transition metal leaching from oxide active material such as Li-rich nickel-cobalt-manganese oxide (HE-NCM) and thus jeopardize the performance of Li-ion batteries. Addition of tris(trimethylsilyl) phosphate / phosphite to carbonate electrolytes was reported to improve the cycle life of Li-ion cells by creating artificial electrode interface [3] and scavenging HF [4]. In the present report we study the impact of TMSPa on gas evolution (O_2, CO_2, POF_3) in HE-NCM full cells using OEMS. Detection of Me_3SiF gas provides further understanding regarding the scavenging activity of TMSPa as such gas results from reactions between TMSPa and fluorides.

Experimental

HE-NCM electrodes were prepared by coating Celgard 2400® polypoplylene sheet with a mixture of 89 %wt HE-NCM (BASF SE), 4.64 %wt conductive carbon Super C65 (Imerys Graphite & Carbon), 1.36 %wt SFG6L (Imerys Graphite & Carbon) and 5 %wt PVdF (polyvinyl-idene fluoride) dispersed in N-methylpyrrolidone (NMP, Sigma-Aldrich). Graphite electrodes were prepared by coating Cu foil with a mixture of 95.7 %wt graphite SFG6 (Imerys Graphite & Carbon), 0.5 %wt conductive carbon Super C65 and 3.8 %wt carboxymethyl cellulose (CMC) binder in water. Electrodes were further punched from HE-NCM (15 mm diameter) and graphite (20 mm diameter) sheets and subsequently dried at 80 and 120 °C, respectively.

The OEMS experiments were performed in a custommade electrochemical cell (Annual Report 2012, p. 47). HE-NCM full cells were cycled between 0 and 4.7 V (all potentials in the report are given vs. Li^+/Li) at C/10 rate. The electrolyte containing 1 %wt TMSPa (Sigma-Aldrich, purity > 98 %) was prepared just before assembling the cell by adding appropriate amount of TMSPa to 1 M $LiPF_6$ fluoroethylene carbonate (FEC) : diethyl carbonate (DEC) (12 : 88) electrolyte.

Results

It can be seen by comparing gas evolution profiles (Figure 1) that TMSPa impacts mostly POF_3 evolution and not O_2 and CO_2. Such effect is more pronounced during the 1st charge.

Detection of Me_3SiF in presence of TMSPa confirms that TMSPa scavenges F^-. Interestingly, Me_3SiF evolves similarly to CO_2. Hence Me_3SiF depends to some extend to the cell potential. During the OCP period, almost no Me_3SiF is detected. This is expected as during OCP only trace amounts of ROH species, which initiate $LiPF_6$ decomposition loop, are present in the cell. The simultaneous immediate production of CO_2 and Me_3SiF at beginning of the 1st charge is related to the reduction of FEC at the graphite electrode, resulting in formation of CO_2 and LiF. Further experiments we ran confirmed that TMSPa reacts with LiF, releasing Me_3SiF.

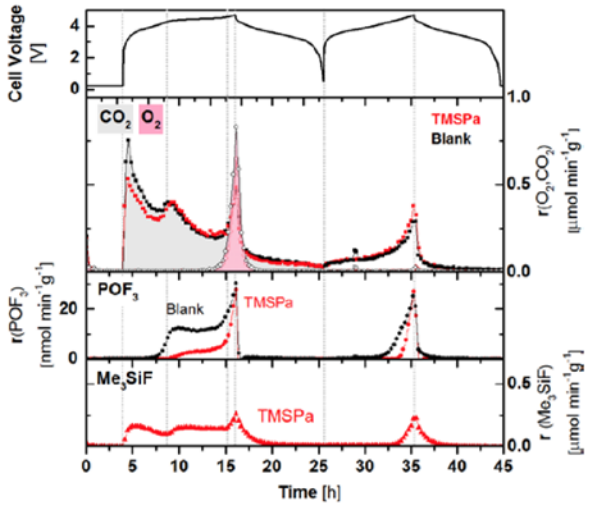

Figure 1. *Potential profile and O_2, CO_2, POF_3 and Me_3SiF evolution rate profiles for HE-NCM full cells with reference electrolyte and electrolyte containing TMSPa.*

Above 4.2 V (activation plateau), reactive oxygen species are released from the active material, enhancing the $LiPF_6$ decomposition loop and POF_3 and HF production. Scavenging of HF by TMSPa results in a decrease of POF_3 amount and constant Me_3SiF release during the plateau. At high potentials (> 4.6 V), HE-NCM surface reconstruction and severe electrolyte oxidation further accelerate strongly the gas release observed at end of charge.

Conclusion

Following Me_3SiF evolution in HE-NCM full cells using *operando* OEMS provides further understanding of the reactivity of TMSPa inside the cell. TMSPa reacts chemically not only with HF but also with other fluoride species such as LiF produced at different steps of the 1st charge.

Acknowledgement

The authors thank BASF SE for fruitful discussion and financial support.

References

[1] A. Guéguen, D. Streich, M. He, M. Mendez, F. Chesneau, P. Novák, E.J. Berg, *J. Electrochem. Soc.* **163**, A1095–1100 (2016).
[2] D. Streich, A. Guéguen, M. Mendez, F. Chesneau, P. Novák, E.J. Berg, *J. Electrochem. Soc.* **163**, A964–970 (2016).
[3] J. Zhang, J. Wang, J. Yang, Y. NuLi, *Electrochim. Acta* **117**, 99–104 (2014).
[4] G Han, S.J. Lee, J. Lee, J.S. Kim, K.T. Lee, N.S. Choi, *ACS Appl. Mater Interfaces* **7**, 8319–590 (2015).

Diffusion of solid reaction products during SEI formation in Li-ion batteries

P. Kitz, P. Novák, E.J. Berg
phone: +41 56 310 3401, e-mail: paul.kitz@psi.ch

Electrolyte is reduced on the surface of the anode during cycling of a Li-ion cell. Solid reaction products form the solid electrolyte interphase (SEI) and hinder further electrochemical decomposition by blocking electron transport. While this process is required for a functioning cell, it is also leading to several key problems: Consumption of Li-ions due to electrolyte decomposition results in an irreversible loss of specific charge, especially during the first cycle. The formation of SEI furthermore introduces an additional diffusion resistance for Li-ions, which increases electrode impedance and lowers the energy density of the cell [1].

One critical aspect of SEI formation, which is often overlooked, is dissolution and diffusion of decomposition products to other cell parts, most notably the cathode. In this study these mass transport processes are investigated using a quartz crystal micro balance with dissipation monitoring (EQCM-D).

Experimental

A special cell design was developed for tracking diffusion of SEI components from the anode to other battery parts (Figure 1). A Super C65 carbon black model working electrode coated on Celgard is cycled against a lithium metal counter electrode between 3 V and 0.2 V vs. Li^+/Li with 0.1 mV/s CV scan rate. The cell is filled with LP47 electrolyte (1 M $LiPF_6$ in EC:DEC 3:7). The electrode stack is placed on a stainless steel mesh separating it from a copper coated QCM-D sensor placed beneath. Since the QCM is not connected to the potentiostat, no electrochemical reactions are expected to occur on the sensor surface. The free diffusion pathway between working electrode and sensor allows dissolved SEI species formed on the carbon black surface during cycling to precipitate on the QCM-D sensor.

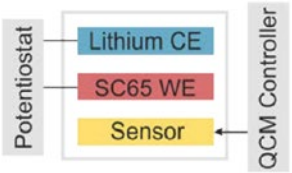

Figure 1. *Experimental setup: Li counter electrode is cycled against a carbon black working electrode in LP47 while QCM-sensor frequency and dissipation changes are monitored.*

The sensor is made of a quartz crystal oscillating in an alternating electrical field due to the piezoelectric effect. The QCM controller monitors resonance frequencies and resonance dissipation values of all odd harmonic overtones up to the 13th order allowing the measurement of sensor mass changes with an accuracy of up to 1.8 ng/cm^2. In case of a rigid, homogeneous and well adhered layer precipitating on the sensor surface, mass accumulation is linearly correlated with a resonance frequency decrease [2]. Deposition of mass on the sensor surface featuring viscoelastic behaviour requires an advanced Voigt model in order to calculate sensor mass changes from resonance frequency and dissipation values.

Results

Figure 2 (top) shows the current flowing through the carbon black model electrode during cyclic voltammetry. Below 1.5 V vs. Li^+/Li electrolyte is reduced and the current increases. Irreversible EC reduction in the first cycle at around 0.8 V vs. Li^+/Li is one of the main processes forming SEI and results in a large current peak.

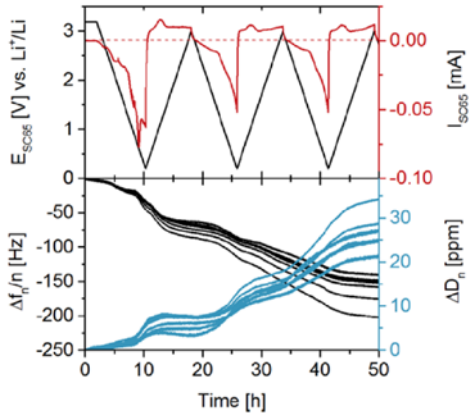

Figure 2. *Top: Current flow through the carbon black working electrode during cyclic voltammetry as a function of time. Bottom: Normalized resonance frequency and dissipation changes (n = 3,5,…,13) of the electrically insulated QCM-D sensor as a function of time.*

Figure 2 (bottom) displays QCM-D sensor resonance and dissipation changes during CV. Even though the QCM-D is not connected to the potentiostat, mass is accumulating on the sensor electrolyte interface. Soluble SEI components diffuse from the anode to the inert cell walls and (partially) precipitate. Especially the reduction of EC in the first cycle results in a major decrease of sensor resonance frequency. Growing resonance dissipation and the separation of normalized resonance frequency values indicate that the formed layer features viscoelastic behaviour. A sensor mass increase of ~12.5 µg/cm^2 after three cycles was calculated by visco-elastic modelling.

Our study proves than SEI components are diffusing from the anode to the other cell parts. These species might not only influence the cathode (electro-) chemical behaviour but could also lead to an increase of cathode impedance and therefore affect cell performance.

Acknowledgement

The authors thank the Swiss National Science Foundation SNSF for financial support (PN: 160540).

References

[1] D. Juarez-Robles, C. Chen, Y. Barsukov, P. P. Mukherjee, *J. Electrochem. Soc.* **164**, A837–A847 (2017).
[2] G. Sauerbrey, *Zeitschrft. f. Phy.* **2**, 206–222 (1959).

Development of a Raman spectro-electrochemical cell

E. Flores, P. Novák, E.J. Berg
phone: +41 56 310 5450, e-mail: eibar.flores@psi.ch

Raman spectroscopy is a versatile and non-destructive tool to characterize the structure and composition of electrode materials for Li-ion batteries. The measurements can be done *operando* due to the optical probing mode of the sample, and fast recording times allow time-resolved experiments during cell operation. [1]

Operando measurements require a dedicated spectro-electrochemical cell in which the electrode materials are cycled and their Raman spectra are collected as they operate. Ideally, the cell permits near-practical electrochemical performance and the detection of well-resolved Raman signals with high time resolution and high signal-to-noise ratios. Meeting those main three requirements leads to several compromises in the cell design.

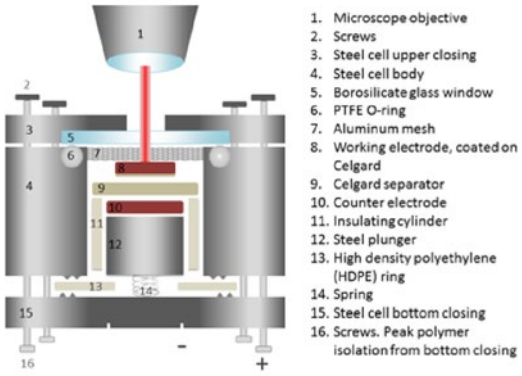

Figure 1. *Schematic representation of the newly developed Raman spectro-electrochemical cell.*

Figure 1 shows a schematic representation of the newly developed Raman spectro-electrochemical cell. The cell components (parts 8, 9, 10) are assembled in a coin-cell type configuration and a glass window (part 5) allows the laser probing of the working electrode (WE) in a top-down fashion. Several design details were implemented to achieve optimal electrochemical performance:

a) a PTFE O-ring (part 6) and a HDPE disc (part 13) have superior sealing properties and keep the cell gas-tight;
b) the counter electrode (part 10) is wider than the working electrode (part 8) for minimizing the sluggish edge Li^+ transport;
c) an aluminium mesh (part 7) distributes the current uniformly at the electrode surface;
d) the new design supports the use of thin (100 µm) Celgard-coated composite electrodes which minimize diffusion overpotentials.

The aluminium mesh separates the WE from the window and increases the laser path through electrolyte-filled space. To avoid electrolyte signals and enhance the bands from the active material, the WE and the separators are only wetted in electrolyte so the space between the window and the WE remains empty and the electrolyte signals are avoided.

Figure 2 compares the performance of the old and new Raman cells using a $LiNi_{0.8}Co_{0.15}Al_{0.05}O_2$ (NCA) composite electrode. NCA was selected because it is a state of the art electrode material with intrinsically weak Raman signals that are difficult to measure *in situ*. [2] The new cell design reduces overpotentials and enables higher practical specific charge of 225 mAh/g, superior to the 125 mAh/g achieved in the old cell, whereby the design required the use of thick (300 um) self-standing electrodes.

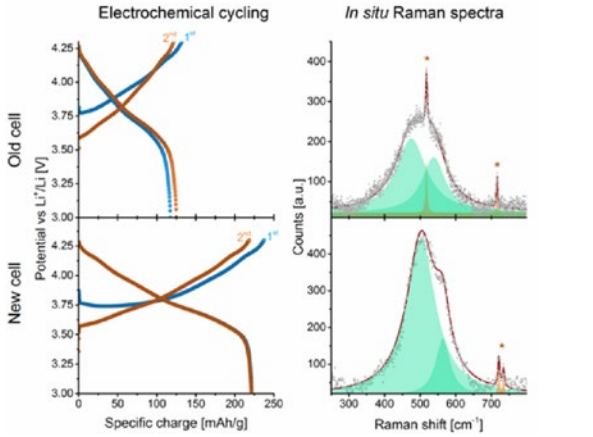

Figure 2. *Compared performances of the old and new Raman cells.*
Left panel: Galvanostatic potential profiles of a $LiNi_{0.8}Co_{0.15}Al_{0.05}O_2$ (NCA) composite electrode cycled vs. Li (1 M $LiClO_4$ in EC : DMC 1 : 1 w, C/20) in the old (top left) and new (bottom left) cells.
Right panel: In situ spectra of a NCA particle in the old (top right) and new (bottom right) cell (2.0 mW, 4 µm laser spot, 100 s exposure).

The Raman spectrum of NCA taken in the old cell (top right) overlaps with electrolyte bands (asterisks). The Raman spectrum of NCA in the new cell (with the same exposure time) has stronger, better-resolved spectral features, weak or even negligible electrolyte bands and reduced baseline noise. The new design records above 250 spectra in a 40 hours cycling.

In summary, a newly developed Raman spectro-electrochemical cell renders superior electrochemical performance, spectral quality and time resolution thanks to a new design that successfully addresses several technical challenges. Ongoing *operando* measurements of NCA composite electrodes reveal rich spectral trends with unprecedented detail, which ultimately will provide further insights into the evolution of NCA lattice dynamics and electronic structure during cycling.

Acknowledgement

Funding from the Swiss National Science Foundation is gratefully acknowledged (PN: 160540).

References

[1] R. Baddour-Hadjean, J.-P. Pereira-Ramos, *Chem. Rev.* **110**, 1278–1319 (2009).
[2] J. Lei, F. McLarnon, R. Kostecki, *J. Phys. Chem. B* **109**, 952–957 (2005).

Injection cell setup for online electrochemical mass spectrometry (OEMS)

C. Bolli, M. He, E.J. Berg
phone: +41 56 310 5091, e-mail: christoph.bolli@psi.ch

Online electrochemical mass spectrometry (OEMS) has been shown to be a valuable tool to study chemical and electrochemical processes in lithium ion batteries (LIB). OEMS gives particular insights into the reactivity of electrolyte–electrode interfaces, [1] the hydrolysis of the electrolyte [2] or in the surface reconstruction of the cathode active material. [3] Our recent studies focus on the effect of electrolyte additives on the gas evolution in LIBs and the formation of *in situ* formed reactive species. [4] However, studying the individual contribution of these molecules to the gassing at different potentials is challenging and several complementary cell configurations are required. In this report we present a cell design, which allows the addition of liquids into an operating Li-ion battery cell via injection.

Experimental

Detailed descriptions of the construction and assembling of the standard OEMS cells as well as calibration and technical information regarding the OEMS setup can be found in previous works. [2] DEC (battery grade, BASF SE), and TMSPa (> 98%, Sigma-Aldrich) were used as received. $LiBF_4$ (99.99 %, Sigma-Aldrich) was dried at 120 °C under vacuum before used.

Results

Figure 1 shows the injection cell that was designed by modifying a standard OEMS cell. An additional inlet was added on the top of the cell to which a short tube was soldered. A septum injector nut containing a standard ¼" gas chromatography septum was attached. The septum allows for a gas-tight system into which liquid samples can be injected via a syringe. The whole setup should thus allow studying the reactivity of the injected compound in an electrochemical cell by mass spectrometry without contamination by air.

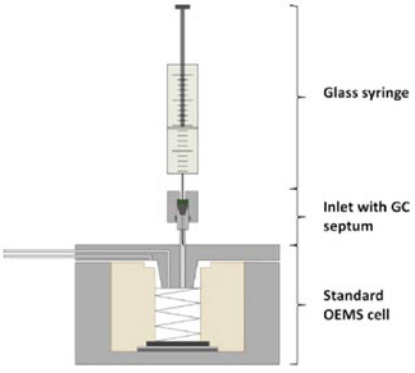

Figure 1. *Schematic drawing of an injection OEMS cell with attached syringe.*

In order to confirm the leak tightness of the system and the general feasibility of the cell, a simple chemical reaction was selected for a proof of concept experiment. The injection cell was filled with a solution of DEC (1 M $LiBF_4$) and an excess of tris(trimethylsilyl) phosphate (TMSPa) was injected. $LiBF_4$ and TMSPa react to form gaseous Me_3SiF and BF_3 according to

$$OP(OSiMe_3)_3 + LiBF_4 \rightarrow LiO_2P(OSiMe_3)_2 + Me_3SiF + BF_3 \quad (1)$$

Figure 2 shows that reaction (1) occurs immediately after injecting the TMSPa into the electrolyte solution whereby both BF_3 and Me_3SiF show an evolution maximum. Afterwards, the evolution rate of both gases decays exponentially, which is a result from the time dependence of reactant mass transport in the DEC solution.

During this experiment we also recorded the mass fragment 32 stemming from O_2 to monitor if any leakage of the septum occurs after the injection. Figure 2 shows that O_2 signal increased directly after the injection, which most likely indicates that a small amount of air diffused in the syringe before the injection. However, the O_2 evolution rate decays rapidly to virtually zero directly after the injection which shows that even the penetrated septum with the syringe is sufficiently tight.

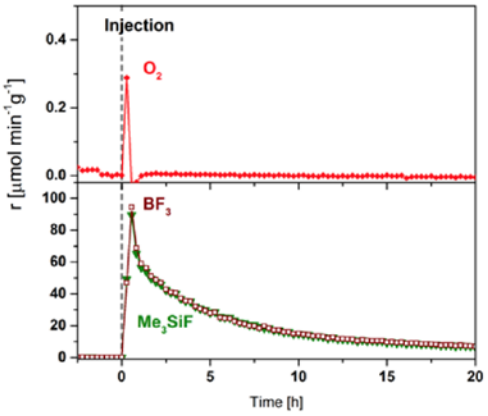

Figure 2. *Evolution rate of O_2 (top), BF_3 and Me_3SiF (bottom) after injection of TMSPa into the injection cell.*

Conclusion

The presented injection cell setup is a valuable tool to study the influence of reactive molecular additives on the gas evolution in operating cells. Further experiments to explore the potential of the injection technique are currently underway.

Acknowledgement

The financial support of BASF SE is acknowledged.

References

[1] D. Streich, A. Guéguen, M. Mendez, F. Chesneau, P. Novák, E.J. Berg, *J. Electrochem. Soc.* **163**, A964–A970 (2016).
[2] A. Guéguen, D. Streich, M. He, M. Mendez, F.F. Chesneau, P. Novák, E.J. Berg, *J. Electrochem. Soc.* **163**, A1095–A1100 (2016).
[3] D. Streich, C. Erk, A. Guéguen, P. Müller, F. Chesneau, E.J. Berg, *J. Phys. Chem. C* **121**, 13481–13486 (2017).
[4] C. Bolli, A. Guéguen, M. Mendez, E.J. Berg, manuscript in preparation.

Real-time observation of the interfacial reactions in all-solid-state Li-ion battery using *operando* XPS

X. Wu, C. Villevieille, P. Novák, M. El Kazzi
phone: +41 56 310 5034, e-mail: xiaohan.wu@psi.ch

All-solid-state lithium ion batteries (SLiB) offer higher energy and power density than conventional Li-ion batteries while ensuring safety during operation by replacing the flammable liquid electrolyte with non-flammable solid electrolyte (SE). [1] Recent progress in the development of SE with high ionic conductivity in the order of 0.1–10 mS/cm increases further the attractiveness of these systems. [2, 3] Despite the significant improvement of the bulk materials properties, degradation of SE at its interface with the active materials (AM) and conductive carbon remains one of the limiting factors affecting the battery performance. In the present study, we develop a novel *operando* XPS cell dedicated for SLiB operation under ultra-high vacuum (UHV) to probe in real-time the evolution of the interface reactivity while cycling the cell. This technique allows to obtain better insights of the interfacial degradation mechanism in a working electrode (WE) and to facilitate the interface engineering for improving SLiB stability and performance.

Experimental

Materials preparation and cell assembly

SE of the composition $(Li_2S)_3$-P_2S_5 (LPS) was synthesized by ball milling using procedure described here. [4, 5] The WE was prepared by hand mixing 50 %wt LPS with 45 %wt $LiCoO_2$ (LCO) and 5 %wt carbon fiber (VGCF). The counter electrode (CE) was made of an indium/LPS/C buffer layer with indium and lithium metal attached. The assembly mimics the procedure for a standard SLiB cell as described here. [5]

Operando X-ray photoemission spectroscopy

XPS measurements were carried out with a VG ESCALAB 220iXL spectrometer (Thermo Fisher Scientific) using focused monochromatized Al Kα radiation (1486.6 eV). The *operando* XPS cell was transferred to the XPS spectrometer using an argon-filled transfer chamber to avoid air exposure and surface modification.

Electrochemical measurements were performed with a VSP-300 (Bio-logic) potentiostat. Due to higher potential of the $InLi_x$ alloy ($x < 1$) counter electrode, a voltage shift of ca. 600 mV was taken into account for the cycling window. [6]

Results

Mechanical pressure during operation is crucial for reliable cell performance of bulk-type SLiB. Maintaining the pressure during XPS measurement is a particular challenge in the cell design, since the photo-electron's pathway cannot be blocked.

We designed an *operando* XPS SLiB cell as can be seen in Figure 1a. The implementation of the slit in the top cell lid ③ ensures maximal mechanical integrity of the structure whilst allowing the penetration of the X-ray with an incidence angle of 30°. On the surface of the WE, the interfaces between LCO, LPS and VGCF particles are exposed to X-ray. The tri-layered cell stack ⑦ is fabricated inside the Polyoxymethylene (POM) ring ② and subsequently transferred to the *operando* XPS cell base ①, thus eliminating any mechanical stress which could be induced if the cell stack had to be removed from the mold. The top lid is pressed on the cell stack by screws ⑤ and contacted to the positive electrode ⑥. Details on the electrical connections can also be found here. [7] The screws were electrically insulated from the lid by a plastic washer ④ to avoid any internal short-circuit.

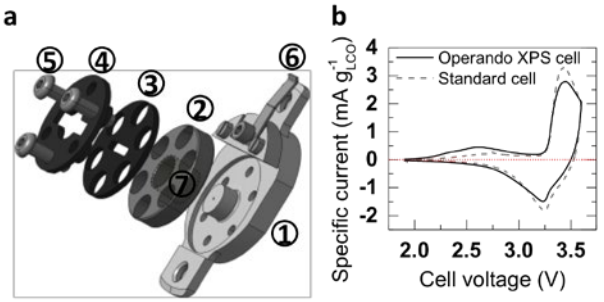

Figure 1. *(a) Operando XPS cell design for all-solid-state battery. (b) Validation of the electrochemical performance of the operando XPS cell by comparing its cycling behavior with the standard SLiB test cell in cyclic voltammetry (CV). The working electrode contains a mixture of LCO/LPS/VGCF in the mass ratio 45/50/5 which is measured against an $InLi_x$ counter electrode.*

In the cyclic voltammetry (scan rate 5 μV s^{-1}), the cycling performance of the *operando* XPS cell in UHV is compared with the standard SLiB cell which operates under 300 MPa mechanical pressure. SE oxidation is observed between 2.1 and 3.2 V in both cell configurations (Figure 1b). Beyond 3.3 V, the obtained charges are mainly attributed to the activity of LCO. In this range, both the *operando* XPS cell and the standard SLiB cell reach ca. 105 mAh g_{LCO}^{-1} during the 1st charge and ca. 93 mAh g_{LCO}^{-1} during the reversible discharge. Based on the onset of the LCO oxidation (10 % of the peak current), no additional overpotential was measured for the *operando* XPS cell in comparison to the standard cell configuration. The negligible overpotential ensures a reliable electrochemistry necessary to correlate any observed degradation products to the correct cell voltage.

Figure 2 depicts the recorded XPS core levels spectra of S2p, P2p, C1s, Li1s, Co3p and Fe3p from the WE. Any decomposition of the SE can be monitored by the chemical shift on both sulfur and phosphorus spectra. The C1s spectra consists of a C–C component originating from the VGCF located at 284.8 eV and several components at higher BE associated with adventitious carbon species from the mesh and the SE as well as C–O and C=O based contaminations. Fe2p and Fe3p core levels detected on the surface are related to the stainless mesh (current collector). The intensities of the Co3p spectra are relatively low due to the low volume fraction of LCO in the electrode. Due to the low signal intensity of Co3p relative to the Li1s signal, we assume that the detected Li1s core level stems mainly from the lithium ions contained in the SE rather than the ones in

LCO. The growth of the tail at higher BE in both S2p and P2p spectra upon cycling indicates the formation of oxidized SE byproducts. The decomposition of the SE is believed to happen mainly at the interface with the VGCF where most of the charge transfers occur and partially on LCO.

Thanks to the *operando* XPS, we can exactly determine the onset of the SE degradation at 2.1 V vs. $InLi_x$ (ca. 2.7 V vs. Li^+/Li). Auvergniot *et al.* attributed the oxidation of sulfur to the formation of polysulfidic species. The shift towards higher BE in the P2p spectra indicates the change of the chemical environment of the phosphorus, i.e., from PS_4^{3-} to P_2S_X.

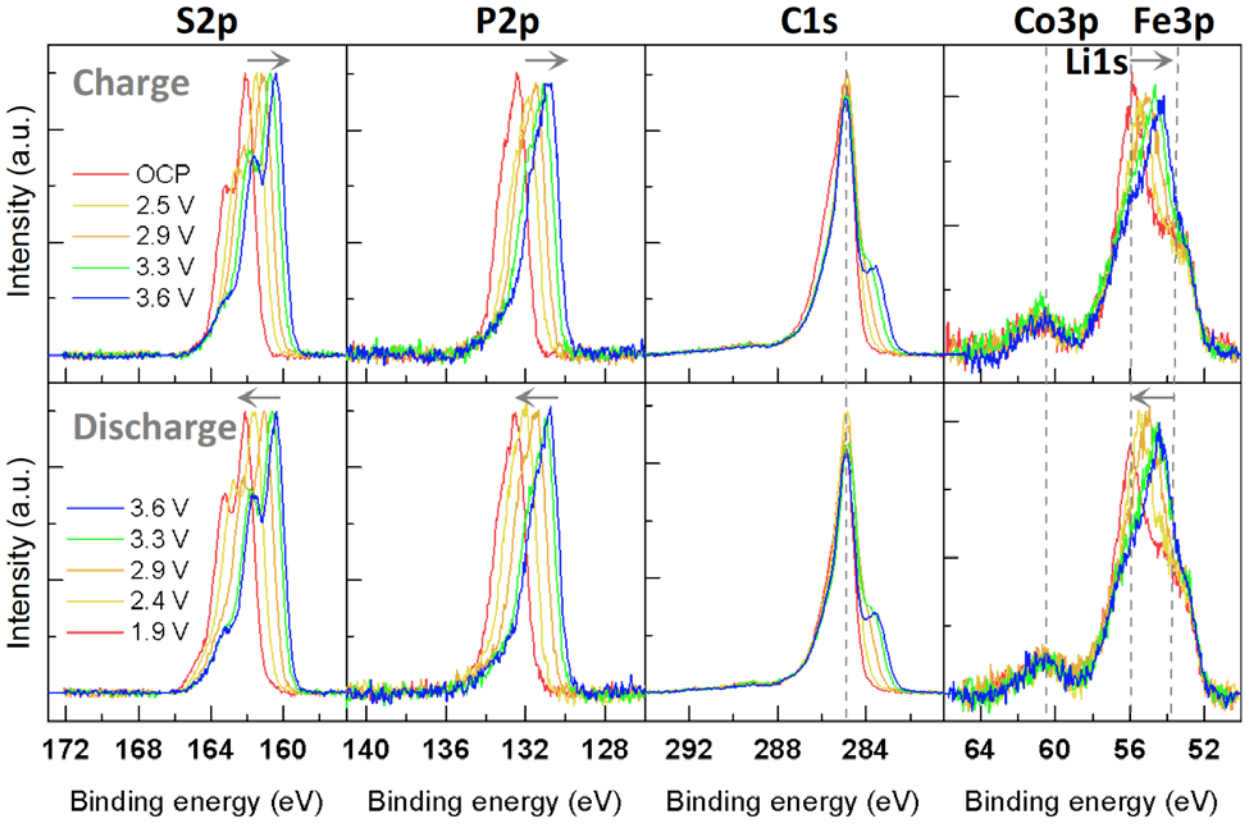

Figure 2. *XPS core levels spectra at each potential recorded during the operando XPS measurement of the LCO/LPS/VGCF electrode.*

Conclusion

In conclusion, our results present a proof-of-concept in advancing the understanding of the SE-electrode interface for SLiB. The *operando* XPS cell offers insight into the real-time evolution of chemical states of the elements at the SE-electrode interface in a complex electrode. The concept of the cell can be widely adapted to a variety of UHV photoelectron techniques as well as to a diversity of SE materials.

Acknowledgement

This work is supported by the Competence Center Energy and Mobility (CCEM) and the Swiss Electric research initiative (SER).

References

[1] Y. Kato, S. Hori, T. Saito, K. Suzuki, M. Hirayama, A. Mitsui, M. Yonemura, H. Iba, R. Kanno, *Nature Energy* **1**, 16030 (2016).
[2] Y. Seino, T. Ota, K. Takada, A. Hayashi, M. Tatsumisago, *Energy Environ. Sci.* **7**, 627–631 (2014).
[3] N. Kamaya, K. Homma, Y. Yamakawa, M. Hirayama, R. Kanno, M. Yonemura, T. Kamiyama, Y. Kato, S. Hama, K. Kawamoto, A. Mitsui, *Nat. Mater.* **10**, 682–686 (2011).
[4] A. Hayashi, S. Hama, H. Morimoto, M. Tatsumisago, T. Minami, *J. Am. Ceram. Soc.* **84**, 477–479 (2001).
[5] X. Wu, M. El Kazzi, C. Villevieille, *J. Electroceramics* **2–4**, (2017).
[6] K. Takada, N. Aotani, K. Iwamoto, S. Kondo, *Solid State Ionics* **86**, 877–882 (1996).
[7] D. Weingarth, A. Foelske-Schmitz, A. Wokaun, R. Kötz, *Electrochem. Commun.* **13**, 619–622 (2011).

SCIENTIFIC ACHIEVEMENTS 2017

Fuel Cells & Electrolysis –

Materials & Diagnostics

Experimental study of the water management in the Autostack-Core Evo2 fuel cell with neutron radiography

M. Cochet, D. Scheuble, U. Hannesen, P. Boillat
phone: +41 56 310 5256, e-mail: magali.cochet@psi.ch

Autostack-Core is a European funded collaboration between different component manufacturers, OEMs and research institutes to develop a high power density fuel cell stack for automotive applications [1]. In the framework of the evolution 2 (EVO2) of this project, we analyzed the water management of the cell. A common issue faced by PEFCs is the flooding of the cell. Water, stemming either from the humidified gases or from the electrochemical reaction, can accumulate in the cell and prevent the reacting gases from reaching the catalyst layer. This can lead to either recoverable losses or irreversible degradation. Here, we investigate the water management of a technical fuel cell under representative conditions, and we evaluate the conditions which have the potential to be harmful in the long term. To accomplish this goal, we use Neutron Radiography (NR) to investigate a single cell of full technical size with conditions representative of an entire stack.

Experimental

The design of the cell was made so that the single cell tested would be representative of a cell in a stack. In particular, 30 mm thick aluminium compression plates (see Figure 1) with a reinforced frame and strong springs were used to ensure a homogeneous pressure and minimal bending of the bipolar plates (BPP) over the entire active area.

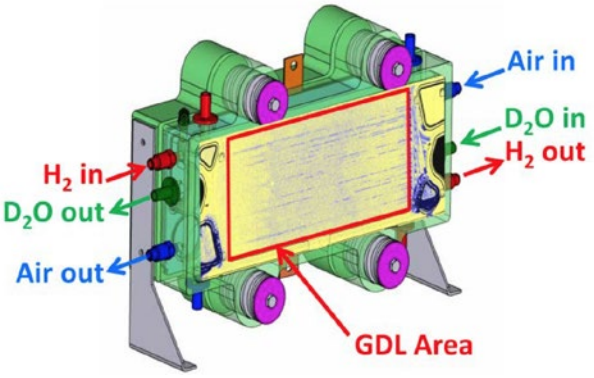

Figure 1. *Autostack test cell for Neutron Imaging, with an example of NR image superimposed to it.*

Another feature that needed to be representative was the thermal management. The compression plates' temperatures were controlled to match the cell temperature profile and minimize the heat exchange with the compression body. The cell itself was cooled by the convection of D_2O in the spacing between the anode and the cathode flowfields. D_2O was used as the coolant because of its lower neutron attenuation compared to H_2O, allowing to minimize the perturbation on the measurement of the water in the cell. NR was performed at the NEUTRA beamline at PSI. Due to the size of the cell tested, we used the largest available field of view of 360 x 380 mm^2. The reachable spatial resolution is low (0.19 mm / pixel and 0.4 mm of effective resolution), but still sufficient to distinguish ribs and channels. An example of NR image is shown on Figure 1. The experimental conditions are summarized in Table 1.

	Anode	Cathode
Coolant inlet temperature	68°C	68°C
Outlet Pressures	2.2 bars	2.0 bars
Dew Point	48.5°C	53°C
Stoichiometric Ratio	1.4	1.6
Mass flow rates	1.2-4.4 NL/min	1.6-12 NL/min
Current Density	0.2 – 1.5 $A.cm^{-2}$	

Table 1. *Experimental conditions.*

Results

The images from Figure 2 are showing the water distribution in the GDL area (300 cm^2) and in the inlets and outlets. At 0.2 A cm^{-2}, water accumulates strongly in the channels when the cell is started. When increasing the current density, however, the water content decreases. This can be attributed to the higher mass flow rates on the anode. With 30 % N_2 on the anode, the water content is lower than with pure H_2, which is consistent with the higher mass flow rates (in particular in the outlet section after most of H_2 has been consumed) and N_2's higher viscosity.

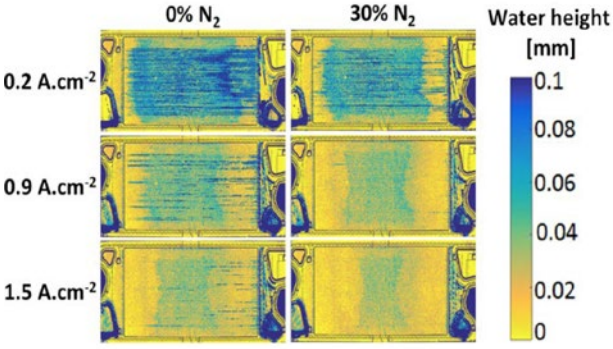

Figure 2. *NR images of the water distribution in the GDL area for various current densities and 2 different N_2 fractions.*

Performances are shown on Figure 3. The resistivity is low and stable at around 45 mΩ·cm^2 for all current densities, and is not strongly influenced by the N_2 content. There is a small performance drop between 30 % and 0 % N_2 which is almost zero for 0.2 A·cm^{-2} but increases with the current density up to about 10 mV for 1.5 A·cm^{-2}. This drop in performance is of the same order of magnitude as the measurement error; however it is quite repeatable, indicating that the presence of N_2 does slightly reduce performances.

Pressure drops on the anode and the cathode are shown on Figure 4. The cathode pressure drop increases linearly with the current density and with the gases mass flow rates, hinting at a laminar flow, unlike the anode pressure drop. This tends to indicate that much more water droplets are accumulated in the anode channels than in the cathode channels. This is also

visible on the radiograms, since the anode outlet (bottom right) is considerably more flooded than the cathode outlet (bottom left).

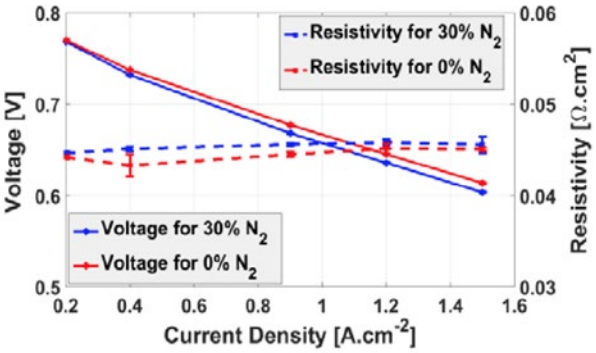

Figure 3. *Voltage and resistivity for different current densities and two anode N_2 contents.*

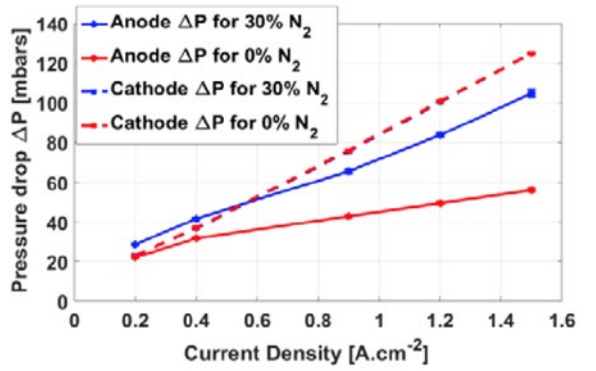

Figure 4. *Anode and cathode pressure drops for different current densities and 2 anode N_2 contents.*

Figure 5 shows the influence of the anode SR on the voltage and the average water height for two different N_2 contents on the anode. The N_2 contents are tested as the presence of big quantities of N_2, due to crossover from the cathode, is a well-known source of cell degradation. By comparing with and without N_2, we can determine how destructive the flooding is. Note that the following curves have been made with different series of measurements at low (from 1 to 1.4) and at high SR (from 1.2 to 2). This brings a slight overlap between 1.2 and 1.4. For the case pure H_2, one can note that the 2 series of experiments do not fully agree on the absolute values. However, the trends agree and the differences can be explained by the history of each series of experiments. For the high SR, from SR = 2 to SR = 1.4, we can see that the voltage does not decrease much (around 10 mV) be it for 0 % or 30 % N_2 content. Similarly, the water height tends to slightly decrease with increasing SR, due to the increased flow rate of gas. Very logically, the water height is lower with 30 % N_2, because of increased mass flow rates and because of the higher molar weight of the N_2, which increases the water vapor uptake. Between SR = 1.4 and SR = 1.2 the voltage drop is higher (more than 20 mV) for both N_2 contents. However the water height behaves differently for the cases with and without N_2. For the case 0 % N_2, water accumulation increases whereas the water height remains almost constant for 30 % N_2.

At very low SR, for the case 0 % N_2, the cell can remain stable up to 15 minutes, even near dead-end mode (SR = 1.03), but the performances are strongly degraded, by more than 100 mV. In the case of 30 %, a stable voltage at the same SR was obtained, however since it was run for only 5 minutes, we cannot be sure the cell would not eventually have failed. Meanwhile, the difference in water height for the two N_2 contents increases with decreasing SR. In the case 0 % N_2 the flowfields are massively flooded, especially near the anode outlet. This flooding can bring fuel starvation on large areas of the membrane, which explains the strong drop in performance. On the other hand, for the case with 30 % N_2, there is very little change in the water level, therefore the very low performances at low SR cannot be explained by flooding. From the NR images, it can be seen that the water tends to accumulate near the H_2 inlet, while the anode outlet is almost dry, indicating that there is probably no reaction there. This would explain the very low performance of the 30 % N_2 case in the absence of flooding.

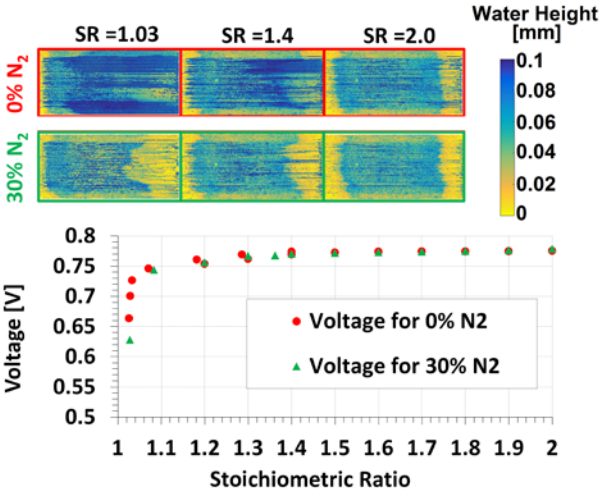

Figure 5. *Influence of the anode SR at $i = 0.2\ A{\cdot}cm^{-2}$ on the voltage and the pressure drop for two anode N_2 contents.*

Conclusions

The impact of N_2 in the anode on the water management of a technical size single fuel cell was studied using neutron radiography.

Two opposite effects were identified: on one hand, the presence of nitrogen strongly reduces the accumulation of water, owing to the increase of the gas flow leaving the cell. On the other hand, the presence of nitrogen can worsen the issue of hydrogen starvation, as observed by the apparition of an apparently inactive region at the anode outlet for very low stoichiometry.

Acknowledgement

All partners of the Autostack-Core consortium as well as the funding by the European Union (FCH JU Project no. 325335) are gratefully acknowledged.

References

[1] A. Martin, L. Jörissen, Symposium on Polymer Electrolyte Fuel Cells 15, PEFC 2015 – 228th ECS Meeting, Phoenix, Arizona, USA, 957–961, October 11–15 (2015).

Selective visualisation of water in gas diffusion layers with neutron dark field imaging

M. Siegwart, R.P. Harti, V. Manzi-Orezzoli, J. Valsecchi, C. Grünzweig, T.J. Schmidt, P. Boillat
phone: +41 56 310 5772, e-mail: muriel.siegwart@psi.ch

Polymer electrolyte fuel cells (PEFCs) are electrochemical devices which convert the chemical energy of hydrogen to electricity and are used in stationary and mobile applications as for example cars. Optimization of water management of fuel cells is an important lever to improve their performance and increase their live time.

Water that is produced by the electrochemical reaction occurring in the fuel cell leaves the cell either in gaseous or liquid form through porous gas diffusion layers (GDLs) which are placed between the electrodes and the gas flow channels. When most of the pores of the GDL are filled with liquid water, the access of gases to the electrodes is blocked and the fuel cell performance drops.

In order to understand the relation between cell parameters (e.g. operation conditions, flow field design, GDL materials), liquid water distribution and performance, methods that allow for visualization and quantification of water in the GDL are of great interest. Conventional neutron transmission imaging is a powerful tool for visualizing the water distribution behind typically used flow field materials such as aluminium or steel during *in situ* experiments. In order to quantify water in the different layers over the cross section, imaging of the cell can be performed with the cell membrane parallel to the beam [1]. To avoid saturation of the signal due to large water thicknesses, the width of the cell is limited to 20–30 mm in this configuration.

Neutron dark-field imaging offers new possibilities to visualize water in the GDL, as this technique is selectively sensitive to microstructures. The dark-field image (DFI) is obtained simultaneously to the conventional transmission image when a neutron grating interferometer [2] is placed in the beam. The produced interference pattern without any sample is a sinusoidal intensity variation with an amplitude that is defined by the characteristics of the interferometer and beam. A sample that contains microstructures in the size range from one to several tens of micrometres and with scattering length densities different from their surroundings causes neutron scattering to ultra-small angles, which results in a reduced amplitude of the sinusoidal interference pattern. The DFI value is a measure for this interference amplitude loss and is measured for every pixel of the image. Because large homogenous structures do not cause coherent neutron scattering at ultra-small angles they do not significantly influence the DFI value. Therefore, dark-field imaging can be applied to selectively visualize and analyse the water distribution in the GDL without disturbance of the signal from water present in flow channels. In addition, this imaging method can also be used to visualize changes in microstructure of the GDL which appear when the GDL is damaged.

Experimental

An in-house constructed aluminium device was used to fill the GDLs with water. In this setup (Figure 1) pressurized water was flowing through a 1 mm deep and wide channel which was covered first with a hydrophilic porous membrane and then with the GDLs. On the other side the drying channel was covered with a hydrophobic porous membrane which prevents water from penetrating into the channel but allows water vapour to diffuse through which enables drying of the GDLs without removing the test device from the beam. The tested GDLs were of type TGP-H-060 plain (Toray, Japan) and H2315 (Freudenberg, Germany) without hydrophobic coating and had an area of 20 x 22 mm^2. In the test device the GDLs were compressed to 150 µm, which is about 75 % of their original thickness. The GDLs were sealed with a rubber gasket.

Figure 1 shows the schematics of the setup. The experiments were performed at the ICON beamline [2] at the Swiss Spallation Neutron Source (SINQ) with a neutron grating interferometer which consists of three gratings [3].

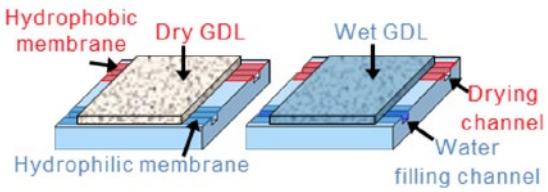

Figure 1. *Experimental setup. Left: dry GDL above dry channel. Right: water filled GDL above water filled channel.*

Results

Figure 2 contains colour coded images which visualise water distributed in a GDL of type Freudenberg H2315. These images were obtained from transmission (Figure 2a and c) and dark-field (Figure 2b and d) images. The total water thicknesses were calculated with the Beer-Lambert law from the transmission images (TIs), using the attenuation coefficient for 4.1 Å (neutron wavelength) for light (Figure 2a) and heavy (Figure 2c) water, respectively. The difference images between the dark-field images (DFIs) of the dry and water filled GDLs are shown in Figure 2b and 2d for light and heavy water, respectively. The corresponding colour scale is shown for each image and emphasizes where the GDL is dry (yellow) and where water is present (blue). The black line around the GDL in the colour coded images illustrates the border of the GDL for a simplified comparison between the images. The profile of the averaged water thickness and DFI value, in the area between the dashed red lines, is shown below the images.

By comparing the dark-field difference images and the water thickness images (WTIs) it becomes evident that some general water distribution patterns are captured by both imagining techniques in the same manner. In all four images (Figure 3a – d) it is visible that the area of the GDL between the red dashed lines is well filled with water while the part adjacent to the top border of the GDL is dry. The higher noise level in the WTI calculated from transmission for heavy water (Figure 3c) compared to light water is due to the lower attenuation coef-

ficient of heavy water. In contrary, the noise level in the DFI of the GDL filled with light water (Figure 3b) is higher compared to the image of the same GDL filled with heavy water (Figure 3d). This originates from the fact that the scattering length density (SLD) is only slightly lower for light water than for air. Contrary to that, the SLD difference between air and heavy water is large and results in a significant DFI value change between the dry and heavy water filled GDL (Figure 3d).

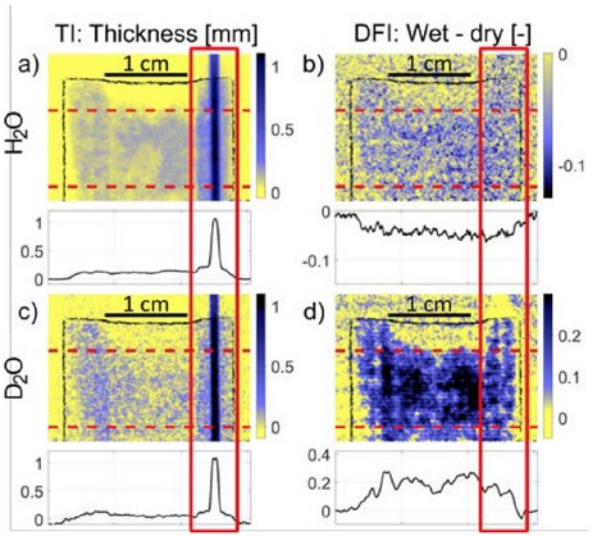

Figure 2. *Colour coded images showing the water distribution in a GDL (Freudenberg H2315):*
yellow = dry blue = water present a, b) H_2O c, d) D_2O
a, c): Water thickness images (WTIs) calculated from transmission images (TIs).
b, d): Difference of DFIs between dry and water filled GDL.
The dashed red lines in the images indicate the area for which the profile is plotted below the images.

The major difference between WTIs and DFIs is visible in the area highlighted with a red box in all images: it is the absence of sensitivity of the DFIs for large water structures such as the 1 mm wide water injection channel. While in the WTIs the contribution from the water in this channel makes the measurement of water in the GDL above nearly impossible, there is still a clearly visible signal from the GDL water in this region in the DFIs that is not disturbed by channel water. As can be seen in Figure 3d the DFI value measured in the area of the water filling channel varies along the channel from strong (blue) to weaker (more yellow). At the current stage, it is not possible to state whether this difference comes from different quantities of water, or from a higher amount of small water droplets having a high surface area, which would lower the DFI value. Thus, a reliable correlation between the DFI value and the amount of water in the GDL is yet to be demonstrated. Nevertheless, these experiments demonstrate that the presence of water in the GDL can be detected even in front of a large accumulation of water in the channel, at least when heavy water is used.

The DFI value of a GDL does not only change when the pores are filled with water instead of air but also when the microstructure of the GDL itself is altered. Therefore, dark-field imaging is also a powerful tool to visualize damages of the GDL.

This is demonstrated with Figure 3 which contains the transmission image (Figure 3a) and the dark-field image (Figure 3b) of a dry GDL (Toray, TGP-H-060 plain) which was damaged during the experiments because it did not withstand the lateral compression of the rubber gasket. In the TI (Figure 3a) the damage of the GDL is invisible whereas a crack is clearly visible in the DFI (Figure 3b). For the sake of clarity the averaged transmission values and DFI values, respectively, between the dashed red lines are also plotted. Here again, we see that, in contrast to the TI, the DFI can identify microstructure variations of the GDL.

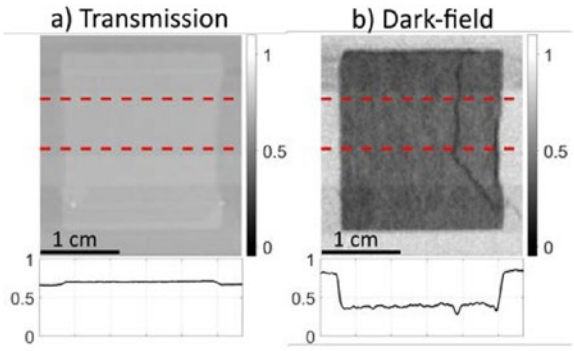

Figure 3. *Signal intensity of damaged GDL:*
a) Transmission, b) Dark-field.
The dashed red lines in the images indicate the area for which the profile is plotted below the images.

Conclusion

Our results show that dark-field imaging allows for visualizing specifically water distributed in the GDL without being sensitive to large water accumulations. Therefore, it is expected that in future experiments the water distribution in the GDL can be studied during the operation of fuel cells without the disturbance of superimposed large water droplets present in the gas flow channels. The high contrast of the DFI value between a D_2O filled and a dry GDL is suitable to reveal water distribution patterns. With the current state of the method the noise level is high and with the small dark-filed contrast obtained with light water (H_2O) it is not possible to obtain a suitable contrast to noise ratio. However, future optimizations of the imaging setup may help to reduce the noise which might enable the method to be used during fuel cell experiments consuming H_2 and light water (for humidification) instead of expensive D_2 and heavy water. Finally, the ability of dark-field imaging to identify GDL damages *in situ* is of potential interest for different kinds of studies that rely on a long continuous experiment time and do not allow for opening the cell (e.g. impact of freeze/thaw cycles or degradation).

Acknowledgment

The authors gratefully acknowledge Dirk Scheuble for building the experimental setup and for his support during experiments. This study is financially supported by the PSI CROSS initiative.

References

[1] P. Boillat, D. Kramer, B.C. Seyfang, G. Frei, E. Lehmann, G.G. Scherer, A. Wokaun, Y. Ichikawa, Y. Tasaki, K. Shinohara, *Electrochem. Commun.* **10** (4), 546–550 (2008).
[2] A.P. Kaestner, S. Hartmann, G. Kuhne, G. Frei, C. Grunzweig, L Josic, F. Schmid, E.H. Lehmann, *Nucl. Instrum. Meth. A* **659** (1), 387–393 (2011).
[3] C. Grünzweig, F. Pfeiffer, O. Bunk, T. Donath, G. Kuhne, G. Frei, M. Dierolf, C. David, *Rev. Sci. Instrum.* **79** (5), (2008).

High resolution visualization of GDL coating with combined X-ray and neutron tomography

V. Manzi-Orezzoli, P. Trtik, J. Eller, J. Halter, T.J. Schmidt, P. Boillat
phone: +41 56 310 4447, e-mail: victoria.manzi@psi.ch

When polymer electrolyte fuel cells operate at high current densities they suffer power limitation due to mass transport losses in the gas diffusion layers (GDLs), which are exacerbated by the accumulation of liquid water.

One standard way to limit these losses consists in applying a hydrophobic coating, generally a fluoropolymer, to the gas diffusion layer (GDL). To obtain an optimal performance, the desirable target is to have a thin fluoropolymer layer around the fibers composing the GDL, homogeneously distributed throughout. This way the complete surface area of the material is hydrophobic without decreasing the porosity.

In practice, coating accumulates mainly in the intersections between fibers and in order to obtain a surface hydrophobic enough to influence cell performance high coating loads have to be applied [1].

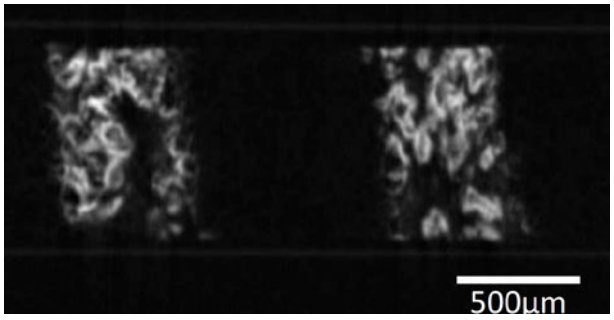

Figure 1. *Neutron tomography of a partially modified GDL, the bright areas correspond to the grafted regions containing ^{157}Gd and dark areas to the unmodified GDL. Only the coating is detectable by this technique.*

The coating load can be easily measured and controlled by weighting but analyzing the coating distribution is a more complex task. Cross-sections of GDLs can be imaged using a scanning electron microscope (SEM), but only one portion of the GDL can be probed at a time and most of the cutting techniques employed have been proven to be specially damaging for the coating. Also, small quantities of coating cannot be properly detected. High resolution X-ray tomography gives a fast and detailed picture of the complete GDL structure, but as with SEM, small quantities of coating cannot be differentiated from the carbon fibers.

We propose to overcome this limitation by combining high resolution X-ray tomography with a high resolution Neutron tomography technique recently developed at Paul Scherrer Institute [2].

Our methodology consists in a staining of the fluoropolymer coating with ^{157}Gd, using radiation grafting of acid groups and subsequent ion exchange [3]. ^{157}Gd has an extremely high neutron cross-section, so by incorporating this isotope exclusively into the coating the technique becomes sensitive to small amounts of coating, without any disturbance from the carbon structure of the GDL (Figure 1). This is the result of the huge cross-section differences of the two relevant elements: For neutrons with a speed of 2'200 m/s the total interaction cross-section of ^{157}Gd is 260'000 barns while that of carbon is 5.5 barns.

Consequently, when the information of the coating provided by neutron tomography is combined with the detailed structure information provided by X-ray tomography we can obtain a precise description of the coating distribution throughout the entire GDL.

Experimental

X-ray tomographic microscopy

The XTM was performed using a Lab-CT scanner Nanotom (General Electric) at PSI. The X-ray tube was set at a voltage of 60 kV and a current of 250 µA using 800 projections with a voxel size of 1.2 µm.

Neutron tomographic microscopy

The neutron tomography was performed at the POLDI beamline of the SINQ spallation source at PSI, using the Neutron Microscope as a detector. Slits were used to collimate the beam to a L/D ratio of 250 to limit the blurring due to beam divergence. The voxel size was 2.4 µm and the estimated effective resolution 10 µm. The reconstruction was done by using 375 projections, 9 images per projection were used with 60 s exposure time each.

All images were corrected using the following steps: noise removal, subtraction of the detector background and scattered neutron background, correction of the beam fluctuation and of the probe displacement. After tomographic reconstruction, the 3D neutron data sets were registered to the X-ray data sets by using control points (Figure 3) and optimizing a linear coordinate transformation.

Synthesis

Commercial GDLs were coated and irradiated following a procedure similar to the one previously reported by Forner *et al.* [3]. The activated samples were grafted by submerging them in a reactor with a 0.5 M Sodium Styrene Sulfonate and 0.5 M Acrylic Acid in water solution. The reactor content was purged with N_2 for 1 h and placed in a water bath for 24 h at 60 °C. After cleaning with water and ethanol the samples were dried and placed in a 0.015 M $^{157}GdCl_3$ solution for 24 h. They were later rinsed with water and dried again. Then, they were cut in squares of approximately 0.7 x 0.7 mm^2 and placed in a 1 mm diameter glass capillary, using aluminium foils in-between to avoid sample movement. The capillary was sealed and used for both X-ray and neutron tomographies.

Results and discussion

In the X-ray tomography the GDL carbon fiber structure is clearly visible, Figure 2 a. The bright spots are related to the coating, which appears brighter due to the higher density of the stained fluoropolymer compared to the carbon fiber.

Fibers in the X-ray tomography suffer from an edge effect, which cause the dark outer border and the light inner border visible around the fibers and the coating. This hinders the detection of thin polymer films around the fibers.

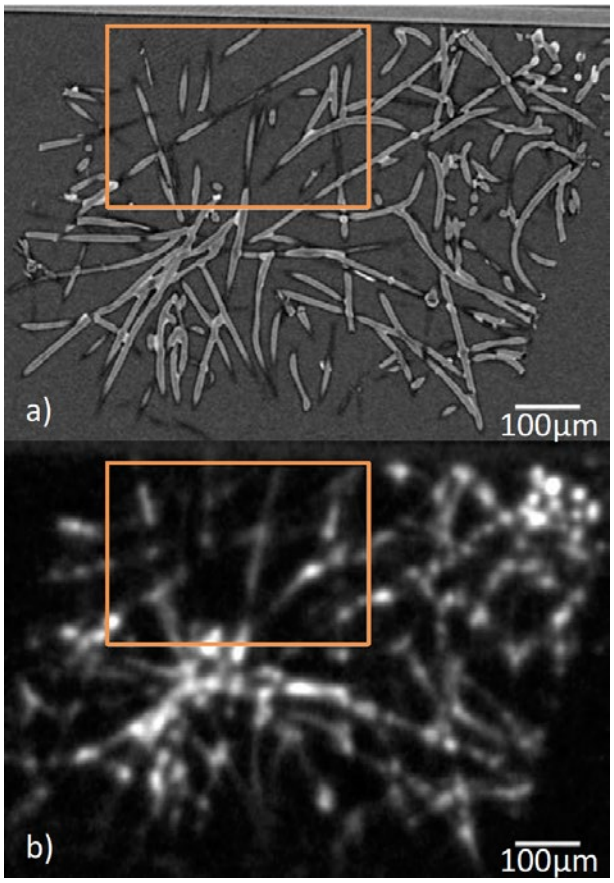

Figure 2. *Tomography slides of a Freudenberg H23 GDL with 9 % FEP coating load applied under vacuum. Slide a) corresponds to X-ray, slide b) to Neutron high resolution tomography after registration. The orange squares highlight the area detailed in Figure 3.*

The neutron data, Figure 2 b, shows that the coating is well distributed along the fibers. Most of the fiber surface appears to be covered by a thin layer of coating, and the majority of the fibers visible in the X-ray tomography can also be detected in the Neutron tomography. This indicates that the coating coverage is homogeneous in the in-plane direction. The region framed by the orange rectangles, expanded in Figure 3, is where more single fibers can be seen. The combined information of X-ray data and Neutron data shows that even with low coating loads there is extensive fiber coverage instead of the coating accumulating exclusively in the fibers intersections.

It is important to consider the differences in resolution and sensitivity of both techniques when evaluating the data. In the red rectangle in Figure 3 a fiber clearly detectable in the neutron image does not fully show in the X-ray image. The Neutron data has less resolution and, when transformed to the X-ray image space, some information will be extended through the reconstruction depending on the error of the transformation.

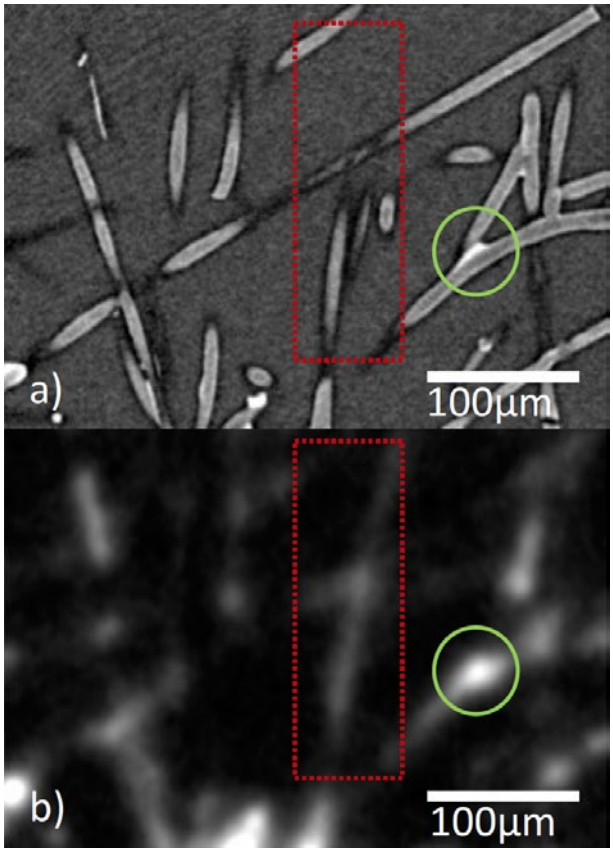

Figure 3. *Inset of Figure 2. a) X-ray and b) Neutron high resolution tomography. The green circle highlights the coating accumulation visible in both techniques. This type of feature was used for the reference control point registration.*

Conclusion

The X-ray and Neutron analysis have been successfully combined. The results show the expected coated accumulations between the fibers intersections and a thin coverage of the fibers homogenously dispersed across and along the GDL which was not appreciated in previous analysis. Further testing of the characterized sample would help to understand and optimize the coating target for GDL.

Acknowledgement

The authors gratefully acknowledge the Swiss National Science Foundation (SNSF) for funding (project no. 172474) and Laura Höltschi and Adrian Mularczyk for scientific discussion and technical support.

References

[1] R. Omrani, B. Shabani, *Int. J. Hydrogen Energy* **42**, 28515–28536 (2017).
[2] P. Trtik, E.H. Lehmann, *J. Phys. Conf. Ser.* **746**, 12004 (2016).
[3] A. Forner-Cuenca, V. Manzi-Orezzoli, J. Biesdorf, D. Streich, L. Gubler, T.J. Schmidt, P. Boillat, M. El Kazzi, *J. Electrochem. Soc.* **163**, F788–F801 (2016).

Convection driven droplet detatchment from gas diffusion layers

A. Mularczyk, A. Lamibrac, F. Marone, T.J. Schmidt, F.N. Büchi, J. Eller
phone: +41 56 310 5726, e-mail: adrian.mularczyk@psi.ch

In polymer electrolyte fuel cells (PEFCs), water generation on the cathode side can lead to the accumulation of water clusters in the gas diffusion layer (GDL) that expand into the gas channel where droplet formation can occur.

Management and removal of liquid water is essential to maintain and improve the overall performance of fuel cells, therefore understanding of the evolution and transport through the porous gas diffusion layer (GDL) structure is of importance.

Using sub-second X-ray tomographic microscopy (XTM) at the TOMCAT beamline of SLS, the liquid water distribution in the GDL and the flow channel was determined. Due to the multi-physical processes in operating fuel cells, combining mass, heat and charge transports, it is difficult to decouple all the phenomena leading to water displacement in *operando* experiments. Therefore an *in situ* experiment, with well-defined boundary conditions has been designed to characterize droplet detachment from the GDL surface.

Experimental

A water injection setup was realized as shown in Figure 1, fed by a syringe pump to adjust and control the rate of injection (350 and 1000 nL/min). A hydrophobic gasket was placed around the injection hole and ensured that the water would spread mainly through the GDL (SGL 25BA, 5 %wt PTFE, compressed to 0.15 mm) towards the gas flow channel. A nitrogen gas flow of 15 m/s was used to create a convective environment in the gas flow channel (0.8 mm width, 0.3 mm height) to induce shear forces on the droplets.

The water injection was monitored using both, fast X-ray 2D radiography as well as computed tomography. This allowed for observation of the average water distribution in the setup with high temporal resolution in 2D (3 ms exposure time) but also in 3D (0.75 s scan time, 2.55 s repeating frequency).

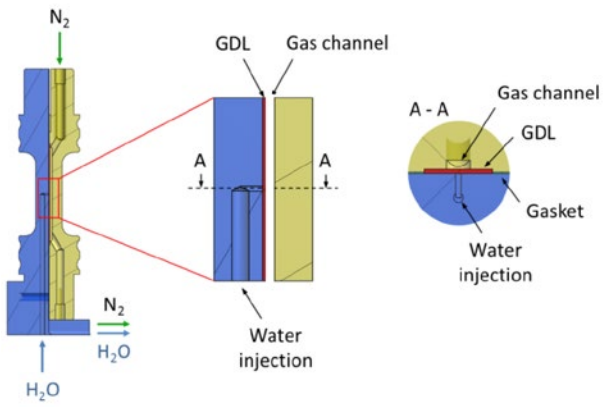

Figure 1. *Experimental setup used for imaging of water injection through the GDL. The sample holder is colored in blue and the flow field with gas flow channel in beige.*

Results

For the different water injection rates, the droplet formation was found to be very periodic, with little to no observable frequency fluctuation.

The droplet growth showed the following repeating pattern: After a short initial period where no water is visible on the GDL surface, a droplet starts growing at the point of break-through. The droplet then grows until it is detaching due to the shear forces of the convective gas flow in the channel.

The droplet diameter was extracted from the radiography data using a circular fit of the droplet and the water volume calculated under the assumption of spherically shaped droplets. To comply with this assumption, the diameter was only determined during the phase of droplet growth where a circular fit was representative of the observed droplet shape. The result of this for two different injection rates is shown in Figure 2.

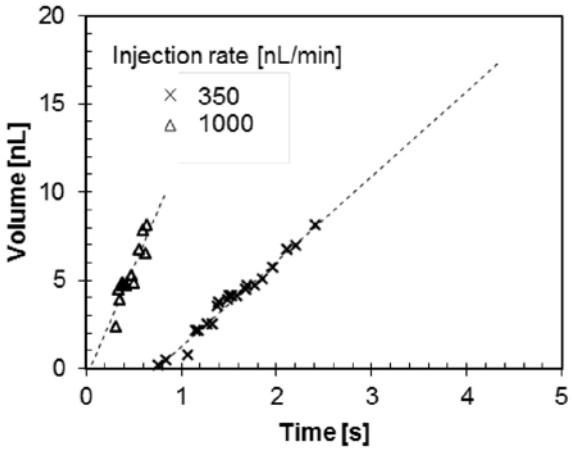

Figure 2. *Droplet volume calculated from observed diameters for injection rates of 350 and 1000 nL per minute. Linear fits are extrapolated to the time where the droplet detaches from the GDL, indicating its final volume.*

For the case of 1000 nL/min water injection, the droplets were smaller and retained a circular shape almost until detachment, while the droplets formed at an injection rate of 350 nL/min grew larger and evolved into a tear shape after a certain droplet size. For both conditions, the gas flow induced deformation started at a droplet volume of about 9 nL. Above this point, an estimate of the water volume can be made using a linear extrapolation of the initial growth rate that is extended to the point in time where droplet detachment was observed. The final droplet volume was estimated to be 17.6 nL at an injection rate of 350 nL/min and 10.3 nL at 1000 nL/min.

To assure, that the vertical orientation of the flow channel in the test setup did not influence the shape of the droplet, the Bond number was calculated with the final estimated droplet volume for each condition using the following equation,

where ρ is the density, σ the surface tension and R the radius of the droplet.

$$Bo = \frac{\rho g R^2}{\sigma} \quad (1)$$

For both injection rates this resulted in values (0.0035 and 0.0025) far smaller than 1, indicating that the effect of gravity on the deformation of the droplet was negligible.

Since all experiments were performed with dry N_2 gas, evaporation occurs on the surface of the droplet but also on the water cluster surface in the GDL. From the estimate of the final droplet size V_d and the frequency of droplet f_D detachment, it is possible to calculate the rate of evaporation by comparing to the water injection rate.

$$\dot{V}_{evap} = \dot{V}_{inj} - \frac{V_D}{f_D} \quad (2)$$

Evaporation was determined to contribute to the water removal with ~150±50 nL at 350 and 1000 nL/min.

Figure 3 compares the water volume inside the GDL, obtained from segmentation of the tomographic data. The water volume is calculated for every 3 µm thick through-plane layer of the discrete voxel based data-set by counting the voxels identified as being occupied by water. Data from multiple scans are shown, corresponding to different stages of droplet growth. Water volume in the GDL near the inlet was found to be high and decreasing towards the gas channel, corresponding to a high saturation near the inlet and a low saturation near the gas channel.

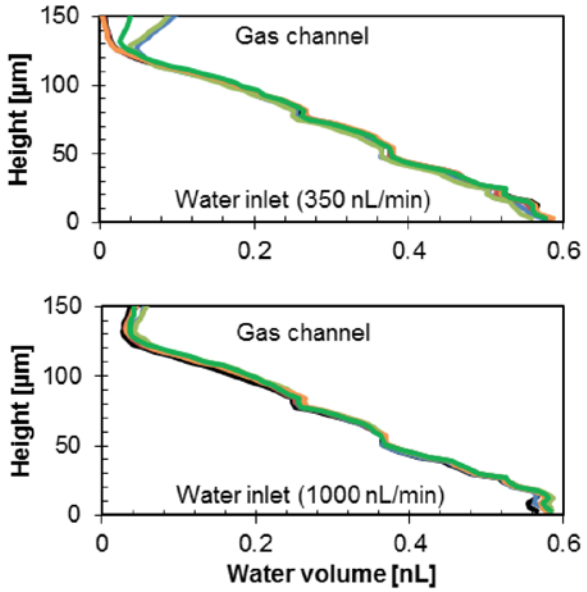

Figure 3. *Water volume calculated for 3 µm thick layers, distributed over the height of the GDL domain, for an injection rate of 350 nL/min (top) and 1000 nL/min (bottom). Colored lines indicate scans taken at varying stages of droplet growth.*

It was found that no changes occurred in the bulk of the GDL when changing the injection rate from 350 to 1000 nL/min. At an injection rate of 350 nL/min, a strong deviation of water volume between scans can be observed in the upper layers of the GDL. The top 30 µm of the GDL are emptied during droplet detachment and have to be refilled before a new droplet can emerge into the gas flow channel. This effect could not be observed for 1000 nL/min injection rate due to the fact that the scan time and the droplet detachment period at this condition are of similar length, resulting in an averaging of all stages of GDL saturation and of the droplet's growth during the tomographic scans.

Conclusions

The water injection rate was found to have a significant impact on the size and frequency of droplets formed on the GDL surface. Higher injection rates lead to smaller but more frequent droplets compared to lower injection rates. For both injection rates, a deformation of the droplet due to the gas flow was observed for droplets with volumes larger than 9 nL. The evaporation rate increased with increasing water injection rate. While no changes in the water distribution inside the bulk GDL domain were observed, the saturation of the top 30 µm of GDL showed a periodic behavior.

Acknowledgement

Funding was provided by the Swiss National Science Foundation (SNSF project no. 407040 153790).

References

[1] A. Lamibrac, J. Roth, M. Toulec, F. Marone, M. Stampanoni, F.N. Büchi., *J. Electrochem. Soc.* **163**, 202–209 (2016).

The impact of phosphoric acid migration on the performance of HT-PEFCs

J. Halter, S. Thomas, S. Knudsen Kær, T.J. Schmidt, F.N. Büchi
phone: +41 56 310 4131, e-mail: jonathan.halter@psi.ch

High temperature polymer electrolyte fuel cells (HT-PEFC) are based on polybenzimidazole (PBI) membranes imbibed with phosphoric acid (PA) as the electrolyte. They operate at temperatures between 160 °C and 200 °C. Since only a fraction of PA interacts with the base polymer, a large amount of PA shows a high degree of mobility and is able to redistribute within the membrane electrode assembly (MEA). At high current densities, PA migrates towards the anode and invades the porous gas diffusion layer (GDL) [1].

On the one side, this can lead to a loss of electrolyte, therefore reducing the durability of HT-PEFCs. On the other hand, PA flooding of the anode GDL is also an obstacle for gas diffusion from the anode gas channels to the catalyst layer. Therefore, an increasing mass transport resistance due to flooding of the anode GDL is expected; resulting in a reduced performance of HT-PEFCs due to flooding of the anode GDL.

A similar phenomenon is known from LT-PEFC, where water is generated at the cathode and increased mass transport resistance occurs due to flooding of the cathode GDL with water [2].

In order to better understand the relation between PA migration and the performance of HT-PEFCs, a method utilizing electrochemical impedance spectroscopy (EIS) was developed. EIS was chosen, due to its sensitivity towards mass transport resistance, as well as being a fast and non-invasive method.

Experimental

All experiments were carried out with MEAs that were assembled in-house using BASF Celtec® membranes with an acid loading of ca. 35 $mg_{H_3PO_4}cm^{-2}$ and a ratio of PA to PBI of about 33. The catalyst layers consisted of Pt/Vulcan XC-72 supported platinum, with 1 $mg_{Pt}cm^{-2}$, coated onto the microporous layer of an SGL-38 carbon paper for both cathode and anode. The active area was 2 cm^2. Pyrolitically surface treated and sealed graphite (POCO Graphite, US) was used as flow field material for both anode and cathode.

A break-in procedure was performed for 80–100 h at 160 °C at a current density of 0.2 Acm^{-2}. Both cathode and anode gases were humidified at room temperature with a constant flow of 1.67 $nLmin^{-1}$ of 10 % hydrogen in nitrogen at the anode and 0.83 $nLmin^{-1}$ of pure oxygen at the cathode for all experiments.

Figure 1 shows the current cycling used. Each current density was held for 4 h to trigger either PA flooding or PA de-flooding. Unless otherwise stated, EIS was measured every 2 minutes with a Biologic SP-300 potentiostat. Impedance spectra were recorded by scanning the frequency from 100 KHz to 100 mHz with 5 points per decade; resulting in a measurement time of ca. 50 s per spectrum. The AC signal applied was 5 % of the DC load.

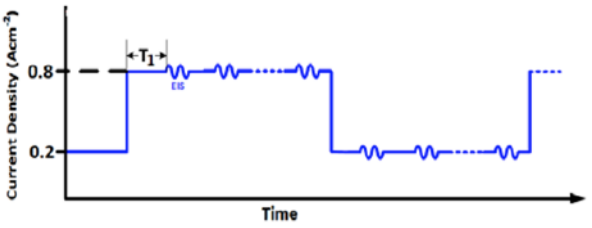

Figure 1. *Current cycling scheme used for all experiments. Both current densities were held 4 h each; EIS measurements performed every T_1 = 2 min.*

Results

Figure 2 shows the EIS spectra after stepping from 0.2 Acm^{-2} to 0.8 Acm^{-2} (positive current step). Over time, an increasing resistance in the low frequency region is observed, typically associated with mass transport in literature [3]. The increasing resistance is related to phosphoric acid migration, based on the fact that the changes in the low frequency regime are amplified with increasing hydrogen dilution.

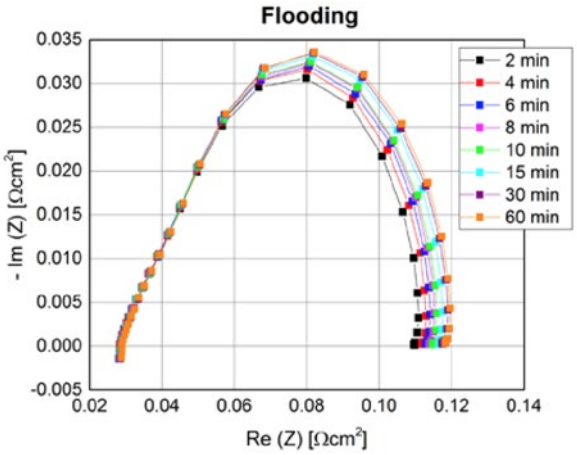

Figure 2. *EIS measurement time series after a positive current step (0.2 to 0.8 Acm^{-2}).*

As for the current increase (i.e. flooding) case, EIS was measured for a negative current step, where a decrease in the low frequency regime can be observed (see Figure 3). The decreasing resistance can be associated with the deflooding of the anode GDL.

The measured spectra can be used to analyse the kinetics of phosphoric acid flooding. Figure 4 shows the normalized real part of the 1 Hz frequency (2 min = 0; 60 min = 1) plotted over time.

It is important to note, that a value of 1 does not mean a phosphoric acid saturation of 100% in the anode GDL, but this corresponds to the highest saturation observed during the experiment. By fitting with an exponential decay function, the time constants for PA flooding and deflooding are obtained, found to be 8.1 ± 0.1 minutes for flooding and 4.8 ± 0.9 minutes for de-flooding.

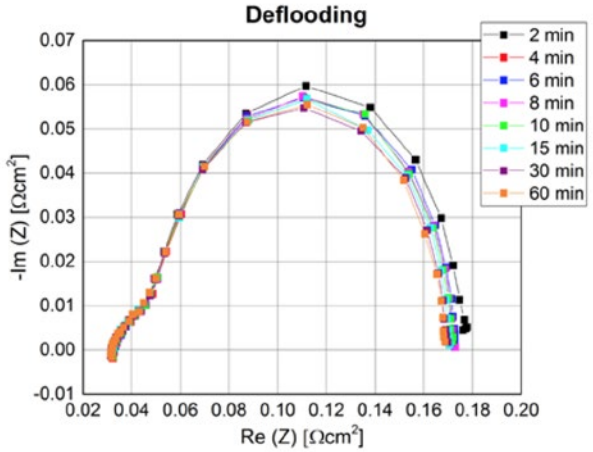

Figure 3. *EIS measurement time series after a negative current step (0.8 to 0.2 Acm^{-2}).*

Despite the increasing mass transport resistance by PA flooding, the cell voltage did not change significantly over time after an increasing current step, but remained constant to about ± 2 mV. This is probably due to the fact, that the increasing transport resistance is compensated by improved kinetics due to different wetting of the catalyst layers. At even lower hydrogen concentrations, one expects the losses due to hydrogen diffusion to become more dominant which would also be reflected in the cell performance.

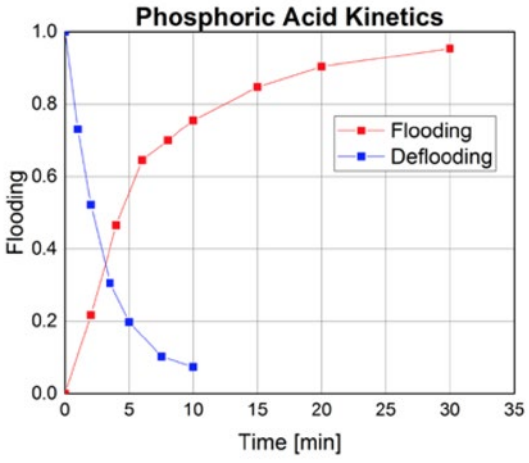

Figure 4. *Kinetic behaviour for phosphoric acid flooding and deflooding of the anode GDL.*

In the present study, a dilution of 10% hydrogen was chosen to reflect operation under reformate gas conditions. Figure 5 shows polarisation curves for different hydrogen concentrations (with pure oxygen at the cathode). For hydrogen concentrations of 25% or higher, no significant mass transport losses can be observed. True diffusion limiting current densities can be observed only for hydrogen concentrations of 4% or lower. At these hydrogen concentrations a current density of 0.8 Acm^2 cannot be achieved anymore. It can therefore be concluded that the impact of phosphoric acid migration on the performance of HT-PEFCs under reformate gas conditions can be neglected.

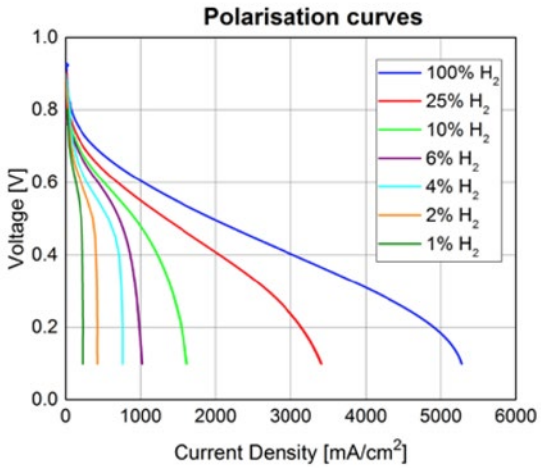

Figure 5. *Polarisation curves for different hydrogen concentrations at the anode and pure oxygen at the cathode at 160 °C.*

Conclusion

In HT-PEFCs, high current density triggers phosphoric acid migration towards the anode. Electrochemical impedance spectroscopy was used to measure the increasing mass transport losses under diluted hydrogen conditions and the time constants for phosphoric acid flooding (8.1 minutes) and deflooding (4.8 minutes) were determined.

However, no significant impact of phosphoric acid migration on the performance of HT-PEFCs under conditions reflecting reformate conditions was observed.

Acknowledgement

Financial support from the CCEM project ADMIST, including funding contributions from the Swiss Federal Office of Energy (BFE), the Swiss Electric Research fund (SER) and BASF SE is gratefully acknowledged. We thank T. Gloor for his support at the testbench.

References

[1] S.H. Eberhardt, M. Toulec, F. Marone, M. Stampanoni, F.N. Büchi, T.J. Schmidt, *J. Electrochem. Soc.* **162**, F310–F316 (2015).
[2] T. Rosen, J. Eller, J. Kang, N.I. Prasianakis, J. Mantzaras, F.N. Büchi, *J. Electrochem. Soc.* **159**, F536–F544 (2012). doi:10.1149/2.005209jes.
[3] S.S. Araya, F. Zhou, V. Liso, S.L. Sahlin, J.R. Vang, S. Thomas, X. Gao, C. Jeppesen, S.K. Kær, *Int. J. Hydrogen Energy.* **41**, 21310–21344 (2016).

Providing secondary control with PEM electrolyzer technology

C. Peter, M. Ammann, A. Selviaridis, F.N. Büchi
phone: +41 56 310 5588, e-mail: christian.peter@psi.ch

Secondary control is the power to be fed to or drawn from the electric grid within in the range of tens of minutes to compensate an imbalance in the grid indicated by frequency deviation (renewable feed in, power outage).

In case of frequency increase, PEM electrolyzer technology is of interest because it provides the possibility to draw power in a dynamic manner from the grid. The power drawn is stored in the form of hydrogen/oxygen gases in tanks and can in due course be re-electrified, analogue to pumped hydro storage power stations. The advantage of electrolysis over the latter technology is that it can be installed and operated practically anywhere, since it is not restricted to geographic conditions as it is the case for pumped hydro storage power plants used for secondary control; therefor fewer power lines and transformers are needed, eventually contributing to a reduction of the overall system costs.

On the Energy System Integration Platform (ESI) at the Paul Scherrer Institute, a Siemens 100 kW PEM balanced pressure electrolyzer (Figure 1) has been installed in order to test the characteristics of the technology. The electrolyzer consists of two subsystems, each with 50 kW nominal power. Each subsystem contains two 25 kW PEM electrolyzer stacks. The tests carried out for secondary reserve capability have been conducted in collaboration with Swissgrid.

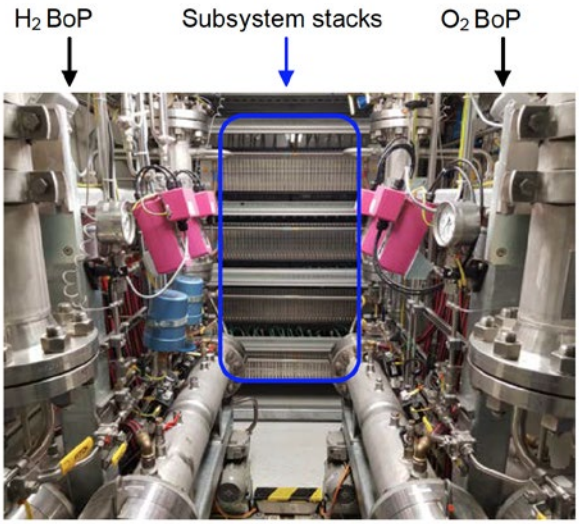

Figure 1. *100 kW Siemens PEM electrolyzer consisting of four stacks and the balance of plant (BoP).*

Experimental

Figure 2 shows a schematic setup of the power to hydrogen process (P2H) as part of the ESI H2-path. The electrolyzer intended to provide secondary reserve is interconnected by a gas cleaning facility (Clean/Dry Gas, Reicat) to the storage tanks. The energy drawn from the grid is transformed by the PEM electrolyzer into hydrogen and oxygen gases and the gases cleaned and dried. The gases stored have the quality 4.5 (99.995 %) and are dried to a dew point below -62 °C.

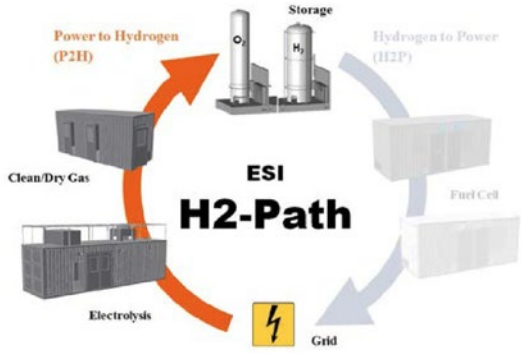

Figure 2. *Schematic of the power to hydrogen process (P2H), consisting of a 100 kW Siemens PEM electrolyzer. Excess energy in the grid can be sunk and stored in the form of gas.*

Results

In the secondary reserve test, a reference profile (AC power) was given to the control system of the P2H process. This then calculated the setpoint (DC power) for the PEM electrolyzer stacks. The reference profile (green) and resulting AC power drawn (red) from the grid are shown in figure 3.

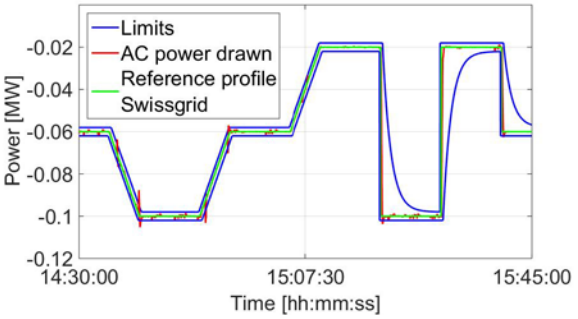

Figure 3. *Secondary power reserve test reference profile (green), drawn power from the grid (red) and boundary limits (blue).*

The power drawn stays within the defined boundary limits with minimal exceptions at stack switching points. The power ramps achieved by the PEM electrolyzer are in the range of +/- 6 kW/s.

Conclusions & Outlook

A 100 kW PEM electrolyzer unit, with a specifically developed control system, was successfully used to demonstrate secondary control capability. Technology intrinsic aspects, like: subsystem and control system design have been identified to influence the response behavior with respect to the test profile. In future, fuel cell technology will be tested with respect to second-ary control, for gas-re-electrification. Combining the two technologies, the overall efficiency will be identi-fied.

Acknowledgement

Financial support from Swissgrid is gratefully acknowledged.

Correlation between the morphology of the porous transport layers and the performance characteristics of a polymer electrolyte water electrolysis cell

U. Babic, T.J. Schmidt, L. Gubler
phone: +41 56 310 5629, e-mail: ugljesa.babic@psi.ch

Polymer electrolyte water electrolysis (PEWE) is a promising technology for large-scale electricity storage (TWh), and providing grid stability. The produced hydrogen (H_2) and oxygen (O_2) can be used to regenerate electricity in periods of low production and high demand or serve as clean transportation fuel for fuel cell electric vehicles. Furthermore, PEWE is the key technology for meeting the decarbonization targets through Power-to-X. PEWE offers advantages over the competing H_2 production technologies (alkaline and solid-oxide electrolyzers) in terms of dynamic operation, compact design and high differential pressure operation.

Improvements in the efficiency are necessary to drive down the cost of produced H_2, which is dominated by the cost of electricity. It is therefore necessary to understand the underlying mechanisms determining the efficiency losses, and use the knowledge for designing the next generation of materials for PEWE [1, 2].

Theory

The PEWE cell voltage (E_{cell}) is a sum of the thermodynamic cell voltage ($E°_{cell}$) and the overpotential, which can be split into ohmic (η_{ohm}), kinetic (η_{act}) and mass transport (η_{mtx}) contributions (Equation 1). η_{ohm} is a result from the cell housing resistance, proton resistance in the electrolyte and contact resistances. η_{act} stems from the electrochemical reactions and is mostly related to the sluggish oxygen evolution reaction (OER). There is still no consensus in the community on the origin of η_{mtx}. It has been argued that they originate from the limitations of the anodic porous transport layer (PTL_{AN}) towards the two-phase flow of water and gas [3]. Ito *et al.* [4] argued that the oxygen evolution could block the supply of water to the catalyst layer (CL) active sites and cause η_{mtx}. In this work we determined the impact of the PTL/CL interface on η_{mtx} by using sintered titanium PTLs with different morphological properties.

$$E_{cell} = E^{o}_{cell}(p,T) + \eta_{act} + \eta_{ohm} + \eta_{mtx} \quad (1)$$

Overpotentials were determined using the Tafel analysis [4, 5]. E_{cell} was iR-corrected using the high frequency resistance (HFR) measured at 10 kHz to obtain the iR-free cell voltage $E_{IR\text{-}free}$. The Tafel slope was fitted in the low current density ($i = 0.01 - 0.08$ A cm^{-2}) region, where we assume no mass transport limitations and purely kinetic control. Extrapolation of the Tafel slope to high j yields η_{act}, under the assumption that there is no change in the reaction mechanism for the OER. Remaining overpotential from the difference of $E_{IR\text{-}free}$ and the Tafel slope is generally considered as η_{mtx}. The proton transport resistance in the CLs ($R_{AN/CA}^{H+}$) was estimated by measuring the AC impedance response of the cell in H_2/N_2 mode, the method commonly used in fuel cell science. The impedance $Z(\omega)$ for the H_2/N_2 cell at low frequencies can be described with

$$Z(\omega)\underset{\omega\to 0}{\approx}\frac{R_{CL}^{H+}}{3}+\frac{1}{j\omega C} \quad (2)$$

This approximation is valid under the assumption that the potential distribution in the CL is uniform. The proton transport losses in the CL appear as $R_{AN/CA}^{H+}/3$ in the polarization curve. The 45 ° region must appear in the data to fit the values for $R_{AN/CA}^{H+}$.

Experimental

An in-house developed test-bench was used to perform the cell characterization. Polarization curves were measured at 60 °C and atmospheric pressure using a Biologic potentiostat with a 75 A booster. H_2 in O_2 concentrations were measured during the operation using the Eaton K1550 gas analyser. The cell was assembled with a 25 cm^2 commercial N117-based catalyst coated membrane (CCM) with Ir-based CLAN and Pt-based CL_{CA}. Sintered Ti PTLs from GKN with designations T5, T10, T20 were used in the anode and cathode cell compartment. Previous X-ray tomographic analysis of these PTLs indicated that the T5 and T10 have similar particle size (~ 50 µm), with T5 having smaller pores than T10. T20 on the other hand has both larger particles (~ 80 µm) and pores in the structure [3]. The cell was conditioned for 12 hours prior to measurements at 60 °C, while cycling the current density between 1 and 2 A cm^{-2}. Measurements of the $R_{AN/CA}^{H+}$ were done in H_2/N_2 operation, with H_2 supplied at 400 ml min^{-1} to the counter/reference electrode, and N_2-rich water supplied to the working electrode at 500 ml min^{-1}. The impedance spectra were collected in the frequency range of 10 kHz – 100 mHz.

Results

Polarization curves indicate substantial differences in the performance of the three cells (Figure 1). The cell with T20 PTLs had higher η_{ohm} compared to the other two, most likely due to increased interfacial contact resistance; as the T20 sintered PTLs have significantly larger pore and particle size. We can determine how much of the η_{mtx} is stemming from the proton transport in the CL_{AN} by extrapolating the R_{AN}^{H+} from the impedance spectra that was measured in the H_2/N_2 cell.

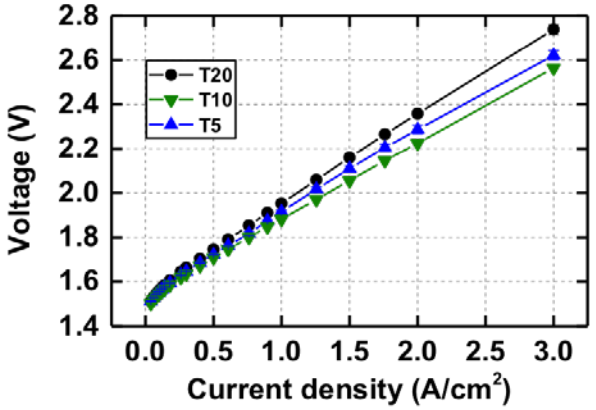

Figure 1. *Polarization curves measured at 60 °C with different PTLs on the anode and cathode.*

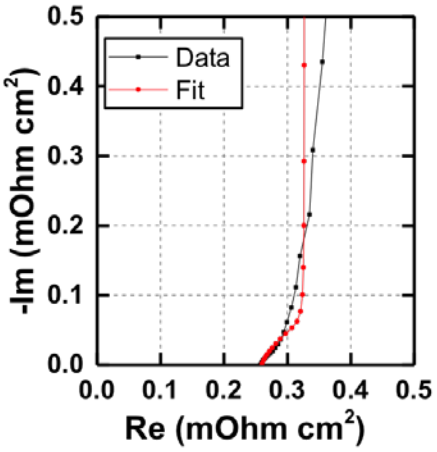

Figure 2. *Impedance data of the H_2/N_2 cell collected at 1.0 V (anode is the WE), and the data fit according to the transmission line model.*

As the impedance response for the C_{LAN} is in good agreement with the model (Figure 2), we extrapolated the low-frequency projection to the real axis to obtain $R_{AN}^{H+}/3$. The impedance spectrum did not have a characteristic 45° slope at high frequencies when the cathode was the WE. Therefore we assumed the losses for the hydrogen electrode to be negligible.

The non-ohmic overpotentials are summarized in Table 1 for the three cells for current densities of 1 and 3 A cm^{-2}. The overpotential due to the proton transport in the anode CL (η_{AN}^{H+}) amounts up to 20 % of the η_{mtx} at 3 A cm^{-2} (T20). The rest of the η_{mtx} (η_{rest}) are more pronounced at higher current density. The origin of these losses is still not clear and warrants further investigation. Our working hypothesis is that η_{rest} stem from the hindrance of water/gas transport through the C_{LAN} structure, depending on the pore/particle size of the PTL_{AN}.

	1 A cm^2			3 A cm^2		
	η_{act} (mV)	η_{AN}^{H+} (mV)	η_{rest} (mV)	η_{act} (mV)	η_{AN}^{H+} (mV)	η_{rest} (mV)
T5	399	8.1	62.6	433	24.3	269
T10	386	11.2	28.5	419	33.6	182
T20	409	20.6	49.6	446	61.7	252

Table 1. *Non-ohmic overpotentials for cells with T5/T10/T20 PTLs at 1 and 3 A cm^{-2} and 60 °C.*

Measurements of H_2 concentrations in O_2 during operation showed significantly larger crossover in the case of T20 compared to the other two cells (Figure 3).

We propose the following explanation: since the T20 PTL has larger particles in the surface structure it compresses the porous C_{LAN}/CL_{CA}. The compression results in the local reductions of the CL porosity, higher gas concentrations under the PTL particles and in turn higher gas crossover. We did not detect any O_2 in H_2, and assume that it is completely reduced on the Pt-based CL_{CA} surface.

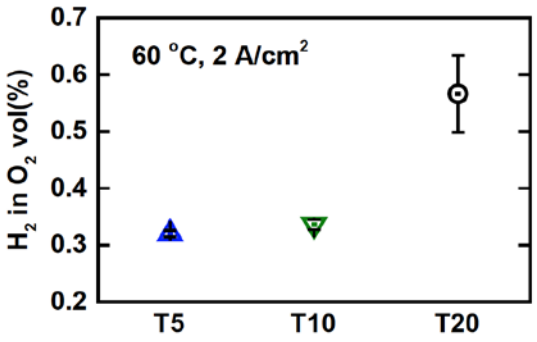

Figure 3. *H_2 in O_2 concentration at 60 °C and 2 A cm^{-2} for T5/T10/T20 cells.*

Conclusions and outlook

We have used the H_2/N_2 method to estimate the proton transport resistance in the catalyst layer ($R_{AN/CA}^{H+}$) using commercial PEWE catalyst coated membranes, and to determine how the surface morphology of the sintered Ti PTL affects these losses.

We found that the PTL surface properties affect the magnitude of R_{AN}^{H+}, while R_{CA}^{H+} appears to be negligible. At 3 A/cm^2, proton transport through the CLAN is causing up to 20 % of the total mass transport overpotential η_{mtx}. Different PTLs resulted in significant variations in the rest overpotential η_{rest}.

Further investigation is ongoing to explain these differences, and determine whether the PTL bulk or the surface properties determine η_{rest} in PEWE cells.

Acknowledgement

Funding by the Swiss Federal Office of Energy (SFOE, grant no. 501198-01) and technical support by Michelle Locher are gratefully acknowledged.

References

[1] M. Carmo, D. L. Fritz, J. Mergel, D. Stolten, *Int. J. Hydrog. Energy* **38**, 4901–4934 (2013).
[2] U. Babic, M. Suermann, F.N. Büchi, L. Gubler, T.J. Schmidt, *J. Electrochem. Soc.* **164**, F387–F399 (2017).
[3] M. Suermann, K. Takanohashi, A. Lamibrac, T.J. Schmidt, F.N. Büchi, *J. Electrochem. Soc.* **164**, F973–F980 (2017).
[4] H. Ito, T. Maeda, A. Nakano, A. Kato, T. Yoshida, *Electrochim. Acta* **100**, 242–248 (2013).
[5] M. Suermann, T.J. Schmidt, F.N. Büchi, *Electrochim. Acta* **211**, 989–997 (2016).

Surface characterization of porous transport layer

T. Schuler, T.J. Schmidt, F.N. Büchi
phone: +41 56 310 5147, e-mail: tobias.schuler@psi.ch

Polymer electrolyte water electrolysis (PEWE) is a promising technology to produce hydrogen in a future renewable based energy system. The dynamic operation enables the integration of intermittent electricity from wind or solar. Surplus electrical energy can thus be converted into chemical energy in the form of hydrogen and stored in tanks or pipelines. To increase the efficiency of the system, fundamental understanding of the three loss categories kinetics, charge and mass transport are essential. The most complex and least understood overpotential is the one related to mass transport in the porous layers. Porous transport layers (PTL) play an important role in the PEWE cell by providing electrical and thermal conductivity and managing water gas transport.

The impact of structural differences of PTLs on the cell performance was reported in literature [1]. It is not clear which structural properties, and/or surface topologies contribute to the mass transport resistance. This paper reports on the development of a 3D roughness analysis tool to quantify the topology of PTLs. A successful analysis enables a comparison to electrochemical performance characterization in further projects as the interface between PTL and catalyst appears to play a role for performance and durability.

Experimental

The roughness characterization of commercially available sintered Ti-powder materials was based on X-ray tomographic microscopy using a Lab CT-scanner (*nanotom m,* General Electric). For imaging a 0.1 mm Cu filter was used to prevent beam hardening effects. The acquisition parameter were chosen to be 120 kV and 1000 ms for single projections. The voxel cube length was 2 µm.

Here data is reported on T10 material (GKN, Germany) cut to 1 x 2 x 20 mm samples, fixed on a PEEK sample holder. Imaging was conducted at ambient conditions. The reconstructed data was segmented by thresholding using the software ImageJ. Figure 1 visualizes the processing chain for the determination of the surface roughness. The stack of vertical slices of the segmented binary images is used as base for the analysis. The distance t_{ij}, from the surface to the first solid pixel (shown in black) is computed at every position *j* along the x-axis and for all slices.

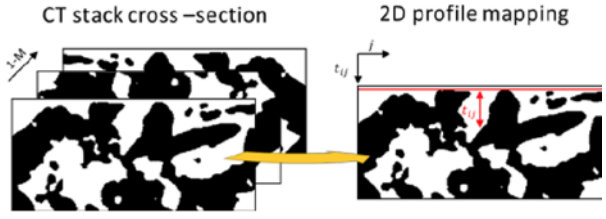

Figure 1. *Schematic of PTL surface roughness analysis: the surface height is determined along the surface of a slice and repeated for all slices of the stack.*

Based on the processed surface height t_{ij} at given position *j* and slice number *i*, the arithmetic average roughness S_a can be calculated for the CT cross-section stack according to equation (1) where *N* represents the length of the cross section slice and *M* the maximum number of slides in the stack.

$$S_a = \frac{1}{MN}\sum_{i=1}^{M}\sum_{j=1}^{N}|t_{ij}| \qquad (1)$$

Results

The computed roughness is plotted in a 2D height diagram for a region of interest of 1 mm x 1 mm in Figure 2. The surface depth of the PTL is represented by differences in color and intensity.

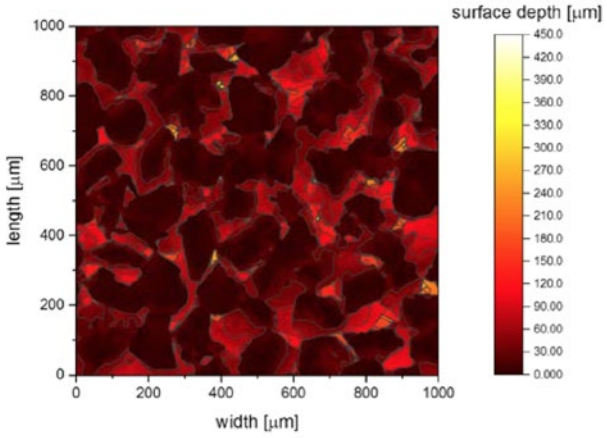

Figure 2. *2D-surface height plot of porous transport layer T10 based on segmented XTM data.*

The represented surface of the T10 porous transport layer features a dense surface consisting of bulky particles. This observation is in accordance with the reported morphological properties of 34.6 % porosity and a mean particle diameter of 58 µm [2]. The total depth range goes up to 45 % of the total PTL thickness. The arithmetic average roughness is calculated to be 31 µm.

Conclusion and outlook

The developed roughness analysis enables new insight into the topological properties of porous transport layers. Further analysis will be conducted for different PTL types and compared to electrochemical performance characterization.

Acknowledgement

Financial support by Swiss Federal Office of Energy (SFOE) is gratefully acknowledged.

Reference

[1] A. Grigoriev, P. Millet, S.A. Volobuev, V.N. Fateev, *Int. J. Hydrogen Energy* **34**, 4968–4973 (2009).
[2] M. Suermann, K. Takanohashi, A. Lamibrac, T.J. Schmidt, F.N. Büchi, *J. Electrochem. Soc.* **164**, 973–980 (2017).

Operando neutron imaging of PEWE cation mitigation

M. Zlobinski, U. Babic, V. Manzi-Orezzoli, M. Siegwart, L. Gubler, T.J. Schmidt, P. Boillat
phone: +41 56 310 5661, e-mail: Mateusz.Zlobinski@psi.ch

Since hydrogen has been introduced as a fuel for mobility and stationary applications, making electrolysers efficient, safe and economical has been a topic of high importance. PEWE (Polymer Electrolyte Water Electrolysers) are especially suitable for high purity hydrogen generation because Anode (H_2O splitting side) and Cathode (H_2 evolution side) are separated gas wise. Another important reason why PEWE is so attractive is that it can generate hydrogen efficiently under pressurised conditions what excludes compressors from the system. In order to make this technology competitive on the market it is necessary to grasp better understanding of processes taking place during operation, including the degradation processes. This study shows a first attempt to image contamination of electrolysers by cations across the membrane which could be another small step to making PEWE durable and efficient. The ultimate goal of this research is to determine the cation behaviour in the MEA under various operating conditions and to tell whether it is possible to regenerate the membrane without cell disassembly or at least slow down the degradation significantly. In order to image cation movement within PEM it was necessary to find a suitable element which is a good neutron absorber and could represent PEWE usual ionic contaminants such as Fe^{3+} relatively well. To this purpose, we chose to mimic the iron contamination using Gadolinium ions, which are found in the same oxidation state and provide an exceptionally high cross section for neutrons.

Experimental setup

Measurements were carried out at SINQ Neutra beamline using a tilted detector assembly to improve the resolution. The used setup features a pixel size of 6 µm and an effective resolution of approximately 20 µm which is enough to investigate the PEM cross section (thickness ~200 µm). The setup used during these experiments was prepared in a way that reproduces normal operating conditions as well as possible ones, even though due to possible test bench contamination it was necessary to use external storage tanks.

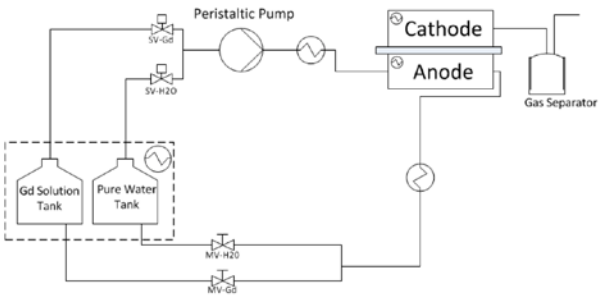

Scheme 1. *Simplified experimental setup schematic.*

The electrolyser key components were mostly provided by commercial suppliers, including MEAs (Membrane Electrode Assemblies) based on N117 membranes delivered by Greenerity. For PTLs (Porous Transport Layers) we used sintered titanium T10 (36 % porosity) material provided by Sika. The cell housing volume was relatively large compared to the active area which minimised the impact of operating conditions on the water temperature. Heating regulation of the system was designed in a way that ensures a stable and desired temperature in the flow fields even if water in the supply tank differs significantly from the temperature set point.

Two feed water tanks were used: one filled with ultrapure water and another one with a Gadolinium salt in ultrapure water solution (concentration 1 mMol). The selection of the supply tank was done using solenoid valves placed before the pump and manually operated valves were used for the return lines. The tanks were assembled in a way that provided relatively uniform temperatures of both fluids inside. The piping providing the fluid to the cell itself was equipped with a controlled heating system.

Results

Initial measurements consisted of several IV curves and a conditioning period i.e. for MEA hydration, PTL hydration and reaching the desired temperatures of the system. The Electrolyser was left operating for 12 hours at a current density of 1 A/cm^2 to analyse the initial degradation rate of the MEA which is caused by the test bench itself, as no ion exchanger was placed in the loop. Once the cell has been characterised the contaminant was introduced in the loop. The response of the system was immediate.

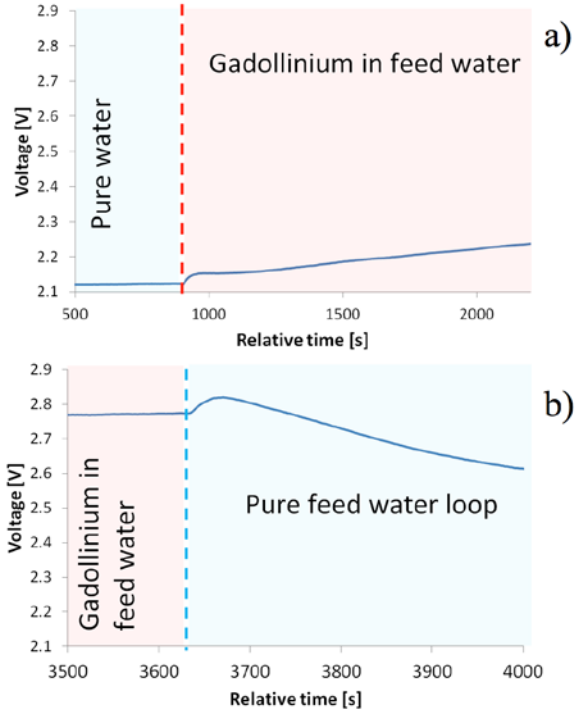

Figure 1. *Cell performance over time depending on feed water content.*

Figure 1 shows the impact of the contaminant in the loop on the cell performance. Once the feed water containing the Gadolinium has been introduced, accelerated degradation occurred. This shows how much electrolyser cells are sensitive to the feed water purity. Upon switching back to the clean water loop steady regeneration could be observed. The mechanism behind the regeneration is yet to be explored.

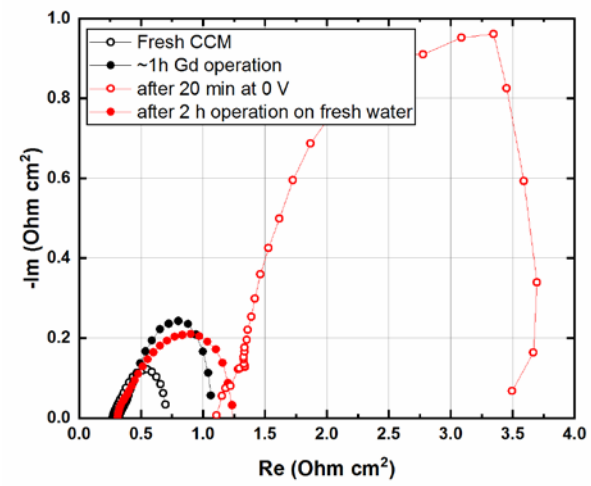

Figure 2. *Impedance spectra, contamination and regeneration.*

The observations from neutron imaging give us hints on the cation content and behaviour.

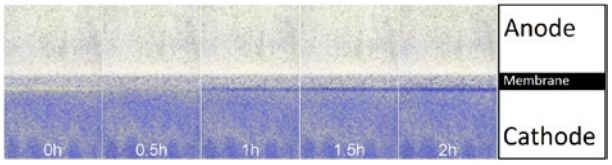

Figure 3. *Gadolinium migration toward Cathode catalyst layer over time under galvanostatic 1 A/cm² operating conditions.*

Figure 3 shows accumulation of Gadolinium cations near the cathode catalyst layer while middle areas of membrane stay relatively pure. This information alone suggests that regeneration methods should focus on utilisation of the cathode compartment for cations removal from the membrane, for example by introducing a slightly acidic environment in that compartment. To further assess how the cations move as a function of current density, investigations with start/stop cycles were conducted.

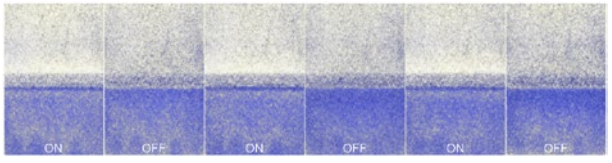

Figure 4. *Cation movement within the membrane during start stop operation cycles.*

The images (Figure 4) show that, as soon as we stop drawing current through the electrolyser, the cations diffuse from the cathode catalyst layer to somewhere else and reappear upon applying current. Such behaviour can partially explain typical short voltage peaks at electrolyser start-ups resulting from cation rearrangement in the MEA. By plotting intensity profiles across the membrane (Figure 5), we clearly see a distinct dip of intensity during ON state as well as an intensity gradient across the membrane.

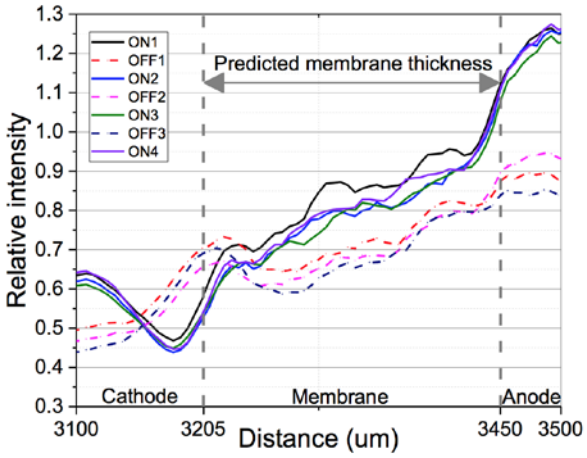

Figure 5. *Intensity profiles across the MEA for ON/OFF.*

We also note that during OFF state average intensity in the membrane decreases meaning that Gadolinium deposited around the cathode catalyst layer diffused back into the membrane.

Conclusions

The presented results using Gd cations to emulate usual contaminants as Fe provided insight into the processes occurring within a heavily contaminated PEWE MEA. The membrane is able to partially regenerate itself provided that the feed water is pure.

The cations were observed to move towards the cathode catalyst layer under the effect of current and to accumulate there, though they seem to be less detrimental in this location than in the membrane or in the anode catalyst layer. Using this observation, it might be possible to design a regeneration procedure using the cathode side under operating conditions.

Acknowledgement

The Swiss Federal Office for Energy is greatly acknowledged for financial support of our research. Additionally, the authors would like to thank SINQ beamline scientists for making preliminary measurements possible.

References

[1] S. Sun, Z. Shao, H. Yu, G. Li, B. Yi, *J. Power Sources* **267**, 515–520 (2014).
[2] X. Wang, L. Zhang, G. Li, G. Zhang, Z. Shao, B. Yi, *Electrochim. Acta* **158**, 253–257 (2015).

SCIENTIFIC ACHIEVEMENTS 2017

Electrocatalysis & Interfaces

Co-electrolysis cells for efficient reduction of carbon dioxide from gas phase at low temperature using bipolar like membrane

A. Pătru, T. Binninger, B. Pribyl, T.J. Schmidt
phone: +41 56 310 2318, e-mail: alexandra.patru@psi.ch

In order to minimize the atmospheric carbon dioxide levels, electrochemical reduction of this gas appears like an attractive option [1]. By efficient electrochemical reduction, CO_2 is converted to fuels or other useful chemicals [2]. The efficiency of such a process depends on the cathode catalyst materials which need favourable electrokinetics towards CO_2 reduction as well as highly rational device engineering [3].

Practically, this process can be realized in a device called a co-electrolyser where the CO_2 is supplied in gas phase on the cathode side.

In this work, two novel cell configurations are presented and investigated for technical CO_2 reduction from gas phase which are based on a highly rational design approach taking into account a variety of subtle, but crucial details that have been overlooked in previous cell designs [2]. The first configuration utilizes a bipolar membrane with the anion conductive (alkaline) side of the bipolar membrane facing towards the cathode. This way, the cathode pH can be maintained at high values desirable for efficient CO_2 reduction. The cation conductive (acidic) side of the bipolar membrane, which faces the anode, prevents carbonate/bicarbonate species of the alkaline side to migrate to the anode and being oxidized there releasing CO_2. This latter process represents a major loss channel for CO_2 in an entirely alkaline membrane system. The bipolar cell configuration has been further optimized in a second cell configuration presented in this work, which enables highly improved energetic efficiency.

Experimental

The electrodes were prepared by spray coating adapted catalytic inks on gas diffusion layers (SGL 24 BC). Different catalyst loadings were used ~0.4 mg_{Pt}/cm^2, ~ 10 $mg_{IrO_2\text{-}TiO_2}/cm^2$ and ~ 3 mg_{Au}/cm^2. For catalyst layer preparation two type of ionomer solutions were used: acidic Nafion® solution 5 %wt from Sigma-Aldrich and, an alkaline ionomer solution prepared from FAA-3 polymer Fumion® (i.e. dissolved in pure ethanol to obtain a 5 %wt ionomer solution).

The used membrane electrode assemblies (MEA) consist of a gas diffusion electrode based on Au «black» (Sigma-Aldrich®) catalyst and an alkaline ionomer, an ionic conductive membrane and an anode which can be Pt/C (47 %wt Pt from Tanaka® TEC10E50E) or IrO_2-TiO_2 (Umicore®). Three membranes were tested: anionic conductive (Fumasep® AA30), bipolar membrane (Fumatech® FBM) and Nafion XL 100 (DuPont). When the Nafion membrane was used an additional alkaline polymer layer was sprayed onto the cathode to protect the cathode catalyst from the Nafion acidity [4]. This type of cell is called «novel configuration».

The electrochemical cells were operated at 40 °C and ambient pressure. For measurements investigating solely the cathode half-cell reaction, the anode catalyst was Pt/C and was fed with pure H_2 at 50 mL/min. In this operation mode, the anode serves both as counter electrode and as reference electrode, corresponding to a pseudo-reversible hydrogen electrode (pseudo-RHE). Cathode and anode gas humidification was achieved by passing through a water-bubbling system, the temperature of which was set to yield 100 % relative humidification. Polarization curves were measured between 0.1 and -2 V vs. RHE with potential scans at 50 mV/s using a Biologic VS 300 potentiostat. Full co-electrolysis cell operation was also tested using IrO_2-TiO_2 anode catalyst. Pure, humidified CO_2 was fed to the cathode at 100 mL/min and highly humidified Ar was fed to the anode. The gas analysis was performed using a mass spectrometer (MS) Omnistar® from Pfeiffer.

Results

The CO_2 reduction reaction (CO_2RR) is pH dependent and in gas phase co-electrolysis systems the reaction pH is defined by the type of polymer electrolyte like in similar electrochemical devices. During co-electrolysis in presence of gaseous CO_2, the following dominant reactions occur on Au catalysts at the cathode side in alkaline conditions:

$$CO_2 + H_2O + 2e^- \rightarrow CO + 2\ OH^- \qquad E = -0.932\ V/RHE \qquad [1]$$

$$2\ H_2O + 2e^- \rightarrow H_2 + 2\ OH^- \qquad E = -0.828\ V/RHE \qquad [2]$$

Generally, the alkaline system appears more promising for the purpose of CO_2RR, because in this condition the parasitic hydrogen evolution reaction (HER) is less favorable when compared to acidic conditions. However, if alkaline membranes are used in a co-electrolyser a severe problem occurs: the pumping of CO_2 from the cathode side to the anode side. The mobile ions inside an «alkaline» anion exchange membrane in the presence of CO_2 are expected to be carbonate (CO_3^{2-}) and bicarbonate (HCO_3^-) species rather than OH^- hydroxide ions.

It is evident from Reactions (1) and (2) that all cathode reactions lead to the formation of OH^- at the cathode in alkaline conditions. This is not only true for the actual CO_2RR, but also for the concomitant hydrogen evolution reaction. In abundance of CO_2, these OH^- are transformed into (bi)carbonate anions. Due to the electrostatic field in the membrane during operation, the (bi)carbonate anions migrate to the anode side where they are oxidized into O_2 and CO_2 according to Reactions (3) and (4):

$$2\ HCO_3^- \rightarrow \tfrac{1}{2}\ O_2 + H_2O + 2e^- + 2\ CO_2 \qquad E = -0.765\ V/RHE \qquad [3]$$

$$CO_3^{2-} \rightarrow \tfrac{1}{2}\ O_2 + 2e^- + CO_2 \qquad E = -0.692\ V/RHE \qquad [4]$$

In other words, for each electron exchanged in the cell reactions, one-half (bi)carbonate anions must flow from the cathode side to the anode side in order to close the electric circuit. This parasitic «CO_2 pumping» from cathode to anode side provides a huge loss channel for CO_2 and, therefore, makes «alkaline» AEM co-electrolyser systems intrinsically inefficient for the desired electrochemical reduction of CO_2. The formation of CO_2 at the anode side as a result of this CO_2 pumping effect was proven in the alkaline cell with results shown in Figure 1.

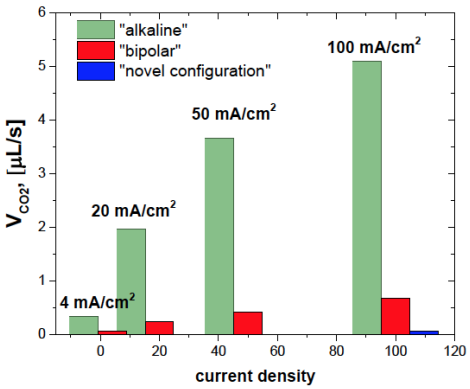

Figure 1. *Volume flows of CO_2 produced at the anode side of full co-electrolyser cells with Au-based cathode and IrO_2-TiO_2 anode catalyst using different membrane configurations. The anode gas composition was analyzed using MS at various cell current densities in galvanostatic mode. Cells were operated at 40 °C under ambient pressure.*

One possible solution to mitigate this problem of CO_2 pumping while maintaining alkaline conditions at the cathode is the use of a bipolar membrane instead of an entirely alkaline membrane. In such configuration, the alkaline anion exchange side of the membrane is facing towards the cathode and the acidic cation exchange side is facing towards the anode. In principle, the acidic side of the membrane prevents the transport of (bi)carbonate species all the way to the anode. Instead, at the internal interface of the bipolar membrane between the alkaline and the acidic layers, (bi)carbonate anions react with protons from the acidic side to form water and CO_2.

The gas analysis at the anode side of a bipolar membrane cell in full co-electrolysis operation, i.e. using IrO_2-TiO_2 as anode catalyst for oxygen evolution reaction, is shown in Figure 1. It is evident that the release of CO_2 at the anode was significantly reduced, but not completely eliminated. Moreover, the bipolar membrane cell provided similar current densities as the alkaline cell, and the CO selectivity remained at the same order of magnitude as shown in Figure 2a and 2b.

Despite the promising results obtained with a bipolar membrane, the formation of water at the internal interface can result in membrane delamination and reduce the system stability. An improved bipolar like cell configuration was proposed to solve this problem, the novel cell configuration. The special design of the cathode catalyst layer in combination with an acidic Nafion membrane is expected to combine several advantages:

- High catalytically active surface area for the CO_2RR is provided by the «alkaline» anion exchange ionomer within the cathode catalyst layer providing an optimal alkaline environment for the reduction of CO_2.
- The membrane delamination is solved by the morphology of the alkaline ionomer thin film which is adjusted to the rough surface of the cathode catalyst layer and H_2O and CO_2 formed at the interface can laterally escape «in plane» at the perimeter of these interface spots back to the cathode electrode pore structure.
- The cation exchange membrane guarantees that the (bi)carbonate anions from the alkaline cathode ionomer are stopped from being transferred to the anode side, thus avoiding parasitic CO_2 pumping from cathode to anode side.
- The use of a cation exchange membrane provides lower electrical resistance than anion exchange membranes or bipolar membranes enabling increased energetic efficiency of the proposed co-electrolysis cell design (Figure 2).

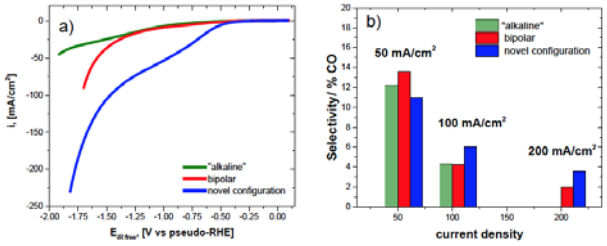

Figure 2. *a) Cathode polarization curves of CO_2 co-electrolysis cells with alkaline membrane, bipolar membrane, and «novel configuration» obtained from linear sweep voltammetry at 50 mV/s, 40 °C and ambient pressure. The cathode was fed with 50/50 %vol CO_2/Ar, while the anode consisted of Pt/C catalyst fed with pure H_2. b) CO selectivities obtained in galvanostatic experiments at various fixed current densities.*

Conclusions

Key elements for efficient electrochemical CO_2 reduction from gas phase in a non-liquid electrolyte cell were identified and combined in a rational design of an optimal co-electrolysis cell configuration. Whereas the competition between CO_2RR and HER requires alkaline environment at the cathode side in order to achieve high CO_2RR selectivity, an all-alkaline cell was shown to lead to significant parasitic CO_2 pumping from the cathode to the anode side. Therefore, in order to preserve high CO_2 utilization efficiency, a bipolar design approach must be utilised with an alkaline side at the cathode and an acidic part that blocks the parasitic CO_2 transport to the anode side. Consequently, a cell configuration with a bipolar membrane demonstrated a significant decrease of CO_2 release at the anode side while maintaining good selectivity for the reduction of CO_2. However, a principal limitation of the bipolar membrane configuration was identified and attributed to the formation of water and CO_2 at the internal alkaline-acidic interface of the bipolar membrane, which could result in membrane delamination. Combining all key requirements in an optimal way, a novel cell configuration was developed containing alkaline ionomer within the cathode catalyst layer, a standard Nafion membrane, and an additional thin film of alkaline ionomer sprayed on top of the cathode catalyst layer in order to protect the latter from the acidity of the Nafion membrane.

Acknowledgement

Kindly acknowledged is financial support from the Swiss Competence Center for Energy Research *Heat and Electricity Storage* (SCCER HaE).

References

[1] J. Durst, A. Rudnev, A. Dutta, Y. Fu, J. Herranz, V.B.R. Kaliginedi, A. Kuzume, A.A. Permyakova, Y. Paratcha, P. Broekman, T.J. Schmidt, *Chimia* **69** (12), 1–8 (2015).

[2] J. Herranz, J. Durst, E. Fabrri, A. Pătru, X. Cheng, A.A. Permyakova, T.J. Schmidt, *Nano Energy* **29**, 4–28 (2016).

[3] C. Delacourt, P.L. Ridgway, J.B. Kerr, J. Newman, *J. Electrochem. Soc.* **155** (1), B42–B49 (2008).

[4] A. Pătru, T. Binninger, B. Pribyl, T.J. Schmidt, patent application number EP 17182823.9.

CO_2 reduction to valuable products: a Differential Electrochemical Mass Spectrometry (DEMS) study

D. Perego, J. Herranz, T.J. Schmidt
phone: +41 56 310 3699, e-mail: daniele.perego@psi.ch

Carbon dioxide is a major contributor to global warming and the possibility of recycling this greenhouse gas is becoming increasingly the focus of the scientific community. The electrochemical reduction of CO_2 (CO_2RR) is an attractive way to utilise this greenhouse gas by converting it into a broad range of useful carbon neutral fuels [1] using renewable energy sources (i.e. wind, solar, geothermal). That would allow not only to store excess energy, but also to eventually close the global carbon cycle [2]. Nevertheless, on top of the high overpotential required to drive this reaction, the CO_2RR suffers from a poor yield/selectivity towards hydrocarbons [3, 4, 5]. So far only carbon monoxide and formate products appear to be economically interesting when produced by electrochemical CO_2 reduction compared to other well established chemical processes [6]. Improvements in this scenario require a better understanding of the fundamental reactions yield on various metal surfaces, along with the development of analytical tools that allow for the quantification of the reaction products. Differential Electrochemical Mass Spectrometry (DEMS) appears as an excellent versatile choice for the operando quantification of the volatile species produced upon CO_2RR [7]. To this scope, we have designed and built an electrochemical flow cell coupled to a MS setup for the study of CO_2-reduction selectivity surfaces.

Mass spectrometry (MS) is widely applied in catalysis research for the quantitative detection of reactants and products with high precision. In many cases, preseparation of the gas mixture is necessary, because of interferences between different gases that contribute to the same mass-to-charge (m/q) ratios and, thus, to the same MS peaks. However, combining MS with a preseparation technique not only makes the overall system more complex, but also prevents online detection of gas, which is the key-feature of the DEMS setup. To overcome such limitation, we developed an MS calibration approach using several different gas mixtures. This calibration method enables unambiguous and quantitative distinction of CO, N_2, and CO_2 via measurement of the MS peaks at (m/q) = 44, 28, and 14. As an example of the possible applications offered by a calibrated DEMS setup, herein we present our results upon studying the CO_2RR on a polycrystalline Au electrode, chosen for its selectivity towards CO production [8] and chemical stability in a broad pH range.

Experimental

The mathematical method used for the calibration and determination of unknown gas compositions is based on the following n-dimensional equation system (where *n* is the number of gas species):

$$\begin{pmatrix} i_1 \\ i_2 \\ \dots \\ i_{n-1} \\ i_n \end{pmatrix} = \begin{pmatrix} a_{1,1} & a_{1,2} & \dots & a_{1,n-1} & a_{1,n} \\ a_{2,1} & a_{2,2} & \dots & \dots & a_{2,n} \\ \dots & \dots & \dots & \dots & \dots \\ a_{n-1,1} & \dots & \dots & \dots & a_{n-1,n} \\ a_{n,1} & a_{n,2} & \dots & a_{n,n-1} & a_{n,n} \end{pmatrix} \cdot \begin{pmatrix} x_1 \\ x_2 \\ \dots \\ x_{n-1} \\ x_n \end{pmatrix}$$

which can be written as

$$\vec{i_i} = A \cdot \vec{x_i} \qquad \vec{i_1}, \vec{i_2}, \dots, \vec{i_n}$$

where vector *i* contains the MS-currents measured at *n* different mass numbers, matrix *A* contains all calibration factors to be derived from the calibration, and vector *x* consists of the different gas concentrations in the mixture. As there are n^2 different calibration vectors, a total of *n* different gas mixtures are needed to determinate all calibration factors for this system. In our context, to calibrate properly the MS, 3 different mixtures with chosen concentrations of H_2, N_2, CO, CO_2 and Ar were used, and a 4th mixture was used to independently verify the results of the calibration. The technical set-up which was used to calibrate the MS is shown in Figure 1.

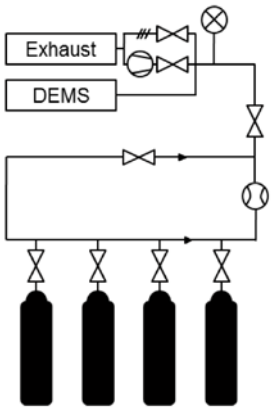

Figure 1. *Technical setup used for DEMS calibration, consisting of four gas cylinders with mixtures of known compositions that can be independently dosed to the DEMS system. Note that the exhaust line allows to evacuate the setup's lines prior to the calibration, as to minimize changes in the composition of the dosed calibration mixture.*

Once the three calibration gases have been measured, all necessary calibration factors were calculated to determine matrix *A*. It is important to highlight that the built setup allows to switch from calibration to electrochemical measurements without introducing any other variables.

The DEMS setup, schematized in Figure 2, consists of an electrochemical flow cell separated from the DEMS' first vacuum chamber by a PTFE porous membrane with 0.02 µm pore size.

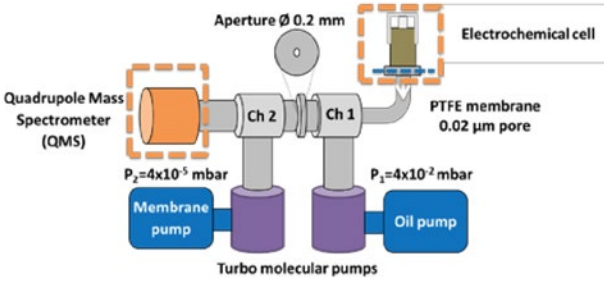

Figure 2. *Scheme of the DEMS setup, consisting of an electrochemical, microfluidic cell connected to a differential, 2-stage mass spectrometry system through a PTFE membrane.*

The PTFE membrane allows the separation of volatile products from the liquid electrolyte, and is also used in the calibration measurements. As a result, the derived calibration factors include not only the MS contribution, but also the permeability of the specific PTFE membrane used in each experiment. An aperture of 0.2 mm diameter results in a differential pressure between the DEMS' first and second vacuum chambers (at $\approx 10^{-2}$ and $\approx 10^{-5}$ mbar, respectively), whereby the latter holds the secondary electron multiplier (SEM), the cross-beam electron impact ion source (CB-IS) and the quadrupole mass analyser (Pfeiffer Vacuum QMA 422).

A polycrystalline Au disk of 5 mm diameter was mechanically polished on a micro-cloth. The disk was then sonicated three times for five minutes in ultrapure water and assembled into the electrochemical flow cell. A solution of 0.1 M $KHCO_3$, saturated with 50 % CO in Ar (pH = 8.1) was used as the electrolyte. A flame-annealed Pt mesh was used as counter electrode, along with a $Hg/HgSO_4$ reference electrode. Potential steps were applied to the system, starting from -1.0 V vs. RHE and decreasing by 100 mV in each step until -1.8 V vs. RHE. Every step was 3 min long and between two steps, 5 cyclic voltammograms were carried out at 100 mV/s in the -0.5 – 0.5 V vs. RHE potential window. The flow of the electrolyte through the microfluidic cell was set to 50 µL/min. Different mass fractions were recorded by the MS during the reaction.

Results

When CO_2RR takes place, in a quasi-neutral environment, at the polycrystalline Au cathode, the principal electrochemical reactions are:

$$CO_2 + H_2O + 2e^- \rightarrow CO + 2\ OH^- \qquad E^0 = -0.103\ V \qquad (1)$$

$$2\ H_2O + 2e^- \rightarrow H_2 + 2\ OH^- \qquad E^0 = 0.0\ V \qquad (2)$$

It has to be noted that also $HCOO^-$ can be produced, which is not volatile and thus not detectable by the DEMS. However since the yield of formate is expected to be < 10 % [5], it is a valid approximation to consider as the main products in our system only H_2 and CO.

In Table 1 all calibration factors for all the relevant species are reported.

Gas species	m/z	Calibration factor [-]
H_2	2	0.007
N_2	28	0.005
CO	28	0.035
Ar	40	0.003
CO_2	44	0.001

Table 1. *Calibration factors for different gas species obtained using an ionizing electron energy of 70 eV, with an emission current of 1 mA, a focus plate and extraction voltages of 14.0 and 250 V, resolution of 50 and an SEM voltage of 1030 V.*

To evaluate the faradaic efficiencies (FE) of CO the following formula has been used

$$FE = \frac{znF}{Q}$$

where *z* is the number of electrons involved in the electrochemical reaction, *n* is the produced number of moles, *F* is the Faraday constant and *Q* is the overall charge transferred within the potential step.

In Figure 3 CO faradaic efficiencies together with current densities (scaled over geometrical area) as a function of the applied potential are shown.

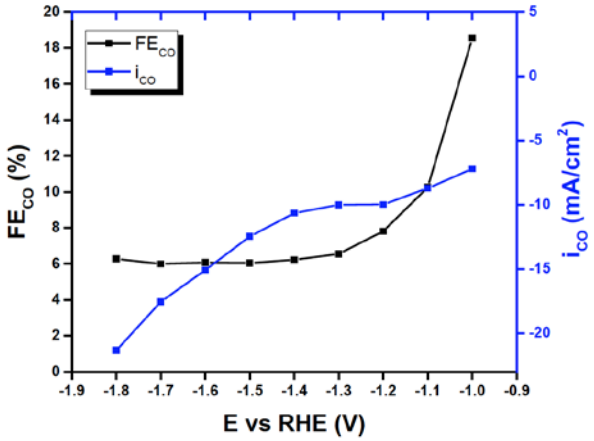

Figure 3. *CO faradaic efficiencies and current densities as a function of the applied potential.*

The results show a maximum CO faradaic efficiency at -1.0 V vs. RHE of about 19 %, reaching a plateau at around 6 % at more negative potentials (≤ -1.3 V vs. RHE). These results are in good agreement with reports by other groups [5, 8], and in a future step we shall explore higher potentials (> -1.0 V vs. RHE) at which the selectivity towards CO formation is expected to be even greater.

Conclusions

We have built a versatile differential electrochemical mass spectrometer setup (DEMS) which allows to quantify with extremely high precision gas products of electrochemical reactions.

With a system of different calibration gas mixtures we have been able to calibrate the MS for gas species overlapping their mass-to-charge ratio (i.e., CO, CO_2 and N_2). Finally we applied the DEMS to the study of CO_2RR on polycrystalline Au, showing a maximum faradaic efficiency for CO production of 19 % at -1.0 V vs. RHE.

References

[1] K.P. Kuhl, E.R. Cave, D.N. Abram, T.F. Jaramilo, *Energy Environ. Sci.* **5**, 7050–7059 (2012).
[2] J. Herranz, J. Durst, E. Fabbri, A. Pătru, X. Cheng, A.A. Permyakova, T.J. Schmidt, *Nano Energy* **29**, 4–8 (2016).
[3] M. Watanabe, M. Shibata, A. Kato, *J. Electrochem. Soc.* **138**, 3382–3389 (1991).
[4] Y. Hori, H. Wakebe, T. Tsukamoto, O. Koga, *Electrochim. Acta* **39**, 1833–1839 (1994).
[5] Y. Hori, A. Murata, K. Kikuchi, S. Suzuki, *J. Chem. Soc., Chem. Commun.* **10**,728–729 (1987).
[6] J. Durst, A. Rudnev, A. Dutta, Y. Fu, J. Herranz, V.B.R. Kaliginedi, A. Kuzume, A.A. Permykova, Y. Paratcha, P. Broekman, T.J. Schmidt, *Chimia* **69**, 1–8 (2015).
[7] K.J.P. Schouten, E.P. Gallent, M.T. M. Koper, *J. Electrochem. Soc.* **716**, 53–57 (2014).
[8] Y. Hori, «*Electrochemical CO_2 reduction on metal electrodes. Modern aspects of electrochemistry*», Springer, 89–189 (2008).

Sputter deposited Cu and CuO_x thin films for electroreduction of CO_2

A. Permyakova, A. Pătru, J. Herranz, T.J. Schmidt
phone: +41 56 310 2084, e-mail: anastasia.permyakova@psi.ch

CO_2 reduction is a problem of great importance for a sustainable energy future. This greenhouse gas can be reduced to useful fuel electrochemically. If the electrical energy used for the reduction reaction comes from a renewable source such as wind or solar, carbon neutral fuel can be generated.

The main challenges of the CO_2 reduction reaction (CO_2RR) are related to reducing of its overpotential, increasing overall faradaic efficiency (FE, %) and improving control over products' selectivity [1–4].

The main objective of this study was to increase catalyst selectivity towards alcohols, ideally as a single liquid product. So far the only catalyst that is able to produce significant amount of alcohols is polycrystalline Cu, however it was also demonstrated that it is possible to tune Cu surface and shift its selectivity (e.g. Ethanol formation).

Such catalysts are described in the literature, one of the examples is a Cu_2O derived Cu catalyst [5, 6]. However, the Cu_2O catalyst surface dynamic and its stability during the reaction process are not fully understood. Some reports claim that Cu_2O is reduced completely and only metallic Cu remains at the surface, whereas others claim partial reduction of Cu_2O and/or lattice oxygen remains at the surface after the electrochemistry [7, 8]. In both cases rough surfaces are studied (nanoparticles or electrodeposited Cu_2O) and it is impossible to deconvolute one effect from another. Therefore, we have studied well defined flat Cu and Cu_2O thin films in order to minimize the surface roughness effects.

Experimental

Cu and Cu_2O (100 nm) thin films were prepared by sputter deposition onto the Si (100) substrate. Under electrochemical measurement conditions, Cu thin films were not mechanically stable. Therefore, heat treatment for 30 minutes at 300 °C and 4 % H_2 in Ar atmosphere was carried out to stabilize Cu on the Si substrate (HT Cu TFs). Surface characterization by XPS and Auger spectra showed that Cu (0) and CuO are present at the surface of HT Cu TFs.

Caesium carbonate (≥ 99.999 % metals basis) from Sigma-Aldrich was used without further purification. Electrolyte solution was prepared with 18.2 MW deionized water from a Millipore system. Electrolyte solution was prepared by bubbling 0.05 M Cs_2CO_3 solution with CO_2 gas purging until a pH of 6.8 was achieved.

Electrochemical measurements were carried out using a Biologic SP-300 potentiostat. CO_2 electrolysis was performed at ambient pressure in a gas-tight custom-made cell made of PEEK. An Ag/AgCl electrode (Harvard Apparatus GmbH) was used as the reference. Data were converted to a Reversible Hydrogen Electrode (RHE) scale by equation:

E vs. RHE = E vs. Ag/AgCl + 0.197 V + 0.0591 x pH (6.8).

Before every electrolysis experiment, the solution resistance was first determined using impedance spectroscopy by scanning from 1 MHz to 10 Hz. Before the cyclic voltammetry and chronoamperometry measurements Ohmic resistance was corrected by potentiostat set to compensate for 85 % of the measured IR drop.

The gas and liquid products analysis was carried out with a gas chromatograph (GC, SRI instruments) equipped with a packed HaySep Dcolumn and a packed MolSieve 5A column. A flame ionization detector (FID) with a methanizer was used to detect hydrocarbons with H_2 as the carrier gas. A thermal conductivity detector (TCD) was used to detect hydrogen with Ar as the carrier gas.

Results

Figure 1 show products distribution for HT Cu TF at different applied potentials. The minimum FE of hydrogen corresponding to an optimum CO_2RR was achieved at -1 V vs. RHE. When compare with the state-of-the-art polycrystalline Cu no significant difference in the product distribution has been observed (see Figure 2).

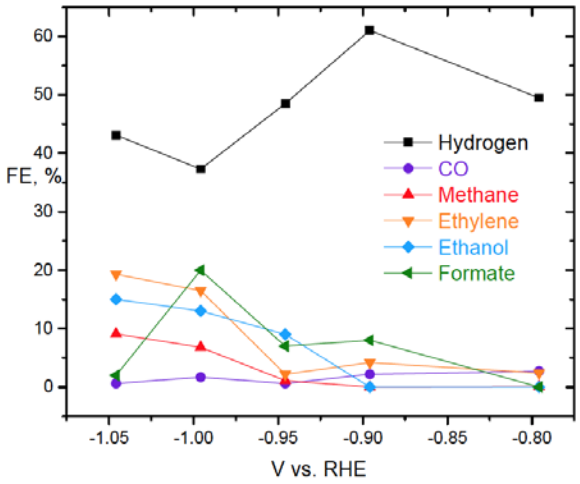

Figure 1. *Faradaic efficiencies of heat treated Cu thin film (HT Cu TF) at different potentials.*

To tune the Cu selectivity towards alcohols formation, Cu_2O surfaces were investigated (Cu_2O TF, 100 nm). Product characterization indicated optimum for Ethanol and Formate at -1 V vs. RHE. However, no major differences in product distribution were obtained with this catalyst compared to the HT Cu TF (Figure 2). And both HT Cu TF and Cu_2O TF behave similar to polycrystalline Cu.

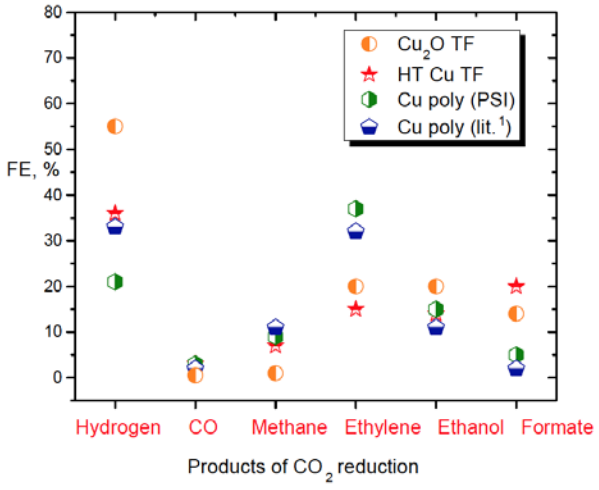

Figure 2. *Comparison of faradaic efficiencies for HT Cu TF, Cu_2O and polycrystalline Cu at -1 V vs. RHE.*

To further understand Cu based electrocatalyst behavior, surface characterization was performed.

The HT Cu TF surface was investigated by XPS after electrochemical measurements. To ensure a thorough surface characterization, measurements were performed under controlled atmosphere. A glove box ventilated with N_2 was used to avoid oxygen contamination during experiment and a N_2 filled chamber was used for transferring a sample to the XPS to avoid oxidation in the air.

Figure 3 shows a comparison between an experiment that was performed on HT Cu TF in the air (blue) and an experiment that was completed under controlled atmosphere using the N_2 glove box (green). After electrochemical experiment with air transfer to the XPS, CuO seems to be reducing to Cu_2O. Whereas, the XPS results for the experiment that was done under controlled atmosphere show that CuO actually appears to be reduced to metallic Cu (not Cu_2O) after CO_2 electroreduction measurements, which could explain why HT Cu TF behaves like polycrystalline Cu.

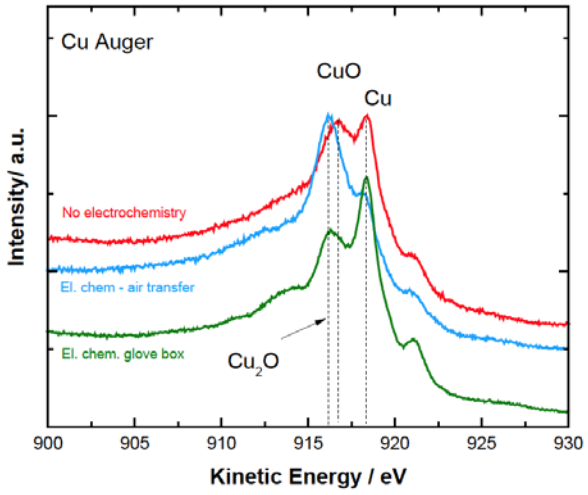

Figure 3. *Auger spectra of HT Cu TF: as deposited (red), after electrochemistry transferred in the air (blue) and after glove box experiment (green).*

Conclusions

Heat treated Cu and 100 nm Cu_2O thin films were investigated for CO_2RR. These samples demonstrate comparable behavior with polycrystalline Cu, i.e. similar product distribution and faradaic efficiencies.

When Cu_2O surface was used no substantial difference was observed in the product distribution. This result can be explained by the fact that Cu_2O could be reduced during the measurement to metallic Cu and the CO_2RR takes place finally on a metallic Cu surface. According to a simple calculation, total reduction of Cu_2O to Cu for a 100 nm Cu_2O layer operating at low potential (-1 V vs. RHE) during the chronoamperometry measurement could take less than 11 seconds.

To further study effects of Cu_2O on the CO_2RR selectivity the oxide thickness must be substantially increased to ensure that the reduction time will be long enough to detect possible forming products. This is an ongoing study in our laboratory.

Acknowledgement

The authors gratefully acknowledge financial support from the Commission of Technology and Innovation Switzerland (CTI) and the Swiss Competence Center for Energy Research *Heat and Electricity Storage* (SCCER HaE).

References

[1] J. Herranz, J. Durst, E. Fabbri, A. Pătru, X. Cheng, A.A. Permyakova, T.J. Schmidt, *Nano Energy* **29**, 4–28 (2016). doi:10.1016/j.nanoen.2016.01.027.
[2] Y. Hori, «*Electrochemical CO_2 reduction on metal electrodes. Modern aspects of electrochemistry*», Springer, 89–189 (2008).
[3] J. Durst, A. Rudnev, A. Dutta, Y. Fu, J. Herranz, V. Kaliginedi, A. Kuzume, A.A. Permyakova, Y. Paratcha, P. Broekmann, T.J. Schmidt, *Chimia* **12**, 69 (2015).
[4] K.P. Kuhl, E.R. Cave, D.N. Abramc, T.F. Jaramillo, *Energy Environ. Sci.* **5**, 7050–7059 (2012).
[5] Y. Chen, C.W. Li, M.W. Kanan, *J. Am. Chem. Soc.* **134**, 9969–19972 (2011).
[6] C.W. Li, J. Ciston, M.W. Kanan, *Nature* **508**, 504–507 (2014).
[7] D. Kim, S. Lee, J.D. Ocon, B. Jeong, J.K. Lee, J. Lee, *Phys. Chem. Chem. Phys.* **17**, 824–830 (2015).
[8] A. Eilert, F. Cavalca, F.S. Robert, J. Osterwalder, C. Liu, M. Favaro, E.J. Crumlin, H. Ogasawara, D. Friebel, L.G.M. Pettersson, A. Nilsson, *J. Phys. Chem. Lett.* **8**, 285–290 (2017).

Versatile calibration method for mass spectrometry of interfering gases such as mixtures of CO, N_2, and CO_2

B. Pribyl, T. Binninger, A. Pătru, S. Bjelić, P. Ruettimann, T.J. Schmidt
phone: +41 56 310 2318, e-mail: bernhard.pribyl@psi.ch

In the context of electrochemical CO_2 reduction reaction (CO_2RR) studies the reaction products can be identified and quantified by various analytical techniques like gas chromatography (GC) [1–3], nuclear magnetic resonance (NMR) spectroscopy [4, 5], or infrared spectroscopy.[6, 7] Among these analysis techniques, GC is the most utilized one. However, this method cannot provide time resolved reaction product distribution during the reaction investigation and unfortunately important catalytic information can be lost.

Mass spectrometry (MS) is widely applied in catalysis research for the quantitative detection of reactants and products at high precision and can be used for on-line detection. However, in many cases, pre-separation of the gas mixture is necessary, because of interferences between different gases that contribute to the same mass-to-charge (m/q) ratios and, thus, to the same MS peaks. Such a case is faced when CO is the main CO_2RR product. Pre-separation can be achieved, e.g., by chromatography and MS can be used subsequently for the quantitative detection of individually separated components [8]. Combining MS with a pre-separation technique not only makes the overall system more complex, but it also prevents on-line MS of gas mixtures with dynamically changing compositions on shorter time scales, which is desired for the study of time-dependent processes. [9]

For getting advantage of the MS on line detection possibility, an advanced calibration method is required to allow the differentiation of the above mentioned interfering gases using MS.

The present work offers a solution to this problem, which is based on an MS calibration using several different calibration gas mixtures. This calibration method enables the unambiguous and quantitative distinction of CO, N_2, and CO_2 at a precision which is competitive with state-of-the-art GC techniques.

Calibration method – principle

For the simultaneous analysis of *n* different gases, *n* different mass-to-charge ratios are selected and the corresponding ion currents of the mass spectrometer are recorded. A linear relation between the relative gas concentrations $x_1,\dots, x_n$ and the measured pressure-normalized ion currents $i_1,\dots, i_n$ is assumed, which can be written in terms of an n-dimensional linear system of equations:

$$\begin{pmatrix} i_1 \\ i_2 \\ \dots \\ i_{n-1} \\ i_n \end{pmatrix} = \begin{pmatrix} a_{1,1} & a_{1,2} & \dots & a_{1,n-1} & a_{1,n} \\ a_{2,1} & a_{2,2} & \dots & \dots & a_{2,n} \\ \dots & \dots & \dots & \dots & \dots \\ a_{n-1,1} & \dots & \dots & \dots & a_{n-1,n} \\ a_{n,1} & a_{n,2} & \dots & a_{n,n-1} & a_{n,n} \end{pmatrix} \cdot \begin{pmatrix} x_1 \\ x_2 \\ \dots \\ x_{n-1} \\ x_n \end{pmatrix}$$

$$\vec{\imath} = A \cdot \vec{x} \qquad \rightarrow \qquad \vec{x} = A^{-1} \cdot \vec{\imath}$$

It is the purpose of the calibration method to determine matrix A and, equivalently, its inverse A^{-1}. This is achieved by performing calibration measurements with *n* different calibration gas mixtures C1, … ,Cn with known composition vectors $\vec{x}_{C1},\dots,\vec{x}_{Cn}$.

There exists a unique matrix T, which maps each vector $\vec{x}_{Ci}$ to the corresponding unit vector $\vec{e}_i = (0,\dots,0,1,0,\dots,0)$ containing 1 at the i^{th} position and 0 elsewhere:

$$T \cdot \vec{x}_{Ci} = \vec{e}_i$$

$$\Rightarrow \vec{x}_{Ci} = T^{-1} \cdot \vec{e}_i = \overrightarrow{(T^{-1})_i}$$

$$\Rightarrow T^{-1} = (\vec{x}_{C1}, \dots, \vec{x}_{Cn}) = X \qquad \rightarrow \qquad T = X^{-1}$$

From equation 2, written for each measured ion current vector $\vec{\imath}_{Ci}$ of the calibration gas mixture $\vec{x}_{Ci}$, it follows:

$$\vec{\imath}_{Ci} = A \cdot \vec{x}_{Ci} = A \cdot T^{-1} \cdot T \cdot \vec{x}_{Ci} = A \cdot T^{-1} \cdot \vec{e}_i = \overrightarrow{(A \cdot T^{-1})_i}$$

$$A \cdot T^{-1} = (\vec{\imath}_{C1}, \dots, \vec{\imath}_{Cn}) = I \qquad \rightarrow \qquad A = I \cdot T = I \cdot X^{-1}$$

Practical Application

The general calibration method can be simplified for the specific case of a gas mixture containing H_2, N_2, CO, CO_2 in Ar as not all gases contribute to each ion current:

$$\begin{pmatrix} i_2 \\ i_{14} \\ i_{28} \\ i_{40} \\ i_{44} \end{pmatrix} = \begin{pmatrix} a_{H2,2} & 0 & 0 & 0 & 0 \\ 0 & a_{N2,14} & a_{CO,14} & 0 & 0 \\ 0 & a_{N2,28} & a_{CO,28} & 0 & a_{CO2,28} \\ 0 & 0 & 0 & a_{Ar,40} & 0 \\ 0 & 0 & 0 & 0 & a_{CO2,44} \end{pmatrix} \cdot \begin{pmatrix} x_{H2} \\ x_{N2} \\ x_{CO} \\ x_{Ar} \\ x_{CO2} \end{pmatrix} + \begin{pmatrix} 0 \\ i_{bgnd,14} \\ 0 \\ 0 \\ 0 \end{pmatrix}$$

For the present case, only secondary ionization products contribute to the (m/q) = 14 MS peak, which results in a very small ion current i_{14} that makes background correction necessary, represented by $i_{bgnd,14}$.

$$\vec{\imath} = A \cdot \vec{x} + \vec{\imath}_{bgnd} \qquad \rightarrow \qquad \vec{x} = A^{-1} \cdot (\vec{\imath} - \vec{\imath}_{bgnd})$$

Using a slightly modified mathematical approach reduces the required number of different, linearly independent calibration gas mixtures to three by exploiting the specific structure of matrix *A*. In total, three linearly independent calibration gas mixtures are needed to determine all calibration factors according to the following equations:

$$\begin{pmatrix} i_{28,C1} \\ i_{28,C2} \\ i_{28,C3} \end{pmatrix} = \begin{pmatrix} x_{N2,C1} & x_{CO,C1} & x_{CO2,C1} \\ x_{N2,C2} & x_{CO,C2} & x_{CO2,C2} \\ x_{N2,C3} & x_{CO,C3} & x_{CO2,C3} \end{pmatrix} \cdot \begin{pmatrix} a_{N2,28} \\ a_{CO,28} \\ a_{CO2,28} \end{pmatrix}$$

$$\vec{\imath}_{28} = X_{28}^T \cdot \vec{a}_{28} \qquad \rightarrow \qquad \vec{a}_{28} = (X_{28}^T)^{-1} \cdot \vec{\imath}_{28}$$

$$\begin{pmatrix} i_{14,C1} \\ i_{14,C2} \\ i_{14,C3} \end{pmatrix} = \begin{pmatrix} x_{N2,C1} & x_{CO,C1} & 1 \\ x_{N2,C2} & x_{CO,C2} & 1 \\ x_{N2,C3} & x_{CO,C3} & 1 \end{pmatrix} \cdot \begin{pmatrix} a_{N2,14} \\ a_{CO,14} \\ i_{bgnd,14} \end{pmatrix}$$

$$\vec{\imath}_{14} = X_{14}^T \cdot \vec{a}_{14} \qquad \rightarrow \qquad \vec{a}_{14} = (X_{14}^T)^{-1} \cdot \vec{\imath}_{14}$$

The calibration factors for (m/q) = 2, 40, and 44 are determined as an average of the three calibration gas measurements.

Experimental

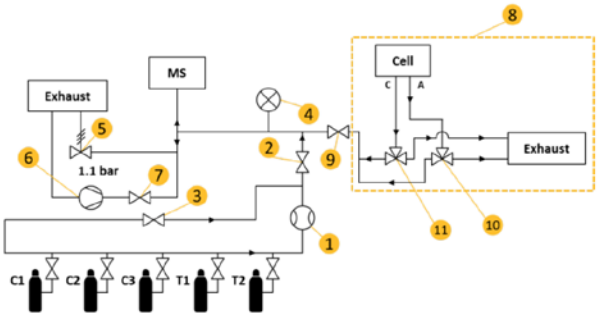

Figure 1. *Technical set-up schematic used for MS calibration and for on-line measurements of CO_2RR products.*

The technical set-up, which was designed for the calibration of the mass spectrometer as well as for the conduction of CO_2RR experiments, is shown in Figure 1. The three gas bottles containing the calibration gas mixtures C1, C2, and C3, as well as two additional gas bottles with test gas mixtures T1 and T2 were connected to the mass spectrometer (MS) with a manual mass flow meter ① and a ball valve ②. As shown in the schematic, an additional bypass ③ of the mass flow meter was installed in order to enable a quick evacuation and refilling of the entire system. A pressure sensor ④ was installed before the inlet to the mass spectrometer. Finally, an overpressure valve ⑤ was placed behind the mass spectrometer, which opened at an absolute pressure of 1.1 bar, ensuring constant pressure and flow conditions during the measurement. Parallel to this valve, a vacuum pump ⑥ was installed which could be used after opening valve ⑦ in order to evacuate the entire system before switching from one calibration gas mixture to another. The sub-system ⑧ shows the electrochemical cell for CO_2RR. Additionally, GC measurements were performed to verify the MS measurements.

Results

After calibrating the mass spectrometer with the multi-gas calibration method described above using the calibration gas mixtures C1, C2, and C3, the quality of the calibration was tested with measurements of the test gas mixtures T1 and T2 with known compositions. Figure 2 shows the good agreement of the MS measurements and GC measurements:

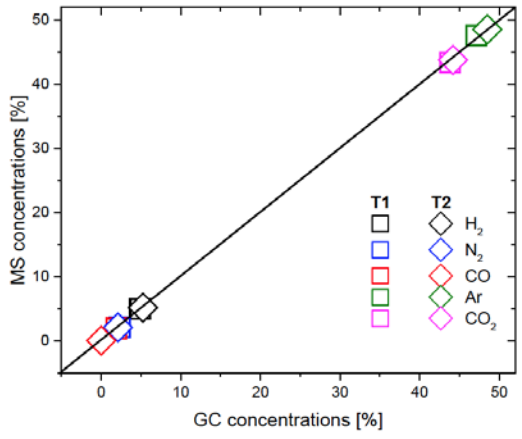

Figure 2. *Comparison of measured gas compositions in mol.% with MS and GC.*

The calibration method has been further applied for the MS analysis of the cathode exhaust gas mixture of a co-electrolysis cell producing CO and H_2 by electrochemical CO_2 reduction. The results are summarized in Table 1 and show successful application of the method.

Gas	Comp. Norm. at OCV	Comp. Norm. at -50mA/cm^2	Comp. Norm. at -100mA/cm^2
H_2	0.04%	1.35%	2.91%
N_2	0.62%	0.61%	1.02%
CO	-0.02%	0.17%	0.10%
Ar	49.74%	49.86%	46.89%
CO_2	49.62%	48.02%	49.08%

Table 1. *MS analysis results of electrochemical CO_2RR products in the cell cathode gas exhaust. Values in mol.%.*

Conclusions

A novel and versatile mass spectrometry calibration method was developed, successfully tested, and applied for the analysis of product gases from an electrochemical cell for CO_2RR. It was demonstrated that this multi-gas calibration method allows a quantitative analysis of interfering gas mixtures, such as CO, N_2, and CO_2, at a precision that is competitive with state-of-the-art analysis techniques such as GC. This versatile calibration method can be also applied for MS analysis of other interfering gas mixtures, and it could dramatically improve the application of mass spectrometry for on-line product gas analysis in heterogeneous catalysis and in electrocatalysis research.

Acknowledgement

Kindly acknowledged is financial support from the Swiss Competence Center for Energy Research *Heat and Electricity Storage* (SCCER HaE) .

References

[1] H. Kim, H.S. Jeon, M.S. Jee, E.B. Nursanto, J.B. Singh, K. Chae, Y.J. Hwang, B.K. Min, *ChemSusChem* **9** (16), 2097–2102 (2016). (doi:10.1002/cssc.201600228).
[2] D.T. Whipple, E.C. Finke, P.J.A. Kenis, *Solid-State Lett.* **13**, B109 (2010).
[3] E. Andrews, S. Katla, C. Kumar, M. Patterson, P. Sprunger, J. Flake, *J. Electrochem. Soc.* **162**, F1373–F1378 (2015).
[4] K.P. Kuhl, E. Cave, D.N. Abram, T.F. Jaramillo, *Energy Environ. Sci.* **5**, 7050–7059 (2012).
[5] Y. Chen, C.W. Li, M.W. Kanan, *J. Am. Chem. Soc.* **134**, 19969–19972 (2012).
[6] B. Innocent, D. Liaigre, D. Pasquier, F. Ropital, J.-M. Leger, K.B. Kokoh, *J. Appl. Electrochem.* **39**, 227–232 (2009).
[7] B. Innocent, D. Pasquier, F. Ropital, F. Hahn, J.-M. Leger, K.B. Kokoh, *Appl. Catal. B Environ.* **94**, 219–224 (2010).
[8] W. Lindinger, J. Hirber, H. Paretzke, *Int. J. Mass Spectrom. Ion Process.* **129**, 79–88 (1993).
[9] F.A. Mellon, «*Encyclopedia of Food Sciences and Nutrition*», Elsevier Science Ltd, 1294–1301 (2003). ISBN: 978-0-12-227055-0.

Highly active nano-perovskite catalysts for oxygen evolution reaction: Insights into activity and stability in alkaline and quasi-neutral pH electrolytes

B.J. Kim, X. Cheng, D.F. Abbott, E. Fabbri, F. Bozza, T. Graule, I.E. Castelli, L. Wiles, A. Niedzwiecki, N. Danilovic, K.E. Ayers, N. Marzari, T.J. Schmidt

phone: +41 56 310 4085, e-mail: joseph.kim@psi.ch

Water electrolysis technology is gaining a lot of attraction as the implementation of renewable energy technologies is challenged by the intermittent production of electricity. In recent developments, members of the perovskite oxide family have been recognized as highly active electrocatalysts capable to facilitate an efficient water oxidation reaction. Perovskite oxides offer opportunities to explore different synergetic effects owing to their capability to accommodate cation substitutions in both the A- and B-sites with another cation element, resulting in $(A_xA'_{1-x})(B_yB'_{1-y})O_3$ compositions. [1]

To date, $PrBaCo_2O_{5+\delta}$ (PBCO) and $Ba_{0.5}Sr_{0.5}Co_{0.8}Fe_{0.2}O_{2+\delta}$ (BSCF) have been demonstrated as two of the most active perovskite catalysts for oxygen evolution reaction (OER), each representing a different structure: a layered order and a random arrangement, respectively.

Under the practical condition during the operation of alkaline exchange membrane water electrolyzers (AEMWEs), the use of high concentration of potassium hydroxide (KOH) solution as the electrolyte opens up vulnerability to carbonation upon operation, which in turn shifts the pH level of the electrolyte towards a quasi-neutral value and decreases the electrolyte conductivity. Thus, this work aims to provide a thermodynamic perspective in understanding the functional stability of the state-of-the-art perovskite catalysts for OER – PBCO and BSCF – both in alkaline and in a quasi-neutral pH environment.

Therefore, this work correlates the observed electrocatalytic behavior with density-functional theory Pourbaix diagrams, which highlight the BSCF stability in alkaline environments but also cation dissolutions at pH 9 for both the perovskite oxides. In this respect, this work highlights the understanding of kinetic parameters at a specific pH is the key to explain their respective OER activities.

Experimental

For the preparation of the PBCO precursor solution, stoichiometric amounts of praseodymium oxide (Pr_6O_{11}, 99.9 %, Auer Remy) were dissolved in water and 5 %vol nitric acid (70 %, Alfa Aesar) at 80 °C, before mixing with stoichiometric amounts of barium carbonate (≥ 99.0 %, Sigma-Aldrich) and cobalt nitrate hexahydrate (99.9 %, Auer Remy), acetic acid (≥ 99.0 %, Fluka) in 25 %vol and N,N-Dimethylformamide (DMF, ≥ 99.8 %, Roth) in 45 %vol. The total metal concentration in solution was fixed to 0.1 M. For the preparation of BSCF refer to our previous work. [2]

Electrochemical study was done using rotating disk electrode voltammetry. All the electrochemical measurements were performed at the standard room temperature using a reversible hydrogen electrode (RHE) as the reference electrode in alkaline media. The membrane electrode assembly and testing were carried out by Proton Onsite; for details refer to our previous work. [2]

Phase stabilities were studied by means of *ab-initio* quantum mechanics simulations in the framework of density-functional theory (DFT) using the Quantum ESPRESSO package [3] to fully relax the two perovskite structures as well as all the competing phases, as described in the Materials Project database [4].

Results

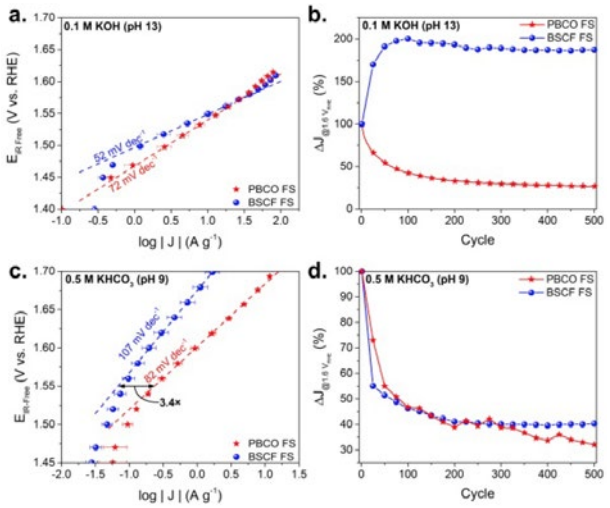

Figure 1. *Electrochemical study results comparing:*
a) Tafel slopes of OER activities and b) mass normalized current densities at every 25 cycles over 500 cycles between 1.0 and 1.6 VRHE of BSCF and PBCO in 0.1 M KOH.
The same comparisons are done in 0.5 M $KHCO_3$:
c) Tafel plots and d) potential cycle.

The comparison of OER activities of BSCF and PBCO in alkaline condition is shown in Figure 1a, whith both perovskites showing similar overpotentials at 10 A g^{-1} (1.55 and 1.54 V_{RHE}, respectively) and current densities at 1.55 V_{RHE} of 13.8 and 10.5 A g^{-1}, respectively. Nevertheless, the difference in their electrocatalytic performance in alkaline condition is evident from their contrasting behaviors during 500 cycles of potential steps between 1.0 and 1.6 V_{RHE} (Figure 1b), which effectively reveals their trend of functional stability. PBCO shows a decreasing trend losing about 74 % (from 33.4 to 8.9 A g^{-1} measured at 1.6 V_{RHE}) of its initial current density, while BSCF reveals an increasing trend, whith the current density amplified by two-folds at the end of the 500 cycles. In this essence, BSCF is revealed to be the most viable OER catalyst candidate at pH 13. Such superior OER performance of BSCF has recently been studied in depth, connecting its electronic configuration to its geometric structural changes. [2]

In a carbonated environment (0.5 M $KHCO_3$), where they function under a quasi-neutral condition, the activities of the selected perovskites are assessed again (Figure 1c). Notice that both perovskite oxides yield higher Tafel slopes under a quasi-neutral condition than compared to in pH 13, presumably

due to the poor proton acceptability in a neutral electrolyte [5]. Referring to Figure 1d both ,BSCF and PBCO, show a similar decreasing trend of current density (~ 60 % and -68 %, respectively, of its' initial activities) as the stability trend in the alkaline electrolyte. While they share a similar stability trend at pH 9, PBCO distinguishes itself as a more appealing OER catalyst due to its higher activity by a factor of 3.4 than that of BSCF. From these observations it is clear that a higher mass activity can initially be achieved by PBCO under a quasi-neutral pH.

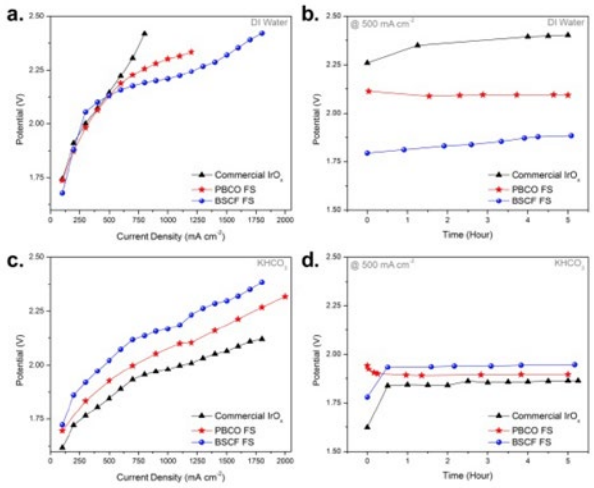

Figure 2. *Performance comparison of BSCF-FS, PBCO-FS, and IrO_2 anode OER catalyst in a technical alkaline exchange membrane water electrolyzer:*
a) Polarization curves and b) voltage vs. time at steady state current density of 500 mA cm^{-2} obtained for membrane electrode assemblies (MEAs) having BSCF-FS, PBCO-FS, and IrO_2 as anodic electrode under non-carbonated condition.
c) and d) present the same results under carbonated condition (1 %wt $KHCO_3$).

The adverse performance of BSCF relative to PBCO in pH 9, which is evidently contrary to that in pH 13, indicates that a dependence exists between the catalytic behavior and the pH level. As to unravel this relationship, DFT calculated Pourbaix diagrams are used as aid to understand the thermodynamic nature of the catalyst materials in aqueous electrochemical environments. According to the Pourbaix diagrams, BSCF in alkaline conditions above pH 12.6 is predicted to be meta-stable with a stability threshold of 0.5 eV $atom^{-1}$. Meanwhile, PBCO is found to be thermodynamically unstable in both pH regimes.

Yet, PBCO-FS shows an initially higher OER in $KHCO_3$ as compared to BSCF-FS. Here, one has to recognize that the dissolution mechanisms during OER are also certainly kinetic processes which obviously cannot be deduced from Pourbaix diagrams alone since they only describe the catalysts under equilibrium conditions. In this respect, it could be postulated that PBCO may exhibit a slower initial dissolution process than BSCF at pH 9 and, hence, may initially demonstrate a higher mass activity.

This difference in activity is once more confirmed by adopting these perovskites as anodic electrode materials in alkaline exchange membrane water electrolyzers (AEMWE). Figure 2 shows AEMWE performances for membrane electrode assemblies (MEA) having BSCF, PBCO, and commercial IrO_2 as anodic electrode.

From the above findings, important remarks are drawn relating thermodynamically stable phases of perovskite catalysts to their respective functional stability. First, the loss of initial activity during the stability test corresponds to the loss of perovskite structure as a result of A- and B-site cation dissolutions. This is evident from the stability tests of PBCO-FS in pH 9 and 13, and BSCF-FS in pH 9. Second, even though the cation dissolution is driven by thermodynamic forces, one should keep in mind that the dissolution is not an immediate process but occurs at a kinetically controlled rate.

Acknowledgement

The authors gratefully acknowledge the Swiss National Science Foundation through its Ambizione Program and the NCCR Marvel, CCEM through the project RENERG2, the Swiss Competence Center for Energy Research *Heat and Electricity Storage* (SCCER HaE) through the Commission for Technology and Innovation, Switzerland, and Paul Scherrer Institute for financial contributions to this work, respectively.

References

[1] E. Fabbri, A. Habereder, K. Waltar, R. Kötz, T.J. Schmidt, *Catal. Sci. Technol.* **4**, 3800–3821 (2014).
[2] E. Fabbri, M. Nachtegaal, T. Binninger, X. Cheng, B.J. Kim, J. Durst, F. Bozza, T. Graule, R. Schäublin, L. Wiles, M. Pertoso, N. Danilovic, K.E. Ayers, T.J. Schmidt, *Nat. Mater.* **16** (9), 925–931 (2017).
[3] P. Giannozzi, S. Baroni, N. Bonini, M. Calandra, R. Car, C. Cavazzoni, D. Ceresoli, G.L. Chiarotti, M. Cococcioni, I. Dabo, A. Dal Corso, S. de Gironcoli, S. Fabris, G. Fratesi, R. Gebauer, U. Gerstmann, C. Gougoussis, A. Kokalj, M. Lazzeri, L. Martin-Samos, N. Marzari, F. Mauri, R. Mazzarello, S. Paolini, A. Pasquarello, L. Paulatto, C. Sbraccia, S. Scandolo, G. Sclauzero, A.P. Seitsonen, A. Smogunov, P. Umari, R.M. Wentzcovitch, *J Phys-Condens Mat.* **21** (2009).
[4] A. Jain, S.P. Ong, G. Hautier, W. Chen, W.D. Richards, S. Dacek, S. Cholia, D. Gunter, D. Skinner, G. Ceder, K.A. Persson, *Appl. Mater.* **1** (2013).
[5] Y. Surendranath, M. Dinca, D.G. Nocera, *J. Am. Chem. Soc.* **131**, 2615–2620 (2009).

Correlating the local structure and electronic properties of nanoparticulate $Ni_xFe_{1-x}O$ with the oxygen evolution activity and stability via *operando* XAS

D.F. Abbott, E. Fabbri, M. Borlaf, F. Bozza, R. Schäublin, T. Graule, T.J. Schmidt
phone: +41 56 310 4323, e-mail: daniel.abbott@psi.ch

Mixed Ni-Fe metal oxides currently represent some of the most attractive anode catalysts for the electrochemical splitting of water due to their low overpotentials for the oxygen evolution reaction (OER) in alkaline electrolytes. Although nickel-based oxides have long been known to be highly active catalysts for the OER, the specific role of Fe on the electrocatalytic activity has only recently become the subject of intensive investigation and discussion. [1–3]

It is now generally accepted that the incorporation of Fe into the NiO structure is a critical component to achieving high OER activity and that even trace impurities in the electrolyte solution have profound effects on the measured electrochemical activity of «pure» NiO. [2] The role of Fe and its effects on the catalyst electronic and local structure, and ultimately the catalyst stability and electrochemical OER activity, is still widely debated. In particular, the effects of Fe on the structural stability of Ni(Fe)O have not yet been fully explored.

Here we demonstrate a practical and scalable flame-spray pyrolysis synthesis capable of producing highly crystalline Ni and Ni-Fe oxide ($Ni_{1-x}Fe_xO_y$) nanoparticles with high surface areas ($SA_{BET} \approx 20–40$ m^2/g). The research presented herein focuses on expanding the fundamental understanding of the influence of Fe on the OER behavior of Ni-Fe oxides with a particular emphasis on the electrochemical stability under OER conditions. The resulting *operando* XANES and EXAFS analyses of the Ni and K edge permits useful insight into the nature of the valence states and rearrangements in local structure that occur under operating conditions representative of alkaline water electrolysis. Combined with a broad range of *ex situ* physical characterization techniques, we then relate the structural, electronic, and morphological changes to the observed electrochemical OER activity and catalyst stability.

Experimental

$Ni_{1-x}Fe_xO$ samples were prepared using the liquid-feed flame spray pyrolysis method. An organic precursor solution was prepared by dissolving the appropriate transition metal salts (nickel(II) nitrate and/or iron(III) nitrate) in a solution of deionized water, acetic acid, and *N,N*-dimethylformamide. The solution was then fed and injected into an oxygen-acetylene flame, where it was combusted at high temperature. The resulting nanoparticulate products were collected on a paper filter.

The electrochemical activity was then measured in a standard 3-electrode cell using the rotating disk electrode (RDE) methodology. Chronoamperometric measurements are used to record the steady-state polarization of each catalyst within the range of 1.0 to 1.7 V_{RHE} in 0.1 M KOH. The current was recorded after allowing two minutes for stabilization. In addition, electrochemical stability measurements were conducted chronoamperometrically by stepping between 1.0 and 1.7 V_{RHE} and holding for 10 seconds at each potential over the course of 500 potential step cycles.

X-ray absorption spectra (Ni K edge) were measured in transmission mode at the SuperXAS beamline at the Swiss Light Source (SLS). The beamline energy was calibrated with Ni reference foil to the Ni K edge position at 8333 eV. The extended X-ray absorption fine structure (EXAFS) data were converted to the photoelectron wave vector *k* by assigning the photoelectron energy origin, E_0, corresponding to $k = 0$, to the first inflection point. The resulting $\chi(k)$ functions were weighted with k^2 to compensate for the dampening of the XAFS amplitude with increasing *k*. These $\chi(k)$ functions were Fourier transformed over 3–14 $Å^{-1}$.

Results

The electrochemical stability of NiO and $Ni_{70}Fe_{30}O$ under OER conditions was evaluated using the rotating disk electrode (RDE) methodology. The start-stop behaviour of an electrolyzer was simulated by stepping between a resting potential (1.0 V_{RHE}) and a potential well into the OER regime (1.7 V_{RHE}). As clearly seen in Figure 1a, there are no signs of catalyst degradation over the course of 500 potential step cycles. In fact, the normalized current increases significantly for the NiO sample, which can be attributed to the drastic increase in the electrochemically active surface area (ECSA) as evidenced by the growth of the Ni^{2+}/Ni^{3+} redox features (Figure 1b).

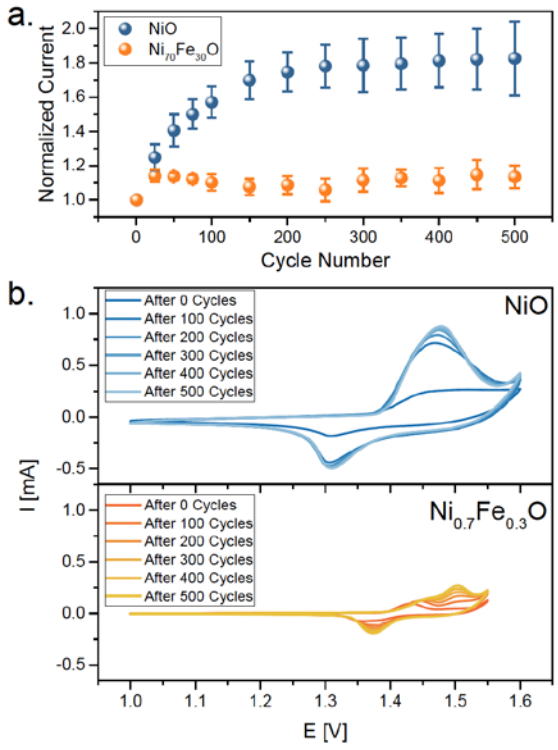

Figure 1. *Stability measurements for NiO and $Ni_{70}Fe_{30}O$ showing the normalized current measured at 1.7 V_{RHE}. a) Electrodes were stepped between 1.00 V and 1.70 V for 500 cycles; and b) the cyclic voltammograms recorded during the stability measurements in 0.1 M KOH.*

These redox features, however, are significantly muted for the $Ni_{70}Fe_{30}O$ sample. Consequently, it can be seen in Figure 1a that the increase in activity over the course of potential cycling for the Fe-containing sample is much less. However, despite the significant increase in ECSA, which is well known to be related to growth of hydrous $Ni(OH)_2$/NiOOH layers [4, 5], the OER activity of NiO measured during a standard polarization measurement is still considerably lower than that of $Ni_{70}Fe_{30}O$ (see Table 1). The aforementioned observations and the notably lower Tafel slope (see Table 1) seem to suggest that Fe increases the OER activity of NiO through a kinetic enhancement while inhibiting the ECSA increase typically gained through hydrous NiOOH layer growth.

Sample	SA_{BET} (m^2/g)	Tafel Slope (mV dec^{-1})	E at 10 A g_{ox}^{-1} (V)	J at 1.7 VRHE (A g_{ox}^{-1})
NiO	21	57.6 ± 0.9	1.606 ± 0.038	22.2 ± 0.2
$Ni_{70}Fe_{30}O$	37	40.9 ± 1.6	1.547 ± 0.002	198.0 ± 4.1

Table 1. *BET surface area and calculated electrochemical parameters from polarization measurements in 0.1 M KOH.*

In order to gain additional information regarding the electronic and local structure of Ni, each sample was investigated via *operando* X-ray absorption spectroscopy (XAS). Figure 2 shows the X-ray absorption near-edge structure (XANES) for the NiO and $Ni_{70}Fe_{30}O$ samples during a standard polarization measurement (1.0 to 1.55 V_{RHE}) in 0.1 M KOH. The shift in the XANES edge position as the applied electrochemical potential is increased indicates that Ni transitions from a 2+ oxidation state to $n \geq 3+$, which likely corresponds to the conversion of $Ni(OH)_2$ to NiOOH [4]. The lack of any shift in the Ni K edge for $Ni_{70}Fe_{30}O$, however, indicates that Fe helps to stabilize the Ni^{2+} and could suggest stabilization of the $Ni(OH)_2$ phase.

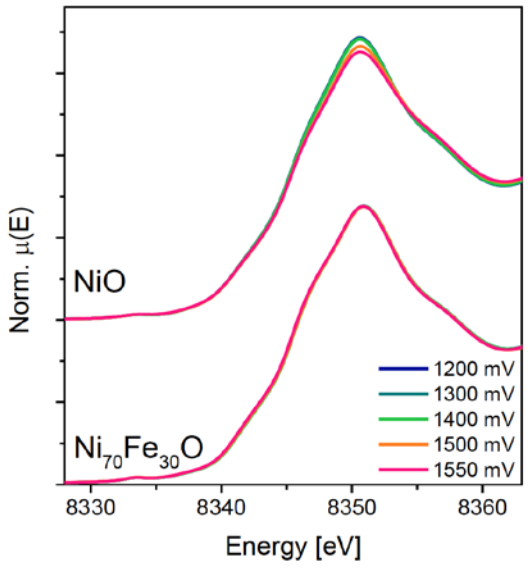

Figure 2. *XANES spectra at the Ni K-edge for NiO and $Ni_{70}Fe_{30}O$ recorded under potential control.*

The Fourier transformed extended X-ray absorption fine structure (FT-EXAFS) spectra for NiO and $Ni_{70}Fe_{30}O$ is shown in Figure 3. A drastic reduction in the first shell peak intensity between 1–2 Å indicates a significant modification of the Ni-O octahedra upon OER polarization in the NiO sample. In addition, a small modification in the Ni-Ni coordination shell can also be observed. This, however, is not the case for the $Ni_{70}Fe_{30}O$ sample. The lack of any observable change in the first or second coordination shells for this sample further indicates that Fe helps to stabilize the local structure upon OER polarization.

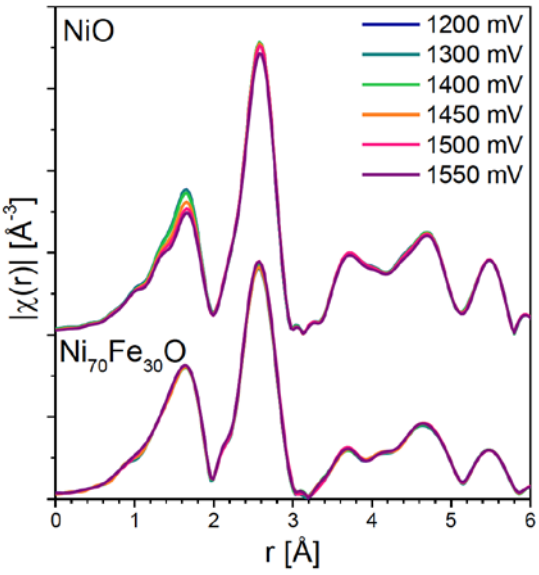

Figure 3. *FT-EXAFS spectra at the Ni K-edge for NiO and $Ni_{70}Fe_{30}O$ recorded under potential control.*

The current study helps to demonstrate that the intentional incorporation of Fe into the NiO structure not only provides an enhancement in the OER activity, but may also improve the structural stability of the oxide lattice by preventing the growth of hydrous NiOOH layers. Additional *operando* XAS measurements recorded during a potential-step stability protocol will help to further elucidate the relationship between structure and stability of Ni-Fe oxides.

Acknowledgement

The authors would like to acknowledge and thank the Competence Center Energy & Mobility (CCEM-CH, Project Renerg2), the Commission for Technology & Innovation Switzerland (CTI) and the Swiss Competence Center for Energy Research *Heat and Electricity Storage* (SCCER HaE) for their financial support.

References

[1] D. Friebel, M.W. Louie, M. Bajdich, K.E. Sanwald, Y. Cai, A.M. Wise, M-J. Cheng, D. Sokaras, T-C. Weng, R. Alonso-Mori, R.C. Davis, J.R. Bargar, J.K. Nørskov, A. Nilsson, A.T. Bell, *J. Am. Chem. Soc.* **137**, 1305–1313 (2015).

[2] L. Trotochaud, S.L. Young, J.K. Ranney, S.W. Boettcher, *J. Am. Chem. Soc.* **136**, 6744–6753 (2014).

[3] M. Görlin, P. Chernev, J. Ferreira de Araújo, T. Reier, S. Dresp, B. Paul, R. Krähnert, H. Dau, P. Strasser, *J. Am. Chem. Soc.* **138**, 5603–5614 (2016).

[4] M.E.G. Lyons, R.L. Doyle, I. Godwin, M. O'Brien, L. Russell, *J. Electrochem. Soc.* **159**, H932–H944 (2012).

[5] I.J. Godwin, M.E.G. Lyons, *Electrochem. Commun.* **32**, 39–42 (2013).

Investigating PEFC anode durability under fuel starvation conditions

S. Henning, R. Shimizu, J. Herranz, T.J. Schmidt
phone: +41 56 310 2125, e-mail: sebastian.henning@psi.ch

Hydrogen-powered polymer electrolyte fuel cells (PEFCs) are promising energy-conversion devices to make local emission-free transportation feasible.

Barriers towards commercialization include high costs for the Pt-based catalysts that accelerate the hydrogen oxidation (anode) and oxygen reduction (cathode) reactions to generate electricity. Cost reductions could be achieved when catalysts with higher durability are utilized, thereby allowing for lower Pt use at the PEFCs' beginning-of-life.

In this respect, catalysts at the anode side with greater stability in case of gross fuel starvation events are needed. Such events can be caused by blockage of hydrogen gas inlets in an anode flow field by liquid water under load and lead to an anode potential increase from the ≈ 0 V at which the hydrogen oxidation reaction typically takes place to ≥ 1.5 V [1]. At these potentials, significant corrosion of the carbon support in commercial Pt on carbon PEFC catalysts and a concomitant activity decrease have been reported [2].

Motivated by our previous study in which unsupported Pt_3Ni aerogel demonstrated remarkable corrosion stability as a PEFC cathode catalyst [3], in this work the applicability of the former material on the anode side was investigated.

Experimental

Pt_3Ni aerogel catalyst was synthesized according to the steps described in Reference [4] and a commercial Pt/C catalyst (47 %wt Pt, TKK, TEC10E50E) was used as a benchmark. Anodic catalyst layers (CLs) on Nafion XL-100 membrane (DuPont) with loadings of ≈ 0.05 mg_{Pt}/cm^2_{MEA} were prepared similar to the procedure in Reference [5].

Following preparation of membrane electrode assemblies (MEAs) using commercial gas diffusion electrodes (Johnson Matthey, 0.4 mg_{Pt}/cm^2_{geom} HISPEC 9100 Pt/HAS on Sigracet GDL 25 BC) and Sigracet GDL 25 BC gas diffusion layers on cathode and anode side, respectively, the MEAs were conditioned in a differential PEFC [5].

The gross fuel starvation was simulated by an accelerated stress test (AST) performed at 80 °C, 100 % RH, ambient pressure, cathode H_2 flow of 100 ml/min and anode N_2 flow of 100 ml/min. Under this condition, 250 potential cycles in a square wave voltammetry pattern between 0 and 1.5 V (with a holding time of 10 s at upper and lower potential limit) were applied.

Results

Figure 1 shows the beginning-of-life polarization curves of MEAs utilizing Pt_3Ni aerogel and Pt/C as anode catalysts, respectively. The great agreement of the data indicates that the performance of aerogel anode CLs is identical to the one of a commercial catalyst.

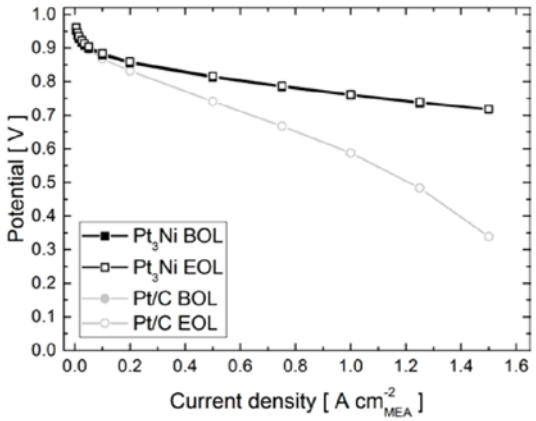

Figure 1. *Beginning- and end-of-life (BOL, EOL) polarization curves at 80 °C, 100 % RH in H_2/O_2 at 1.5 bar_{abs} for Pt_3Ni aerogel and Pt/C MEAs (anode loadings ≈ 0.05 mg_{Pt}/cm^2_{MEA}). Note that curves for Pt_3Ni aerogel at BOL, EOL and for Pt/C BOL are superimposed.*

Interestingly, the fuel cell starvation AST causes strong performance deterioration for the Pt/C system, whereas the aerogel MEA is not affected at all. To investigate the causes for this different durability behaviour, the evolution of electrochemical surface areas (ECSAs) of the anode catalysts throughout the AST was studied and is summarized in Figure 2. It becomes obvious that the I/E curve performance deterioration for Pt/C coincides with an ECSA reduction of ≈ 70 %. This decrease is ascribed to carbon corrosion in the AST's potential regime that can trigger Pt particle detachment and collapse of the CL structure as previous studies have demonstrated [2, 3].

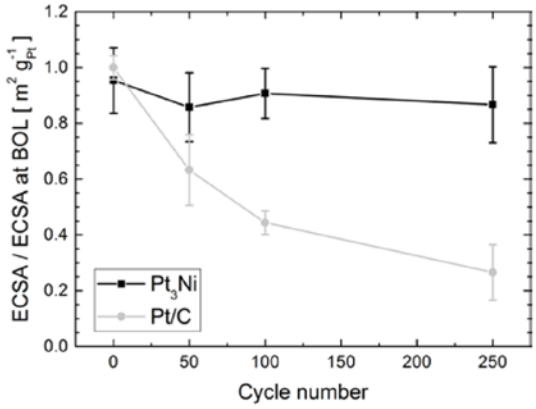

Figure 2. *Evolution of electrochemical surface areas (ECSAs) normalized to the respective beginning-of-life (BOL) values for Pt_3Ni aerogel and Pt/C anode CLs (loading ≈ 0.05 mg_{Pt}/cm^2_{MEA}) throughout the fuel starvation AST.*

Again in agreement with the constant cell performance displayed in Figure 1, Pt_3Ni aerogel shows a very minor ECSA loss

of ≈ 10 %, most likely due to the absence of a corrodible C-support.

Lastly, cross sections of the Pt/C anode CL at the end-of-life were cut by a focused ion beam and analysed by scanning electron microscopy (SEM). The SEM image in Figure 3A shows CL domains with almost no porosity, which could be an indication of the catalyst layer structure collapse mentioned above. Moreover, the CL thickness at EOL is ≈ 50 % lower than at BOL (not shown here), thereby further supporting this hypothesis.

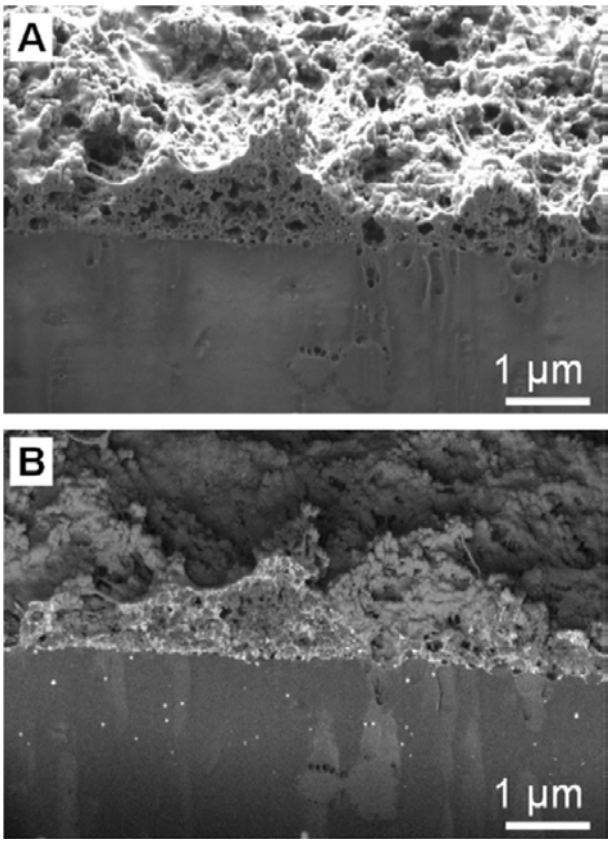

Figure 3. *End-of-life cross section scanning electron microscopy images for Pt/CB anode CLs captured with a secondary electron (A) and backscattered electron detector (B).*

Another interesting feature of degraded Pt/C CLs becomes visible upon analysing the image obtained with a backscattered electron detector (Figure 3B). On this image white spots corresponding to large Pt nanoparticles (up to 50 nm) are discernible in the membrane layer that point towards Pt dissolution (oxidation) and redeposition (reduction) as an additional degradation mechanism [6].

Ultimately, this work demonstrates that Pt_3Ni aerogel constitutes a promising PEFC anode catalyst material with vastly improved durability under fuel cell starvation conditions compared to a commercial Pt/C material. Future work will focus on further investigating the reasons behind the different stability of these two materials.

Acknowledgement

The authors thank Laura Kühn from the Chair of Physical Chemistry, Technische Universität Dresden, for synthesis of the Pt_3Ni aerogel catalyst that was used in this study. Financial support from SNF (20001E_151122/1) and DFG (EY 16/18-1) is greatly acknowledged.

References

[1] P. Rodriguez, T.J. Schmidt, «*Encyclopedia of Applied Electrochemistry*», Springer New York, New York, NY, 1606–1617 (2014).
[2] J. Speder, A. Zana, I. Spanos, J.J.K. Kirkensgaard, K. Mortensen, M. Hanzlik, M. Arenz, *J. Power Sources* **261**, 14–22 (2014).
[3] S. Henning, J. Herranz, H. Ishikawa, B.J. Kim, D. Abbott, L. Kühn, A. Eychmüller, T.J. Schmidt, *J. Electrochem. Soc.* **164**, F1136–F1141 (2017).
[4] S. Henning, L. Kühn, J. Herranz, J. Durst, T. Binninger, M. Nachtegaal, M. Werheid, W. Liu, M. Adam, S. Kaskel, A. Eychmüller, T.J. Schmidt, *J. Electrochem. Soc.* **163**, F998–F1003 (2016).
[5] S. Henning, H. Ishikawa, L. Kühn, J. Herranz, E. Müller, A. Eychmüller, T.J. Schmidt, *Angew. Chem. Int. Ed.* **56**, 10707–10710 (2017).
[6] Y. Shao-Horn, W.C. Sheng, S. Chen, P.J. Ferreira, E.F. Holby, D. Morgan, *Top. Catal.* **46**, 285–305. (2007).

Boosting Pt oxygen reduction reaction activity by tuning the oxide support

E. Fabbri, T.J. Schmidt
phone: +41 56 310 2795, e-mail: emiliana.fabbri@psi.ch

Durability is currently a challenging issue for polymer electrolyte fuel cells (PEFCs). At present, state-of-the-art PEFC cathode catalysts consist of Pt nanoparticles supported on high surface area carbon (Pt/C), which is very prone to oxidization at high potentials, causing loss of mass activity during start/stop events. [1] Doped SnO_2 is a very interesting support material for Pt electrocatalysts since it can combine conductivity, high surface area, and stability under PEFC cathodic operating conditions. Improved durability and, at times, higher oxygen reduction reaction (ORR) activity have been observed for Pt catalysts supported on doped SnO_2, compared to Pt/C. [2–4]

In this study, several dopants have been introduced into the SnO_2 lattice using thin-film model electrodes, in order to gain insights into the effect of the dopant element on the ORR activity of the supported Pt nano-catalysts. We can show that the ORR activity of the supported Pt nanoparticles depends significantly on the SnO_2 dopant element and, in the best case, can exceed that of Pt/C electrodes by more than a factor of 2.

Experimental

Doped SnO_2 thin films were deposited as described previously on glassy carbon substrates by magnetron sputtering. [5] For each dopant, the doping concentration was varied using metal chips incorporated into the Sn target. The electronic conductivity of the doped SnO_2 supports was analysed by a four-point probe method (FPP 5000 Veeco Instrument). 2 $\mu g_{PT}\,cm^{-2}$ was deposited onto the doped SnO_2 and onto a glassy carbon support as described previously [5], resulting in 2–10 nm interconnected Pt nanoparticles.

Electrochemical measurements were carried out at room temperature in a three-electrode glass cell using a Biologic VMP3 potentiostat. The Hg/Hg_2SO_4 reference electrode was calibrated vs. the reversible hydrogen electrode (RHE). Initially the electrodes were cycled 20 times at 50 $mV\,s^{-1}$ between 0.05 and 1.1 V_{RHE} in N_2-purged 0.1 M $HClO_4$ (SupraPure, Merck AG). The electrochemically active surface area (ECSA) was determined as described in Reference [6]. For the ORR experiments, polarization curves were recorded in O_2-saturated electrolyte in the cathodic scan direction at 5 $mV\,s^{-1}$ and 1600 rpm and reported after IR correction using impedance spectroscopy. Mass transport-corrected kinetic currents were derived from the ORR polarization curves using the Koutecky-Levich equation and normalized to the corresponding ECSA to obtain the specific kinetic ORR current (j_{spec}).

Results

Figure 1 shows the specific kinetic ORR current (j_{spec}) at 0.9 V_{RHE} for all the investigated samples (including Pt deposited on glassy carbon, GC/Pt) vs. the support conductivity. In case of Sb–SnO_2/Pt electrodes, the highest ORR activity is observed for the most conductive support, but there is not a linear trend between support conductivity and activity. Also for all the other samples no correlation between ORR activity and support conductivity does occur, and the highest activity is not observed for the most conductive support. Furthermore, it is possible to observe that the activity of Nb–SnO_2/Pt exceeds by more than a factor of 2 that of GC/Pt.

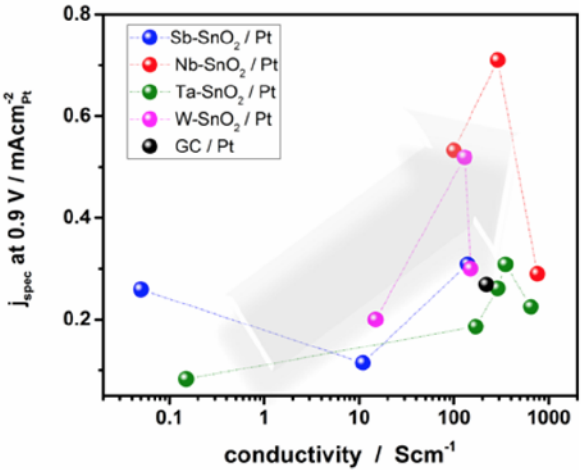

Figure 1. *Specific ORR activity at 0.9 V vs. RHE for the doped SnO_2/Pt electrodes and GC/Pt plotted as a function of the support conductivity.*

Figure 1 certainly suggests that the use of an oxide support with low electronic conductivity would lead to low ORR activity for the supported Pt nanoparticles, due to inefficient Pt electronic connectivity, and, thus, to low Pt utilization. Above a certain threshold value (approx. > 10 Scm^{-1}), however, support conductivity no longer determines ORR activity. Thus, other factors must influence the specific ORR activity of doped SnO_2/Pt electrodes. Metal-support interactions can play a substantial role in the ORR activity of Pt supported on oxides and should be further investigated in order to explain the significant differences in ORR activity observed in this study.

Acknowledgement

The authors thank Umicore GmbH & Co KG and the Competence Center for Energy and Mobility Switzerland (CCEM) for financial support within the project DuraCat.

References

[1] A. Rabis, P. Rodriguez, T.J. Schmidt, *ACS Catal.* **2**, 864–890 (2012).
[2] T. Binninger, R. Mohamed, A. Pătru, K. Waltar, E. Gericke, X. Tuaev, E. Fabbri, P. Levecque, A. Hoell, T.J. Schmidt, *Chem. Mater.* **29**, 2831–2843 (2017).
[3] K. Kakinuma, Y. Chino, Y. Senoo, M. Uchida, T. Kamino, H. Uchida, S. Deki, M. Watanabe, *Electrochim. Acta* **110**, 316–324 (2013).
[4] M. Yin, J. Xu, Q. Li, J. O. Jensen, Y. Huang, L.N. Cleemann, N.J. Bjerrum, W. Xing, *Appl. Catal. B* **144**, 112–120 (2013).
[5] A. Rabis, D. Kramer, E. Fabbri, M. Worsdale, R. Kötz, T. J. Schmidt, *J. Phys.Chem.C* **118**, 11292–11302 (2014).
[6] T. Binninger, E. Fabbri, R. Kötz, T.J. Schmidt, *J. Electrochem. Soc.* **161**, H121–H128 (2014).

Quantifying Pt-nanoparticle detachment and growth under PEFC-relevant potential cycling conditions through combined XAS and SAXS

J. Herranz, M. Povia, T. Binninger, M. Nachtegaal, T.J. Schmidt
phone: +41 56 310 5562, e-mail: juan.herranz@psi.ch

The demanding conditions in many catalyzed processes often lead to morphological and/or compositional changes of the catalytic materials, which can in terms cause a decrease of their operational efficiency. The carbon-supported platinum nanoparticle (Pt/C) catalysts used in polymer electrolyte fuel cell (PEFC) cathodes constitute an archetypical example of such issues, and their limited service life hinders the commercialization of this technology. [1] Post-mortem characterization of degraded Pt/C materials has allowed to differentiate two degradation mechanisms, [2] namely (i) dissolution of the Pt in smaller nanoparticles and subsequent re-deposition on larger ones upon operation within ≈0.6–1.0 V vs. the reversible hydrogen electrode (V_{RHE}); and (ii) carbon support corrosion and Pt nanoparticle detachment due to the high potentials (> 1.5 V_{RHE}) upon PEFC startup/shutdown.

This understanding should be extended to more complicated electrocatalyts like the Pt-based alloys envisaged for future PEFC cathodes. [1] In this context, *operando* characterization techniques capable of studying these materials under real operation conditions shall prove crucial. Specifically, X-ray absorption spectroscopy (XAS) can track changes in the composition, oxidation state and coordination environment, while small angle X-ray scattering (SAXS) provides information regarding the catalyst's morphology (i.e., particle size distribution and/or shape). Therefore, we have developed a setup to perform XAS and SAXS quasi-simultaneously and under electrochemical *operando* conditions. For probing this system, we studied two Pt/Cs with similar particle sizes but carbon supports with different graphitization extents, for which different corrosion resistances are expected.

Experimental

XAS and SAXS measurements were performed on Pt/C samples (with ≈1.5 mg_{Pt}/cm_{geom}^2) mounted in a custom-made electrochemical flow cell, [3] using 0.1 M $HClO_4$ at a flow rate of 50 µL min^{-1} as the electrolyte, and at a constant temperature of 60 °C. The catalysts of choice were 30 %wt Pt on conventional Vulcan or graphitized Black Pearls carbon blacks (Pt/C vs. Pt/C_{graph}, respectively; Tanaka Kikinzoku Kogyo Co.). Each electrode was conditioned by recording 25 cyclic voltammograms (CVs, 50 mV/s) between 0.05 and 1.2 V_{RHE}. The degradation protocol consisted of 250 CVs between 0.5 and 1.5 V_{RHE} (50 mV/s). CVs (10 mV/s, 0.05–1.0 V_{RHE}), XAS and SAXS were acquired just after conditioning and after 25, 50, 100 and 250 potential cycles; during the latter spectroscopic/scattering measurements, the cell potential was held at 0.45 V_{RHE}. SAXS were systematically acquired at photon energies of 11.3 and 11.454 keV, while XAS were recorded in the 11.4–12.46 keV range.

Results

Figure 1 displays the evolution of the average diameter of the Pt-nanoparticles in the Pt/C samples (derived from the fitting of the SAXS to a log-normal distribution) as a function of the cycle number in the degradation protocol. Both catalysts feature similar nanoparticle growth trends, indicating that the latter only depends on the particles' initial size, as it is expected from the growth mechanism discussed above. [2] On the other hand, upon monitoring the changes in the height of the XAS absorption edge (proportional to the Pt-concentration in the catalyst layer), significant differences are observed between Pt/C and Pt/C_{graph} (cf. Figure 2). Specifically, the former lost ≈5 % of its initial Pt-content, whereas no significant Pt-loss was observed for Pt/C_{graph} – a result consistent with the improved corrosion resistance expected for the catalyst with a graphitized support.

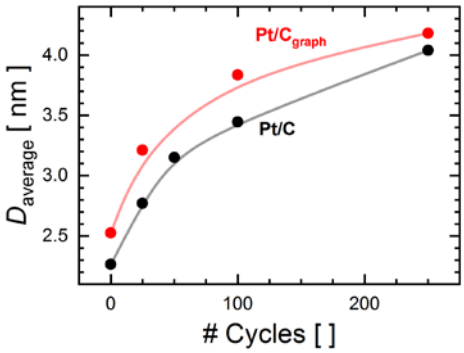

Figure 1. *Evolution of the average nanoparticle diameter (derived from fitting of the SAXS) with the electrochemical cycle number (0.5–1.5 V_{RHE}, 50 mV/s), for 30 %wt Pt on Vulcan or graphitized Black Pearls carbon blacks (Pt/C vs. Pt/C_{graph}).*

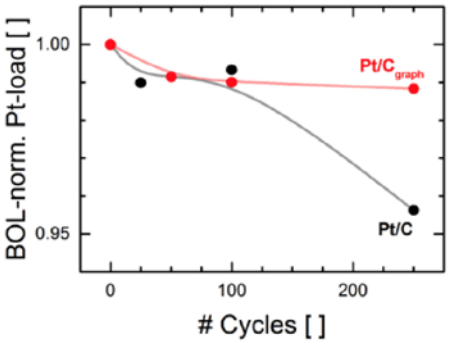

Figure 2. *Electrochemical cycle-dependent loss of Pt in the flow cell catalyst layer, derived from the height of the XAS absorption edge, and normalized vs. the beginning-of-life (BOL) value.*

In summary, our results agree with previous experimental reports on Pt/C materials, and thus validate the SAXS and XAS setup. Future work shall therefore be devoted to extend its use to other (electro)catalysts.

References

[1] O. Gröger, H.A. Gasteiger, J.-P. Suchsland, *J. Electrochem. Soc.* **162** (14), A2605–A2622 (2015).
[2] Y. Shao-Horn, W.C. Sheng, S. Chen, P.J. Ferreira, E.F. Holby, D. Morgan, *Top. Catal.* **46**, 285–305 (2007).
[3] T. Binninger, E. Fabbri, A. Pătru, M. Garganourakis, J. Han, D.F. Abbott, O. Sereda, R. Kötz, A. Menzel, M. Nachtegaal, T.J. Schmidt, *J. Electrochem. Soc.* **163** (10), H913–H920 (2016).

Impact of the pyrolysis temperature on the performance of Fe-based oxygen reduction catalyst for polymer electrolyte fuel cell cathodes

K. Ebner, J. Herranz, B. Kim, T.J. Schmidt
phone: +41 56 310 3977, e-mail: kathrin.ebner@psi.ch

Due to their high power-to-weight ratio, emission-free operation, and fast fueling and start up time, polymer electrolyte fuel cells (PEFCs) are excellently suited energy conversion devices for the electric-automotive sector [1]. In order to further improve the economic feasibility of such systems, efforts have been made to reduce the excessive cost of the cells' cathode catalyst by substituting state-of-the-art Pt-catalysts with materials based on abundant metals like iron [2]. Certain examples of such non-noble metal catalysts (NNMCs) have been shown to be a viable replacement in terms of initial performance, featuring activities towards the oxygen reduction reaction (ORR) that are commensurate with those observed for Pt-catalysts [3, 4].

Despite this outstanding initial performance, NNMCs' widespread application is hindered by the catalysts' instability. While the reason for this remains poorly understood, it is believed to be partially caused by the materials' inhomogeneous composition, which not only consists of active sites (typically pictured as a four-fold N-coordinated Fe(II)-ion) but also of inactive side phases (e.g. Fe-carbides or -oxides). The latter could catalyze side reactions such as hydrogen peroxide decomposition to aggressive hydroxyl radicals and possibly contribute to the depletion of ORR-active sites and membrane poisoning [5].

To gain insight into the contribution of composition-related deactivation to the overall instability, a refined synthesis approach which offers precise composition control is imperative. With this motivation, we presented a pyrolysis-based synthesis pathway for the preparation of Fe-based NNMCs in which polyacrylonitrile is used as C- and N-precursor, a Fe-phenanthroline complex as the metal source, and sodium carbonate, a thermally decomposable compound, as a pore inducing agent [6]. The latter was chosen to offer porosity control while going hand in hand with the need for inexpensive catalyst production (as compared to approaches based on the use of costly metalorganic frameworks [4, 7, 8]).

In order to elucidate the role of pyrolysis temperature in the composition and the electrochemical performance of the resulting catalysts, this crucial synthesis parameter is systematically modified in this work. Consecutively, the obtained materials are studied by the means of electrochemical activity measurements through rotating disc electrode (RDE) voltammetry as well as surface- and bulk-sensitive characterization techniques (N_2-physisorption, X-ray photoelectron and absorption spectroscopies). Our work sheds light on the correlation of synthesis parameters, the catalysts' composition, and their electrochemical activity, thus enabling improvement and fine-tuning of these crucial features and building the foundation for future durability and degradation studies.

Experimental

Sodium carbonate, the so called pore inducing agent (PIA), and polyacrylonitrile (C- and N-precursor) in a weight ratio of 2:1 are stirred in separate containers in dimethylformamide overnight at 80 °C. Subsequently, they are mixed, stirred for another hour and then the amount of iron(II)phenanthroline complex needed for an initial iron content of 0.1 %wt Fe (i.e. on the basis of all precursors' masses) is added to the mixture. The latter complex is prepared beforehand in 10 mL dimethylformamide mixing iron acetate and 1,10-phenanthroline in a molar ratio of 1:5. After full evaporation of the solvent, the precursors are ball milled prior to a heat treatment step under nitrogen environment at a set temperature for 30 minutes. The product is then washed overnight in 0.1 M perchloric acid, filtered (filter size: 0.45 µm) and water-washed. The resulting dry powder is submitted to a second heat treatment step in 5 % hydrogen in argon for 60 min at 950 °C.

The electrochemical activity towards the oxygen reduction reaction of the prepared catalysts is measured by RDE voltammetry. A reversible hydrogen electrode (RHE) is used as the reference electrode, while a gold mesh serves as the counter electrode. The working electrode is prepared by drop casting a catalyst ink with an ionomer-to-catalyst mass ratio of 0.3 on a 5 mm diameter, mirror polished glassy carbon, as to reach a catalyst loading of 500 µg cm^{-2}. Measurements are performed in nitrogen/oxygen saturated 0.1 M perchloric acid rotating at 1600 rpm with a scan rate of 5 mV s^{-1} at room temperature. The kinetically controlled ORR-activity at an iR-corrected potential of 0.8 V vs. RHE is then calculated according to Equation (4) in Reference [9].

To determine their surface area, the samples are out-gassed overnight at 200 °C and the N_2-adsorption and -desorption isotherms (at 77 K) are measured for relative pressures ranging from 0.03 to 1. The BET-equation is applied for the range $0.03 \leq p/p0 \leq 0.11$ to estimate the total surface area.

X-ray photoelectron spectroscopy (XPS) with an Al Kα source was the method of choice for resolving the elemental composition of the catalysts' surface. Calibration of the obtained spectra is performed with the C1s-peak at 284.6 eV.

For imaging the materials, transmission electron microscopy (TEM) is employed (TECNAI F30 operated at 300 kV).

Bulk characterization of the material with X-ray absorption spectroscopy is carried out at Swiss Light Source's SuperXAS beamline. Measurements are performed in the range of -80 eV to +700 eV with respect to the iron K-edge (7112 eV).

Results

In Figure 1, changes in catalytic activity, surface N-content and total surface area with the first heat treatment temperature are depicted. As deduced from this Figure, the catalytic activity is strongly influenced by the first heat treatment temperature, whereby the maximum activity is reached at 750 °C. While the surface area increases with increasing temperature owing to a higher degree of decomposition of the PIA, the surface N-content decreases. This is likely due to a loss of nitrogen during the pyrolysis of polyacrylonitrile (e.g. in the form of NH_3 or

HCN) which becomes more extensive when the temperature is increased [10, 11]. Thus, the comparison with the trend in catalytic activity strongly suggests that microporosity and surface N-content have a combined effect on the catalysts' activity possibly along with other factors as the catalysts' final iron content.

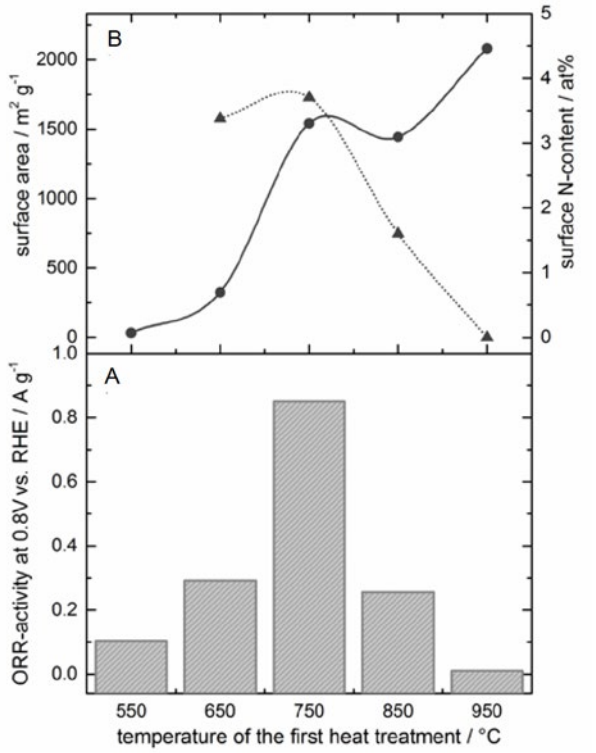

Figure 1. *Effect of the first heat treatment temperature on*
A) the catalysts' ORR-activity at 0.8 V vs. RHE (derived from RDE voltammetry measurements and
B) their surface area (from N_2-sorption measurements, left-hand Y-axis) and surface N-content (from XPS, right-hand Y-axis).

Furthermore, TEM was used to further investigate the NNMCs' composition, which turned out to be strongly dependant on the first heat treatment temperature: while in the TEM image of the catalyst treated at 750 °C iron side phases are clearly detectable (Figure 2, left) these are not observed upon inspection of multiple locations in the sample treated at 650 °C (right).

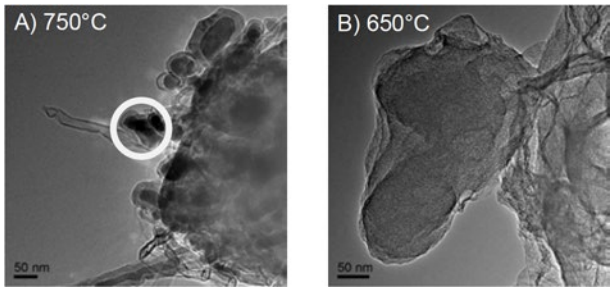

Figure 2. *TEM images of catalysts prepared using a first heat treatment temperature of 750 °C (A), or 650 °C (B) respectively. For a treatment at higher temperature numerous Fe-based side phases (with a darker contrast, example highlighted) are detectable, whereas no side phases are observed for the sample treated at lower temperature.*

To verify these results with a bulk technique, X-ray absorption spectroscopy was employed. The Fourier-transformed spectra derived from these measurements (not shown here) indicate that Fe-Fe scattering contributions attributed to the side phases are only detectable for the 750 °C catalyst, whereas the 650 °C catalyst only displays features attributed to Fe-N scattering, thus confirming the hypotheses on the catalysts' compositions derived from the TEM images.

The data reported show a strong correlation between the first heat treatment temperature and the catalytic performance and surface properties of the resulting catalyst materials. XPS- and BET-results indicate that, while the surface area increases with increasing heat treatment temperature, the surface N-content decreases. Therefore, none of these parameters seems to be the sole factor determining electrochemical activity, which reaches the maximum when treated at 750 °C. More likely, there are combined effects of surface N-content and porosity and presumably other parameters on the activity. Moreover, the heat treatment temperature plays an important role in the formation of inorganic side phases which in turn could take part in certain deactivation mechanisms of Fe-based non-noble metal catalysts.

Ultimately, the information obtained during this study will contribute to enabling a controlled and well-defined synthesis, and opens up the doors to preparing non-noble metal catalysts with fine-tuned properties and composition building the foundation for future durability studies.

Acknowledgement

Financial support by the Swiss National Science Foundation (SNF) through the Ambizione Energy grant PZENP2_173632 is greatly acknowledged by the authors.

References

[1] A. Alaswad, A. Baroutaji, H. Achour, J. Carton, A. Al Makky, A.G. Olabi, *Int. J. Hydrogen. Energy.* **41** (37), 16499–16508 (2016).
[2] F. Jaouen, «*Non-Noble Metal Fuel Cell Catalysts*», Éditions Wiley, 29–118 (2014). ISBN: 978-3-527-33324-0.
[3] M. Shao, Q. Chang, J.-P.Dodelet, R. Chenitz, *Chem. Rev.* **116** (6), 3594–3657 (2016).
[4] E. Proietti, F. Jaouen, M. Lefevre, N. Larouche, J. Tian, J. Herranz, J.-P. Dodelet, *Nat. Comm.* **2**, 1–6 (2011).
[5] D. Banham, S. Ye, K. Pei, J. Ozaki, T. Kishimoto, Y. Imashiro, *J. Power Sources* **285**, 334–348 (2015).
[6] J. Herranz, T.J. Schmidt, *Annual Report 2016 – Electrochemistry Laboratory*, 83–84 (2016).
[7] K. Strickland, E. Miner, Q. Jia, U. Tylus, N. Ramaswamy, W. Liang, M.-T. Sourgrati, F. Jaouen, S. Mukerjee, *Nat. Commun.* **6**, 7343 (2015).
[8] V. Goellner, C. Baldizzone, A. Schuppert, M.T. Sougrati, K. Mayrhofer, F. Jaouen, *Phys. Chem. Chem. Phys.* **16** (34), 18454–62 (2014).
[9] U.I. Kramm, J. Herranz, N. Larouche, T.M. Arruda, M. Lefèvre, F. Jaouen, P. Bodgdanoff, S. Fiechter, I. Abs-Wurmbach, S. Mukerjee, J.-P. Dodelet, *Phys. Chem. Chem. Phys.* **14** (33), 11673–11688 (2012).
[10] W.J. Burlant, J.L. Parsons, *J. Polym. Sci.* **22** (101), 249–256 (1956).
[11] N. Grassie, R. McGuchan, *Eur. Polym. J.* **6** (9), 1277–1291 (1970).

A combined XAS and SAXS setup for the *operando* study of carbon supported Pt nanoparticle catalysts

M. Povia, J. Herranz, T. Binninger, M. Nachtegaal, T.J. Schmidt
phone: +41 56 310 5232, e-mail: mauro.povia@psi.ch

Carbon supported Pt nanoparticle (Pt/C) catalysts are the main component of the anode and cathode electrodes in polymer electrolyte fuel cells (PEFCs). These materials are known to suffer from degradation upon extended PEFC operation and startup-shutdown, jeopardizing the device's service life and the technology's market penetration. [1] While the use of *ex situ*, post-mortem characterization tools has led to a good understanding of the mechanisms causing this degradation, *operando* techniques can provide further insight on these processes, especially when tackling more complex systems like the multi-metallic, Pt-based alloy catalysts implemented in state-of-the-art PEFCs.

With this motivation, we have developed a new setup (at the Swiss Light Source's SuperXAS beamline) to perform X-ray absorption spectroscopy (XAS) and small angle X-ray scattering (SAXS) measurements quasi-simultaneously and under electrochemically-relevant *operando* conditions. The choice to combine these two specific techniques is based on SAXS's capabilities to provide information about the morphology (i.e., particle size distribution, average diameter and specific surface area) of samples within the nanometer scale, while with XAS we can monitor changes in the oxidation state, chemical composition and coordination environment.

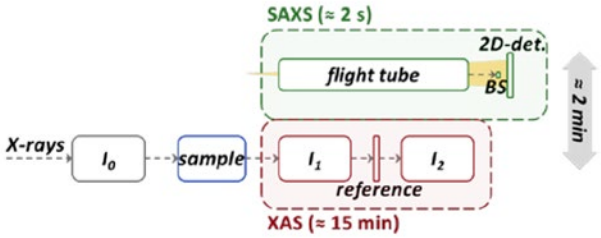

Figure 1. *Scheme of the combined XAS and SAXS setup, where «I_0», «I_1» and «I_2» refer to the ion chambers used to measure the intensity of the incident beam, and after the sample of interest and the reference used for energy calibration, respectively, and «BS» is the beam stopper needed to protect the 2D-detector («2D-det») used in the SAXS measurements. Note that the parts of the setup specific to SAXS and XAS (dashed boxes) are mounted on a common, laterally movable platform that allows transitioning among techniques in ≈ 2 minutes.*

Figure 1 shows a schematic representation of the setup, whereby the first ion chamber measures the intensity of the incoming beam during XAS and SAXS data acquisition (I_0). The adjacent «sample» box represents the electrochemical flow cell designed by Binninger *et al.*, in which the sample of interest is submitted to electrochemical protocols. [2] Next, the components in the red and green boxes refer to the ion chambers (I_1, I_2) and reference sample needed for XAS measurements, and to the flight tube, beam stopper («BS») and 2D-detector required for SAXS, respectively; these are placed on a mechanical platform that allows transitioning among techniques in less than two minutes. Unlike previous setups combining both techniques presented in the literature, [3] this configuration includes a reference sample (cf. «reference» in Figure 1) that allows for a precise energy calibration of the XAS measurement, crucial to extract precise information in the vicinity of the absorption edge (providing information, e.g., about to the sample's oxidation state). To test the validity of the system, we chose to use it to study the well-understood electrochemical degradation of Pt/C under potential cycling conditions relevant to the application of this material in PEFC cathodes.

Experimental

Electrochemical experiments in a flow cell at room temperature were prepared and conducted following the procedures developed by Binninger *et al.* [2] The catalyst material for working electrode fabrication was 30 %wt Pt on graphitized Black Pearls carbon black (Pt/BP-g, Tanaka Kikinzoku Kogyo Co). The electrolyte was 0.1 M $HClO_4$ in water. After assembly, the flow cell was connected to a potentiostat (BioLogic Science Instruments), and the Pt/C electrode was conditioned by recording 25 cyclic voltammograms (CVs, at 50 mV/s) between 0.05 and 1.2 V vs. the reversible hydrogen electrode (RHE). The subsequent degradation protocol consisted of performing CVs between 0.5 and 1.5 V vs. RHE at 50 mV/s. Before beginning the degradation protocol and after 25, 50, 100 and 250 degradation cycles, CVs were recorded in the potential window 0.05–1.0 V vs. RHE (at 10 mV s^{-1}), and SAXS and XAS measurements were performed holding the potential at 0.45 V vs. RHE (whereby Pt should remain in the reduced state). SAXS data were acquired at two different X-ray photon energies (E1 = 11.3 keV and E2 = 11.454 keV) in order to extract Pt Anomalous SAXS (A-SAXS) profiles which were analysed with the SASFit software. [4]

XAS spectra were acquired in the X-ray photon energy range of 11.4 to 12.46 keV, and analysed using the Demeter software package. [5] Following normalization of the XAS spectra, the corresponding Fourier transforms (Figure 3) were fitted in the k-range of 1.3 to 3.1 $Å^{-1}$ using a wave amplitude of 0.726 and one Pt-Pt shell model.

Results

Figure 2 shows the energy-dependent SAXS curves recorded after electrochemically conditioning the Pt/BP-g sample. The difference between the two curves, represented by the circles, is the A-SAXS profile, which is only proportional to the scattering contribution of the Pt nanoparticles. These A-SAXS curves were fitted by a least square method using a log-normal distribution of the nanoparticle radius (see red line in Figure 2). The particle size distributions derived from these fits (not shown) were used to derive the average particles dimeter (<D>).

Figure 3 displays the progressive increase of <D> with the number of electrochemical cycles in the degradation protocol, caused by the dissolution of smaller Pt nanoparticles and re-deposition onto larger ones (i.e., so-called electrochemical Ostwald ripening) occurring upon Pt-oxidation and -reduc-

tion. [1, 6] Moreover, the height of the XAS absorption jump (proportional to the Pt-concentration in the electrode) remained constant in the course of the degradation experiment (not shown) – an observation consistent with the negligible detachment of Pt-nanoparticles from the carbon support surface, in terms caused by the corrosion resistance of the graphitized carbon black used in this experiment.

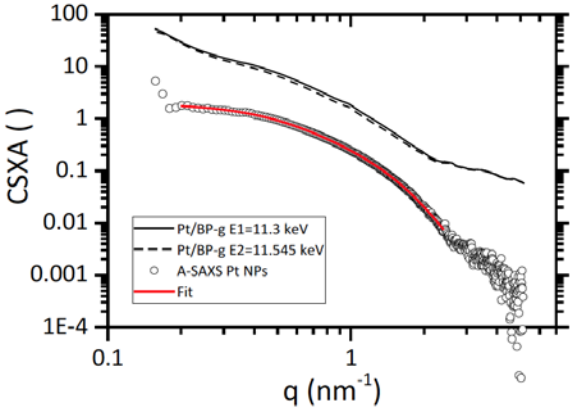

Figure 2. *SAXS curves measured at 11.300 or 11.545 keV (solid vs. dashed black lines, respectively) just after electrode conditioning, along with the corresponding difference (represented by hollow circles) and least-square fit (solid red line) to a log-normal distribution.*

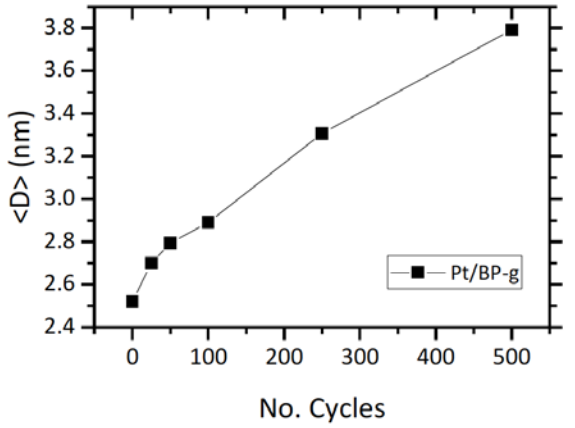

Figure 3. *Change in the nanoparticle average diameter (<D>, derived from the fitting of the A-SAXS scattering curves to a log-normal distribution) with the number of electrochemical degradation cycles (0.5–1.5 V vs. RHE at 50 mV/s in 0.1 M $HClO_4$ at room temperature).*

Finally, to illustrate the complementing information that can be derived from both techniques, Figure 4 displays the relation between the average nanoparticle diameter values derived from the SAXS results and the Pt-Pt bond distance estimated on the basis of the XAS data. These results excellently match the correlation among both variables reported by Lei *et al.* [7] (who used transmission electron microscopy to estimate <D>), which is included in Figure 4 for comparison.

In summary, this study portraits the applicability of a novel, combined XAS and SAXS setup to study time-dependent processes implying simultaneous changes in the composition and morphology of nanoparticles. Specifically, the results obtained for electrochemically-degraded Pt/C are in excellent agreement with previous reports regarding this material, and confirm the validity of our experimental approach.

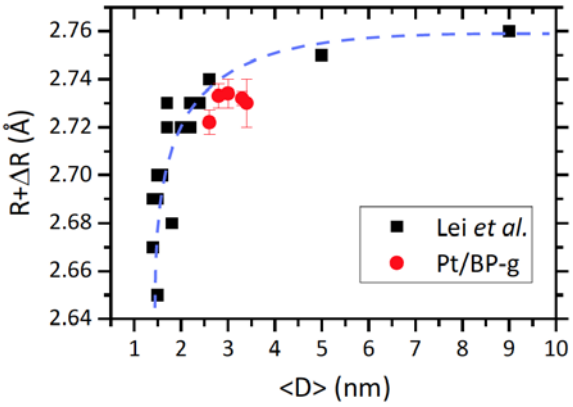

Figure 4. *Change in the Pt-Pt 1st shell bonding distance (R + ΔR) as a function of the Pt-nanoparticles' average diameter (<D>), as derived from the XAS and SAXS data obtained throughout the electrochemical degradation experiment. For comparison, the data reported by Lei et al. [7] (who estimated <D> using transmission electron microscopy) is also included. Note that the dashed line is a mere guide to the eye.*

Acknowledgement

Technical support from Mr. Christian Marmy, Mr. Urs Vogelsang and Mr. Patric Ascher is greatly acknowledged. We also want to thank Dr. Ana Diaz and Dr. Joachim Kohlbrecher for their support with the SAXS data analysis.

References

[1] P.J Ferreira, G.J. la O', Y. Shao-Horn, D. Morgan, R. Makharia, S. Kocha, H.A. Gasteiger, *J. Electrochem. Soc,* **152**, A2256–A2271 (2005).
[2] T. Binninger, E. Fabbri, A. Pătru, M. Garganourakis, J. Han, D.F. Abbott,O. Sereda, R. Kötz, A. Menzel, M. Nachtegaal, *J. Electrochem. Soc* **163**, H913–H920 (2016).
[3] H.G. Haubold, X.H. Wang, H. Jungbluth, G. Goerigk, W. Schilling, *J. Mol. Struct.* **383**, 283–289 (1996).
[4] I. Breßler, J. Kohlbrecher, A.F. Thünemann, *J. Appl. Crystallogr.* **48**, 1587–1598 (2015).
[5] B. Ravel, B. Newville, *J. Synchrotron Radiat.* **12**, 537–541 (2005).
[6] J. Tillier, T. Binninger, M. Garganourakis, A. Pătru, A.E. Fabbri, T.J. Schmidt, O. Sereda, *J. Electrochem. Soc.* **163**, H913–H920 (2016).
[7] Y. Lei, S. Lee, S.K.B. Low, C.L. Marshall, J.W. Elam, *ACS Catal.* **6**, 3457–3460 (2016).

THE ELECTROCHEMISTRY LABORATORY

Facts & Figures

STRUCTURE 2017

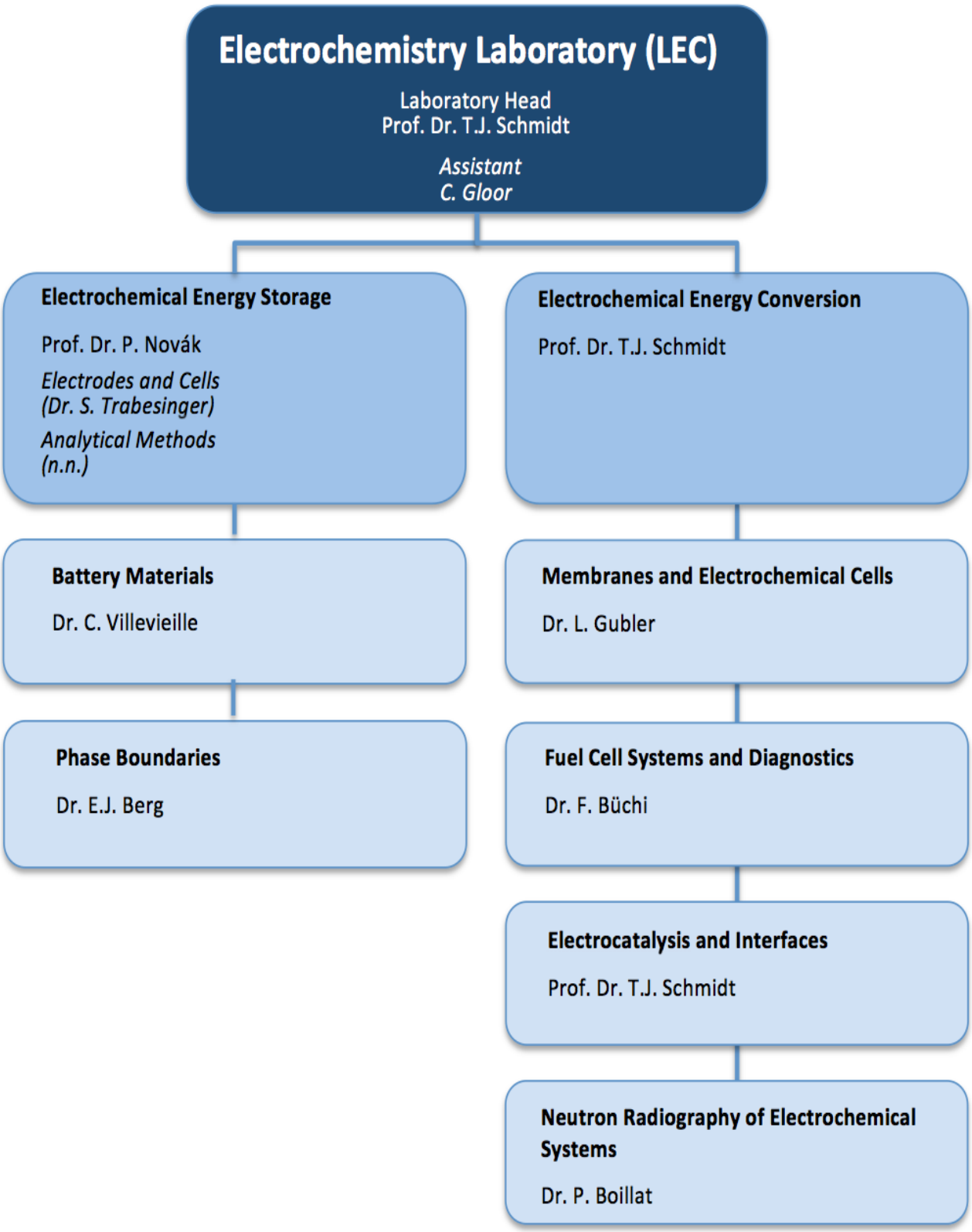

PERSONNEL 2017

Staff

Dr. Daniel ABBOTT (Post Doctoral Researcher)
Martin AMMANN (Technician)
Dr. Erik J. BERG (Group Leader)
Dr. Juliette BILLAUD BOUVILLE (Post Doctoral Researcher)
Dr. Tobias BINNINGER (Scientist)
Dr. Pierre BOILLAT (Group Leader)
Dr. Christoph BOLLI (Post Doctoral Researcher)
Dr. Felix BÜCHI (Group Leader)
Dr. Xi CHENG (Post Doctoral Researcher)
Dr. Magali COCHET (Scientist)
Dr. Joanna CONDER (Scientist)
Dr. Benjamin DECOOPMAN (Post Doctoral Researcher)
Dr. Mario EL KAZZI (Scientist)
Dr. Jens ELLER (Scientist)
Dr. Emiliana FABBRI (Scientist)
Cordelia GLOOR (Assistant)
Thomas GLOOR (Technician)
Dr. Lorenz GUBLER (Group Leader)
Dr. Aurélie GUÉGUEN (Scientist)
Dr. Juan HERRANZ SALANER (Scientist)
Dr. Fabian JESCHULL (Post Doctoral Researcher)
Christoph JUNKER (Technician)
Hermann KAISER (Technician)
Dr. Sreeyuth LAL (Post Doctoral Researcher)
Dr. Adrien LAMIBRAC (Post Doctoral Researcher)
Michelle LOCHER (Technician)
Dr. Elena MARELLI (Post Doctoral Researcher)
Dr. Cyril MARINO (Scientist)
Christian MARMY (Technician)
Prof. Dr. Petr NOVÁK (Section Head)
Dr. Anastasia A. PERMYAKOVA (Post Doctoral Researcher)
Dr. Tiphaine POUX (Post Doctoral Researcher)
Dr. Alexandra PĂTRU (Scientist)
Christian PETER (Engineer)
Dr. Rosa ROBERT SANCHEZ (Scientist)
Florian RUNTSCH (Engineer)
Dr. Sébastien SALLARD (Scientist)
Dirk SCHEUBLE (Engineer)
Prof. Dr. Thomas J. SCHMIDT (Laboratory Head)
Dr. Yuri SURACE (Post Doctoral Researcher)
Dr. Sigita TRABESINGER-URBONAITE (Project Leader)
Stephan TSCHUMI (Engineer)
Dr. Bing SUN (Post Doctoral Researcher)
Dr. Claire VILLEVIEILLE (Group Leader)
Dr. Laura VITOUX (Post Doctoral Researcher)

PhD Students

Ugljesa BABIC
Kathrin EBNER
Giulio FERRARESI
Eibar Joel FLORES CEDEÑO
Jonathan HALTER
Sebastian HENNING
Adrian HEINRITZ
Laura HÖLTSCHI
Baejung KIM
Paul KITZ
Daniela LEANZA
Maria Victoria MANZI OREZZOLI
Marta MIROLO
Adrian MULARCZYK
Olga NIBEL
Fabio OLDENBURG
Mauro POVIA
Bernhard PRIBYL
Tomasz ROJEK
Simon SCHNEIDER
Tobias SCHULER
Maximilian SCHUSTER
Muriel SIEGWART
Michel SUERMANN
Susan TAYLOR
Simon TSCHUPP
Xiaohan WU
Hong XU
Mateusz ZLOBINSKI

The Electrochemistry Laboratory, December 2016.

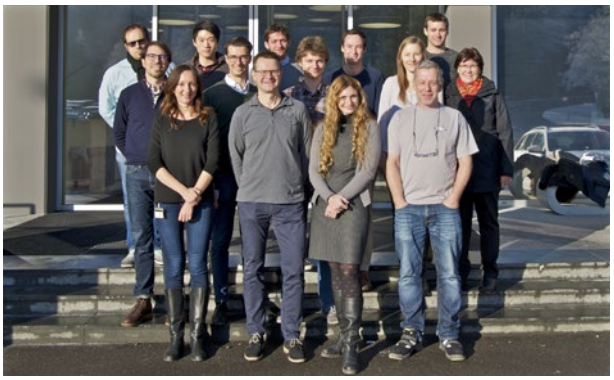

Electrocatalysis and Interfaces Group, December 2017.

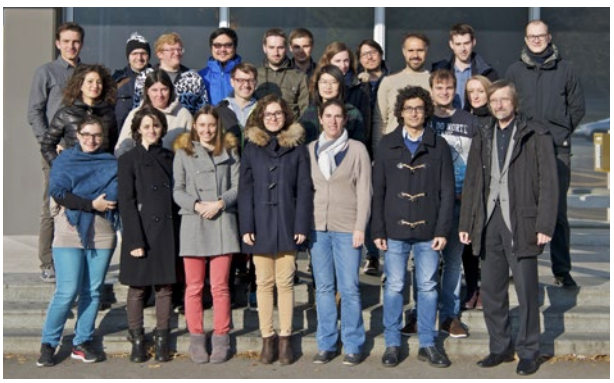

Energy Storage Section, December 2017.

Fuel Cells Systems and Diagnostics Group, December 2017.

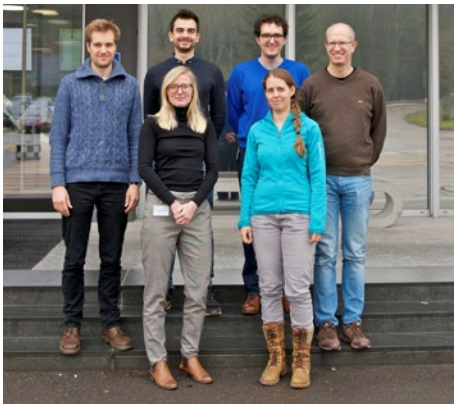

Membranes and Electrochemical Cells Group, December 2017.

Neutron Radiography of Electrochemical Systems Group, December 2016.

DISSERTATIONS 2017

Simon A. Tschupp

Model catalysts fabricated via interference lithography and their electrochemical characterization

Ph.D. Thesis No. 24293, ETH Zürich, April 2017.

Examiners: Prof. Dr. T.J. Schmidt, PSI Villigen/ETH Zürich
Prof. Dr. J.A. van Bokhoven, PSI Villigen/ETH Zürich
Dr. J. Herranz, PSI Villigen
Dr. Y. Ekinci, PSI Villigen

Michel Suermann

Pressurized polymer electrolyte water electrolysis: electrochemical characterization and energetic evaluation

Ph.D. Thesis No. 24476, ETH Zürich, July 2017.

Examiners: Prof. Dr. T.J. Schmidt, PSI Villigen/ETH Zürich
Prof. Dr. A. Wokaun, PSI Villigen/ETH Zürich
Dr. F.N. Büchi, PSI Villigen

Olga Nibel

Component development for all-vanadium redox flow batteries: Membrane design and cell characterization

Ph.D. Thesis No. 24647, ETH Zürich, September 2017.

Examiners: Prof. Dr. T.J. Schmidt, PSI Villigen/ETH Zürich
Prof. Dr. G. Storti, ETH Zürich
Dr. L. Gubler, PSI Villigen

Susan M. Taylor

Investigation of the electrochemical reactions involved in all-vanadium redox flow cells

Ph.D. Thesis No. 24590, ETH Zürich, August 2017.

Examiners: Prof. Dr. T.J. Schmidt, PSI Villigen/ETH Zürich
Prof. Dr. M. Kovalenko, ETH Zürich
Dr. A. Pătru, PSI Villigen

Martin Reichardt

Lithium chromium-based polyanions and derivatives as multiple-redox electrode materials in Li-ion batteries

Ph.D. Thesis No. 24778, ETH Zürich, December 2017.

Examiners: Prof. Dr. P. Novák, PSI Villigen/ETH Zürich
Prof. Dr. M. Niederberger, ETH Zürich
Dr. C. Villevieille, PSI Villigen
Dr. S. Sallard, PSI Villigen

EXCHANGE STUDENTS, DIPLOMA THESES, SUMMER STUDENTS, GUEST SCIENTISTS

Elisabeth Nilsson
ETH Zürich

Solution-casting of polybenzimidazole Membranes for Vanadium Redox Flow batteries
January – March 2017
(Membranes and Electrochemical Cells).

Simon Schneider
ETH Zürich

Bio-template-assisted synthesis of cathode material for Na-ion batteries
February – June 2017
(Electrochemical Energy Storage).

Katrine Elsoe
ETH Zürich

Preparation of catalyst coated membranes for water electrolysis cells
February – May 2017
(Membranes and Electrochemical Cells).

Adrian Heinritz
ETH Zürich

Kinetic studies of Ce(III)/Ce(IV) redox-couple on gold electrodes
March – July 2017
(Electrocatalysis and Interfaces).

Neal Cardoza
Purdue University, West Lafayette, IN, USA

Determining factors for the cycling performance of lithium polysulphide battery cells
June – August 2017
(Electrochemical Energy Storage).

Jan Janousek
University of Chemistry and Technology, Prague, Czech Republic

Surface modification of high voltage NCM cathodes using polymer coating
June – September 2017
(Electrochemical Energy Storage).

Elisabeth Nilsson
KTH Royal Institute of Technology, Stockholm, Sweden

Bilayered PBI/Nafion membranes for Vanadium Redox Flow batteries
June – August 2017
(Membranes and Electrochemical Cells).

Frédéric Schlattner
ETH Zürich

Impact of super-paramagnetic iron oxide nanoparticles on the performance of graphite in lithium-ion batteries
July 2017
(Electrochemical Energy Storage).

Ryo Shimizu
University of Yamanashi, Yamanashi, Japan

Noble metal aerogels for PEFC anodes
June – December 2017
(Electrocatalysis and Interfaces).

Benjamin Amoroso
ETH Zürich

Wettability experiments for fuel cell and electrolyzer materials
August – September 2017
(Fuel Cell Systems and Diagnostics).

Valentina Stampi-Bombelli
EPF Lausanne

Model based determination of PEFC membrane hydration distribution
September 2016 – January 2018
(Fuel Cell Systems and Diagnostics).

Alexander Arndt
Humboldt Universität zu Berlin, Berlin

Functionalization of polymerfilms for Vanadium Redox Flow batteries with improved power density
September 2017 – February 2018
(Membranes and Electrochemical Cells).

Fusen Huang Tsinghua University Beijing, Beijing	*Distinction of liquid water and ice in PEFC with neutron imaging technology during sub-zero start-up process* September – November 2017 (Neutron Radiography of Electrochemical Systems).
Rokas Paulius Petrauskas Vilnius University, Vilnius, Lithuania	*Si–C composites for high-energy Li-ion battery negative electrodes* September – December 2017 (Electrochemical Energy Storage).
Darryl Nater ETH Zürich	*Investigation of succinic anhydride as an electrolyte additive in lithium ion batteries* September 2017 – January 2018 (Electrochemical Energy Storage).
Taro Kimura University of Yamanashi, Yamanashi, Japan	*Gas feed polymer electrolyte water electrolysis* October 2017 – March 2018 (Fuel Cell Systems and Diagnostics).
Elisabeth Nilsson KTH Royal Institute of Technology, Stockholm, Sweden	*Drivers and mitigation of gas crossover in polymer electrolyte water electrolyzers* November 2017 – April 2018 (Membranes and Electrochemical Cells).

.

SEMINAR, INVITED SPEAKERS

Prof. Peter G. Bruce
University of Oxford, Department of Materials, Oxford, Great Britain

Storing energy with oxygen: oxygen redox chemistry in solids and aprotic solvents
February 22, 2017.

Prof. Arnulf Latz
Helmholtz Institute Ulm, DLR, Ulm, Germany

Theory based modeling and simulation of batteries: Lithium insertion and beyond from microstructure to cell scale
March 22, 2017.

Ing. Petr Krtil, Csc.
J. Heyrovsky Institute of Physical Chemistry, Prague, Czech Republic

Rational design of alloy electrocatalysts – Nuts and bolts of multifunctional catalyst optimisation
March 30, 2017.

Dr. Marie-Liesse Doublet
Institut Charles Gerhardt, Université Montpellier, Montpellier, France

Conceptual vs. computational approaches to high energy density materials for Li-ion batteries
April 21, 2017.

PSI Catalysis Symposium:

Prof. Hans-Joachim Freund
Department of Chemical Physics, Fritz-Haber-Institut der Max-Planck-Gesellschaft, Berlin, Germany

Model Systems in Heterogeneous Catalysis at the Atomic Level
May 18, 2017.

Prof. Makoto Uchida
Fuel Cell Nanomaterials Center, University of Yamanashi, Kofu, Yamanashi, Japan

Improvement of cell performance in low-Pt-loading cathode catalyst layers prepared by the electrospray method for PEFCs
June 6, 2017.

PSI Catalysis Symposium:

Dr. Vojislav Stamenkovic
Argonne National Laboratory, Argonne, IL, USA

Design and synthesis of advanced electrocatalysts
September 28, 2017.

PSI Catalysis Symposiume:

Prof. Johannes Lercher
TU Munich, Germany and
PNNL – Institute for Integrated Catalysis, Pacific Northwest National Laboratory, Richland, WA, USA

Lessons from enzymes - On the role of steric constraints and chemical environments for catalysis
November 30, 2017.

AWARDS

Minglong He

The 2016 Chinese Government Award for Outstanding Self-financed Students Abroad

China Scholarship Council, Beijing, P.R. China,
January 25, 2017.

Giulio Ferraresi

Best Poster Prize
G. Ferraresi, M. El Kazzi, C.L. Tsai, S. Uhlenbruck, P. Novák, C. Villevieille
All-solid-state Li battery based on c-$Li_7La_3Zr_2O_{12}$ solid electrolyte and alloy anode materials.

20th Topical Meeting – International Society of Electrochemistry (ISE), Buenos Aires, Argentina,
March 19–22, 2017.

Fabio Oldenburg

Poster Award 2017
F. Oldenburg, T.J. Schmidt, L. Gubler
Novel membrane design strategies towards high performance vanadium flow batteries.

6th International Seminar on Green Energy Conversion,
Koumi, Nagano, Japan,
September 13–15, 2017.

Sebastian Eberhardt

PSI Impuls Preis 2017
For his PhD Thesis «Phosphoric acid electrolyte redistribution and loss in high temperature polymer electrolyte fuel cells».

Verein PSI-Impuls, Paul Scherrer Institut, Villigen, Switzerland,
November 22, 2017.

CONFERENCES – SYMPOSIA

5th Symposium of SCCER HaE Storage May 9, 2017.

Heat and Electricity Storage – 5th Symposium

Organizers:

Thomas J. Schmidt, SCCER HaE Storage/Electrochemistry Laboratory
Jörg Roth, Ursula Ludgate, SCCER Heat and Electricity Storage

Contributions from (in order of appearance):

Philip Hassler, IFJ Institut für Jungunternehmen AG, CH
Jan Wurzbacher, Climeworks, CH
Guillaume Jung, PARK INNOVAARE, CH
Daniel Steitz, novoMOF, CH
Viola Becattini, IET, EHTZ, CH
Cornel Fink, LCOM, EPFL, CH
Bae-Jung Kim, ECL, PSI, CH
Jachin Gore, Institut für Energietechnik, HSR, CH
Abhishek Malhotra, Energy Politics Group, ETHZ, CH
Peter Trawitzki, Energiedienst, D
Hilmi Buqa, Leclanché, CH
Adrian Spillmann, Bühler, CH
MGuillaume Bourtourault, FAFCO SA, CH
Jörg Worlitschek, HSLU, CH

From left to right: *Jörg Roth, Abhishek Malhotra, Daniel Steitz, Cornel Fink, Thomas J. Schmidt, Hilmi Buqa, Viola Becattini, Bae-Jung Kim, Jörg Worlitschek, Adrian Spillmann, Peter Trawitzki, Guillaume Bourtourault, Cordelia Gloor, Guillaume Jung, Ursula Ludgate.*

33rd PSI Electrochemistry Symposium May 10, 2017.

From the Lab to the Markets

Organizers:
Thomas J. Schmidt, Cordelia Gloor, Electrochemistry Laboratory
Jörg Roth, Ursula Ludgate, SCCER Heat and Electricity Storage

Contributions from (in order of appearance):
Steven J. Visco, PolyPlus Battery Company, USA
Peter Axmann, Zentrum für Sonnenenergie- und Wasserstoff-Forschung Baden-Württemberg, Stuttgart, Germany
Nigel Brandon, Imperial College London, Great Britain
Mark F. Mathias, General Motors, USA
Cortney K. Mittelsteadt, GINER INC., USA

From left to right: *Jörg Roth, Cordelia Gloor, Steven J. Visco, Petr Novák, Mark F. Mathias, Felix N. Büchi, Peter Axmann, Lorenz Gubler, Cortney K. Mittelsteadt, Nigel Brandon, Ursula Ludgate, Thomas J. Schmidt.*




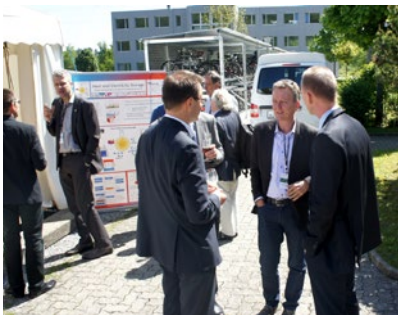


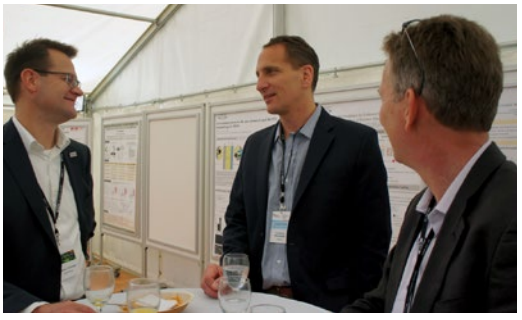


Plenary talks, poster session, lunch and discussions …

REVIEW ACTIVITIES OF THE LABORATORY

Journals

A ACS Applied Materials & Interfaces ♦ ACS Macro Letters ♦ Advanced Energy Materials ♦ Advanced Functional Materials ♦ Advanced Materials ♦ Advanced Materials Interfaces ♦ Angewandte Chemie International Edition ♦ Applied Surface Science

C Carbon ♦ Chemical Science ♦ Chemical Reviews ♦ Chemistry of Materials ♦ ChemSusChem

E ECS Electrochemistry Letters ♦ Electrochemistry Communications ♦ Electrochimica Acta ♦ Electrocatalysis ♦ Energy and Environmental Science ♦ Energy Technology

F Fuel Cells

I International Journal of Hydrogen Energy ♦ Ionics

J Journal of the American Chemical Society ♦ Journal of the Electrochemical Society ♦ Journal of Fuel Cell Science and Technology ♦ Journal of Materials Chemistry A ♦ Journal of Membrane Science ♦ Journal of Molecular Liquids ♦ Journal of Physical Chemistry ♦ Journal of Power Sources ♦ Journal of Solid State Electrochemistry ♦ Journal of Synchrotron Radiation

N Nature ♦ Nature Chemistry ♦ Nature Communications ♦ Nature Energy ♦ Nature Materials ♦ Nature Scientific Reports

P Physical Chemistry Chemical Physics

R Radiation Physics and Chemistry ♦ RSC Advances

S Science ♦ Solid State Ionics

Organisations

A Agence National de la Recherche, France ♦ Alexander von Humboldt-Stiftung, Germany

D Danish Council of Strategic Research ♦ Deutsche Forschungsgemeinschaft

E ETH Zürich Research Commission ♦ European Commission Research Executive Agency ♦ European Research Council

F FFG Österreichische Forschungsförderungsgesellschaft ♦ Fonds National de Recherche (FNR), Luxembourg

G Gordon Research Conferences

I Indipendent Research Fund, Denmark

N National Sciences and Engineering Research Council of Canada ♦ National Science Foundation, USA ♦ Netherlands Organisation for Scientific Research NWO

S SNF (Schweizerischer Nationalfonds) ♦ Society in Science

T The Research Council of Norway ♦ The Royal Swedish Academy of Scienes

Q Qatar National Research Fund

V Volkswagen Stiftung

External Dissertations: Review Activities

Thomas J. Schmidt:

- Peter Stahl, Universität Stuttgart, Germany
- Laura Kühn, TU Dresden, Germany
- Karim Waiz, ETH Zürich
- Marta Bon, ETH Zürich

Sigita Trabesinger:

- Justina Gaidukevic, Vilnius University, Lithuania

Claire Villevieille:

- Laura Landers, Collège de France, France
- Philippe Dumaz, Université Grenoble-Alpes, France

INDUSTRIAL PARTNERS

Collaborations with Industrial Partners

The Laboratory had the pleasure to collaborate with the following industrial partners during the year 2017:

A Aigys AG, Mellingen

B BASF SE, Ludwigshafen, Germany

C Cellera, Caesarea, Israel

D Daimler NuCellSys GmbH, Kirchheim/Teck-Nabern, Germany

E ElringKlinger, Dettingen, Germany

H Heraeus Detschland GmbH & Co KG, Hanau, Germany

I IBM Zürich Research Laboratory, Rüschlikon ♦ IMERYS Graphite & Carbon, Bodio

O Osmotex AG, Thalwil

P Proton OnSite, Wallingford, CT, USA

S Saft SA, Bordeaux, France ♦ Siemens AG, Erlangen, Germany ♦ Swiss Hydrogen SA, Fribourg

T Toyota Motor Europe, Zaventem, Belgium

U UMICORE AG & Co. KG, Hanau, Germany

DOCUMENTATION

Project Collaborations with External Partners

BFE

P. Boillat Project leader	*In situ study of water transport processes in polymer electrolyte electrolysers with neutron imaging*
F.N. Büchi Project leader	*Reducing Transport Losses in Polymer Electrolyte Electrolysis*
F.N. Büchi Project leader	*Autostack Industrie*
L. Gubler Project leader	*ELYTEMP - Polymer electrolyte water electrolysis at elevated temperature for reduced cost of hydrogen for energy applications*
L. Gubler Project leader	*ELYDEG – Understanding of degradation signatures in water electrolyzers operated with variable input*
L. Gubler Project leader	*RFBmem – Chemistry and stability of grafted membranes for redox flow batteries*
T.J. Schmidt Project leader	*RENERG^2 (Renewable Energies in Future Energy Supply)*

CCEM

C. Bach, T.J. Schmidt Project leaders	*RENERG^2 (Renewable Energies in Future Energy Supply)* with ETH Zürich, Empa Dübendorf, EPF Lausanne, ZAHW Winterthur
F.N. Büchi Project leader	*ADMIST (Advanced Understanding of Micro Structures in Fuel Cells and Batteries through X-ray Imaging)* with Laboratory for Nanoelectronics ETH Zurich

EU

F.N. Büchi Project leader	*Auto-Stack CORE (Automotive Fuel Cell Stack Cluster Initiative for Europe)*

KTI

F.N. Büchi Co-Leader Capacity Area 2	*SCCER Mobility: Efficient Technologies and Systems for Mobility*
P. Novák Work package leader	*SCCER Heat & Electricity Storage: Materials, systems, and modelling*
S. Trabesinger Project leader	*High capacity carbon-based composite anode active materials for lithium-ion battery electrodes*
T.J. Schmidt Director	*Swiss Competence Center for Energy Research – Heat & Electricity Storage*

T.J. Schmidt Principal Investigator	*SCCER Heat & Electricity Storage: Catalytic and Electrocatalytic CO_2 Reduction*

PSI Research Commission

T.J. Schmidt Co-Project leader	*Improved Insight into Catalysis Mechanisms via Nanopatterned Metal Structures (Nanocat)* Cross Initiative with Prof. J. Gobrecht; Prof. J.A. van Bokhoeven

SNSF

E.J. Berg Project leader	*Interphase formation on high voltage and energy Li-ion cathodes* SNSF Ambizione Energy
P. Boillat Project leader	*Porous materials with patterned wettability for advanced fuel cell water management strategies: improvement of durability and in situ performance*
F.N. Büchi, J. Eller Project leaders	*Sub-second dynamics of liquid water transport in polymer electrolyte fuel cells revealed by 4D X-ray Tomographic Microscopy*
F.N. Büchi, J. Eller Project leaders	*Coupled multi-phase transport in porous layers for fuel cells utilizing evaporative cooling*
F.N. Büchi Co-project leader	*NFP70: Designing multifunctional materials for proton exchange membrane fuel cells* with Institute for Computational Physics, ZHAW Winterthur
E. Fabbri Project leader	*Designing novel electrocatalysts for fuel cells and electrolyzers by tailoring perovskite surface properties* SNSF Ambizione Project
L. Gubler Project leader	*Radiation grafted proton conducting membranes for high-temperature polymer electrolyte fuel cells*
J. Herranz Project leader	*Composition / porosity effects on the activity, performance and stability of non-noble metal, O_2-reduction catalysts for polymer electrolyte fuel cells* SNSF Ambizione Energy Project
T.J. Schmidt Project leader	*Designing nano-extended multimetallic aerogel fuel cell catalysts for oxygen reduction reaction* with TU Dresden, Germany
T.J. Schmidt Experimental project leader	*NCCR Marvel Experimental Platform Project* Development of advanced electrocatalysts for water splitting: Correlation between electronic structure, surface properties and electrochemical activity.
C. Villevieille Project leader	*Surface and interface investigations of high energy density electrodes for sodium-ion batteries*

Industry

L Gubler Project leader	*Bestimmung von Gaspermeationseigenschaften von Brennstofzellenmembranen* NuCellSys GmbH, Kirchheim/Teck-Nabern, Germany
L Gubler Project leader	*Study of full cell reaction mechanism of lithium-ion batteries using 5V spinel materials* Hitech Zentrum Aargau AG, Brugg Aigys AG, Mellingen

P. Novák Project leader	*Forschungsnetzwerk «Elektrochemie und Batterien»* BASF SE, Ludwigshafen, Germany
S. Trabesinger Project leader	*Graphite für Lithiumionen-Batterien* Imerys Graphite & Carbon, Bodio
C. Villevieille Project leader	*X-ray tomography applied to all-solid-state-batteries* Toyota Motor Europe NV/SA, Brussels, Belgium
C. Villevieille Project leader	*Development and electrochemical investigation of novel solid electrolyte for all-solid-state Li-ion batteries* Saft SA, Bordeaux, France

Teaching Activities

University Level Teaching

Prof. Dr. P. Novák	*Elektrochemie* ETH Zürich, HS 2017.
Prof. Dr. T.J. Schmidt	*Renewable Energy Technologies 2* ETH Zürich, FS 2017.
Prof. Dr. T.J. Schmidt	*Physical Electrochemistry & Electrocatalysis* ETH Zürich, FS 2017.

Contributions to Courses at Universities, FHL, and other Institutes

L. Gubler	*Renewable Energy Technologies 2, Energy Conversion and Storage* ETH Zürich, May 2, May 9, May 16, May 30, 2017.
L. Gubler	*Energy Storage Systems* Lucerne University of Applied Sciences and Arts, May 3, 2017.

Publications

Peer Reviewed Papers

D.F. Abbott, M. Meier, G.R. Meseck, E. Fabbri, S. Seeger, T.J. Schmidt
Silicone nanofilament-supported mixed nickel-metal oxides for alkaline water electrolysis
doi: 10.1149/2.0201704jes, J. Electrochem. Soc. 164 (4) F203–F208 (2017).

R. Asakura, P. Novák, R. Robert
Colloidal synthesis and electrochemistry of surface Coated Nano-$LiNi_{0.80}Co_{0.15}Al_{0.05}O_2$
doi: 10.1149/2.1431712jes, J. Electrochem. Soc. **164**, A2617–A2624 (2017).

U. Babic, M. Suermann, F.N. Büchi, L. Gubler, T.J. Schmidt
Identifying critical gaps for polymer electrolyte water electrolysis development
doi: 10.1149/2.1441704jes, J. Electrochem. Soc. **164**, F387–F399 (2017).

T. Binninger, R. Mohamed, A. Pătru, K. Waltar, E. Gericke, X. Tuaev, E. Fabbri, P. Levecque, A. Höll, T.J. Schmidt
Stabilization of Pt nanoparticles due to electrochemical transistor switching of oxide support conductivity
doi: 10.1021/acs.chemmater.6b04851, Chem. Mater. **29**, 2831–2843 (2017).

T. Binninger, T.J. Schmidt, D. Kramer
Capacitive electronic metal-support interactions: Outer surface charging of supported catalyst particles
doi: 0.1103/PhysRevB.96.165405, Phys. Rev. B **96**, 165405 (2017).

P. Boillat, E.H. Lehmann, P. Trtik, M. Cochet
Neutron imaging of fuel cells – Recent trends and future prospects
doi: 10.1016/j.coelec.2017.07.012, Curr. Opin. Electrochem. **5**, 3–10 (2017).

L. Boulet-Roblin, D. Sheptyakov, P. Borel, C. Tessier, P. Novák, C. Villevieille
Crystal structure evolution via operando neutron diffraction during long-term cycling of customized 5 V full Li ion cylindrical cells $LiNi_{0.5}Mn_{1.5}O_4$ vs. graphite
doi: 10.1039/C7TA07917F, J. Mater. Chem. A. **5**, 25574–25582 (2017).

B. Cai, S. Henning, J. Herranz, T.J. Schmidt, A. Eychmüller
Nanostructuring noble metals as unsupported electrocatalysts for polymer electrolyte fuel cells
doi: 10.1002/aenm.201700548, Adv. Energy Mater. **7**, 1700548 (2017).

X. Cheng, E. Fabbri, B. Kim, M. Nachtegaal, T.J. Schmidt
Effect of ball milling on the electrocatalytic activity of $Ba_{0.5}Sr_{0.5}Co_{0.8}Fe_{0.2}O_3$ towards the oxygen evolution reaction
http://dx.doi.org/10.1039/C7TA00794A, J. Mater. Chem. A **5**, 13130 (2017).

J. Conder, C. Villevieille, S. Trabesinger, P. Novák, L. Gubler, R. Bouchet
Electrochemical impedance spectroscopy of a Li-S battery. Part 1: Influence of the electrode and electrolyte compositions on the impedance of symmetric cells
doi: 10.1016/j.electacta.2017.05.041, Electrochim. Acta **244**, 61–68 (2017).

J. Conder, C. Villevieille, S. Trabesinger, P. Novák, L. Gubler, R. Bouchet
Electrochemical impedance spectroscopy of a Li-S battery. Part 2: Influence of separator chemistry on the lithium electrode/electrolyte interface
doi: 10.1016/j.electacta.2017.09.148, Electrochim. Acta **255**, 379–390 (2017).

J. Conder, R. Bouchet, S. Trabesinger, C. Marino, L. Gubler, C. Villevieille
Direct observation of lithium polysulphides using operando X-ray diffraction
doi: 10.1038/nenergy.2017.69, Nature Energy **2**, 17069 (2017).

J. Eller, J. Roth, F. Marone, M. Stampanoni, F.N. Büchi
Critical review – Operando properties of gas diffusion layers: Saturation and liquid permeability
doi: 10.1149/2.0881702jes, J. Electrochem. Soc. **164**, F115–F126 (2017).

E. Fabbri, A. Rabis, Y. Chino, M. Uchida, T.J. Schmidt
Boosting Pt oxygen reduction reaction activity by tuning the tin oxide support
https://doi.org/10.1016/j.elecom.2017.09.006, Electrochem. Commun. **83**, 90–95 (2017).

E. Fabbri, D.F. Abbott, M. Nachtegaal, T.J. Schmidt
Operando X-ray absorption spectroscopy: A powerful tool toward water splitting catalyst development
https://doi.org/10.1016/j.coelec.2017.08.009, Curr. Opin. Electrochem. **5**, 20–26 (2017).

E. Fabbri, M. Nachtegaal, X. Cheng, T. Binninger, J. Durst, F. Bozza, T. Graule, R. Schäublin, L. Wiles, M. Pertoso, N. Danilovic, K.E. Ayers, T.J. Schmidt
Dynamic surface self-reconstruction is the key of highly active perovskite nano-electrocatalysts for water splitting
doi:10.1038/nmat4938, Nat. Mater. **16**, 925–931 (2017).

K. Fic, M. He, E.J. Berg, P. Novák, E. Frąckowiak
Comparative operando study of degradation mechanisms in carbon-based electrochemical capacitors with Li_2SO_4 and $LiNO_3$ electrolytes
doi: 10.1016/j.carbon.2017.05.061, Carbon **120**, 281–293 (2017).

A. Forner-Cuenca, V. Manzi-Orezzoli, P.M. Kristiansen, L. Gubler, T.J. Schmidt, P. Boillat
Mask-assisted electron radiation grafting for localized through-volume modification of porous substrates: Influence of electron energy on spatial resolution
doi: 10.1016/j.radphyschem.2017.01.036, Radiat. Phys. Chem. **135**, 133–141 (2017).

J.J. Gallet, M.G. Silly, M. El Kazzi, F. Bournel, F. Sirotti, F. Rochet
Chemical and kinetic insights into the thermal decomposition of an oxide layer on Si(111) from millisecond photoelectron spectroscopy
doi: 10.1038/s41598-017-14532-4, Scientific Reports **7**, 14257 (2017).

P.A. García-Salaberri, D.G. Sanchez, P. Boillat, M. Vera, K.A. Friedrich
Hydration and dehydration cycles in polymer electrolyte fuel cells operated with wet anode and dry cathode feed: A neutron imaging and modeling study
doi: 10.1016/j.jpowsour.2017.03.155, J. Power Sources **359**, 634–655 (2017).

S. Henning, L. Kühn, J. Herranz, M. Nachtegaal, R. Hübner, M. Werheid, A. Eychmüller, T.J. Schmidt
Effect of acid washing on the oxygen reduction reaction activity of Pt-Cu aerogel catalysts
doi: 10.1016/j.electacta.2017.03.019, Electrochim. Acta **233**, 210–217 (2017).

S. Henning, J. Herranz, H. Ishikawa, B.J. Kim, D. Abbott, L. Kühn, A. Eychmüller, T.J. Schmidt
Durability of unsupported Pt-Ni aerogels in PEFC cathodes
doi: 10.1149/2.0131712jes, J. Electrochem. Soc. **164**, F1136–F1141 (2017).

S. Henning, H. Ishikawa, L. Kühn, J. Herranz, E. Müller, A. Eychmüller, T.J. Schmidt
Unsupported Pt-Ni aerogels with enhanced high-current performance and durability in fuel cell cathodes
doi: 10.1002/anie.201704253, Angew. Chem. Int. Ed. **56**, 10707–10710 (2017).

L. Holzer, O. Pecho, J. Schumacher, P. Marmet, O. Stenzel, F.N. Büchi, A. Lamibrac, B. Münch
Microstructure-property relationships in a gas diffusion layer (GDL) for polymer electrolyte fuel cells, Part I: Effect of compression and anisotropy of dry GDL
doi: 10.1016/j.electacta.2017.01.030, Electrochim. Acta **227**, 419–434 (2017).

L. Holzer, O. Pecho, J. Schumacher, P. Marmet, F.N. Büchi, A. Lamibrac, B. Münch
Microstructure-property relationships in a gas diffusion layer (GDL) for polymer electrolyte fuel cells, Part II: Pressure-induced water injection and liquid permeability
doi: 10.1016/j.electacta.2017.04.141, Electrochim. Acta **241**, 414–432 (2017).

A. Iranzo, A. Salva, P. Boillat, J. Biesdorf, E. Tapia, F. Rosa
Water build-up and evolution during the start-up of a PEMFC: Visualization by means of neutron imaging
doi: 10.1016/j.ijhydene.2016.11.076, Int. J. Hydrogen Energ. **42**, 13839–13849 (2017).

W. Karim, S.A. Tschupp, J. Herranz, T.J. Schmidt, Y. Ecinci, J.A. van Bokhoven
State-of-the-art nanofabrication in catalysis
doi: 10.2533/chimia.2017.1, Chimia **71**(4), 160–169 (2017).

B. Kim, D.F. Abbott, X. Cheng, E. Fabbri, M. Nachtegaal, F. Bozza, I.E. Castelli, D. Lebedev, R. Schäublin, C. Copéret, T. Graule, N. Marzari, T.J. Schmidt
Unravelling thermodynamics, stability, and oxygen evolution activity of strontium ruthenium perovskite oxide
doi: 10.1021/acscatal.6b03171, ACS Catal. **7**, 3245–3256 (2017).

D. Lebedev, M. Povia, K. Waltar, P.M. Abdala, I.E. Castelli, E. Fabbri, M.V. Blanco, A. Fedorov, C. Copéret, N. Marzari, T.J. Schmidt
Highly active and stable iridium pyrochlores for oxygen evolution reaction
doi: 10.1021/acs.chemmater.7b00766, Chem. Mater. **29**, 5182–5191 (2017).

C. Marino, M. El Kazzi, E.J. Berg, M. He, C. Villevieille
Interface and safety properties of phosphorus-based negative electrodes in Li-ion batteries
doi: 10.1021/acs.chemmater.7b01128, Chem. Mat. **29**, 7151–7158 (2017).

C. Marino, E. Marelli, C. Villevieille
Impact of cobalt content in $Na_{0.67}Mn_xFe_yCo_zO_2$ (x + y + z =1), a cathode material for sodium ion batteries
doi: 10.1039/c7ra00566k, RSC Advances **7**(23), 13851–13857 (2017).

C. Marino, T. Block, R. Pöttgen, C. Villevieille
$CuSbS_2$ as a negative electrode material for sodium-ion batteries
doi: 10.1016/j.jpowsour.2016.12.100, J. Power Sources **342**, 616–622 (2017).

C. Marino, N. Dupré, C. Villevieille
Elucidation of reaction mechanism of Ni_2SnP in Li-ion and Na-ion systems
doi: 10.1016/j.jpowsour.2017.08.096, J. Power Sources **365**, 339–347 (2017).

O. Nibel, T. Rojek, T.J. Schmidt, L. Gubler
Amphoteric ion-exchange membranes with significantly improved vanadium barrier properties for all-vanadium redox flow batteries
doi: 10.1002/cssc.201700610, ChemSusChem **10**, 2767–2777 (2017).

O. Nibel, S.M. Taylor, A. Pătru, E. Fabbri, L. Gubler, T.J. Schmidt
Performance of different carbon electrode materials – Insights into stability and degradation under real vanadium redox flow battery operating conditions
doi: 10.1149/2.1081707jes, J. Electrochem. Soc. **164**, A1608–A1615 (2017).

O. Nibel, M. Bon, M. Agiorgousis, T. Laino, L. Gubler, T.J. Schmidt
Unraveling the interaction mechanism between amidoxime groups and vanadium ions at various pH conditions
doi: 10.1021/acs.jpcc.6b12540, J. Phys. Chem. C **121**, 6436–6445 (2017).

E. Oakton, D. Lebedev, M. Povia, D. Abbott, E. Fabbri, A. Fedorov, M. Nachtegaal, C. Copéret, T.J. Schmidt
IrO_2/TiO_2: A high-surface-area, active and stable electrocatalyst for oxygen evolution reaction
doi: 10.1021/acscatal.6b03246, ACS Catal. **7**, 2346–2352 (2017).

M. Oezaslan, A.-K. Herrmann, M. Werheid, A. Frenkel, M. Nachtegaal, C. Dosche, C. Laugier-Bonnaud, H.-C. Yilmaz, L. Kühn, E. Rhiel, N. Gaponik, A. Eychmüller, T.J. Schmidt
Structural analysis and electrochemical properties of bimetallic Pd-Pt aerogels prepared by a two-step gelation process
doi: 10.1002/cctc.201600667, ChemCatChem **9**, 798–808 (2017).

F.J. Oldenburg, T.J. Schmidt, L. Gubler Lorenz
Tackling capacity fading in vanadium flow batteries with amphoteric membranes
doi: 10.1016/j.jpowsour.2017.09.051, J. Power Sources **368**, 68–72 (2017).

M. Pichler, W. Si, F. Haydous, H. Téllez, J. Druce, E. Fabbri, M. El Kazzi, M. Döbeli, A. Wokaun, D. Pergolesi, T. Lippert
$LaTiO_xN_y$ thin film model systems for photocatalytic water splitting: Physicochemical evolution of the solid-liquid interface and the role of the crystallographic orientation
doi: 10.1002/adfm.201605690, Adv. Funct. Mater. **27**, 1605690 (2017).

T. Rojek, L. Gubler, M.M. Nasef, E. Abouzari-Lotf	*New polyvinylamine containing adsorbent for CO_2 capturing prepared by radiation induced grafting of N Vinylformamide onto UHMWPE and hydrolysis* doi: 10.1021/acs.iecr.7b00862, Ind. Eng. Chem. Res. **56**, 5925–5934 (2017).
M.A. Safi, N.I. Prasianakis, J. Mantzaras, A. Lamibrac, F.N. Büchi	*Experimental and pore-level numerical investigation of water evaporation in gas diffusion layers of polymer electrolyte fuel cells* doi: 10.1016/j.ijheatmasstransfer.2017.07.050, Int. J. Heat Mass Transfer **115**, 238–249 (2017).
M. Saito, S. Kosaka, T. Fujinami, Y. Tachikawa, H. Shiroishi, D. Streich, E.J. Berg, P. Novák, S. Seki	*A new concept of an air-electrode catalyst for Li_2O_2 decomposition using MnO_2 nanosheets on rechargeable Li-O_2 batteries* doi: 10.1016/j.electacta.2017.08.183, Electrochim. Acta **252**, 192–199 (2017).
S. Sallard, D. Sheptyakov, C. Villevieille	*Improved electrochemical performances of Li-rich nickel cobalt manganese oxide by partial substitution of Li^+ by Mg^{2+}* doi: 10.1016/j.jpowsour.2017.05.028, J. Power Sources **359**, 27–36 (2017).
S. Schmidt, S. Sallard, D. Sheptyakov, P. Novák, C. Villevieille	*Ligand influence in Li-ion battery hybrid active materials: Ni methylenediphosphonate vs. Ni dimethylamino methylenediphosphonate* doi: 10.1039/C7CC01982C, Chem. Commun. **53**, 5420–5423 (2017).
S. Schmidt, S. Sallard, D. Sheptyakov, M. Nachtegaal, P. Novák, C. Villevieille	*Fe and Co methylene diphosphonates as conversion materials for Li-ion batteries* doi: 10.1016/j.jpowsour.2016.12.090, J. Power Sources **342**, 879–885 (2017).
T. Schott, R. Robert, P.A. Ulmann, P. Lanz, S. Zürcher, M.E. Spahr, P. Novák, S. Trabesinger	*Cycling behavior of silicon-containing graphite electrodes. Part A: Effect of the lithiation protocol* doi: 10.1021/acs.jpcc.7b05919, J. Phys. Chem. C **121**, 18423–18429 (2017).
T. Schott, R. Robert, S. Pacheco Benito, P.A. Ulmann, P. Lanz, S. Zürcher, M.E. Spahr, P. Novák, S. Trabesinger	*Cycling behavior of silicon-containing graphite electrodes. Part B: Effect of the silicon source* doi: 10.1021/acs.jpcc.7b08457, J. Phys. Chem. C **121**, 25718–25728 (2017).
T. Schott, J.L. Gómez-Cámer, C. Bünzli, P. Novák, S. Trabesinger	*The counterintuitive impact of separator-electrolyte combinations on the cycle life of graphite-silicon composite electrodes* doi: 10.1016/j.jpowsour.2017.01.055, J. Power Sources **343**, 142–147 (2017).
T. Schott, J.L. Gómez-Cámer, P. Novák, S. Trabesinger	*Relationship between the properties and cycle life of Si/C composites as performance enhancing additives to graphite electrodes for Li-ion batteries* doi: 10.1149/2.0701702jes, J. Electrochem. Soc. **164**, A190–A203 (2017).
D. Sheptiyakov, L. Boulet-Roblin, P. Borel, C. Tessier, P. Novák, C. Villevieille	*Crystal structure evolution via operando neutron diffraction during long-term cycling of a customized 5 V full Li-ion cylindrical cell $LiNi_{0.5}Mn_{1.5}O_4$ vs. graphite* doi: 10.1039/c7ta07917f, J. Mater. Chem. A **5**, 25574–25582 (2017).
V. Sproll, M. Handl, R. Hiesgen, K.A. Friedrich, T.J. Schmidt, L. Gubler	*Membrane architecture with ion-conducting channels through swift heavy ion induced graft copolymerization* doi: 10.1039/C7TA07323B, J. Mater. Chem. A **5**, 24826-24835 (2017).
V. Sproll, T.J. Schmidt, L. Gubler	*Effect of glycidyl methacrylate (GMA) incorporation on water uptake and conductivity of proton exchange membranes* doi: 10.1016/j.radphyschem.2017.08.025, Rad. Phys. Chem. **144**, 276–279 (2018).
D. Streich, C. Erk, A. Gueguen, P. Mueller, F.F. Chesneau, E.J. Berg	*Operando monitoring of early Ni-mediated surface reconstruction in layered lithiated Ni-Co-Mn oxides* doi: 10.1021/acs.jpcc.7b02303, J. Phys. Chem. C **121**, 13481–13486 (2017).

M. Suermann, K. Takanohashi, A. Lamibrac, T.J. Schmidt, F.N. Büchi	*Influence of operating conditions and material properties on the mass transport losses of polymer electrolyte water electrolysis* doi: 10.1149/2.13517109jes, J. Electrochem. Soc. **164**, F973–F980 (2017).
M. Suermann, A. Pătru, T.J. Schmidt, F.N. Büchi	*High pressure polymer electrolyte water electrolysis: Test bench development and electrochemical analysis* http://dx.doi.org/10.1016/j.ijhydene.2017.01.224, Int. J. Hydrogen Energy **42**, 12076–12086 (2017).
M. Suermann, T. Kiupel, T.J. Schmidt, F.N. Büchi	*Electrochemical hydrogen compression: Efficient pressurization concept derived from an energetic evaluation* doi: 10.1149/2.1361712jes, J. Electrochem. Soc. **164**, F1187–F1195 (2017).
B. Sun, E.J. Berg	*Electrochemical and chemical modifications of electrode surfaces and interphases for Li-ion batteries* doi: 10.1016/b978-0-12-409547-2.13141-5, Encyclopedia of Interfacial Chemistry: Surface Science and Electrochemistry (2017).
S.M. Taylor, A. Pătru, E. Fabbri, T.J. Schmidt	*Influence of surface oxygen groups on V(II) oxidation reaction kinetics* doi: 10.1016/elecom.2016.12.003, Electrochem. Comm. **75**, 13–16 (2017).
S.A. Tschupp, S.E. Temmel, N. Poyatos Salguero, J. Herranz, T.J. Schmidt	*Novel numerical partitioning model for the Koutecký-Levich analysis of electrochemical flow cells with a combined channel–wall-jet geometry* doi: 10.1149/2.0441711jes , J. Electrochem. Soc. **164**, E3448–E3456 (2017).
L.O. Vogt, C. Villevieille	*Elucidation of the reaction mechanisms of isostructural $FeSn_2$ and $CoSn_2$ negative electrodes for Na-ion batteries* doi: 10.1039/C6TA10535A, J. Mater. Chem. A **5**, 3865–3874 (2017).
K. Waiz, S.A. Tschupp, J. Herranz, T.J. Schmidt, Y. Ekinci, J.A. van Bokhoven	*State-of-the-art nanofabrication in catalysis* doi: 10.2533/chimia.2017.160, Chimia **71**, 160–169 (2017).
X. Wu, M. El Kazzi, C. Villevieille	*Surface and morphological investigation of the electrode/electrolyte properties in an all-solid-state battery using a Li_2S-P_2S_5 solid electrolyte* doi: 10.1007/s10832-017-0084-z, Journal of Electroceramics **38**, 207–214 (2017).
H. Xu, M. Bührer, F. Marone, T. J. Schmidt, F. N. Büchi, J. Eller	*Fighting the noise: Towards the limits of subsecond X-ray tomographic microscopy of PEFC* doi: 10.1149/08008.0395ecst, ECS Trans. **80**(8), 395–402 (2017).
L. Zhang, G. Chen, E.J. Berg, J.M. Tarascon	*Triggering the in situ electrochemical formation of high energy density cathode material from MnO_2* doi: 10.1002/aenm.201602200, Adv. Energy Mater. **7**, 1602200 (2017).

Talks

Invited Talks

E.J. Berg — *Unveiling irreversible side-reactions in Li-ion batteries with online electrochemical mass spectrometry*
232nd Electrochemical Society Fall Meeting, MD, USA, October 4, 2017.

E.J. Berg — *Electrode/electrolyte stability in Li-ion batteries: Operando gas analysis*
Heraeus-Seminar in-operando characterization of energy materials, Bad Honnef, Germany, August 24, 2017.

E.J. Berg — *Advanced characterization of interfaces in Li-ion batteries*
Seminar at the Department of Physics, Chalmers Technical University, Sweden, April 7, 2017.

J. Billaud — *Enhanced rate performance in electrode materials for lithium-ion batteries*
International Battery Seminar & Exhibit, Fort Lauderdale, USA, March 20–23, 2017.

P. Boillat — *Use of $^{1}H - ^{2}H$ isotope exchange with neutron radiography in fuel cell research*
21st International Conference on Solid State Ionics, Padova, Italy, June 22, 2017.

F.N. Büchi — *Tomographic imaging - Insights into membrane degradation and water management*
GM - Global Propulsion Systems, Pontiac, MI, USA, October 6, 2017.

F.N. Büchi — *Phosphoric acid migration in HT-PEFC*
231th ECS Meeting, New Orleans, LA, USA, June 29, 2017.

F.N. Büchi — *Herausforderungen von Power-to-Gas Anlagen – die ESI-Plattform am PSI*
Siemens Energy-Systems Kunden Tag, Zürich-Oerlikon, June 16, 2017.

F.N. Büchi — *Application of fuel cells for UPS*
8th European HPC Infrastructure Workshop, Mendrisio, April 6, 2017.

J. Eller — *Revealing sub-second dynamics of liquid water transport in polymer electrolyte fuel cells by 4D X-ray tomographic microscopy*
21st International Conference of Solid State Ionics, Padua, Italy, June 18–23, 2017.

L. Gubler — *Addressing transport selectivity and cycling stability in vanadium redox-flow batteries using an amphoteric membrane*
Asilomar Conference on Polymers for Fuel Cells, Energy Storage, and Conversion, Pacific Grove CA, USA, Feb 26 – March 1, 2017.

P. Novák — *Operando characterization of battery materials*
CHAINS 2017: Chemistry for the Future, Veldhoven, The Netherlands, December 6, 2017.

P. Novák — *Energy storage in batteries: Facts versus wishful thinking*
«Aperitivo con Energia», Lugano, September 28, 2017.

P. Novák — *Unraveling the ageing phenomena in NCM based cells*
Tokyo University of Science, Tokyo, Japan, March 13, 2017.

P. Novák — *Surface and bulk studies of Sn-alloys for Na-ion batteries*
ESICB Meeting, Kyoto, Japan, March 11, 2017.

P. Novák	*Lithium-sulphur batteries: Pitfalls and opportunities* IBA 2017 – International Battery Association Meeting, Nara, Japan, March 8, 2017..
T.J. Schmidt	*Water electrolysis and the oxygen evolution reaction* Ecole Polytechnique de Lausanne, Lausanne, December 15, 2017.
T.J. Schmidt	*Technology gaps for water electrolysis and the oxygen evolution reaction* Fritz Haber Institute, Berlin, Germany, December 12, 2017.
T.J. Schmidt	*Die Energiespeicher der Zukunft, Podiumsdiskussion* Das Energiesystem der Zukunft, Zürich, November 28, 2017.
T.J. Schmidt	*Speicherung als Schlüssel zur Energieversorgung von Morgen* Werkleiterseminar des Schweizerischen Gasverbands, Brunnen, November 24, 2017.
T.J. Schmidt	*Concepts of durable PEFC cathode catalysts* IEA Topical Meeting on Electrocatalysis for Fuel Cells, Berlin, Germany, November 15, 2017.
T.J. Schmidt	*Strategies on oxygen evolution catalyst developments for polymer electrolyte water electrolyzers* University of Cape Town and HySA/Catalysis, Cape Town, South Africa, November 2, 2017.
T.J. Schmidt	*Joint SCCER activity: Power-to-X* Bioenergy in Dialogue, 4th Biomass for Swiss Energy Future Conference, Brugg, September 2017.
T.J. Schmidt	*Commercialization of electrocatalysts in energy applications* Topsoe Catalysis Forum – Electrocatalysis 2017, Munkerupgaard, Denmark, August 24, 2017.
T.J. Schmidt	*Energiespeicher von morgen – die Grundlage der Versorgungssicherheit* Podiumsdiskussion, Smart Energy 2017 – Chancen Ergreifen, Rüschlikon, July, 2017.
T.J. Schmidt	*Fundamentals and applications of nano-sized perovskites for the oxygen evolution reaction* Lorentz Workshop Fundamental Electrocatalysis – Theory Meets Experiments, Leiden, Netherlands, June 26, 2017.
T.J. Schmidt	*The oxygen evolution reaction: The enigma in water electrolysis* International Conference on Electrolysis, Copenhagen, Denmark, June 12, 2017.
T.J. Schmidt	*The oxygen evolution reaction on nano-scaled perovskites* ECS Spring Meeting 2017, New Orleans, USA, May 31, 2017.
T.J. Schmidt	*Noble metal aerogels: From model studies to polymer electrolyte fuel cell performance* MRS Spring Meeting 2017, Phoenix, USA, April 19, 2017.
T.J. Schmidt	*The oxygen evolution reaction on nano-sized perovskites* MRS Spring Meeting 2017, Phoenix, USA, April 18, 2017.
T.J. Schmidt	*New membrane structures for vanadium redox flow batteries* Next Generation Energy Storage 2017, San Francisco, USA, February 16, 2017.
S. Trabesinger	*Challenges of lithium–sulphur battery chemistry* The International Conference dedicated to the 215th birth anniversary of Ignacy Domeyko «There is no Future without the Past. Science on the Interface of 19th–21^{st-} Centuries»; Vilnius, Lithuania, July 28–30, 2017.

C. Villevieille	*On the way to low cost Na-ion batteries* 68th Annual Meeting International Society of Electrochemistry (ISE), Providence, RH, USA, August 27 – September 1, 2017.
C. Villevieille	*Synchrotron and neutron based techniques applied to batteries, Solid State Ionics conference* 21st International Conference on Solid State Ionics (SSI), Padua, Italy, June 18–23, 2017.
C. Villevieille	*Operando studies of all-solid-state-batteries* 2nd FimPART conference, Bordeaux, France, July 11–13, 2017.
C. Villevieille	*Les batteries sodium, mythe ou réalité ?* Mobility days, Martigny, April 26, 2017.

Contributed Talks

D.F. Abbott, E. Fabbri, M. Borlaf, F. Bozza, R. Schäublin, T. Graule, T.J. Schmidt	*Correlating the local structure and electronic properties of nanoparticulate $Ni_xFe_{1-x}O$ with the electrochemical oxygen evolution activity via operando X-ray absorption spectroscopy* 2017 MRS Fall Meeting, Boston, USA, November 26 – December 1, 2017.
U. Babic, T.J. Schmidt, L. Gubler	*Towards understanding of component aging in dynamically operated polymer electrolyte water electrolyzers* 6th European PEFC and Electrolyser Forum, Lucerne, July 4–7, 2017.
J. Billaud, E. H.R. Tsai, M. Holler, M. Guizar-Sicairos, C. Villevieille	*Probing ageing mechanisms of Li-rich Mn, Ni, Co oxides in 3D using ptychographic tomography* Lithium Battery Discussions (LiBD), Arcachon, France, June 11–16, 2017.
C. Bolli, A. Guéguen, M. Mendez, E.J. Berg	*In situ monitoring of F^- formation in lithium ion batteries by OEMS* 268th Annual International Society of Electrochemistry Meeting, Providence, RI, USA, August 29, 2017.
F.N. Büchi, S. Lal. J. Eller, A. Lamibrac	*Evaporation of water from gas diffusion layers* 14th Symposium on Fuel Cell and Battery Modeling and Experimental Validation, Karlsruhe, Germany, March 3, 2017 and 232nd ECS Meeting, National Harbor, MD, USA, October 2, 2017.
X. Cheng, E. Fabbri, M. Nachtegaal, I.E. Castelli, M. El Kazzi, Raphael Haumont, Nicola Marzari, T.J. Schmidt	*Oxygen evolution reaction on perovskites: A combined experimental and theoretical study* International Conference on Electrolysis, Copenhagen, Denmark, June 12–15, 2017.
M. Cochet, A. Forner-Cuenca, V. Manzi, M. Siegwart, D. Scheuble, P. Boillat	*Novel concept for evaporative cooling of fuel cells: An experimental study based on neutron imaging* 6th European PEFC & Electrolyser Forum, Lucerne, July 4–7, 2017.
K. Ebner, J. Herranz, T.J. Schmidt	*A novel synthesis approach towards Fe-based non-noble metal oxygen reduction catalysts with finely tunable composition* E-MRS 2017 Fall Meeting, Symposium A: Materials for energy storage, production & harvesting applications, Warsaw, Poland, September 18–21, 2017.
E. Fabbri, M. Nachtegaal, X. Cheng, T. Binninger, T.J. Schmidt	*Insights into perovskite nano-catalysts as oxygen electrodes for the electrochemical splitting of water* 6th European PEFC & Electrolyser Forum, Lucerne, July 4–7, 2017.

G. Ferraresi, C. Villevieille, L. Czornomaz, P. Novák, M. El Kazzi	*Thin films of Si/Sn and SiO_2/SnO_2 as model anodes in Li ion batteries: Understanding the electrode/electrolyte interface reactions* 20th Topical Meeting of the International Society of Electrochemistry, Buenos Aires, Argentina, March 19–22, 2017.
L. Gubler, O. Nibel, T.J. Schmidt	*Amphoteric ion exchange membranes for vanadium flow batteries with higher transport selectivity and cycle stability* The International Flow Battery Forum (IFBF) 2017, Manchester United Kingdom, June 27–29, 2017.
S. Henning, H. Ishikawa, L. Kühn, J. Herranz, A. Eychmüller, T.J. Schmidt	*Pt-Ni Aerogels as cathode catalysts in polymer electrolyte fuel cells* 6th European PEFC and Electrolyser Forum, Lucerne, July 4–7, 2017.
S. Henning, H. Ishikawa, L. Kühn, J. Herranz, A. Eychmüller, T.J. Schmidt	*Durability of unsupported Pt-Ni aerogel cathodes in polymer electrolyte fuel cells* 68th Annual Meeting of the International Society of Electrochemistry, Providence, USA, August 27 – September 1, 2017.
S. Henning, H. Ishikawa, L. Kühn, J. Herranz, A. Eychmüller, T.J. Schmidt	*Investigating the durability of unsupported Pt-alloy aerogel cathodes* ECS Fall Meeting, National Harbor, USA, October 4, 2017.
J. Herranz, K. Ebner, B.-J. Kim, S. Henning, M. Nachtegaal, T.J. Schmidt	*A new approach for the synthesis of Fe-based O_2-reduction catalysts for PEFCs* 6th European PEFC and Electrolyser Forum, Lucerne, July 4–7, 2017.
J. Herranz, K. Ebner, B.-J. Kim, M. Nachtegaal, T.J. Schmidt	*A new approach for the synthesis of composition-controlled, Fe-based O_2-reduction catalysts for polymer electrolyte fuel cells* 232nd ECS Meeting, National Harbor (MD, USA), October 1–5, 2017.
B. Kim, X. Cheng, D.F. Abbott, E. Fabbri, F. Bozza, T. Graule, I.E. Castelli, L. Wiles, A. Niedzwiecki, N. Danilovic, K.E. Ayers, N. Marzari, T.J. Schmidt	*Understanding perovskites as electrocatalyst for oxygen evolution reaction* Swiss Competence Center for Energy Research *Supply of Electricity* (SCCER-SoE), May 9, 2017 and 232nd ECS Annual Fall Meeting, National Harbor, MD, USA, October 1–5, 2017.
S. Lal, A. Lamibrac, J. Eller, F.N. Büchi	*Analysis of water distribution and evaporation rate in gas diffusion layers* 6th European PEFC & Electrolyser Forum, Lucerne, July 4–7, 2017.
A. Lamibrac, F.N. Büchi, J. Eller	*Effects of GDL compression on SGL binder domains* 232th ECS Meeting, Symposium on Polymer Electrolyte Fuel Cells 17, National Harbor, MD, USA, October 1–5, 2017.
D. Leanza, C.A.F. Vaz, P. Novák, M. El Kazzi	*Monitoring the chemical and structural surface changes on single particles of commercial-like Li-ion battery electrodes* 20th Topical Meeting of the International Society of Electrochemistry, Buenos Aires, Argentina, March 19–22, 2017.
D. Leanza, C.A.F. Vaz, P. Novák, M. El Kazzi	*Nanoscale XPEEM spectroscopy reveals the origin and nature of the LTO electrode surface reactivity* 231st ECS Meeting, New Orleans, LA, USA, May 28 – June 1, 2017.
D. Leanza, C.A.F. Vaz, I. Czekaj, P. Novák, M. El Kazzi	*The controversial surface reactivity of $Li_4Ti_5O_{12}$ in the aprotic electrolyte disclosed with XPEEM* 68th ISE Annual Meeting, Providence, RI, USA, August 27 – September 1, 2017.

V. Manzi-Orezzoli, A. Forner-Cuenca, L. Gubler, T.J. Schmidt, P. Boillat	*Towards patterned wettability in gas diffusion media for PEFCs* 14th Symposium on Fuel Cell and Battery Modelling and Experimental Validation – ModVal 14, Karlsruhe, Germany, March 2–3, 2017.
V. Manzi-Orezzoli, A. Forner-Cuenca, M.Siegwart, L. Gubler, T.J. Schmidt, P. Boillat	*Synthesis of microporous layers with patterned wettability for polymer electrolyte fuel cells* 6th Symposium on Hydrogen, Fuel Cells and Advanced Batteries, Porto, Portugal, June 9–23, 2017.
E. Marelli, C. Marino, C. Villevieille	*Exploring the cobalt impact in the sodium-ion cathode materials P2-$Na_{0.67}Mn_iFe_jCo_kAl_zO_2$ (i+j+k+z=1)* European Materials Research Society Fall Meeting (E-MRS), Warsaw , Poland, September 18–21, 2017.
C. Marino, M. El Kazzi, E. J. Berg, M. He, C. Villevieille	*Interface and safety properties of Phosphorus-based negative electrodes in Li-ion batteries* 68th Annual Meeting International Society of Electrochemistry (ISE), Providence, RH, USA, August 27 – September 1, 2017.
O. Nibel, T.J. Schmidt, L. Gubler	*Highly selective ion exchange membranes for the all-vanadium redox flow battery* E-MRS Spring Meeting, Strasbourg, France, June 22–26, 2017.
F.J. Oldenburg, T.J. Schmidt, L. Gubler	*Tackling capacity fading with amphoteric membranes* The International Flow Battery Forum (IFBF) 2017, Manchester, United Kingdom, June 27–29, 2017.
A. Pătru, T. Binninger, B. Pribyl, T.J. Schmidt	*Progress in electrochemical CO_2 reduction in gas phase–design of efficient co-electrolyser systems* 232nd Meeting of the Electrochemical Society, National Harbor, USA, October 1–5, 2017.
H. J. Peng, S. Trabesinger, C. Villevieille, K. Leitner, H. Wolf, P. Novák	*Unraveling the ageing phenomena in NCM based cells* 68th ISE Annual Meeting, Providence, RI, USA, August 27 – September 1, 2017.
A. Permyakova, A. Pătru, J. Herranz, T.J. Schmidt	*Selectivity and efficiency of heat treated sputter deposited thin films of copper towards the carbon dioxide electro-reduction* 232nd Meeting of the Electrochemical Society, National Harbor, USA, October 1–5, 2017.
A. Permyakova, A. Pătru, J. Herranz, T.J. Schmidt	*Study of modified Cu thin films for electrochemical reduction of carbon dioxide* 6th European PEFC & Electrolyser Forum, Lucerne, July 4–7, 2017.
R. Robert, P. Novák	*Structural changes and microstrain in $Li_xNi_{0.8}Co_{0.15}Al_{0.05}O_2$ ($0 \le x \le 2$) electrode under overcharge and overdischarge* European Materials Research Society Spring Meeting, Strasbourg, France, May 22–26, 2017.
T. Schuler, T.J. Schmidt, F.N. Büchi	*Structural characterization of porous transport layers for polymer electrolyte water electrolysis cells* 6th European PEFC & Electrolyser Forum, Lucerne, July 4–7, 2017.
M. Siegwart, V. Manzi-Orezzoli, R. Woracek, M. Strobl, A. Tremsin, T.J. Schmidt, P. Boillat	*Neutrons for fuel cells: Conventional and time-of-flight imaging* ESS Science Day, Lund, Sweden, June 14, 2017.

M. Siegwart, R.P. Harti, M.V. Manzi-Orezzoli, J. Vallsecchi, C. Grünzweig, T.J. Schmidt, P. Boillat	*Visualization of water in gas diffusion layers with neutron dark-field imaging* European Fuel Cell Technology & Applications Conference - Piero Lunghi Conference, Naples, Italy, December 12–15, 2017.
M. Siegwart, V. Manzi-Orezzoli, R. Harti, J. Valsecchi, C. Gruenzweig, T.J. Schmidt, P. Boillat	*Visualization of water in fuel cell gas diffusion layers by neutron dark field imaging* 232nd Meeting of the Electrochemical Society, National Harbor, USA, October 1–5, 2017.
B. Sun, C. Sångeland, D. Brandell, J. Mindemark, E.J. Berg	*Electrochemical degradation processes of solid polymer electrolytes in Li-ion batteries: An online electrochemical mass spectrometry (OEMS) study* 232nd Electrochemical Society Fall Meeting, MD, USA, October 5, 2017.
Y. Surace, T. Schott, P. Lanz, S. Zürcher, M.E. Spahr, P. Novák, S. Trabesinger	*Long term cycling stability of SnO_2-graphite electrodes* MRS Fall Meeting 2017, Boston, MA, USA, November 26 – December 1, 2017.
H. Xu, T.J. Schmidt, F.N. Büchi, J. Eller	*Quantification of feature detectability of subsecond X-ray tomographic microscopy of PEFC* 6th European PEFC & Electrolyser Forum, Lucerne, July 4–7, 2017.
H. Xu, M. Bührer, F. Marone, T.J. Schmidt, F.N. Büchi, J. Eller	*Fighting the noise: Towards the limits of subsecond X-ray tomographic microscopy of PEFC* 232th ECS Meeting, Symposium on Polymer Electrolyte Fuel Cells 17, National Harbor, MD, USA, October 1–5, 2017.

Patents

J. Herranz, T.J. Schmidt	*Non-noble Metal oxygen reduction electrocatalysts using non-porous porosity precursors* EP 17001391, filed 2017.
A. Pătru, T. Binninger , B. Pribyl, T.J. Schmidt	*Co-electrolysis cell design for efficient CO_2 reduction from gas phase at low temperature* EP 17182823.9, filed July 2017

Posters

U. Babic, T.J. Schmidt, L. Gubler	*Degradation related phenomena in polymer electrolyte water electrolyzers (PEWE)* 6th International Seminar on Green Energy Conversion, Nagano, Japan, September 15–17, 2017.
J. Billaud, E. H.R. Tsai, M. Holler, M. Guizar-Sicairos, C. Villevieille	*Probing ageing mechanisms of Li-rich Mn, Ni, Co oxides using 3D ptychographic tomography* Lithium Battery Discussion (LiBD), Arcachon, France, June 11–16, 2017.
J. Billaud, F. Bouville, T. Magrini, C. Villevieille, A. R. Studart	*Enhanced rate performance in graphite electrodes for Li-ion batteries* Lithium Battery Discussion (LiBD), Arcachon, France, June 11–16, 2017.
T. Binninger, B. Pribyl, A. Pătru, S. Bjelic, D. Perego, P. Reuttimann, T.J. Schmidt	*Calibration method for mass spectrometry of interfering gases such as mixtures of CO, N_2, and CO_2* SCCER Heat and Electricity Storage, 6th Symposium, Martigny, October 25, 2017.

K. Ebner, J. Herranz, B.-J. Kim, T.J. Schmidt	*A novel synthesis approach towards Fe-based non-noble metal oxygen reduction catalysts with finely tunable composition* 33rd PSI Electrochemistry Symposium, Villigen, May 9–10, 2017 and SCS Fall Meeting 2017, Berne, August 9–10, 2017.
G. Ferraresi, M. El Kazzi, C.L. Tsai, S. Uhlenbruck, P. Novák, C. Villevieille	*Alloy-based electrodes for all-solid-atate Li-ion batteries based on garnet Ta-substituted $Li_7La_3Zr_2O_{12}$ solid electrolyte* 21st International Conference on Solid State Ionics (SSI), Padua, Italy, June 18–23, 2017.
G. Ferraresi, M. El Kazzi, C.-L. Tsai, S. Uhlenbruck, P. Novák, C. Villevieille	*All-solid-state Li battery based on c $Li_7La_3Zr_2O_{12}$ solid electrolyte and alloy anode materials* 20th Topical Meeting of the International Society of Electrochemistry, Buenos Aires, Argentina, March 19–22, 2017.
E. Flores, P. Novák, E.J. Berg	*Operando Raman spectroscopy of $LiNi_{0.8}Co_{0.15}Al_{0.05}O_2$ based Li-ion cathodes* LiBD 8 – 8th Lithium-Ion Battery Discussions, Arcachon, France, June 11–16, 2017.
E. Flores, P. Novák, E.J. Berg	*Operando single-particle Raman spectroscopy of NCA based Li-ion positive electrodes* LiBD 8 – 8th Lithium-Ion Battery Discussions, Arcachon, France, June 11–16, 2017 and Heraeus-Seminar in-operando characterization of energy materials, Bad Honnef, Germany, August 24, 2017.
P. Kitz, H. Kaiser, P. Novák, E.J. Berg	*Interfacial reactions in Li-ion batteries investigated by combining electrochemical quartz crystal microbalance and electrochemical impedance spectroscopy* LiBD 8 – 8th Lithium-Ion Battery Discussions, Arcachon, France, June 11–16, 2017 and Heraeus-Seminar in-operando characterization of energy materials, Bad Honnef, Germany, August 24, 2017.
A. Guéguen, C. Bolli, M. Mendez, E.J. Berg	*The role of TMSPx additives in stabilizing high-energy Li-ion batteries evidenced by operando gas analysisphoric acid invasion/withdrawal in GDLs using X-ray tomographic microscopy* International Battery Association Meeting, Nara, Japan, March 5–10, 2017.
A. Lamibrac, A. Mularczyk, J. Eller, F. Marone, F.N. Büchi	*Fast XTM imaging: Time resolved water transport and breakthrough in gas diffusion layer* 14th Symposium on Fuel Cell and Battery Modelling and Experimental Validation, Karlsruhe, Germany, March 2–3, 2017.
M. Mirolo, D. Leanza, C.A.F. Vaz, P. Novák, M. El Kazzi	*Structural and chemical surface investigation of NCA electrodes during early stages of cycling using XPS and XPEEM spectroscopy* LiBD 8 – 8th Lithium Battery Discussion – Electrode Materials, Arcachon, France, June 11–16, 2017.
A. Mularczyk, A. Lamibrac, F. Marone, F.N. Büchi, J. Eller	*Synchrotron based characterization of droplet detachment from gas diffusion layers* 647. WE-Heraeus-Seminar: Next Generation PEM Fuel Cells: Strategic Partnerships for Tackling Multiscale Challenges, Bad Honnef, Germany, July 2–5, 2017.
G. Nagy, V. Sproll, U. Gasser, T.J. Schmidt, L. Gubler, S. Balog	*Correlation between structure and performance-related properties of radiation-grafted proton-conducting membranes* International Conference on Neutron Scattering (ICNS) 2017, Daejeon, Korea, July 9–13, 2017, TuP 121.
FJ. Oldenburg, T.J. Schmidt, L. Gubler	*Novel membrane design strategies towards high performance vanadium flow batteries* 6th International Seminar on Green Energy Conversion, Nagano, Japan, September 15–17, 2017.
A. Pătru, T. Binninger, B. Pribyl, T.J. Schmidt	*Rational design of electrochemical cell configurations for co-electrolysis of carbon dioxide in gas phase at low temperature* Swiss Chemical Society meeting, Bern, August 21–22, 2017.

H. J. Peng, C. Villevieille, H. Wolf, K. Leitner, P. Novák, S. Trabesinger	*Direct proof of oxidation-and-transport processes within Li ion cells* IBA 2017 – International Battery Association Meeting, Nara, Japan, March 5–10, 2017.
A. Permyakova, A. Pătru, J. Herranz, T.J. Schmidt	*Behavior of sputter deposited thin films of Cu and Cu oxide towards CO2 electroreduction* SCCER Heat and Electricity Storage, 6th Symposium, Martigny, October 25, 2017.
T. Schuler, T.J. Schmidt, F.N. Büchi	*Analysis of porous transport layers for proton exchange water electrolysis* ICE 2017, International Conference on Electroylsis, Copenhagen, Denmark, June 12–15, 2017.
M. Siegwart, R. Woracek, M. Strobl, V. Manzi, A. Tremsin, T.J. Schmidt, P. Boillat	*Distinction of liquid water and ice with neutron imaging* 14th Symposium on Fuel Cell and Battery Modelling and Experimental Validation – ModVal 14, Karlsruhe, Germany, March 2–3, 2017.
S.M. Taylor, A. Pătru, O. Nibel, L. Gubler, T.J. Schmidt	*Insights into performance and degradation of carbon based negative electrode in the all vanadium redox flow cell* IFBF Meeting, Manchester, UK, June 26–29, 2017.
A.O. Tezel, S. Sunde, D.K. Streich, A. Guéguen, J.L. Gómez-Cámer, P. Novák, A.M. Svensson	*Effect of a boron based anion receptor on graphite anode for Li-ion batteries* IBA 2017 – International Battery Association Meeting, Nara, Japan, March 5–10, 2017.
X. Wu, C. Villevieille, P. Novák, M. El Kazzi	*XPS characterization of an interface between a Li_3PS_4 solid electrolyte and common lithium-ion battery electrode materials* LiBD 8 – 8th Lithium Battery Discussion – Electrode Materials, Arcachon, France, June 11–16, 2017.
X. Wu, M. El Kazzi, C. Villevieille	*Screening interfacial stability of various electrode materials cycled with a-Li_3PS_4 solid electrolyte using XPS* Lithium Battery Discussion (LiBD), Arcachon, France, June 11–16, 2017.
X. Wu, C. Villevieille, P. Novák, M. El Kazzi	*Interfacial investigation of common lithium-ion battery electrode materials using a Li_3PS_4 solid electrolyte* 21st International Conference on Solid State Ionics (SSI), Padua, Italy, June 18–23, 2017.
H. Xu, T.J. Schmidt, F.N. Büchi, J. Eller	*Contrast to noise ratio evaluation for X-ray computed tomographic imaging of water in PEFCs* 14th Symposium on Fuel Cell and Battery Modeling and Experimental Validation, Karlsruhe, Germany, March 2–3, 2017.

Conferences & Workshops Organizations

F.N. Büchi, T.J. Schmidt	*17th Symposium on Polymer Electrolyte Fuel Cells PEFC 17* 232nd ECS Meeting, National Harbour, MD, USA, October 1–6, 2017. Members of Organizing committee

Members in External Committees

P. Novák	*International Meetings on Lithium Batteries LLC* Director
P. Novák	*CIC Energigune, Vitoria, Spain* Member of Scientific Committee
P. Novák	*Qatar National Research Fund (QNRF)* Expert Evaluator
P. Novák	*The 3rd International Forum on Progress and Trends in Battery and Capacitor Technologies, Vitoria-Gasteiz, Spain* Member of the Scientific Advisory Committee
P. Novák	*Symposium Series «Advanced Battery Power Conference»* Member of Scientific Advisory Board
T.J. Schmidt	*The Journal of the Electrochemical Society* Associate Editor
T.J. Schmidt	*Kopernikus Project Power-to-X* Member of Scientific Council
T.J. Schmidt	*Swiss Hydrogen SA, Fribourg* Board of Directors
T.J. Schmidt	*European Academy of Sciences Advisory Council* Working Group Member *Dedicated Energy Storage (Task: Filing of Advisory Document for European Commission)*
T.J. Schmidt	*The Electrochemical Society* Individual Membership Committee
T.J. Schmidt	*Competence Center Energy & Mobility Switzerland* Member of Steering Board
T.J. Schmidt	*Technical University of Denmark, Lyngby* *4M Centre – Mechanisms, Materials, Manufacturing and Management – Interdisciplinary Fundamental Research to Promote Commercialization of HT-PEMFC* Member of Technical Steering Committee
T.J. Schmidt	*University of Cape Town (South Africa)* Member of Technical Steering Committee *HySA/Catalysis*

S. Trabesinger	*The Research Council of Norway (RCN)* Member of Peer Review Panel/Expert Evaluator
S. Trabesinger	*Qatar National Research Fund (QNRF)* Expert Evaluator
S. Trabesinger	*European Commission, Research Executive Agency* Expert Evaluator/Monitor

Editorial Work

F.N. Büchi, T.J. Schmidt (Co-Editors)	*Polymer Electrolyte Fuel Cells 17 (PEFC 17)* ECS Transactions **80** (8), The Electrochemical Society, Pennington, NJ, USA (2017).
T.J. Schmidt (Co-Editor)	*Selected Proceedings from the 231st ECS Meeting, New Orleans, LA, 2017* ECS Transactions **77** (11), The Electrochemical Society, Pennington, NJ, USA (2017).
T.J. Schmidt (Co-Author)	*Valuing dedicated storage in electricity grids* EASAC Policy Report 33 (2017). ISBN: 978-3-8047-3729-7. http://www.easac.eu/energy/reports-and-statements/detail-view/article/valuing-ded.html.
C. Gloor, L. Gubler, T.J. Schmidt	*PSI Electrochemistry Laboratory Annual Report 2016* doi: 10.3929/ethz-a-007047464, ISSN 1661-5379

Paul Scherrer Institut :: 5232 Villigen PSI :: Switzerland :: Tel. +41 56 310 21 11 :: Fax +41 56 310 21 99 :: www.psi.ch